7-10-2014 12:00 AM

The Influence of Microstructure on the Corrosion of Magnesium Alloys

Robert M. Asmussen
The University of Western Ontario

Supervisor
Dr. David Shoesmith
The University of Western Ontario

Graduate Program in Chemistry
A thesis submitted in partial fulfillment of the requirements for the degree in Doctor of Philosophy

THE INFLUENCE OF MICROSTRUCTURE ON THE CORROSION OF MAGNESIUM ALLOYS

(Thesis format: Integrated Article)

by

R. Matthew Asmussen

Graduate Program in Chemistry

A thesis submitted in partial fulfillment
of the requirements for the degree of
Doctor of Philosophy

School of Graduate and Postdoctoral Studies
Western University
London, Ontario, Canada

Abstract

This thesis reports a series of investigations into the influence of microstructure on the corrosion of Mg alloys. Mg alloys are prime candidates for the light-weighting of automobiles however any extensive applications are limited by their high corrosion rates. The corrosion resistance is further hindered by the susceptibility of Mg alloys to microgalvanic coupling occurring between the Mg matrix and the secondary microstructures in the alloys. This process and the individual contributions to it must be understood to improve Mg alloy design for automotive applications, develop methods for extending the lifetime of Mg alloys and developing models to successfully predict the corrosion behaviour of Mg alloys.

An experimental procedure for tracking corrosion on lightweight alloys has been developed using a combination of microscopy and corrosion studies using commercial sand cast magnesium AM50 alloys. Corrosion penetration depths were measured and characterized with CLSM and SEM/XEDS, respectively. Corrosion depths on α-grains in the alloys were expressed as a function of their Al content. Al-rich β-phases and eutectic α-phase microstructures were observed to be most corrosion resistant due to an enrichment of Al, identified with TEM, near the oxide/alloy interface. Sand cast alloys were found to be susceptible to major corrosion events in regions with depleted Al content.

The corrosion of sand, graphite and die cast Mg AM50 alloy were compared in 1.6 wt% NaCl solution to determine the influence of microstructure size and distribution of Al. The differences in corrosion mechanism were determined using electrochemical impedance spectroscopy and the morphology and distribution of corrosion damage

determined using scanning electron microscopy and confocal scanning laser microscopy. The corrosion performance improved in the order sand cast < graphite cast < die cast. This was shown to be due to the increasing tightness of the α-Mg/β-phase/Al-containing microstructural network, which lead to an increased protection of the surface by Al-enriched eutectic and a decrease in the probability of initiating a major damage site on an α-Mg region with low Al content.

Al-Mn intermetallic particles are active cathodes in the microgalvanically-coupled corrosion of Mg alloys. Domes of corrosion product, mainly $Mg(OH)_2$, collect on the particles as corrosion proceeds. The electrochemical behaviour (corrosion potential, potentiodynamic polarization, and potentiostatic measurements) of two Al-Mn intermetallic materials (Al- 11 wt% Mn and Al-25 wt% Mn) has been studied in 0.275 M NaCl and 0.138 M $MgCl_2$ solutions to simulate the cathodic behaviour of Al-Mn particles during the corrosion of a Mg alloy. Following a 20 h polarization at -1.55 V (vs. SCE), the Al-Mn intermetallic suffered dealloying of Al and the growth of Al hydroxide and Mn-oxide containing surface layers. A similar electrochemical treatment in $MgCl_2$ solution lead to the accumulation of a $Mg(OH)_2$ layer on the alloy surface which lowers cathodic reactivity and partially protects the intermetallic from dealloying. This electrochemical simulation of behaviour experienced on the microscale by Al-Mn intermetallics on corroding Mg alloys confirms the appearance of corrosion product domes on Al-Mn intermetallics during the corrosion of Mg alloys is an indication of their cathodic behaviour.

The corrosion behaviour of Mg alloy ZEK100 was investigated in water and in chloride containing environments. The alloy comprised an α-Mg matrix and a wide

spread dispersion of T-phase (Mg_7Zn_3Nd) and Zr-rich particles present as secondary phases. Potentiodynamic polarization measurements showed the corrosion resistance of the ZEK100 improved with decreasing chloride content. Intermittent immersions in 0.16 wt% NaCl showed corrosion occurred preferentially along grain boundaries interlinking the secondary phase particles some of which acted as active cathodes microgalvanically-coupled to the α-Mg matrix. This grain boundary sensitivity appeared to be a consequence of the depletion of the alloying elements, especially Zn, at these locations. Of the three types of secondary phase identified, T-phase, Zr and Fe-containing Zr particles, the latter were the dominant active cathodes. This was demonstrated by experiments in pure water when grain boundary corrosion was avoided and active cathodes could be identified by a small surrounding zone of corroded α-Mg and an accumulated dome of corrosion product on the active particle.

The suppression of the corrosion of AM50 Mg alloys in NaCl solutions was investigated using galvanic coupling and chronopotentiometric techniques. When galvanically coupled to pure Mg, sand, graphite and die cast AM50 alloys yielded a net cathodic current between -15 $\mu A/cm^2$ and -30 $\mu A/cm^2$, and limited corrosion damage was observed on the coupled surfaces compared with uncoupled surfaces. This protective effect was artificially simulated chronopotentiometrically by applying cathodic current to the die cast AM50 alloy. Current densities as low as -0.1 $\mu A/cm^2$ were found to resist the initiation of extensive corrosion. This effect is attributed to the ability of the applied current to satisfy the cathodic demand for current at microstructural features such as Al-Mn intermetallics leading to a temporary decoupling of the microgalvanic linkage between the particles and the α-Mg matrix.

The corrosion of the sand cast AM50 alloy has been studied in ethylene glycol containing 3 mM NaCl using a range of electrochemical techniques including electrochemical impedance spectroscopy and scanning electrochemical microscopy. Scanning electron microscopy and energy dispersive X-ray analyses were used to locate and elementally analyze the microstructural features of the alloy and to locate and correlate their relationship to SECM mapping. Confocal scanning laser microscopy was used to observe the nature and distribution of corrosion damage. By switching from an aqueous corrosion medium to ethylene glycol, it was shown that the corrosion of sand cast AM50 alloy was significantly suppressed thereby quenching H_2 evolution. The corrosion activity of the AM50 alloy was mapped using the feedback mode of scanning electrochemical microscopy. Ferrocenemethanol, serving as a redox mediator, can be used as a cathodic site contrasting agent exposing the reactive anodic areas of the corroding surface. These studies confirmed that the corrosion mechanism of Mg is the same in ethylene glycol as it is in water, and that studies in this solvent can be used to elucidate the reaction features obscured by rapid corrosion in water.

This thesis provides an essential contribution to the understanding of the microscaled corrosion of Mg alloys. The methodology developed can be further applied to a wide range of Mg alloys to investigate their behaviour. An *ex-situ* identifier of cathodic activity, a corrosion product dome, was confirmed; allowing for ease of identification of microgalvanic cathodes in future investigations. New approaches to controlling the corrosion rate of Mg alloys were also reported involving the application of small cathodic currents and introduction of ethylene glycol as the exposure medium.

Keywords:

magnesium alloys, corrosion, magnesium, microscopy, lightweight alloys, cathodic protection,

Co-authorship Statement

This thesis contains published data. For the work I was the lead investigator and writer and performed the experimental portions with assistance from:

Chapter 3 P. Jakupi assisted with CLSM experimental design, M. Danaie performed TEM analysis, G. Botton and D. Shoesmith assisted with editing.

Chapter 4: W. Binns assisted with electrochemical measurements, P. Jakupi and D. Shoesmith with editing.

Chapter 5: R. Partovi-Nia performed XRD analyses, W. Binns, P. Jakupi and D. Shoesmith assisted with editing.

Chapter 6 : W. Binns, P. Jakupi and D. Shoesmith assisted with editing.

Chapter 8: W. Binns assisted with electrochemical measurements, SECM was performed at McGill University by P. Dauphin Ducharme and U. M. Tafashe, J. Mauzeroll, P. Jakupi and D. Shoesmith assisted with editing.

Acknowledgements

This thesis would not have been remotely possible without the guidance and support of my supervisor, Dr. Dave Shoesmith. His mentorship allowed me to grow as a researcher and made my doctoral studies a fully enjoyable experience. I can't begin to express my gratitude in words for the opportunities granted and example set by him throughout the past 3.5 years. The only way of saying thanks is to take the lessons learnt from him, in research and life, and continue applying them throughout my career. That, of course, does not include choice of pro-sports teams to back

The members of the Shoesmith group, past and present, made my time in the lab productive and highly enjoyable. Specifically, Dr. Pellumb Jakupi who has been a part of this Mg project since its launch in May 2011 has been an invaluable co-worker and friend. It was not only corrosion knowledge I gained from working with him, but mainly the importance of selling yourself and your research to the scientific community and the importance of going just for one. Jeff Binns, whose introduction to this project coincided directly with its rapid growth, despite sometimes ruining our aura of success with a Canadiens hat. Dr. Jian Chen for being a great friend to have in the work place and also the greatest resource of knowledge I had at my disposal during this time, even when he had "just one question for me". Dr. Jaime Noel (old-clyde, new-clyde, nuclide), Dr. Dmitrij Zagidulin, and Dr. Zack Qin for their contributions, assistance and considerable knowledge during the term of my thesis.

I must thank my collaborators on this project: Dr. Gianluigi Botton and Dr. Mohsen Danaie from the Canadian Centre for Electron Microscopy at MacMaster University and Dr. Janine Mauzeroll, Dr. Ushula Tefashe and Philippe Dauphin

Ducharme from McGill University for their contributions and hospitality during research stints at both universities during the previous three years.

I owe an indescribable amount of gratitude to my parents, Kim and Brenda Asmussen, who never pushed or pressured me, let me choose my own path and have been nothing but supportive along the way. I attribute my successes, both previous and in the future, to the values and work ethic they have provided me. My siblings, Mike and Nerd, for the support they offer and friendship I can always count on from both of them. And to all my friends near and far, for the good times, the bad times and that one time…..

For her love, encouragement and witty bant…..ah who am I kidding, to Susan for being the best addition to my life and always reminding me no matter how tough things got, it was probably worse in Petawawa.

And for their contributions to my sanity over the past couple of years, I would like to thank the makers of great craft beer everywhere, Hot Italian Sandwiches, Shmokey Rob's, smooth (and needed) drams of scotch, DDP Yoga and the country roads around London.

This thesis is dedicated to my two biggest supporters,

The two men whom I try to mold myself after every day of my life,

The two men who instilled my character and drive,

And the two men who I wish were here to see this achievement,

Giovanni Cebrario and Jerrold Asmussen.

Table of Contents

Abstract ii

Co-authorship Statement vii

Acknowledgements viiii

Table of Contents xi

List of Symbols and Acronyms xix

List of Tables xxii

List of Figures xxiiii

Chapter One - Introduction 1

1.1 Introduction 1

1.2 Magnesium and its Alloys 7

1.3 Aqueous Corrosion 10

1.3.1 Thermodynamics of Corrosion 10

1.3.2 Kinetics of Corrosion 16

1.4 Corrosion of Magnesium and its Alloys 22

1.4.1 Corrosion of Mg 22

1.4.2 The Corroding Surface of Mg and its Alloys 24

1.4.3 Magnesium's Great White Buffalo: The Negative Difference Effect and Mg^+ 26

1.4.4 Magnesium and the Electrochemical Series 28

1.4.5 Role of Alloying Elements in the Corrosion of Mg Alloys. 30

1.4.5.1 Aluminum 30

1.4.5.2 Other Alloying Elements 31

1.4.6 Corrosion Behaviour of Mg Alloys 33

1.4.7 Microstructural Effects on Corrosion 35

1.4.7.1 Grain Size 36

1.4.7.2. Al-Mn Intermetallics 37

1.4.7.3 β-phase 37

1.5 Scope of Thesis 39

1.6 References 41

Chapter Two - Experimental: 55

2.1 Microscopy 55

2.1.1 Scanning Electron Microscopy (SEM) 55

2.1.1.1 Instrumentation 55

2.1.1.2 SEM Experimental Details 57

2.1.2 Focused Ion Beam (FIB) 59

2.1.3 Confocal Laser Scanning Microscopy (CLSM) 60

2.1.3.1 Instrumentation 60

2.1.4 Transmission Electron Microscopy (TEM) 62

2.1.4.1 Instrumentation 62

2.1.4.2 TEM Experimental Details 63

2.2 Sample Preparation 63

2.3 Intermittent Immersion Experiments 66

2.4 Chromium Treatment of Mg Alloys 68

2.5 Electrochemistry 70

2.5.1 Electrochemical Measurements 70

2.5.2 Electrochemical Impedance Spectroscopy (EIS) 72

2.5.3 EIS Experimental Details 75

2.6 References 76

Chapter Three – Tracking the Corrosion of Sand Cast AM50 Mg Alloys in Chloride Environments 79

3.1 Introduction 79

3.2 Experimental 80

3.2.1 Sample Preparation 80

3.2.2 Instrumentation 81

3.2.3 Tracking Corrosion on the Microscale 82

3.2.4 Surface Montage Imaging 82

3.3 Results 83

3.3.1 Corrosion Behaviour of Sand Cast AM50 Alloys in 1.6 wt. % NaCl 83

3.3.2 Role of Al in the Corrosion of Sand Cast AM50 Alloys 91

3.3.3 Major Corrosion Events on Sand Cast AM50 Alloys 97

3.4 Discussion 101

3.5 Summay and Conclusions 102

3.6 References 103

Chapter Four – The Microstructural Effects on Corrosion of AM50 Magnesium Alloys 106

4.1 Introduction 106

4.2 Experimental 107

4.2.1 Sample Preparation 107

4.2.2 Instrumentation 108

4.2.3 Intermittent Immersion Experiments 109

4.2.4 Electrochemical Analysis 110

4.3 Results 111

4.3.1 Alloy Characterization 111

4.3.2 Electrochemical Behaviour 115

4.3.3 Corrosion Behaviour in 1.6 wt. % NaCl 118

4.4 Discussion 124

4.5 Summary and Conclusions 127

4.6 References 127

Chapter Five – Simulating the Behaviour of Cathodic Sites in Mg Alloy Corrosion: The Behanviour of Al-Mn Alloys in NaCl and $MgCl_2$ 133

5.1 Introduction 133

5.2 Experimental 135

5.2.1 Materials 135

5.2.2 Electrochemical Measurements 136

5.2.3 Surface Analysis 136

5.3 Results 137

5.3.1 Al-Mn Intermetallics 137

5.3.2 Electrochemical Behaviour 139

5.3.3 Surface Behaviour 143

5.4 Discussion 151

5.5 Summary and Conclusions 156

5.6 References 157

Chapter Six – The Influence of Microstructure on the Corrosion of Mg Alloy ZEK100 162

6.1 Introduction 162

6.2 Experimental 163

6.2.1 Sample Preparation 163

6.2.2 Instrumentation 164

6.2.3 Electrochemical Measurements 164

6.2.4 Intermittent Immersion Experiments 165

6.3 Results 165

6.3.1 Surface Imaging 165

6.3.2 Electrochemical Effect of Chloride Ion Concentration 168

6.3.3 Intermittent Immersions in Chloride Solutions 168

6.3.4 Intermittent Immersions in Pure Water 181

6.4 Discussion 186

6.5 Summary and Conclusions 190

6.6 References 191

Chapter Seven – Sacrifical Anode and Cathodic Protection of Mg Alloys 196

7.1 Introduction 196

7.2. Experimental 197

7.2.1 Sample Preparation 197

7.2.2 Microscopy 198

7.2.3 Galvanic Coupling Experiments 198

7.2.4 Galvanostatic Control 198

7.3 Results 199

7.3.1 AM50 Alloy Coupled to Pure Mg 199

7.3.2 Chronopotentiometric Control of Die Cast AM50 Corrosion 201

7.4 Discussion 209

7.5 Summary and Conclusions 215

7.6 References 215

Chapter Eight – Reducing the Corrosion Rate of Mg Alloys Using Ethylene Glycol for Advanced Elctrochemical Imaging 220

8.1 Introduction 220

8.2 Experimental 221

8.2.1 Materials 221

8.2.2 Sample Preparation 222

8.2.3 Electrochemical Measurements 222

8.2.4 Electron Microscopy 223

8.2.5 Scanning Electrochemical Microscopy (SECM) 223

8.3 Results 224

8.3.1 AM50 Alloy Microstructure 224

8.3.2 Electrochemical Behaviour 224

8.3.3 Corrosion Process Control 228

8.3.4 Microstructure Behaviour in Ethylene Glycol 230

8.3.5 Scanning Electrochemical Microscopy in Ethylene Glycol 232

8.4 Discussion 239

8.5 Summary and Conclusions 242

8.6 References 243

Chapter Nine – Summary and Future Work 248

9.1 Summary 248

9.2 Future Work 252

Curriculum Vitae 255

List of Symbols and Acronyms

Symbols

A	transfer coefficient
a	activity
β	Tafel coefficient
b	Tafel slope
C	capacitance
d	diameter
e^-	electron
E	electrochemical potential
E_{CORR}	corrosion potential
E°	standard potential
ΔE	electrochemical potential difference
F	Faraday's constant
ΔG_{rxn}	Gibbs free energy change
K_{sp}	solubility product
I	absolute current
I_{CORR}	corrosion current
I_o	exchange current
i	current density
j	imaginary number
λ	wavelength
m	mass
M	molar mass

n	mol of electrons
η	overpotential
θ	phase angle
R	universal gas constant
R_p	polarization resistance
t	time
μ	chemical potential
μ°	standard chemical potential
ν	stoichiometric coefficient
V	applied potential
ω	angular frequency
wt%	weight percent
Z	impedance
Z’	real impedance
Z”	imaginary impedance

Acronyms

AC	alternating current
AOI	area of interest
ASTM	American Society for Testing of Materials
BSE	backscattered electrons
CLSM	confocal laser scanning microscopy
GM	General Motors Corporation
EELS	electron energy loss spectrometer
EDS	energy dispersive x-ray spectroscopy

EDX	energy dispersive x-ray spectroscopy
EIS	electrochemical impedance spectroscopy
FcMeOH	ferrocenemethanol
$FcMeOH^+$	ferroceniummethanol
LEIS	localized electrochemical impedance spectroscopy
FIB	focused ion beam
MEC	microelectrochemical cell
NDE	negative difference effect
PDP	potentiodynamic polarization
RE	rare earths
SECM	scanning electrochemical microscopy
SCE	saturated calomel electrode
SHE	standard hydrogen electrode
SE	secondary electrons
SEM	scanning electron microscopy
SKPFM	scanning Kelvin probe force microscopy
STEM	scanning transmission electron microscopy
SVET	scanning vibrating electrode technique
TEM	transmission electron microscopy
UWO	University of Western Ontario
XEDS	energy dispersive x-ray spectroscopy
XRD	x-ray diffraction spectroscopy

List of Tables

Table 1. 1 - List of common alloy elements and their effect in Mg alloy systems 8

Table 1. 2 - List of common Mg alloys and their applications 9

Table 1. 3 - The electrochemical series showing the standard reduction potentials for elements relevant to this thesis [61]..... 29

Table 1. 4 - List of comparative corrosion rates of Mg alloys 34

Table 5. 1 - Quantitative XEDS data of the major elements from the corresponding spectra in Figure 1 (c)……..139

List of Figures

Figure 1. 1 - a) Predicted fuel consumption by automotive fleet in Canada b) resulting emission by-product production (ton x 10^5 CO_2, NO_x, CO. SO_2 tons) 2

Figure 1. 2 - Canadian green house gas emissions by sector 3

Figure 1. 3 - improvement in fuel economy (orange) and engine efficiency (red) from the inception of fuel efficiency regulations to the present 5

Figure 1. 4 - the relationship between fuel economy and vehicle weight 6

Figure 1. 5 - Pourbaix diagram for the Al-water system at 25 °C and $[Al^{3+}] = 10^{-6}$ M .. 13

Figure 1. 6 - - Butler-Volmer relationship for a reversible metal dissolution/deposition reaction. The solid line represents the measurable current and the dashed lines are the partial currents for the two reactions 18

Figure 1. 7 - Butler-Volmer relationship for a metal dissolution/deposition reaction and an oxidant/reductant reaction. When coupled, the anodic component of one reaction and the cathodic component of the other have equal currents at E_{CORR} 19

Figure 1. 8 - Current-potential relationships for the anodic and cathodic half reactions plotted as Evans diagrams. The red markers indicate a system with an accelerated anodic process..... 21

Figure 1. 9 - Pourbaix diagram for the Mg-water system 23

Figure 1. 10 - Schematic of the accumulated corrosion product on Mg materials showing an outer platelet-like layer of $Mg(OH)_2$ and an inner layer of MgO 25

Figure 2. 1 - Schematic of a scanning electron microscope 56

Figure 2. 2 - Schematic showing the excitation volume caused by an incident electron beam and regions from which different signals are generated 58

Figure 2. 3 - Standard configuration of a confocal laser scanning microscope 61

Figure 2. 4 - Customized setup for CLSM analyses of corroded samples. 61

Figure 2. 5 - SEM BSE micrographs showing an AM50 Mg alloy surface in different stages of sample preparation and the gradual revealing of the alloy microstructure at a) 1200 grit SiC, b) 2400 grit SiC c) 4000 grit SiC, d) 3-µm diamond paste and e) colloidal silica polishing steps. 65

Figure 2. 6 - Experimental set up for intermittent immersion experiments. 65

Figure 2. 7- SEM images showing relocating of a selected AOI on a ZEK100 Mg alloy: a) location of AOI relative to scratch, b) the selected AOI, c) the surface with the scratch following a 24 h immersion in 0.16 wt% NaCl, d) the corroded AOI..... 67

Figure 2. 8 - SEM BSE micrographs of a AM60 Mg alloy following 48 h of immersion in 1.6 wt% NaCl showing; a) the corrosion damage observed in the middle region of the sample and b) identical corrosion damage located near the artificial scratch..... 69

Figure 2. 9 – CLSM micrographs of a) a colloidal silica polished AM50 Mg alloy displaying residual scratches marked with green arrows, b) following 96 h of immersion in 1.6 wt% NaCl; the green arrows show the same residual scratches are still visible 69

Figure 2. 10 - 3D CLSM micrograph of an AZ31 Mg alloy surface exposed for 48 h in 0.16 wt% NaCl: a) with the accumulated corrosion product on the surface and b) following removal of the corrosion product with chromium treatment..... 71

Figure 2. 11 - SEM micrographs of an AM50 sand cast sample a) after 12 h of immersion in 1.6 wt % NaCl and removal of the corrosion product and b) after a 12 h subsequent exposure of a location where major damage has occurred as a consequence of removing the corrosion product 71

Figure 2. 12 - The current response to a sine-wave potential input expected in an EIS experiment; θ indicates the phase angle between the two signals 73

Figure 2. 13 - Example of the estimation of Rp from a Nyquist EIS plot. Using the experimental data (red) the semicircle is extrapolated to the real axis (Z') to find Rp 73

Figure 3. 1 - a) SEM backscatter image of a selected area of interest (AOI) on a sand cast AM50 alloy and the corresponding EDX maps for b) Mg, c) Al, d) Mn 84

Figure 3. 2 - SEM and CLSM images of the AOI on an AM50 sample corroded through successive wet-dry cycles following a) 0 h, b) 24 h, c) 48 h, d) 72 h and e) 96 h exposure. The intermetallic marked with the arrow in a) is displayed in Figure 3.5. 85

Figure 3. 3- SEM micrograph of a sand cast corroded surface after 96 h continuous exposure in 1.6 wt% NaCl 87

Figure 3. 4 - Progress of corrosion near a β-phase region following a) 24 h, b) 48 h, c) 72 h, and d) 96 h of immersion in 1.6 wt% NaCl 89

Figure 3. 5 - Progress of corrosion near an Al-Mn intermetallic from Figure 2a) following a) 24 h, b) 48 h, c) 72 h, d) 96 h of immersion in 1.6 wt% NaCl. The white arrow in d) shows a Al-Mn intermetallic with no corrosion product dome..... 90

Figure 3. 6 - Identification of the location of α-grains on sand cast AM50 alloys using EDX mapping. Grains were numbered for further analysis shown in Figure 3.8. 92

Figure 3. 7- a) CLSM image showing the location of a depth profile line scan in green (bottom to top) and b) the corresponding changes in depth throughout the successive immersions. The β-phases are highlighted in grey. 92

Figure 3. 8 - The relationship between corrosion depth on α-grains and their Al content as a function of corrosion exposure time. 94

Figure 3. 9 - a) A FIB cross section of a β-phase region including the adjacent only slightly corroded region after 96 h of corrosion: b) a TEM slide of the selected region; c) O, Mg and Al EDX maps of the area marked in green; d) similar EDX maps of the red area shown in b). 95

Figure 3. 10 - a) an AOI on a sand cast AM50 alloy prior to corrosion, which was subsequently immersed for 24 h in 1.6 wt% NaCl: b) the AOI (red box) following the immersion surrounded by a major corrosion event..... 96

Figure 3. 11 - a) Montage image of a polished sand cast AM50 surface and images of the same area following b) 2 h, c) 3h and d) 4h of immersion in 1.6 wt% NaCl. New damage sites are marked with arrows..... 98

Figure 3. 12 - Progression of areas which sustained major corrosion events: the corrosion damage is observed to penetrate into the alloy but not to spread across the surface. 100

Figure 4. 1 - a) SEM image of a polished sand cast AM50 sample and the corresponding EDX maps showing the distribution of b) Al, c) Mg and d) Mn throughout the area of interest..... 112

Figure 4. 2 - a) SEM image of a polished graphite cast AM50 alloy and the corresponding EDX maps showing the elemental distribution of b) Al, c) Mg and d) Mn 113

Figure 4. 3 - a) SEM image of a polished die cast AM50 sample and the corresponding EDX maps showing the distribution of b) Al, c) Mg and d) Mn throughout the AOI ... 114

Figure 4. 4 – polarization (PDP) curves for the sand cast (green), graphite cast (blue) and die cast (red) AM50 alloys in 1.6 wt% NaCl at a scan rate of 0.5 mV/s after 20 min at E_{CORR} 116

Figure 4. 5 - Progression of E_{CORR} of the polished sand cast (green), graphite cast (blue) and die cast (red) AM50 alloys recorded in 1.6 wt% NaCl 116

Figure 4. 6 - Nyquist plots for the sand cast (green), graphite cast (blue) and die cast (red) alloys recorded in 1.6 wt% NaCl after 10 h exposure..... 117

Figure 4. 7 - a): SEM micrographs and CLSM images of the sand cast AM50 alloy after a sequence of 24 h intermittent immersions in 1.6 wt% NaCl The red arrow identifies domes of corrosion product appearing over sites of higher cathodic activity, b) SEM micrographs and CLSM images of the graphite cast AM50 alloy after a sequence of 24 h immersions in 1.6 wt% NaCl c) SEM micrographs and CLSM images of the die cast AM50 alloy after a sequence of 24 h immersions in 1.6 wt% NaCl. The red arrows indicate the location of a major corrosion event 119

Figure 4. 8 - SEM montage micrographs of the graphite cast AM50 after a) polishing, b) 2 h and c) 4 h intermittent immersions in 1.6 wt% NaCl. The red arrow in c) shows the first major event to initiate 121

Figure 4. 9 - SEM montage micrographs of die cast AM50 after a) polishing, b) 2 h and c) 4 h intermittent immersions in 1.6 wt% NaCl 121

Figure 4. 10 - Stereo micrographs of the a) sand, b) graphite and c) die cast AM50 alloys following a 24 h immersion in 1.6 wt% NaCl. The white blotches on the sand and graphite cast is the accumulation of corrosion product in the α-Mg regions while damage propagates laterally on the die cast 123

Figure 5. 1 - a) SEM micrograph of a polished AZ31 Mg alloy surface, b) SEM micrograph of the Al-Mn intermetallic marked with the white arrow in (a), c) XEDS spectra of the locations marked in (b), d) SEM micrograph of the domes of corrosion product that appeared above the Al-Mn intermetallic particles marked with the red arrow in (a) following 24 h immersion in 0.275 M NaCl 138

Figure 5. 2 - a) I) SEM backscatter micrograph of the a) Al-11Mn and b) Al-25 Mn surface following polishing and the corresponding XEDS maps for II) Al, III) Si and IV) Mn 140

Figure 5. 3 - Evolution of E_{CORR} over a 12 h period of immersion in 0.275 M NaCl and 0.138 M $MgCl_2$ for the Al-11Mn and Al-25Mn electrodes 142

Figure 5. 4 - PDP scans recorded on the Al-11Mn and Al-25Mn intermetallics in 0.275 M NaCl and 0.138 M $MgCl_2$ from E_{CORR} to -1.55 V at a scan rate of 1 mV/s 142

Figure 5. 5 - Potentiostatic current density vs. time profiles recorded on the Al-11Mn and Al-25Mn electrodes at -1.55 V in 0.138 M $MgCl_2$ and 0.275 M NaCl 143

Figure 5. 6 - optical micrographs of the Al-11Mn surface following a 20 h exposure to a) 0.275 M NaCl at E_{CORR}, b) 0.138 M $MgCl_2$ at E_{CORR} , b) 0.275 M NaCl at -1.55 V, and c) 0.138 M $MgCl_2$ at -1.55 V 144

Figure 5. 7 - a) SEM micrograph of the surface of the Al-11Mn electrode and b) the corresponding XEDS spectra recorded after 20 h cathodic polarization at -1.55 V in 0.275 M NaCl..... 146

Figure 5. 8 - a) SEM image of a FIB on the Al-11Mn electrode after cathodic polarization at -1.55 V in 0.275 M NaCl. The oxide/base metal interface is marked with the dashed line b) corresponding XEDS spectra for the locations indicated in (a) 147

Figure 5. 9 - a) SEM micrograph of the Al-11 Mn surface following cathodic polarization for 20 h at -1.55 V in 0.138 M $MgCl_2$, b) FIB cross section through the surface layer with the red dotted line denoting the substrate/layer interface and c) XEDS spectra recorded at the locations labelled in (b)..... 149

Figure 5. 10 - spectra identifying the phases present on the Al-11Mn electrodes after cathodic polarization in (a) 0.275 M NaCl and (b) 0.138 M $MgCl_2$ solution..... 150

Figure 6. 1 - a) BSE SEM micrographs of the ZEK100 surface. An intermetallic particle is marked with the red arrow. The corresponding XEDS maps for b) Mg, c) Zn, d) Zr 166

Figure 6. 2 - a) SEM micrographs of the particle marked by the blue arrow in Figure 1a), b) SEM micrograph of the particle marked with the red arrow in Figure 1a); and c) the XEDS spot analysis of the corresponding areas marked in the SEM images..... 167

Figure 6. 3 - a) BSE SEM micrograph of the particle in Figure 2 (b) and the corresponding XEDS maps for b) Mg, c) Nd and d) Zn..... 169

Figure 6. 4 – Potentiodynamic polarization scans recorded on a freshly polished ZEK100 sample at a scan rate of 0.167 mV/s following 1 h at E_{CORR} in 1.6 wt% NaCl (black), 0.16 wt% NaCl (red) and 0.016 wt% NaCl 170

Figure 6. 5 - SE SEM micrographs of a ZEK100 sample following a) 24 h, and b) 48 h immersions in a 1.6 wt% NaCl solution 171

Figure 6. 6 - Evolution of E_{CORR} recorded on a ZEK100 sample in a 0.16 wt% NaCl solution. At 24 h the sample was removed for analysis, and then re-immersed again in a new solution for an additional 24 h..... 171

Figure 6. 7 - SEM micrographs of a selected area of interest on a ZEK100 sample: a) and d) original polished surface : after 24 h of immersion (b) and e)) and 48 h of immersion (c) and f)) in a 0.16 wt% NaCl solution. The red arrows are reference points for two particles present in the AOI..... 173

Figure 6. 8 - 2.5D CLSM micrographs of an AOI on the ZEK100 following a) 24 h and b) 48 h immersion in a 0.16 wt% NaCl solution. A3D CLSM reconstruction of the AOI following c) 48 h immersion in a 0.16 wt% NaCl solution and d) following a chrome treatment to remove corrosion product..... 175

Figure 6. 9 – SE SEM micrographs of the ZEK100 sample surface after 48 h of immersion in a 0.16 wt% NaCl solution showing a) the grain boundary regions filled with corrosion product, b) following removal of the corrosion product, c) magnified image of the corroded grain boundary..... 176

Figure 6. 10 - SE SEM micrograph of a) a corrosion product dome present on the ZEK100 after 48 h corrosion in a 0.16wt% NaCl solution , and b) following removal of the corrosion product showing the particles beneath the deposit: XEDS maps for c) Zn, d) Nd, e) Zr, f) Fe..... 178

Figure 6. 11 - a) SEM image of two particles on the ZEK100 surface prior to corrosion and the corresponding XEDS maps for b) Mg, c) Zr, d) Fe, e) Nd, f) Zn..... 179

Figure 6. 12 – a) SE SEM micrograph of the particles shown in Figure 11 following 6 h of immersion in a 0.16 wt% NaCl solution, b)SE SEM micrograph of the cathodic sites

on the same sample after 6 h of immersion, c) dome of corrosion product indicating cathodic behaviour of the particle shown in the red box in (b): and the corresponding XEDS maps of the site for d) Mg, e) Zr, f) Fe 180

Figure 6. 13 – The progress of corrosion of on a ZEK100 sample in NanoPure^{TM} water monitored by SEM showing an AOI after a) 24 h, b) 48 h, c) 96 h, d) 192 h: the progress of corrosion around the particle at the bottom of the AOI after e) 24 h, f) 48 h, g) 96 h, h) 192 h of immersion 182

Figure 6. 14 – a) BSE SEM micrograph of the ZEK100 surface after 192 h of immersion in water, b) BSE SEM micrograph of the area marked with the red box in (a) and the corresponding XEDS maps for c) Zn, d) Nd, e) Zr and f) O, g) SE SEM micrograph of a separate particle on the ZEK100 surface and its corresponding XEDS maps for h) Zr and i) Fe 183

Figure 6. 15 – a) SE SEM micrograph of a corrosion product dome on the surface of the ZEK100 sample after 192 h of immersion in NanoPure water: b) SE SEM micrograph of a FIB cross at ¼ depth into the dome, c) FIB cross section at a location deeper into the dome; d) SEM image revealing particle below corrosion product dome (marked with red arrow), e) XEDS spectrum of the region marked with the red box in d)..... 185

Figure 6. 16 – Stereo micrographs comparing the bulk corrosion damage on the ZEK100 following a) 24 h of exposure in 0.16wt% NaCl and b) 192 h of exposure in NanoPure^{TM} water. The rolling direction (RD) of the samples is indicated with the arrow..... 187

Figure 7. 1 - Coupling current-time profiles measured on a galvanic couple between pure Mg and sand cast (red), graphite cast (green) and die cast (blue) AM50 alloys. The

Mg surface served as the working electrode and the corrosion damage accumulated is shown in the inset..... 200

Figure 7. 2 - Stereomicrographs showing the distribution of corrosion damage following a 48 h immersion uncoupled in a1.6 wt% NaCl solution of a) sand cast , b) graphite cast , c) die cast AM50 alloys and following 48 h of galvanic coupling of the d) sand cast, e) graphite cast and f) die cast AM50 alloys to pure Mg..... 202

Figure 7. 3 - Chronopotentiometric profiles recorded on the die cast AM5O in a 1.6 wt% NaCI solution with applied cathodic current densities of -100 $\mu A/cm^2$ (red), -1 $\mu A/cm^2$ (green) and -0.1 $\mu A/cm^2$ (blue)..... 203

Figure 7. 4 - Stereomicrographs of the die cast AM50 alloy following 96 h of immersion in a1.6 wt % NaCl solution: a) immersion with no electrochemical control, b) -100 $\mu A/cm^2$, c) -1 $\mu A/cm^2$ and d) -0.1 $\mu A/cm^2$ applied cathodic currents. 205

Figure 7. 5 - SEM micrographs of die cast AM 50 following 96 hr of immersion in a 1.6wt% NaCl solution: a) natural corrosion conditions; b) -1 $\mu A/cm^2$ cathodic current applied; c) -0.1 $\mu A/cm^2$ cathodic current applied. 206

Figure 7. 6 - a) The progression of E_{CORR} on a die cast AM50 alloy (blue) and potential recorded with an applied current hold of -10 µA (red) in a 1.6 wt% NaCl solution. The black arrow marks the location of a significant corrosion event. Stereomicrographs showing the surface of die cast AM50 alloy after exposure at b) E_{CORR} and c) -10µA galvanostatic hold and d) magnified view of the corrosion track initiated..... 208

Figure 7. 7 - Chronopotentiometric plots recorded the die cast AM50 alloy in a 1.6 wt % NaCl solution with application of a) -1 $\mu A/cm^2$ and b) -0.1 $\mu A/cm^2$ 210

Figure 7. 8 - Schematic illustration showing the microgalvanic coupling process on a Mg alloy : a) naturally corroding AM50 surface and b) a chronopotentiometrically controlled surface 213

Figure 8. 1 - The microstructure of a sand cast AM50 Mg alloy displaying the common microstructural features in a) SEM BSE image, and XEDS maps of (b) Mg, (c) Al, and (d) Mn. A β-phase structure is marked in the images with a green arrow and an Al-Mn intermetallic particle with a red arrow. 225

Figure 8. 2 - Evolution of ECORR measured on a sand cast AM50 Mg alloy in 3 mM NaCl in water (black) and ethylene glycol (red)..... 227

Figure 8. 3 - A PDP scan measured on a sand cast AM50 Mg alloy in 3 mM NaCl in ethylene glycol (red) and 3 mM NaCl in water 227

Figure 8. 4 - Progression of E_{CORR} measured on a sand cast AM50 Mg alloy over a 48 h exposure period in 3 mM NaCl + ethylene glycol with 2 mL additions of water made after 3 h and 25 h. 229

Figure 8. 5 - Nyquist plots recorded on a sand cast AM50 Mg alloy after 20 h exposure in 3 mM NaCl in water (black) and ethylene glycol (red). Inset: magnification of the high frequency response in the aqueous solution..... 229

Figure 8. 6 - a) Progress of E_{CORR} measured on a sand cast AM50 Mg alloy in 3 mM NaCl + ethylene glycol. EIS measurements were made just before and after the addition of 25 mL of water at ~ 2h: (b) Nyquist plots, and (c), (d) Bode plots recorded just before (black) and after (red) water addition 231

Figure 8. 7 - Back-scattered SEM micrographs of graphite cast AM50 Mg alloy a) polished surface, b) following 72 h in 0.016 wt% NaCl in ethylene glycol, c) an Al-Mn intermetallic marked in (a), d) the intermetallic following exposure having collected a mass of corrosion product 233

Figure 8. 8 - Montage SEM map recorded on a sand cast AM50 Mg alloy. The red box shows the location chosen for SECM measurements 234

Figure 8. 9 - area. The red arrow indicates two Al-Mn particles used to relocate this area in images. (a) A cyclic voltammogram recorded on the Pt microelectrode in 1 mM FcMeOH in ethylene glycol at 10 mV/s; (b) approach curves recorded at locations 1 and 2 (Figure 10 (a)) and the theoretically fitted approach curves (△ and ○) . I and II show the calculated approach curves for a diffusion limited reaction and an insulating unreactive surface, respectively. 236

Figure 8. 10 -(a) SECM map recorded on a sand cast AM50 Mg alloy in 1 mM FcMeOH + ethylene glycol using a Pt microelectrode polarized at 500 mV located 10 μm above the surface and rastered across the surface at 10 μm/s: (b) an overlay of SEM and SECM images of the same 236

Figure 8. 11 - (a) SEM BSE micrograph of the AOI on the sand cast AM50 Mg alloy following the SECM measurement shown in Figure 10; and (b) SEM SE micrograph of the AOI. Red arrows identify the same Al-Mn intermetallics in each micrographk 238

Fi gure 8. 12 - 3D CLSM micrographs of a) AM50 Mg alloy exposed for 24 h in ethylene glycol and b) the AOI on the AM50 Mg alloy following the SECM measurement in Figure 8.10 showing slight damage accumulation in regions which

generated positive feedback current in the SECM experiment; The red arrow shows the location of the two Al-Mn intermetallic particles. 238

Chapter One

Introduction

1.1 Introduction

Roads in Canada cover a distance of 1.4 million km, the equivalent of three and a half trips to the moon [1]. As a result of this vast coverage the transportation sector accounts for ~30 % of Canada's energy demand, a level which is continuously growing [2]. The petroleum demand of the transportation industry in Canada has grown from 79.6 million tons in 1990 to 103.1 million tons in 2011 [1]. Figure 1.1 (a) shows the expected fuel consumption by the automotive contribution to the transportation sector up to 2035 [1]. An increase in gasoline consumption is expected up to 2025, after which it is predicted to decrease to current levels by 2035. The emission by-products of petroleum based fuels (CO_2, CO, NO_x) are harmful to the environment and detrimental to air quality in urban areas. Figure 1.1 (b) shows the predicted annual Canadian production of these by-products, and a direct trend between emission production and gasoline consumption can be observed. By comparison to other sectors in Canada, the contribution to green house gas emissions by the transportation sector is the largest and expected to grow, Figure 1.2 [3].

In order to disturb the predicted trend, and lessen the environmental strain created by the automotive industry two main approaches are being pursued: 1) improvements in fuel efficiency and 2) powering the automotive fleet with alternative fuel sources. Beginning in the mid-1970's as a response to petroleum embargoes and increased competition from foreign automotive manufacturers, both Canada and the United State implemented fuel efficiency guidelines for automotive manufacturers, and the Canadian

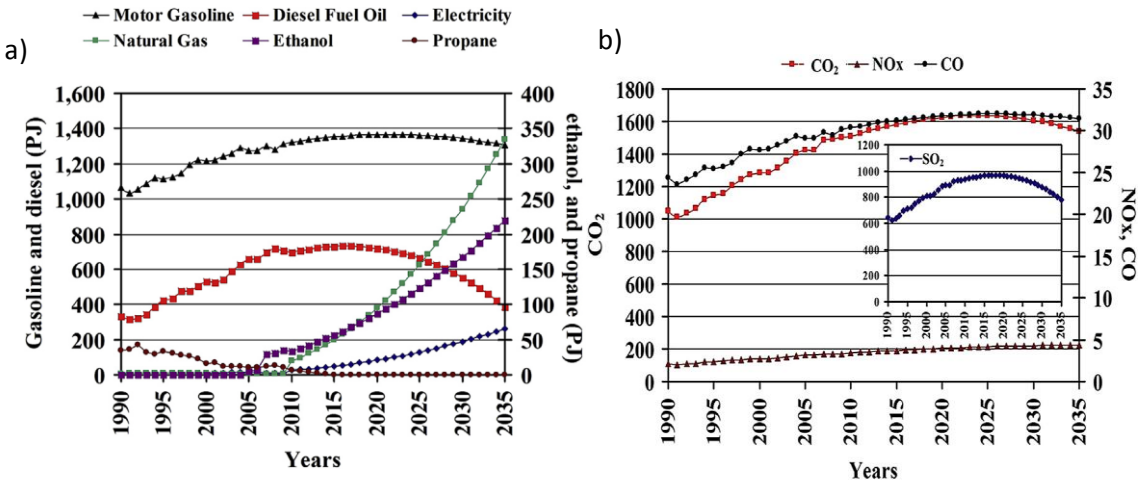

Figure 1. 1 - a) Predicted fuel consumption by automotive fleet in Canada b) resulting emission by-product production (ton x 10^5 CO_2, NO_x, CO. SO_2 tons) [1].

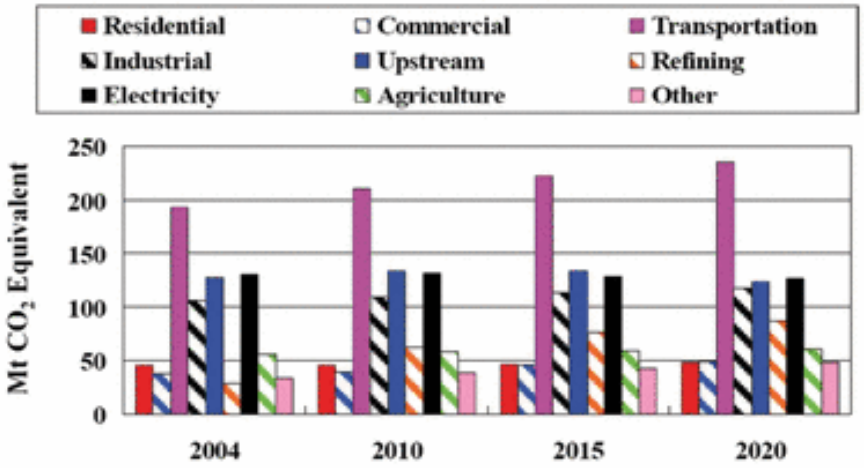

Figure 1. 2 - Canadian green house gas emissions by sector [3].

vehicle fleet has met these standards and out-performed the U.S. fleet annually [4]. The implementation of these laws have resulted in decreased fuel consumption and improved engine efficiency through improved vehicle, engine and drive train design, Figure 1.3 [4]. Alternative fueled, electric and hybrid vehicles have also been introduced to the market with sales increasing annually. Restrictions in Li-ion battery technology, as well as relatively low mileage per charge, have limited low cost and vast implementation of electric vehicles in North America (~150 km) [5].

Specifically, General Motors (GM) addressed this environmental concern and is set to reduce the CO_2 footprint of individual vehicles by 20% by 2020 [6]. Complementing fuel and engine technology advancement to meet this goal is the introduction of alternate structural materials in automobiles. A reduction in overall weight improves the fuel efficiency of vehicles, as shown in Figure 1.4 [7]. GM has acknowledged this benefit and will reduce the weight of vehicles by up to 15% by 2017 [6]. The most direct approach to lowering vehicle weight is replacement of steel and other heavy fabrication materials in vehicles with lightweight materials such as Al alloys, and the focus of this work, Mg alloys.

Auto-racing was the first vehicle sector to use lightweight Mg alloys in the 1920's, and Volkswagen became the first commercial vehicle to include Mg alloys on its Beetle in 1936 [8]. Today Mg alloys are included in the construction of a variety of vehicle components such as front end carriers, brackets, seats, wheels, transfer cases and instrument panels on a range of vehicles from the Ford F150 to the Chevrolet Corvette. To meet the auto industry's goal of weight reduction an increase in vehicle make up coming from lightweight materials is imminent. This project was funded by GM-Canada

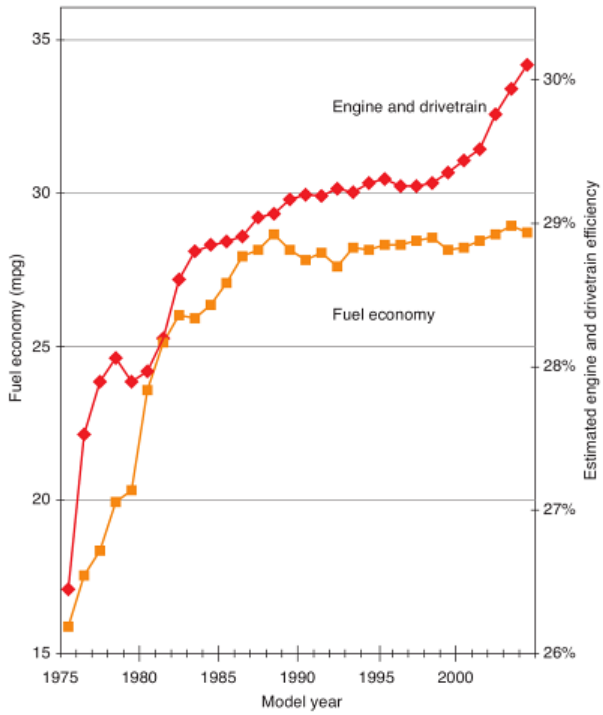

Figure 1. 3 - improvement in fuel economy (orange) and engine efficiency (red) from the inception of fuel efficiency regulations to the present [4].

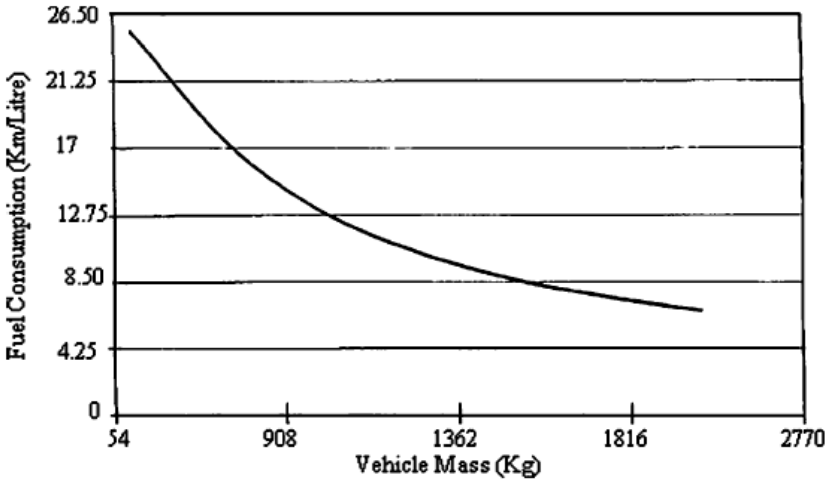

Figure 1. 4 - the relationship between fuel economy and vehicle weight [7].

to investigate the microstructure influenced corrosion behaviour of lightweight Mg alloys which are included or are candidates for inclusion in the vehicle fleet.

1.2 Magnesium and its Alloys

The primary advantage of Mg and Mg alloys is their light weight, with a density of 1.74 g/cm^3 [7]. This is 35 % lighter than Al (2.7 g/cm^3) and nearly five times lighter than steel (7.9 g/cm^3) [8]. Pure Mg has poor physical properties and alloying is necessary to tailor these properties to the specific requirements of a lightweight system. Magnesium alloys are also ductile, easily castable and have good damping characteristics [9]. These properties have led to its presence as a structural material in automobiles, aircraft, aerospace, ballistics, electronics, bio-implants and armor [7, 9-10].

Mg is alloyed with many other elements to garner selected characteristics and the common alloying elements, and the reason for their use, are shown in Table 1.1.

Varying the compositions of the additives can generate alloys fit for a desired application. Much work has been done in the development of Mg alloys and new compositions are constantly being developed to fill the lack of fundamental knowledge of magnesium alloys [9]. Some recent developments have seen the introduction of Mg-Zn-Sm [16], Mg-As [17], Mg-Li [18], Mg-Sr [19], Mg-Gd [20] in the past year. These alloys can potentially join the list of commonly used Mg alloys, shown in Table 1.2.

Table 1. 1 - List of common alloy elements and their effect in Mg alloy systems

Element	Alloy Designation	Properties	Ref
Ag	Q	Improve elevated temperature properties and creep when present with rare earths	[11]
Al	A	Improve castability, precipitation hardeners produced, corrosion protection	[11], [12]
Ca	X	Grain refinement, improves creep resistance, improve high temperature properties	[11], [13], [14]
Rare Earths (Ce, La, Nd)	E	Improve creep resistance, castability, grain refining, age hardening	[13], [15]
Si	S	Improves creep resistance	[13]
Sr	J	Improve creep resistance	[14]
Mn	M	Purification	[12]
Y	W	Improve tensile properties, grain refining	[13]
Zn	Z	Ductility and castability	[13]
Zr	K	Grain refiner, purification	[11], [12]

Table 1. 2 - List of common Mg alloys and their applications

Name	Composition (Balance Mg, wt%)	Example Uses	Ref
AZ31	3% Al-1% Zn-0.20%Mn	Aircraft fuselage, cell phones, laptops	[7], [20]
AZ91	9% Al- 0.7 % Zn, 0.13 % Mn	Door mirror brackets, valve and cam covers, die casting	[9], [20]
AM50	5% Al- 0.13 % Mn trace Si	Steering wheel arm, seats	[9]
AM60	6% Al- 0.13 % Mn	Car seat frames, steering wheel, inlet manifolds	[9][20]
ZE41	4% Zn – 1 % Nd	Ballistics, aircraft parts	[9]
QE22	2% Ag – 2% Nd	Aerospace	[21]
ZK 60	6% Zn - <1 % Zr	Military components, tent poles, sports equipment	[9]
WE 43	4.3 % Y – 3 % RE – 0.4 % Zr	Helicopter transmission, race car	[22], [23], [24]

One of the factors (along with cost and formability) standing in the way of extended application of Mg alloys is their poor corrosion resistance. Overcoming this deficiency begins with fully understanding the processes influencing the corrosion of Mg and its alloys.

1.3 Aqueous Corrosion

1.3.1 Thermodynamics of Corrosion

In the corrosion process of a material an interfacial reaction occurs between the material and its environment, in which the material is oxidized and an environmental species (H_2O, O_2) is reduced. The two processes form an electrochemical redox couple and, as an example: the corrosion of Mg materials in aqueous environments involves the coupling of two reactions [25]:

$$\text{Anodic: } Mg \rightarrow Mg^{2+} + 2\,e^- \tag{1.1}$$

$$\text{Cathodic: } 2\,H_2O + 2\,e^- \rightarrow H_2 + 2\,OH^- \tag{1.2}$$

The driving force for the corrosion process is the difference in equilibrium potentials for the two coupled half reactions. The tendency for the reaction to proceed is given by the molar Gibbs free energy change (ΔG_{rxn}):

$$\Delta G_{rxn} = \sum \nu_p \mu_p - \sum \nu_r \mu_r \tag{1.3}$$

Where μ_p and μ_r are the product and reactant chemical potentials and ν_p and ν_r are the stoichiometric coefficients. The chemical potential, μ, of a substance is defined as:

$$\mu = \mu^{\circ} + RT ln\, a \tag{1.4}$$

in (1.4) R is the universal gas constant, 8.314 J $K^{-1}mol^{-1}$, T is the temperature, μ° is the standard chemical potential of the species and *a* is the activity of the species. The Gibbs free energy of an electrochemical reaction at equilibrium can be defined as:

$$\Delta G_{rxn} = -nF\Delta E \tag{1.5}$$

where n is the number of moles of electrons exchanged in the reaction, F is Faraday's constant (96485 $C \cdot mol^{-1}$) and ΔE is the potential difference between the electrodes carrying the anodic and cathodic reactions ($\Delta E = E_{red} - E_{ox}$). Combining the three equations, 1.3, 1.4, and 1.5 yields the equilibrium potential (E_e) for a half reaction expressed by the Nernst equation. For dissolution of a metal species the equilibrium potential is defined as:

$$M_{(s)} \rightarrow M^{n+} + n\, e^{-} \tag{1.6}$$

$$(E_e)_{M^{n+}/M} = (E^o)_{M^{n+}/M} - \frac{RT}{nF} \ln a_{M^{n+}} \tag{1.7}$$

and for its coupled cathodic process, the equilibrium potential is:

$$Ox + n\, e^{-} \rightarrow Red \tag{1.8}$$

$$(E_e)_{Ox/Red} = (E^o)_{Ox/Red} - \frac{RT}{nF} \ln \frac{a_{red}}{a_{ox}} \tag{1.9}$$

where E° is the standard potential for the half reaction and *a* is the activity of the species. The common way to display the Nernst equation for chemical and electrochemical reactions of a material in aqueous environments is on a plot of potential vs. pH, known as a Pourbaix diagram [26].

The equilibrium between Al and water will be used as an example since the behaviour of Al is essential to portions of this work. The Al metal dissolution reaction is given by the reduction reaction:

$$Al^{3+}_{(aq)} + 3\,e^- \rightarrow Al_{(s)} \quad E°= -1.66\ V\ (vs\ SHE) \tag{1.10}$$

The Nernst equation for the reaction is:

$$(E_e)_{Al^{3+}/Al} = (E^o)_{Al^{3+}/Al} - \frac{RT}{nF}\ln\frac{1}{a_{Al^{3+}}} \tag{1.11}$$

Substituting in the known values gives (converting ln to log)

$$(E_e)_{Al^{3+}/Al} = -1.66 - \frac{0.059}{3}\log a_{Al^{3+}} \tag{1.12}$$

For a given temperature and Al^{3+} concentration, $(E_e)_{Al^{3+}/Al}$ is constant and independent of pH and will show up as a horizontal line in the Pourbaix diagram. The Pourbaix diagram of Al is shown in Figure 1.5 with E displayed vs. the saturated calomel electrode (-0.242 V vs. SHE) at $[Al^{3+}] = 10^{-6}$ M. The transition between Al and Al^{3+} is denoted by the red line in Figure 1.5. At the conditions on the red line Al and Al^{3+} will be in equilibrium with one another while at potentials above this line, the Al metal is not stable and will dissolve as Al^{3+}, and the Al will continue to dissolve until a new equilibrium is established in the system. At potentials below this line the Al exists as metallic Al and is stable. Any Al^{3+} present at potentials below the line will be reduced to $Al_{(s)}$.

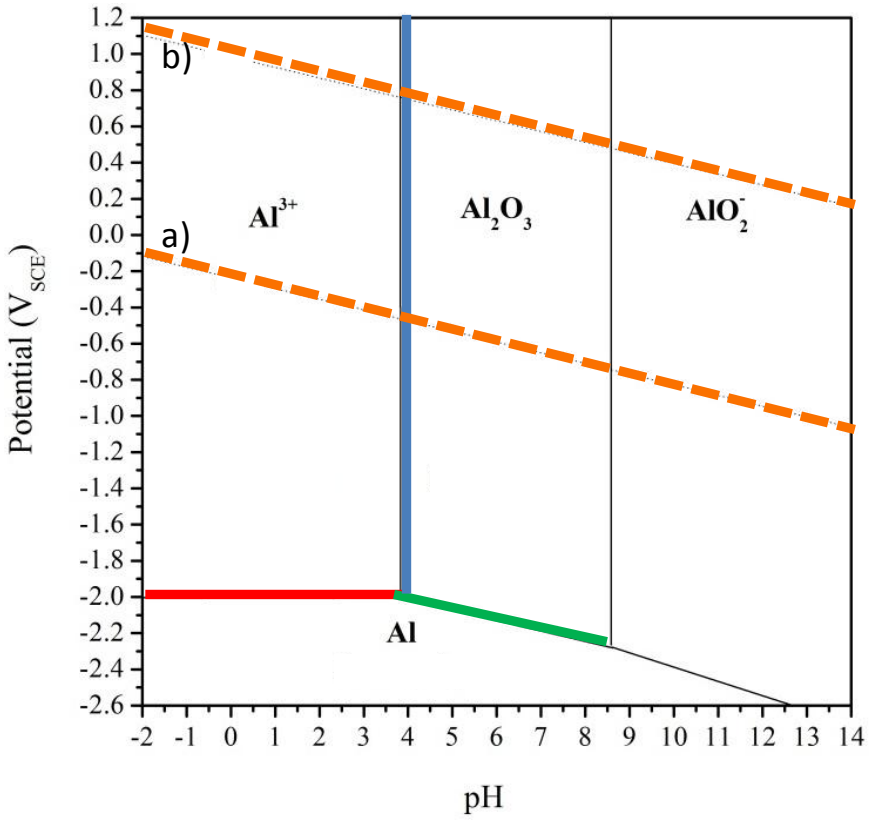

Figure 1. 5 - Pourbaix diagram for the Al-water system at 25 °C and $[Al^{3+}] = 10^{-6}$ M [27].

Metal dissolution reactions are not limited to solely electrochemical reactions and can involve water, protons, oxygen and other species. In this system, Al can react with water to form Al_2O_3 in the reaction:

$$Al_2O_{3(s)} + 6\ H^+_{(aq)} + 6\ e^- \rightarrow 2\ Al_{(s)} + 3\ H_2O_{(l)}\ E^o = -1.55\ V\ (vs\ SHE) \quad (1.13)$$

for which the Nernst equation is,

$$(E_e)_{Al_2O_3/Al} = -1.55 - \frac{0.059}{6}\log\frac{1}{a_{H^+}^6} \quad (1.14)$$

and can be rearranged to:

$$(E_e)_{Al_2O_3/Al} = -1.55 - 0.059\,pH \quad (1.15)$$

Now the equilibrium potential of this reaction is dependent on pH due to the involvement of protons, and will show up as a straight line with a slope of -0.059, marked in green in Figure 1.5. Above this line, Al_2O_3 is the stable species, while below it, metallic Al is stable. This equilibrium line between Al and Al_2O_3 theoretically extends into the stability region of Al^{3+} defined previously. Al^{3+} and Al_2O_3 can convert between one another via the following reaction:

$$2\ Al^{3+}_{(aq)} + 3\ H_2O_{(l)} \leftrightarrows Al_2O_{3(s)} + 6\ H^+_{(aq)} \quad (1.16)$$

This equilibrium reaction is a chemical reaction, and is independent of potential and depends only on the solubility product of the equilibrium, K_{sp}.

$$K_{sp} = \frac{a_{H^+}^6}{a_{Al^{3+}}^2} = 10^{-11.4} \quad (1.17)$$

In Figure 1.5, a $[Al^{3+}] = 10^{-6}$ M was used to construct the Pourbaix diagram and substitution of this value into the K_{sp} equation reveals this equilibrium is established at pH = 3.9. Therefore a vertical line, the blue line in Figure 1.5, represents the pH at which Al^{3+} and Al_2O_3 are in equilibrium with one another. The lines for the other reactions involving Al, $Al \rightarrow AlO_2^-$ and $Al_2O_3 \rightarrow AlO_2^-$ are calculated in a similar fashion.

There are two more lines of interest in the Pourbaix diagram, shown as orange dashes labelled (a) and (b) in Figure 1.5. These lines represent the oxidative and reductive decomposition of water in the following two reactions:

$$2\ H_2O + 2\ e^- \leftrightarrows H_2 + 2\ OH^- \text{ (a)} \quad (1.18)$$

$$2\ H_2O \leftrightarrows O_2 + 4\ H^+ + 4\ e^- \text{ (b)} \quad (1.19)$$

The equilibrium potentials for these reactions are also defined by the Nernst equation, are pH dependent and appear as lines with slopes of -0.059. In the region between the two lines water is stable. However, if the reacting surface is polarized to a potential below (line (a)) or above (line (b)) the line, the water reaction can be the coupled reaction to the metal species reaction. For example, the equilibrium line for Al^{3+}/Al is at a potential below the water equilibrium line for water reduction up to pH 4. Due to this scenario, Al is thermodynamically unstable in H_2O at pH <4 and will oxidize to Al^{3+} by coupling to the reduction of water. Between pH 4 and 9, Al will form a solid Al_2O_3 that could protect the metal from corrosion. This oxide will grow when Al oxidation is coupled with water reduction. Above pH 9, Al can corrode once again to AlO_2^- in water. Pourbaix diagrams are highly informative for the identification of possible species existing in a corrosion system, however care must be taken in interpreting them. While an oxide may be formed, the physical properties of the oxide

layer determine the extent of its protection to the base metal. The Pourbaix diagram also lacks kinetic information about the reacting system, which will be discussed in the next section.

1.3.2 Kinetics of Corrosion

When anodic and cathodic half reactions are coupled in a corrosion process they form a short circuited galvanic cell. The positive current from the anodic half reaction(s) (metal dissolution) is (are) equal and opposite in sign to the cathodic current from the reduction of the oxidant(s). This current is carried via electrons in the metal and by ions in solution. The resulting corrosion current, I_{CORR}, is defined as:

$$I_{CORR} = I_{anodic} = | I_{cathodic} | \tag{1.20}$$

If I_{CORR} is known, Faraday's law can be applied to calculate the amount of material corroded:

$$I_{CORR} = \frac{nFm}{Mt} \tag{1.21}$$

where n is mol of electrons passed, F is Faraday's constant (96485 $C \cdot mol^{-1}$), m is the mass of corroded material (g), M is the molecular weight of the material ($g \cdot mol^{-1}$) and t is the exposure time (s). However, the I_{CORR} is not readily measurable with an ammeter as the current flowing at the corroding surface is short circuited. Electrochemical analyses can be employed to determine I_{CORR} and E_{CORR} information about the corroding system. Focusing on a reversible metal dissolution/deposition reaction, $M \leftrightarrows M^{n+} + n\ e^-$, the Butler-Volmer equation, equation 1.22, shows the current-potential relationship for the process:

$$I = I_o \left[e^{\frac{\alpha F \eta}{RT}} - e^{\frac{(1-\alpha) F \eta}{RT}} \right] \quad (1.22)$$

where α is the transfer coefficient, η is the overpotential for the half reactions (a measure of how far away from the equilibrium potential, E_e, the reaction is), I_o is the exchange current. Figure 1.6 graphically demonstrates the Butler-Volmer relationship for this reversible process. The solid line is the measureable current while the dashed lines are the partial currents for the two half reactions. At sufficiently large overpotentials ($\eta = E - E_e$) one of the half reactions dominates and the measured current becomes equal to I_A or I_C. However, near E_e, both half reactions are occurring and the measured current is the sum, $I_A + (-I_C)$.

For a sufficiently high anodic overpotential, the cathodic component of the Butler-Volmer equation (far right term in equation 1.22) becomes negligible and the Butler-Volmer equation condenses to:

$$I = I_a = I_o e^{\frac{\alpha F \eta}{RT}} \quad (1.23)$$

which can be written logarithmically as,

$$\text{Log } I_a = \log I_o + 2.303 \frac{\alpha F}{RT} \eta \quad (1.24)$$

A plot of log I_a vs η would yield a straight line with an intercept I_o and a slope given by,

$$\frac{\alpha F}{2.303 RT} \quad (1.25)$$

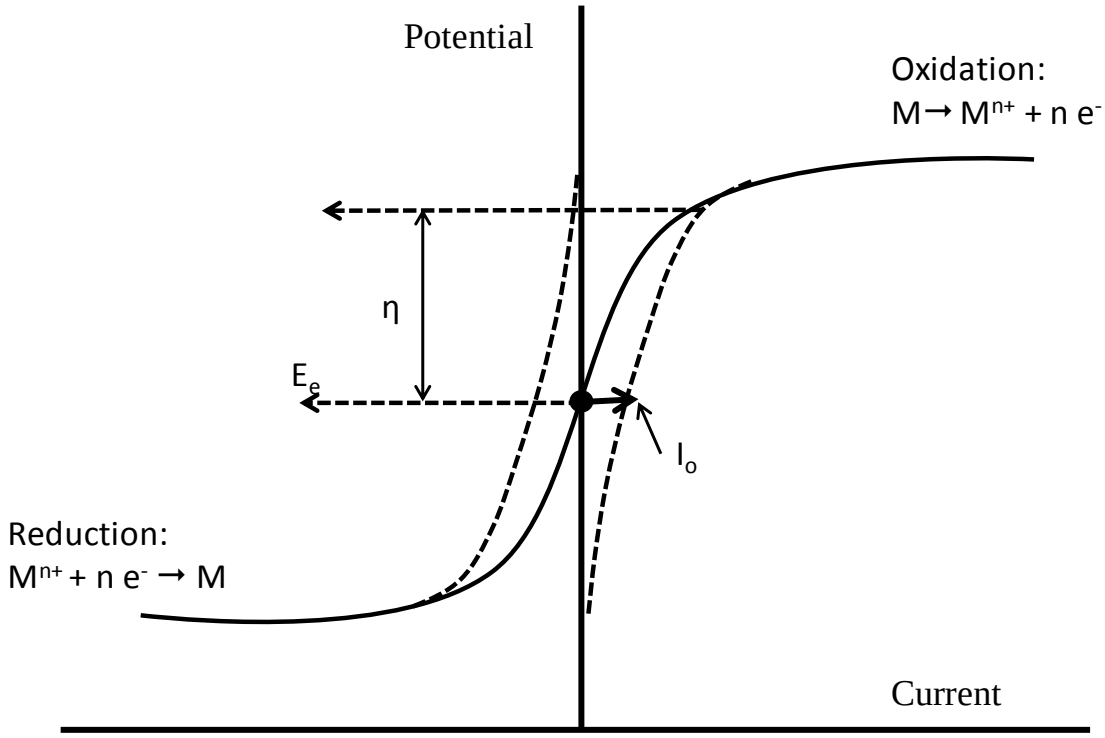

Figure 1. 6 - - Butler-Volmer relationship for a reversible metal dissolution/deposition reaction. The solid line represents the measurable current and the dashed lines are the partial currents for the two reactions.

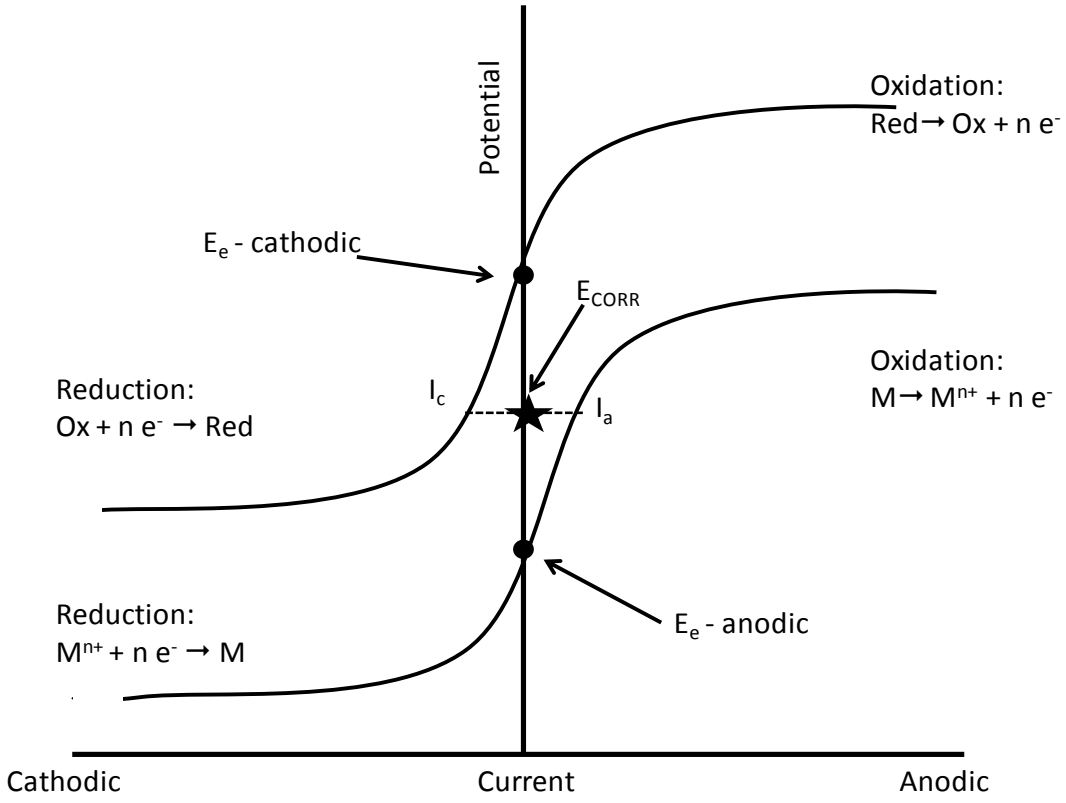

Figure 1. 7 - Butler-Volmer relationship for a metal dissolution/deposition reaction and an oxidant/reductant reaction. When coupled, the anodic component of one reaction and the cathodic component of the other have equal currents at E_{CORR}.

This term is deemed the Tafel coefficient, β. The same procedure can be carried out at high cathodic overpotentials.

For a corrosion reaction the anodic half of one reaction (e.g., the metal dissolution reaction) couples with the cathodic half of another (the oxidant reduction) reaction. If the equilibrium potentials of the two reactions are sufficiently separated then these reactions will be irreversible and only one of the two exponential terms in the respective Butler-Volmer equations will be required. A Butler-Volmer-like equation can be written for the corrosion reaction,

$$I = I_{CORR}\left[e^{\frac{\alpha_a F \eta_a}{RT}} - e^{\frac{-\alpha_c F \eta_c}{RT}}\right] \tag{1.26}$$

where α_a and α_c are the anodic and cathodic half reaction transfer coefficients and η_a and η_c are the anodic and cathodic half reactions. Figure 1.7 shows the coupling of two half reactions and their Butler-Volmer relationship. The potential established by the coupled reactions under open circuit conditions is the corrosion potential (E_{CORR}). At this potential both the anodic current (I_a) from the metal dissolution reaction and cathodic current (I_c) from the reduction of the oxidant are equal to one another. Both of the half reactions are polarized away from their respective E_e until equal currents are established. The overpotentials (η) in equation 1.26 are given by the difference between E_e and E_{CORR} for the two half reactions involved.

The influence of the kinetics of the two half reactions on E_{CORR} is best shown in an Evans diagram of potential vs. log I, Figure 1.8. The E_{CORR} of a system, and the resulting I_{CORR}, can be shifted as the half reaction kinetics are altered. In a corroding system, if the kinetics of the cathodic reaction rate remain the same (black line), and the

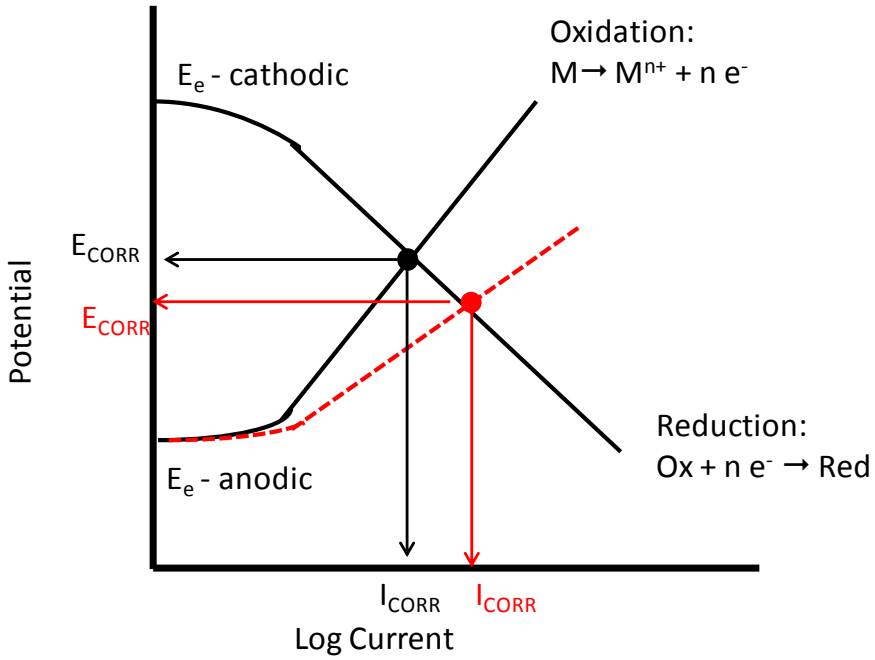

Figure 1. 8 - Current-potential relationships for the anodic and cathodic half reactions plotted as Evans diagrams. The red markers indicate a system with an accelerated anodic process.

anodic reaction kinetics are accelerated (red line) in which case higher currents would be observed at lower potential, E_{CORR} is lowered to a less positive value, and I_{CORR} would increase. A commonly applied trend is a decrease in E_{CORR} corresponds to an increase in I_{CORR}.

1.4 Corrosion of Magnesium and its Alloys

1.4.1 Corrosion of Mg

The corrosion of Mg appears a simple process, but is heavily debated. The simplicity of the general corrosion behaviour of Mg is seen in the Mg-H_2O Pourbaix diagram, Figure 1.9 [28]. Mg can only exist in its metallic state at very low potentials (< -2.4 V vs. SHE), and will be oxidized to Mg^{2+} above this potential. $Mg(OH)_2$ is the thermodynamically stable corrosion product above pH 8, and should be controlled by its K_{sp} (5.6×10^{-12}). This is an unusually straightforward system compared with many other metal-H_2O systems [26]. Two species are listed in the Pourbaix diagram whose existence is debatable (denoted with a ? in Figure 1.9): univalent Mg^{+} and MgO_x. Their importance will be discussed in subsequent sections.

With the equilibrium potential for Mg oxidation positioned well below the water stability region in the Pourbaix diagram (line (a)), the reduction of water is a readily available cathodic reaction to drive Mg. The corrosion half reactions are commonly reported as [25]:

$$\text{Anode} : Mg_{(s)} \rightarrow Mg^{2+} + 2\,e^{-} \quad (1.27)$$

$$\text{Cathodic:}\ 2\,H_2O_{(l)} + 2\,e^{-} \rightarrow H_{2(g)} + 2\,OH^{-}_{(aq)} \quad (1.28)$$

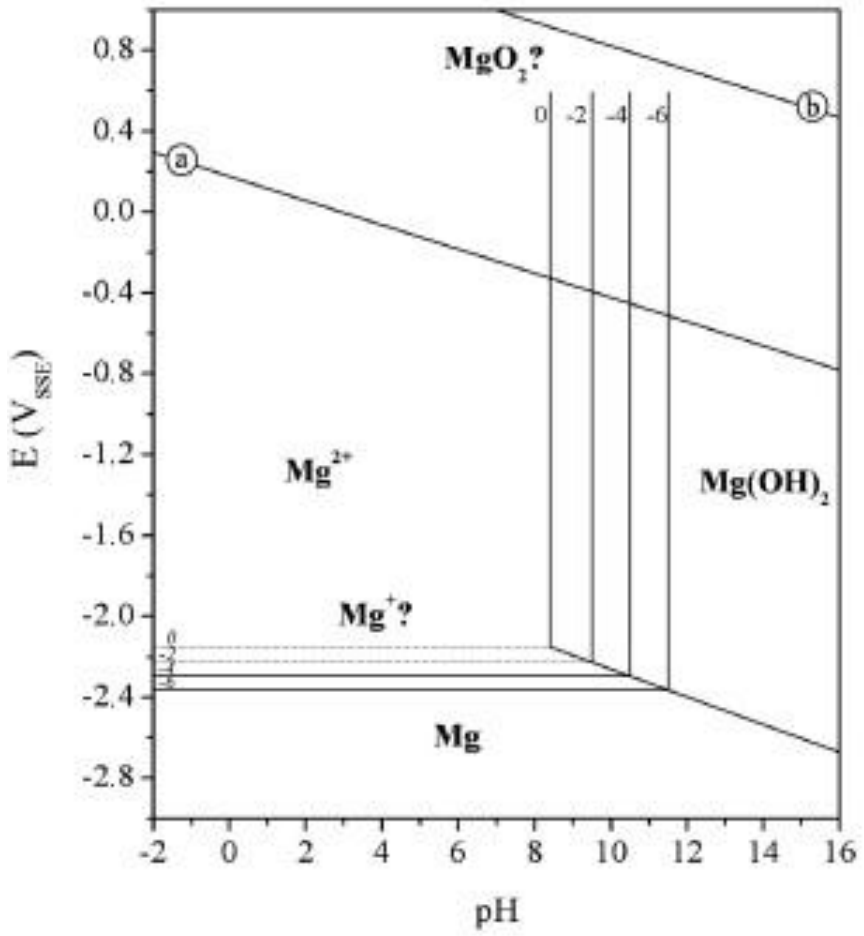

Figure 1. 9 - Pourbaix diagram for the Mg-water system [23].

which combine to yield the overall reaction of [29]:

$$Mg_{(s)} + 2\ H_2O_{(l)} \rightarrow Mg^{2+}_{(aq)} + 2\ OH^-_{(aq)} + H_{2(g)} \quad (1.29)$$

Since the difference in E_e between the two half reactions is extremely large the corrosion kinetics are fast and the generation of OH^- will increase the interfacial pH eventually leading to the deposition of $Mg(OH)_2$,

$$Mg^{2+}_{(aq)} + 2\ OH^-_{(aq)} \rightarrow Mg(OH)_{2(s)} \quad (1.30)$$

However, since H_2 is also formed, gas evolution from the Mg surface prevents the depositing $Mg(OH)_2$ from forming a compact layer, and the resulting deposited corrosion product has a broken, porous, platelet-like structure, which does not passivate the Mg surface [30-32].

1.4.2 The Corroding Surface of Mg and its Alloys

The corrosion products formed on Mg and its alloys have been reported to be an outer layer of $Mg(OH)_2$ and an inner compact layer of MgO [30-35], and this structure is shown schematically in Figure 1.10 [36]. It has been suggested that the MgO is a "protective" air form film on the material surface, but this has not been unequivocally demonstrated [37]. On alloy surfaces, a mixed Mg/Al oxide has been identified [38] and shown to be present in the outermost regions of the corrosion product layer [31]. At the base of this layer it has been reported that an Al layer is formed [33, 36, 39] and is linked to the corrosion resistance. In Zn-containing Mg alloys, a accumulated Zn layer has also been reported to form at the corrosion product/alloy interface which has also been suggested to enhance corrosion resistance [31]. The accumulation of corrosion product on

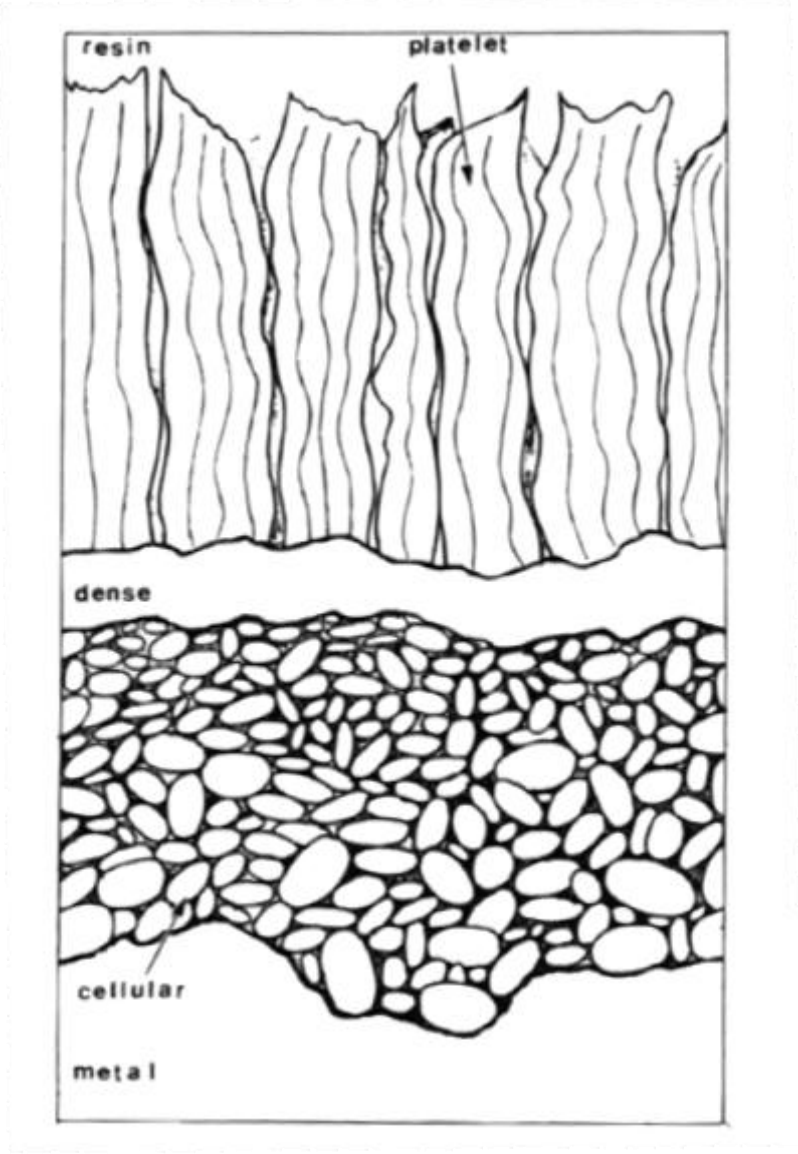

Figure 1. 10 - Schematic of the accumulated corrosion product on Mg materials showing an outer platelet-like layer of $Mg(OH)_2$ and an inner layer of MgO [36].

Mg alloys does not occur homogeneously with areas covered by substantial deposits, and domes of corrosion product developing as corrosion progresses [28, 40].

This accumulated corrosion product layer does not passivate the alloy under non alkaline conditions (< pH 13) [41] due to its porous nature [42]. However, the development of the corrosion product layer has been linked to decreased corrosion rates [33, 43] most likely a consequence of reduced cathodic kinetics [40, 44].

1.4.3 Magnesium's Great White Buffalo: The Negative Difference Effect and Mg^{+}

In the Pourbaix diagram for the Mg-H_2O system, unipositive Mg^{+} is commonly included although its existence is commonly debated in the literature. It is claimed that the existence of Mg^{+} as an intermediate in Mg corrosion can be attributed to the peculiar behaviour of Mg under anodic polarization. It would normally be expected that when Mg is polarized to a potential anodic to E_{CORR} by the imposition of an applied current, two effects would be expected: 1) the anodic half reaction rate should be increased (oxidation of Mg to Mg^{2+}), and 2) the cathodic half reaction rate should be decreased (reduction of H_2O water to H_2). However, the measured amount of $H_{2(g)}$ evolved when an anodic current is applied is higher than the amount evolved at E_{CORR}: this has been termed the negative difference effect (NDE) [45]. The widely reported explanation of this effect involves the participation of unipositive Mg species (Mg^{+}) in the corrosion process [12, 37, 42-43, 45-49]. In electrochemical reactions involving more than one electron, it is rare that electron transfer occurs in a single step [25], and it has been suggested that Mg is initially oxidized to Mg^{+}, which subsequently undergoes a chemical reaction to evolve H_2:

$$Mg \rightarrow Mg^{+} + e^{-} \quad (1.29)$$

$$Mg^{+} + H_2O \rightarrow Mg^{2+} + OH^{-} + \tfrac{1}{2} H_2 \quad (1.30)$$

The proposed explanation for this effect is that the anodic current applied increases the generation of Mg^{+} which can either be further oxidized to Mg^{2+}or evolve more H_2 by reaction (1.32), despite the applied anodic polarization. However, the presence of Mg^{+} as a surface species has never been spectroscopically identified or analytically isolated [25]. The existence of Mg^{+} is based on the observation that permanganate is reduced on an anodically polarized Mg alloy surface in Na_2SO_4, and the assumption that the only available reducing agent would be Mg^{+} [50]. Recently, it has been shown that at the negative potentials around the E_{CORR} of Mg (~ -1.6 V vs SCE), SO_4^{2-} is converted to SO_2, making this the reducing agent for permanganate rather than Mg^{+} [51].

Recent investigations have called the unipositive Mg^{+} explanation into question [25, 52-58], on the basis that the amount of evolved hydrogen does directly correlate to the amount of dissolved Mg (as Mg^{2+}) based on measured corrosion rates via mass loss, hydrogen collection and electrochemical measurements. No chemical step appears to be involved since the Faradaic ratio between the amount of Mg dissolved and the integrated applied current is nearly equal to one [58]. It has been suggested that the increased H_2 evolved under anodic control is a result of an increased cathodic capability of the Mg electrode as it is oxidized [57,59] and possibly through enrichment of elements which are cathodic to Mg [60].

It is reasonable to presume that the sites cathodically active on a corroding Mg material surface at E_{CORR} will retain some of their cathodic capability under anodic

control and contribute to the dissolution of Mg. The importance of such cathodic sites in the corrosion of Mg alloys will be a focal point in the studies presented in this thesis. While the origin of the NDE is still uncertain, its importance in completely understanding the corrosion of Mg materials cannot be understated.

1.4.4 Magnesium and the Electrochemical Series

The poor corrosion resistance of Mg-based materials is not only a result of its thermodynamic instability in an aqueous environment as summarized in the Pourbaix diagram, Figure 1.9. The electrochemical series ranks redox couples according to their standard reduction potentials (E^o). Species with more negative E^o values have a higher tendency to release electrons through oxidation, while those with more positive E° are more likely to accept electrons and reduce. An electrochemical series of elements relevant to this work is shown in Table 3 with all potentials reported vs. the standard hydrogen electrode (SHE).

As can be seen, Mg sits near the top of the electrochemical series, thus earning its designation as the most active structural material (Ca is not considered a structural material). A consequence of this position, is that, when in electrical contact, a redox couple with a lower equilibrium potential in that specific environment than Mg can form a galvanic couple with Mg, the latter serving as the anode and the more noble material as the cathode [61]. This possibility complicates the alloying of Mg with other elements, which are inevitably below Mg in the electrochemical series, and thus can induce a self-corrosion process within the alloy.

Table 1. 3 - The electrochemical series showing the standard reduction potentials for elements relevant to this thesis [61].

Element	$E°_{reduction}$ / vs SHE
$Ca^{2+} + 2\ e^- \rightarrow Ca$	-2.87 V
$Mg^{2+} + 2\ e^- \rightarrow Mg$	-2.37 V
$Y^{3+} + 3\ e^- \rightarrow Y$	-2.37 V
$Nd^{3+} + 3\ e^- \rightarrow Nd$	-2.31 V
$Al^{3+} + 3\ e^- \rightarrow Al$	-1.66 V
$Zr^{4+} + 4\ e^- \rightarrow Zr$	-1.45 V
$Zn^{2+} + 2\ e^- \rightarrow Zn$	-0.76 V
$Cr^{3+} + 3\ e^- \rightarrow Cr$	-0.74 V
$Fe^{2+} + 2\ e^- \rightarrow Fe$	-0.41 V
$Ni^{2+} + 2\ e^- \rightarrow Ni$	-0.23 V
$Sn^{2+} + 2\ e^- \rightarrow Sn$	-0.14 V
$Fe^{3+} + 3\ e^- \rightarrow Fe$	-0.04 V
$Cu^{2+} + e^- \rightarrow Cu^+$	0.16 V
$Cu^{2+} + 2\ e^- \rightarrow Cu$	0.34 V
$Ag^+ + e^- \rightarrow Ag$	0.80 V

1.4.5 Role of Alloying Elements in the Corrosion of Mg Alloys.

A wide range of elements have been tried as alloying additions to Mg to improve its properties. The more common alloying elements are listed in Table 1.1. When selecting an alloying element, its influence on the corrosion properties of the alloys must be taken into consideration. There is a notion in the literature that, due to galvanic coupling, no alloy can attain equivalent corrosion rates to pure Mg which contains no potential localized cathodes [64].

1.4.5.1 Aluminum

The most regularly used alloying addition to Mg is Al, and its effects on the corrosion performance of Mg alloys warrants its own discussion. Increasing the amount of Al in Mg alloys improves their strength and causes a decrease in ductility due to the formation of β- phase ($Mg_{17}Al_{12}$) and introduction of a eutectic phase (mixture of α-Mg and β) [63]. It is generally accepted that the addition of Al to Mg alloys improves the overall corrosion performance [12]. Additions of > 2 wt% [12], > 5 wt% [64], > 8 wt% [65] and > 9.6 wt% [66] of Al to Mg have been reported to generate an increase in corrosion resistance. However, there exists a compositional limit to the benefits gained from alloying with Al, although this limit is uncertain and reported to be both 10 wt % [12] and 23.4 % [67]. This range of uncertainty demonstrates the complex role Al-content plays in the corrosion of Mg alloys. Two consistently reported observations are that an increase in Al-content in a Mg alloy generates a positive increase in both the E_{CORR} [67] and the Volta potential [38]. Increasing the Al content also decreases the purity of the alloy through the possible formation of a stable Al-Fe phase in the casting melt and, as a result, Mn is commonly added with Al to prevent formation of this phase

[28]. The effect of Al on the corrosion of Mg alloys is best assessed not by considering the bulk Al content but by investigating its effect on the alloy microstructure, as will be discussed in section 1.4.7.

1.4.5.2 Other Alloying Elements

The roles played by other alloying elements in the corrosion processes of Mg alloys are varied. Zn is an alloying addition in the most frequently used series of Mg alloys (AZ-series). Increasing the Zn content of a Mg alloy has been shown to reduce the corrosion rate [40] possibly by becoming enriched at the surface of the allow during corrosion [32]. The presence of Zn within the β-phase of Mg alloys has also been reported to make the β-phase a stronger cathode [67].

Zr use in Mg alloys is based on its excellent grain refining properties and can be used to stabilize the α-Mg matrix [12]. A Zr content < 0.5 wt% has been reported as an effective level to improve alloy corrosion resistance [12], with the Zr scavenging Fe in the casting melt, thereby lowering its content in the alloy [37]. Above 0.5 wt% Zr has a detrimental effect on the corrosion properties of the alloy. The Fe scavenging effect of Zr will be revisited in Chapter 6.

The RE elements are also added to Mg as grain refiners. In a similar manner to Zr, REs can scavenge Fe and reduce its cathodic activity through the formation of a RE-Fe phase which is less cathodic to Mg than Fe [68]. Some RE phases (containing Ce and La) are not considered cathodic with respect to the Mg matrix and, thus, their addition is not considered detrimental to corrosion resistance [69]. In some cases REs have been incorporated into the oxide film on the Mg alloy, making it more compact and increasing

corrosion resistance [70]. Early studies considered the RE elements together as a group and treated their effect on corrosion as a general influence, although specific RE elements can induce different, not always advantageous, responses. For example, La and Ce reduced the corrosion resistance of the Mg alloy EZ33 in the presence of chloride compared with other RE containing alloys [71]. Dy additions up to 10 wt% can improve corrosion resistance, with an even distribution of Dy further improving the resistance through the formation of a more compact corrosion product layer [72]. Er can be incorporated into the lattice of deposited $Mg(OH)_2$ on an alloy surface, resulting in an improved corrosion resistance [73].

A RE more commonly alloyed with Mg is Nd. Nd containing alloys have shown improved corrosion resistance over the AZ series since fewer cathodic sites were present in the Nd containing alloy [74]. By contrast, MgNd particulates have also been observed to act cathodically in Mg alloys [41] and to disappear during corrosion [75]. Although not a traditional RE element due to its lighter weight, Y is commonly grouped with the REs due to its occurrence in ores containing other RE elements. Its addition to Mg alloys has been shown to both reduce [41] and improve corrosion resistance, the latter by the growth of a Y_2O_3 layer with some passive characteristics [37, 76]. In a study of binary Mg-RE systems, equal additions of three RE (La, Nd, Ce) showed highest corrosion resistance from the Mg-La alloy, followed by the Mg-Nd and then by the Mg-Ce [77].

Given its position above Mg in the electrochemical series, Ca has been utilized successfully as an alloying element with Mg mainly due to its biocompatibility in bone implants. There is evidence to show Ca additions have a positive influence on the corrosion resistance of Mg at levels up to 0.6 wt% [78] and up to 2.0 wt% in a Mg-Al

alloy [79]. This improvement is reported due to a reduced grain size from Ca addition and an increased coverage of Ca-containing phases acting as a corrosion barrier.

Si is commonly added to Mg alloys in small amounts (< 1.0 wt%) to improve creep resistance. It forms $MgSi_2$ particles in the microstructure, which have Volta potentials nearly equal to that of pure Mg and are considered inactive in the corrosion process [37, 80]. Si additions to the AZ91 alloy had little effect on corrosion performance of the alloy, but when added along with Sb (which on its own decreases corrosion resistance) an improvement in corrosion resistance over AZ91 was observed [81].

Other elements reported to promote corrosion resistance are In and Sn which reduce the porosity of the corrosion product layer [82]. Ni additions have surprisingly also been shown to improve the corrosion resistance [37]. Mg alloys are rarely binary systems and are formed as ternary, quaternary systems where the alloying elements can have synergistic effects on structural and corrosion properties.

1.4.6 Corrosion Behaviour of Mg Alloys

The corrosion of Mg alloys can be studied using a variety of techniques such as mass loss, hydrogen collection, and various electrochemical techniques including electrochemical impedance spectroscopy, all of which should provide corrosion rates in agreement with one another [58]. Mg alloys are susceptible to galvanic corrosion when coupled to a second material which is more noble in the galvanic series of material [83] as well as microgalvanic corrosion within the alloy itself. The complexity of Mg alloy

corrosion can be appreciated by comparing reported corrosion resistances for common Mg alloys, as shown in Table 1.4.

Table 1. 4 - List of comparative corrosion rates of Mg alloys.

Corrosion Resistance	Medium	Method	Ref
AZ80 > AZ91 > AZ31	NaCl	EIS	[84]
AM60 > AZ31	NaCl	Weight Loss	[85]
AZ91 > AM50	Na_2SO_4	EIS	[43]
Pure Mg > AZ91 > ZE41	NaCl	Weight Loss, Hydrogen	[53]
Pure Mg = AZ31 >AZ91 > AM30 > AM60 > ZE41	NaCl	Hydrogen	[53]
WE43 > ZE41 > AZ91	NaCl	Weight Loss	[75]
ZK60 > AM60 > AZ31 > AZ91	NaCl	EIS, Electrochem	[20]
AE42 > ZAC8506 > AZ91	NaCl	Weight loss	[41]
AZ91 > AZ61 > AZ31	NaCl	Weight Loss	[86]
AZ91 > AM60 > AM20	NaCl Air	Weight loss	[30]
ZK31 = WE54 > EZ33	NaCl + NaOH	Electrochem, EIS	[71]
NZ30 > AZ91	NaCl	Weight Loss	[74]
AZ 31 > AZ 61 > AP 65 > Mg	$Mg(ClO_4)_2$	EIS	[87]

No consistent trend exists, even in this small sampling of published studies. The two main reasons for these discrepancies are: (i) the presence of contaminants, and (ii) microstructural effects.

Impurities introduced during casting, such as Cu, Fe, Ni can have detrimental effects on alloy corrosion resistance when present above a certain tolerance limit for the alloy [63]. When present Cu congregates in the β-phase, making it a much stronger cathode [41]. Fe on the other hand can be freely distributed within the Mg matrix, or form cathodic Fe-Al or Fe-secondary metal phases. Mn is added to the casting melt to form insoluble Mn-Fe complexes that will sink to the bottom of the melt thereby reducing the Fe content in the final cast [88]. However, some residual Fe inevitably remains and can congregate in Mn-containing phases, of which those with higher Fe:Mn ratio will have enhanced catalytic activity [89]. The presence of contaminants can not only influence the bulk corrosion performance of the alloys, but also that of individual microstructure features.

1.4.7 Microstructural Effects on Corrosion

Due to composition, casting procedure and post-processing microstructural changes can be induced in Mg alloys. Altering the microstructure can have a direct effect not only on the physical properties of the alloy, but also on its corrosion performance. While the Pourbaix diagram of Mg can thermodynamically predict the products of a Mg corrosion process, it does not account for the microstructural influences which can be major [90]. The three most common influences of microstructure are grain size, and the presence of β-phase and intermetallic compounds. A study of such influences is a major

focal point of the research described in this thesis, and only brief summaries of these effects are reviewed here.

1.4.7.1 Grain Size

The grain size in Mg alloys is strongly affected by the casting procedure [91, 92], and can influence not only the physical properties of the alloy, but also its corrosion performance. The size of the grains in Mg alloys has frequently been reported to affect the corrosion behaviour, with a decrease in grain size causing a decrease in corrosion rate [93]. This has been shown to be the trend in many Mg alloys such as AZ31 [85, 94-96] AZ91 [93, 97], ZK60 [98] and rare earth containing systems [99]. It has been suggested that the beneficial effect of reducing grain size arises from the formation of a better passive layer [85], an improvement in the protection capabilities of the β-phase network [46], and a reduction in cracking of the corrosion product layer [96]. Conflictingly, there are reports that a decrease in grain size leads to an increase in corrosion rate [22].

The elemental distribution as a result of grain size can also influence the corrosion behaviour, as will be discussed in this thesis. Higher Al content in the centre of Mg grains in Mg-Al alloys can increase the corrosion resistance of the grain [38, 100], but can also initiate grain boundary corrosion [97]. However, it is clear from available literature that, besides grain size, other microstructural factors such as microgalvanic coupling and self-protecting processes also influence corrosion [90]. A case can be made to claim that while grain size will affect anodic kinetics, chemical effects will control cathodic kinetics [98].

1.4.7.2 Al-Mn Intermetallics

Segregation during casting leads to the precipitation of intermetallic phases in the final material; e.g., Al-Mn intermetallics in Al-containing Mg alloys. This intermetallic forms as a result of the addition of Mn to scavenge contaminant Fe from the alloy. In the casting melt, Al-Mn-Fe can precipitate in the molten Mg, and these precipitates can either sink to the bottom of the crucible or become embedded in the cast during solidification [69, 97]. The microgalvanic corrosion of Mg-Al alloys has long been attributed to coupling of the matrix to the Mg-Al β-phase, with intermetallics generally ignored (see Section 1.4.7.3). However, the Volta potential of Al-Mn intermetallics is more positive than that of the β-phase when compared to that of the Mg matrix, making the intermetallic potentially the most likely cathodic sites [80]. Several studies have identified Al-Mn intermetallics as active cathodes in the corrosion of Mg alloys [12, 28, 35, 41, 89, 97, 101-102]. This has been attributed to the Fe content of the intermetallic [41, 103], despite a report that Fe may not be required [12], and the initiation of an altered electrolyte layer above the intermetallic in atmospheric corrosion [38]. On the contrary, evidence has also been presented to show the intermetallics remain inactive during corrosion [67, 96].

1.4.7.3 β-phase

As a result of saturation of Al in the casting melt, the β-phase ($Mg_{17}Al_{12}$) is a common component of Mg-Al alloys when the overall Al content is > 3 wt%. The precipitation of β-phase increases the strength of the alloy besides influencing the corrosion behaviour, although conflicting roles for the β-phase have been claimed. The β-phase has been reported to be a cathode driving the microgalvanic corrosion of Mg

alloys [104-106]. Several factors have been reported to contribute to the improved cathodic ability of the β-phase: large grains in Mg alloys [46, 104], the β-phase having improved cathodic capability over Al-Mn and intermetallics [67], improved cathodic ability with increased Zn content in Mg-Al-Zn alloys [67] and enhanced corrosion resistance of AZ31 which does not have β-phase over AZ91 which does [20].

On the contrary, the β-phase has also been reported as a promoter of corrosion resistance in Mg alloys [10, 104]. This improvement in corrosion resistance has been shown in many studies and attributed to a number of features and processes; (i) the β-phase does not couple cathodically with the Mg matrix [84], (ii) removal of the β-phase by heat treatment decreases the corrosion resistance [107]; (iii) an increase in the number of fine β-phase particles increases corrosion resistance [107], (iv) application of a surface mechanical attrition treatment (SMAT) removes the β-phase and decreases corrosion resistance [108], (v) an increase in exposure time increases the amount of exposed β-phase leading to an increased corrosion resistance [106], and (vi) the skin on a die cast Mg has a high fraction of small β-phase and, consequently, an increased corrosion resistance over the bulk material [46]. It has been proposed that small grain sizes allow the β-phase become a corrosion barrier, while increasing grain size initiates the cathodic activity of the β-phase [104]. The influence by the β-phase on corrosion of Mg alloys is best considered in terms of the distribution of the β-phase in the alloy microstructure [104-106, 109-110].

The β-phase has an E_{CORR} in aqueous chloride environments below the water stability region, making it susceptible to corrosion [27]. When present in a Mg alloy, the β-phase has a much slower dissolution rate than the α-Mg matrix, leading to its corrosion

barrier properties [111]. It also has a lower corrosion rates than the eutectic phase of Mg alloys (supersaturated region which is a mix of α-Mg and β-phase) [112]. The β-phase has been observed to undergo corrosion in high chloride environments, although it is not clear if this is actually due to corrosion of the β-phase or to corrosion damage to the α-Mg surrounding the β-phase which undermines it allowing it to fall out [113]. While the role of β-phase is important in the corrosion of Mg alloys, the controlling influence appears to be a combination of microstructural effects and features and their distribution in the alloy. A primary focus of this thesis is the investigation of these influences.

1.5 Scope of Thesis

The goal of the research presented in this thesis was the study of the influence of microstructure on the corrosion of Mg alloys. Many of the previous reports on Mg alloy corrosion and the role played by the alloy microstructure are limited to bulk characteristics and corrosion measurements. This work investigated corrosion propagation of Mg alloys on the microscale using a same spot analysis approach in which specific areas of interest on the alloy surface were investigated with electron microscopy prior, during and after corrosion. In doing so, the role played by specific microstructural features could be identified. A combination of scanning electron microscopy, X-ray energy dispersive spectroscopy, confocal laser scanning microscopy, transmission electron microscopy and the focused ion beam were utilized for such investigations. In this thesis, full analyses are presented on the role of microstructural features on corrosion of the Mg alloys AM50 and ZEK100.

The effect of the distribution of the secondary microstructural features was investigated through a study of three casts of the AM50 Mg alloy: sand cast, graphite cast

and die cast. By selecting three casts of the same alloy, compositional effects are limited and the main variable existing is the size and distribution of the secondary microstructure features. These materials also allow for the influence of the Al distribution throughout the alloys to be studied. A combination of electrochemical techniques and electron microscopy were utilized for this investigation.

The protective, deleterious or benign roles of the microstructural features in Mg alloys are critical to an understanding of the corrosion behaviour. In the AM50 alloys, the Al-Mn intermetallics appear to function as strong cathodes in microgalvanic corrosion, making an understanding of their behaviour a key requirement. The nature of their behaviour was investigated using custom fabricated Al-Mn alloys in a series of electrochemical and microscopic analyses. The Al-Mn alloys were representative materials for the Al-Mn intermetallics commonly found in Mg alloys and tested in chloride solution containing either Na^+ or Mg^{2+}, the latter to simulate the environments near a corroding Mg alloy surface.

The approach of locating the same area of interest on a Mg alloy surface through intermittent immersion experiments was extended to a non-Al containing Mg alloy, ZEK100. Little previous work has been reported on the corrosion behaviour of ZEK100, especially lacking is the role of the secondary microstructure features on the alloy's corrosion behaviour. Utilizing electrochemical techniques (E_{CORR}, polarization) and microscopic analyses (SEM, FIB, CLSM) identification of local cathodes and anodes in partaking in the corrosion process was performed. The influence of chloride on the corrosion behaviour of ZEK100 was also investigated.

A possible way to control the corrosion rate of Mg alloys may be achieved through control over the cathodic half reaction in the microgalvanic coupling occurring on the alloy surface. The application of a sacrificial pure Mg electrode to Mg alloys was investigated to observe any influence on corrosion rate. An investigation into galvanostatic cathodic protection of Mg alloys was also carried out and analysis done with optical and electron microscopy and compared with natural aerated corrosion behaviour.

This cathodic control may also been applied from a chemical approach as well. By minimizing the amount of water in the system, the microgalvanically coupled corrosion process would be limited by the available water or need to utilize a second reduction process, such as oxygen reduction. Ethylene glycol was selected for this purpose as the corrosion media. An investigation into the corrosion behaviour of Mg alloy AM50 in ethylene glycol was performed using E_{CORR}, polarization and electrochemical impedance spectroscopy and compared to the corrosion behaviour in an aqueous environment. Scanning electrochemical microscopy was performed above a corroding AM50 surface in ethylene glycol, using the redox mediator ferrocene methanol as in indicator of anodic activity.

1.6 References

1. F. Motasemi, M.T. Afzal, A.A. Salema, M. Mohavvemi, M. Shekarchian, F. Zarifi, R. Mohsin "Energy and exergy utilization efficiencies and emission performance of Canadian transportation sector, 1990-2035" *Energy* 64 (2014) 355-366

2. Natural Resources Canada "Energy use data handbook" http://oee.nrcan.gc.ca/publications/statistics/handbook11/pdf/handbook11.pdf (2012) Accessed 02/04/2014

3. D. Karman, G. Rideout, W. Bailey, A. Green, P. Eggleton "Transportation Emissions: Sources and Regulations" Air Quality Management, Springer Netherlands (2014) 203-235

4. G. Nemet "Automobile Fuel Efficiency Standards" Energy Technology Innovation Cambridge University Press (2013) 176-191

5. L. Lu, X. Han, J. Li, J. Hua, M. Ouyang "A review of the key issues for lithium ion battery management in electric vehicles" *J. Power Sources* 226 (2013) 272-288

6. Environmental Leader "GM to cut vehicle weight 'up to 15%' by 2017" http://www.environmentalleader.com/2013/03/11/gm-to-cut-vehicle-weight-up-to-15-by-2017/ Accessed 30/03/2014

7. M. Kulekci "Magnesium and its alloys applications in automotive industry" *Int. J. Adv. Manuf. Tech.* 39 (2008) 851-865

8. H. Friedrich, S. Schumann "Research for a new age of magnesium in the automotive industry" *J. Mater. Proceess Technol.* 117 (2001) 276-281

9. D. Eliezer, E. Aghion, F.H. Froes "Magnesium science, technology and applications" *Adv. Perf. Mat.* 5 (1998) 201-212

10. T.L. Jones, J.P. Labukas, B.E. Placzankis, K. Kondoh "Ballistic and corrosion analysis of new military grade magnesium alloys AMX602 and ZAXE1711 for armor application" *Army Research Lab* ARL-TR-5931 (2012) 1-60

11. I. Polmear Light Alloys from Traditional Alloys to Nanocrystals Elsevier: Amsterdam, 2006

12. G. Song "Recent Progress in Corrosion and Protection of Magnesium Alloys" *Adv. Eng. Mat.* 7 (2005) 563-586

13. M.O. Pekguleryuz, A. A. Kaya "Creep resistant magnesium alloys for powertrain applications" *Adv. Eng. Mat.* 5 (2003) 866-878

14. A.A. Luo "Recent magnesium alloy developments for elevated temperature applications" *Int. Mat. Rev.* 49 (2004) 13-30

15. A. Atrens, N. Winzer, W. Dietzel, P.B. Srinivasan, G. Song "Stress corrosion cracking (SCC) of magnesium (Mg) alloys" Corrosion of Magnesium Alloys Woodhead Publishing, Philidelphia, PA 2011

16. X. Xia, A. Sanaty-Zadeh, C. Zhang, A.A. Luo, X.Q. Zeng, Y.A. Chang, D.S. Stone "Thermodynamic modelling and experimental investigation of the magnesium-zinc-samarium alloys" *J. Alloys and Compounds* 593 (2014) 71-78

17. N. Birbilis, G. Williams, K. Gusieva, A. Samaniego, M.A. Gibson, H.N. McMurray. "Poisoning the corrosion of magnesium".*Electrochem. Commun.* 34 (2013) 295-298.

18. I. Shin, E.A. Carter "First-principles simulations of plasticity in body-centered-cubic magnesium-lithium alloys" *Acta Mater.* 64 (2014) 198-207

19. N. Li, Y. Zheng "Novel magnesium alloys developed for biomedical application: A review" *J. Mater. Sci. Technol.* 29 (2013) 489-502

20. Y. Cheng, T. Qin, H. Wang, Z. Zhang "Comparison of corrosion behaviour of AZ31, AZ91, AM60 and ZK60 magnesium alloys" *Trans. Nonferrous Met. Soc. China* 19 (2009) 517-524

21. Y. Kojima, T. Aizawa, S. Kamodo "Magnesium alloys development towards the 21st century" *Mat. Sci. For.* 350 (2000) 19-30

22. K.V. Kutniy, I.I. Papirov, M.A. Tikhonovsky, A.I. Pikalov, S.V. Sivtzov, L.A. Pirozhenko, V.S. Shokurov, V.A. Shkuropatenko "Influence of grain size on mechanical and corrosion properties of magnesium alloy for medical implants" *Materialwiss. Werkstofftech*. 40 (2009) 242-246

23. J. Hamilton, S.T. Brennan, Y. Sohn, B. Davis, R. Delorme, K. Cho "Microstructural characteristics of high rate plastic deformation in Elektron WE43 magnesium alloys" *Mag. Tech. 2012* John Wiley & Sons Inc. Hoboken nj, USA, ch79

24. N. Zaludova "Mg-RE alloys and their applications" *WDS '05 Proc. Contributed Papers* (2005) 643-648

25. G.S. Frankel, A. Samaniego, N. Birbilis "Evolution of hydrogen at dissolving magnesium surfaces" *Corros. Sci*. 70 (2013) 104-111

26. M. Pourbaix, Atlas of the Electrochemical Equilibria, NACE, 1974

27. N.L. Sukiman, X. Zhou, N. Birbilis, A.E. Hughes, J.M.C. Mol, S.J. Garcia, X. Zhou, G.E. Thompson "Durability and corrosion of aluminum and its alloys: overview, property space, techniques and developments" Aluminum Alloys – New Trends in Fabrication and Applications Intech, 2013 47-98

28. A. Pardo, M.C. Merino, A.E. Coy, R. Arrabal, F. Viejo, E. Matykina "Corrosion behaviour of magnesium/aluminum alloys in 3.5 wt% NaCl" *Corros. Sci.* 50 (2008) 823-834

29. R. Lindstrom, J.E. Svensson, L.G. Johansson "The influence of carbon dioxide on the atmospheric corrosion of some magnesium alloys in the presence of NaCl" *J. Electrochem. Soc.* 149 (2002) B103-B107

30. J.H. Nordlien, K. Nisancioglu, S. Ono, N. Masuko "Morphology and structure of water-formed oxides on ternary MgAl Alloys" *J. Electrochem. Soc.* 144 (1997) 461-466

31. R.C. Phillips, J.R. Kish "Nature of surface film on matrix phase of Mg alloy AZ80 formed in water" *Corrosion* 69, (2013) 813-820

32. M. Danaie, R.M. Asmussen, P. jakupi, D. Shoesmith, G. Botton "The role of aluminum distribution on local corrosion resistance of the microstructure in a sand-cast AM50 alloy" *Corros. Sci.* 77 (2013) 151-163

33. L. Wang, T. Shinohara, B.P Zhang "XPS study of the surface chemistry on AZ31 and AZ91 magnesium alloys in dilute NaCl solution" *Appl. Surf. Sci.* 256 (2010) 5807-5812

34. M. Taheri, M. Danaie, J.R. Kish "TEM examination of the film formed on corroding Mg prior to breakdown" *J. Electrochem. Soc.* 161 (2014) C89-C94

35. M. Taheri, J.R. Kish "Nature of surface film formed on Mg exposed to 1 M NaOH" *J. Electrochem. Soc.* 160 (2013) C36-C41

36. J.H. Nordlien, K. Nisancioglu, S. Ono, N. Masuko "Morphology and structure of oxide films formed on MgAl alloys by exposure to air and water" *J. Electrochem. Soc.* 143 (1996); 25642573

37. G. Song, A. Atrens "Understanding magnesium corrosion: A framework for improved alloy performance" *Adv. Eng. Mat.* 5 (2003) 837-857

38. M. Jonsson, D. Persson, R. Grubner "The initial steps of atmospheric corrosion on magnesium alloy AZ91D" *J. Electrochem. Soc.* 154 (2007) C684-C691

39. S.J. Splinter, N.S. McIntyre "The initial interaction of water vapour with Mg-Al alloy surfaces at room temperature" *Surf. Sci.* 314 (1994) 157-171.

40. Y. Song, E. Han, D. Shan, C.D. Yim, B.S. You "The effect of Zn concentration on the corrosion behaviour of Mg-xZn alloys" *Corros. Sci.* 65 (2012) 322-330

41. R.C. Zeng, J. Zhang, W. Huang, W. Dietzel, K.U. Kainer, C. Blawert, W. Ke "Review of studies on corrosion of magnesium alloys" *Trans. Nonferrous Met. Soc. China* 16 (2006) s763-s771

42. L. Lacroix, C. Blanc, N. Pebere, B. Tribollet, V. Vivier "Localized approach to galvanic coupling in an aluminum-magnesium system" *J. Electrochem. Soc.* 156 (2009) C259-C265

43. G. Baril, C. Blanc, N. Pebere "AC impedance spectroscopy in characterizing time-dependent corrosion of AZ91 and AM50 mangesium alloys" *J. Electrochem. Soc.* 148 (2001) B489-B496

44. W. Liu, F. Cao, A. Chen, L. Chang, J. Zhang, C. Cao "Effect of chloride ion concentration on electrochemical behaviour and corrosion product of AM60 magnesium alloy in aqueous solutions" *Corrosion* 68 (2012) 045001

45. G. Song "Corrosion electrochemistry of magnesium and its alloys" Corrosion of Magnesium Alloys Woodhead Publishing, Philidelphia, PA 2011

46. G. Song, A. Atrens, M. Gargusch "Influence of microstructure on the corrosion of die cast AZ91D" *Corros. Sci.* 41 (1999) 249-273

47. Z. Shi, M. Liu, A. Atrens "Measurement of the corrosion rate of magnesium alloys using Tafel extrapolation" *Corros. Sci*. 52 (2010) 579-588

48. G. Galicia, N. Pebere, B. Tribollet, V. Vivier "Local and global electrochemical impedances applied to the corrosion behaviour of an AZ91 magnesium alloy" *Corros. Sci.* 51 (2009) 1789-1794

49. Z. Shi, A. Atrens "Comments on the paper entitled "Observations of the galvanostatic dissolution of pure magnesium" by N.T. Kirkland, G. Williams, N. Birbilis" *Corros. Sci.*77 (2013) 403-406

50. R. L. Petty, A.W. Davidson, J. Kleinberg "The anodic oxidation of magnesium metal: evidence for the existence of unipositve magnesium" *J. Am. Chem. Soc.* 76 (1954) 363-366

51. G.S. Frankel, A. Samaniego, B. Hurley "Studies of the Mg dissolution mechanism" Presentation in CORROSION 2014, Mar 11, 2014 San Antonio, TX

52. N.T. Kirkland, G. Williams, N. Birbilis 'Observations of the galvanostatic dissolution of pure magnesium" *Corros. Sci.* 65 (2012) 5-9

53. G. Williams, H.N. McMurray "Localised corrosion of magnesium in chloride containing electrolyte studied by a scanning vibrating electrode technique" *J. Electrochem. Soc.* 155 (2008) C340-C349

54. N.T. Kirkland, G. Williams, N. Birbilis "Repsonse to comments from Shi and Atrens on the paper "Observations of the galvanostatic dissolution of pure magnesium" *Corros. Sci.* 77 (2013) 407-409

55. L. Rossrucker, K.J.J Mayrhofer, G.S. Frankel, N. Birbilis "Investigating the real time dissolution of Mg using online analysis by ICP-MS"*J. Electrochem. Soc.* 161 (2014) C115-C119

56. G. Williams, N. Birbilis, H.N. McMurray "The source of hydrogen evolved from a magnesium anode" *Electrochem. Commun.* 36 (2013) 1-5

57. N. Birbilis, A.D. King, S. Thomas, G.S. Frankel, J.R. Scully "Evidence for enhanced catalytic activity of magnesium arising from anodic dissolution" *Electrochim. Acta* (2014) http://dx.doi.org/10.1016/j.electacta.2014.03.133

58. A.D. King, N. Birbilis, J.R. Scully "Accurate electrochemical measurement of magnesium corrosion rates; a combined impedance, mass-loss and hydrogen collection study" *Electrochim. Acta* 121 (2014) 394-406

59. G. Williams, H. Dafydd, R. Subramanian "Chloride ion concentration effects on passivity breakdown in magnesium" *ECS Trans.* 58 (2014) 23-34

60. Taheri, M., Kish, J. R., Birbilis, N., Danaie, M., McNally, E. A., McDermid, J. R. "Towards a Physical Description for the Origin of Enhanced Catalytic Activity of Corroding Magnesium Surfaces" *Electrochimica Acta,* 116 (2014) 396-403.

61. P. Atkins, J. de Paula Atkin's Physical Chemistry (2001) OUP Oxford, England, 7th Edition

62. M.C. Zhao, M. Liu, G. Song, A. Atrens "Influence of pH and chloride ion concentration on the corrosion of Mg alloy ZE41" *Corros. Sci*. 50 (2008) 3168-3178

63. M. Liu, P.J. Uggowitzer, A.V. Nagasekhar, P. Schmutz, M. Easton, G. Song, A. Atrens "Calculated phase diagrams and the corrosion of die cast Mg-Al alloys" *Corros. Sci.* 51 (2009) 602-619

64. T.J. Warner, N.A. Thorne G. Nussbaum, W.M. Stobes "A cross sectional TEM study of corrosion initiation in rapidly solidified magnesium based ribbons" *Surf. And Interface Anal.* 19 (1992) 386-392

65. O. Lunder, J.E. Lein, T.K. Aune, K. Nisancioglu "The role of magnesium aluminum ($Mg_{17}Al_{12}$) phase in the corrosion of magnesium alloy AZ91" *Corrosion* 45 (1989) 741-748

66. F. Hehmann, F.H. Froes, W. Young "Rapid solidification of aluminum, magnesium and titanium" *J. Metals* 39 (1987) 14-21

67. S. Mathieu, C. Rapin, J. Steinmetz, P. Steinmetz "A corrosion study of the main constituent phases of AZ91 magnesium alloys" *Corros. Sci.* 45 (2003) 2741-2755

68. W. Mercer, J. Hillis "The critical contaminant limits and salt water corrosion of magnesium AE42 alloy" *SAE Technical Paper* 920073 (1992)

69. W. Liu, F. Cao, L. Chang, Z. Zhang, J. Zhang "Effect of rare earth element Ce and La on corrosion behaviour of AM60 Mg alloy" *Corros. Sci.* 51 (2009) 1334-1343

70. F. Rosalbino, E. Angelini, S. De Negri, A. Saccone, S. Delfino "Electrochemical behavior assessment of novel Mg rich Mg-Al-RE alloys (RE = Ce, Er)" *Intermetallics* 14 (2006) 1487-1492

71. R. Pinto, M.G.S. Perrerira, M.J. Carmezim, M.F. Montemor "Passive behaviour of magnesium alloys (Mg-Zr) containing rare earth elements in alkaline media" *Electrochim. Acta* 55 (2010) 2482-2489

72. L. Yang, Y. Huang, Q. Peng, F. Feyerabend, K. Kainer, R. Willumeit, N. Hort "Mechanical and corrosion properties of binary Mg-Dy alloys for medical applications" *Mat. Sci. Eng. B.* 176 (2011) 1827-1834

73. F. Rosalbino, E. Angelini, S. Denegri, A. Saccone, S. Delfino "Effect of erbium addition on the corrosion behaviour of Mg-Al alloys" *Intermetallics* 13 (2005) 55-60

74. J.W. Chang, L.M. Peng, X.W. Guo, A. Atrens, P.H. Fu, W.J. Ding, X.S. Wang "Comparison of the corrosion behaviour in 5 % NaCl solution of Mg alloys NZ30K and AZ91D" *J. Appl. Electrochem.* 38 (2008) 207-214

75. T. Valente "Grain boundary effects on the behaviour of WE43 magnesium castings in simulated marine environment" *J. Mat. Sci. Lett.* 20 (2001) 67-69

76. H.B. Yao, Y. Li, A.T.S. Wee "Passivity behaviour of melt-spun Mg-Y alloys" *Electrochim. Acta* 48 (2003) 4197-4204

77. N. Birbilis, M.A. Easton, A.D. Sudholz, S.M. Zhu, M.A. Gibson "The corrosion of binary magnesium-rare earth alloys" *Corros. Sci.* 51 (2009) 683-689

78. Y. Wan, G. Xiong, H. Luo, F. He, Y. Huang, X. Zhou "Preparation and characterization of a new biomedical magnesium-calcium alloy" *Mat. Design* 29 (2008) 2034-2037

79. K.H. Kim, N.D. Nam, J.G. Kim, K.S. Shin, H.C. Jung "Effect of calcium addition on the corrosion behaviour of Mg-5Al alloy" *Intermetallics* 19 (2011) 1831-1838

80. F. Andreatta, I. Apachitei, A.A. Kodentsov, J. Dzwonczyk, J,, Duszczyk "Volta potential of second phase particles in extruded AZ80 magnesium alloy" *Electrochim. Acta* 51 (2006) 3551-3557

81. A. Srinivasan, S. Ningshen, U.K. Mudali, U.T.S. Pillai, B.C. Pai "Influence of Si and Sb additions on the corrosion behaviour of AZ91 magnesium alloy" *Intermetallics* 15 (2007) 1511-1517

82. Z. Yu, H.Y. Zhao, X.D. Hu, D.Y. Ju "Effect of elements Zn, Sn and In on microstructures and performances of AZ91 alloy" *Trans. Nonferrous Met. Soc. China* 20 (2010) s318-s323

83. Designation: G82-98 "Standard guide for development and use of a galvanic series or predicting galvanic corrosion performance" *ASTM Standard* ASTM International, 2009

84. A. Pardo, M.C. Merino, A.E. Coy, F. Viejo, R. Arrabal, S. Feliu Jr. "Influence of microstructure and composition on the corrosion behaviour of Mg/Al alloys in chloride media" *Electrochim. Acta* 53 (2008) 7890-7902

85. J. Liao, M. Hotta, N. Yamamoto "Corrosion behaviour of fine grained AZ31B magnesium alloy" *Corros. Sci.* 61 (2012) 208-214

86. D. Eliezer, P. Uzan, E. Aghion "Effect of second phase on the corrosion behaviour of magnesium alloys" *Mat. Sci. Forum* 419-422 (2003) 857-866

87. R. Udhayan, D. P. Bhatt "On the corrosion behaviour of magnesium and its alloys using electrochemical techniques" *J. Power Sources* 63 (1996) 103-107

88. I.J. Polmear "Magnesium alloys and applications" *Mat. Sci. Tech.* 10 (1994) 1-16

89. H. Matsubara, Y. Ichige, K. Fujita, H. Nishiyama, K. Hoduchi "Effect of impurity Fe on corrosion behaviour of AM50 and AM60 magnesium alloys" *Corros. Sci.* 66 (2013) 203-210

90. C. Hoog, N. Birbilis, Y. Estrin "Corrosion of pure Mg as a function of grain size and processing" *Adv. Eng. Mat.* 10 (2008) 579-582

91. A. Bowles, K. Nogita, M. Dargusch, C. Davidson, J. Griffiths "Grain size measurements in Mg-Al high pressure die castings using electron back-scattered diffraction" *Mat. Trans.* 45 (2004) 3114-3119

92. A. V. Nagasekhar, M.A. Easton, C.H. Caceras "Solute content and the grain microstructure of high pressure die cast magnesium-aluminum alloys" *Adv. Eng. Mat.* 11 (2009) 912-919

93. (17) K. Ralston, N. Birbilis "Effect of grain size on corrosion: A review" *Corrosion* 66 (2010) 075005-1-13

94. M. Alvarez-Lopez, M.D. Pereda, J.A. del Valle, M. Fernandez-Lopez, M.C. Garcia-Alonso, O.A. Ruano, M.L. Escudero "Corrosion behaviour of AZ31 magnesium alloy with different grain sizes in simulated body fluid" *Acta Biomaterialia* 6 (2010) 1793-1771

95. N.N. Aung, W. Zhou "Effect of grain size and twins on the corrosion behaviour of AZ31B magnesium alloy" *Corros. Sci.* 52 (2010) 589-594

96. J. Liao, M. Hotta, S. Motoda, T. Shinohara "Atmospheric corrosion of two field exposed AZ31B magnesium alloys" *Corros. Sci.* 71 (2013) 53-61

97. G. Ballerini, U. Bardi, R. Bignucolo, G. Ceraolo "About some corrosion mechanisms of AZ91D magnesium alloy" *Corros. Sci.* 47 (2005) 2173-2184

98. D. Orlov, K.D. Ralston, N. Birbilis, Y. Estrin :Enhanced corrosion resistance of Mg alloy ZK60 after processing by integrated extrusion and equal channel angular processing" *Acta Materialia* 59 (2011) 6176-6186

99. G.R. Argade, S.K Panigrahi, R.S. Mishra "Effects of grain size on the corrosion resistance of wrought magnesium alloys containing neodymium" *Corros. Sci.* 58 (2012) 145-151

100. N. Aung, W. Zhou "Effect of heat treatment on corrosion and electrochemical behaviour of AZ91D magnesium alloy" *J. Appl. Electrochem.* 32 (2002) 1397-1401

101. A. Coy, F. Viejo, F. Garcia-Garcia, Z. Liu, P. Skeldon, G. Thompson "Effect of excimer laser surface melting on the microstructure and corrosion performance of the die cast AZ91D magnesium alloy" *Corros. Sci.* 52 (2010) 387-397

102. Y. Ma, J. Zhang, M. Yang "Research on microstructure and alloy phases of AM50 magnesium alloy" *J. Alloys and Compounds* 470 (2009) 515-521

103. G. Morozova "Phase composition and corrosion resistance of magnesium alloys" *Met. Sci. and Heat Treatment* 50 (2008) 100-104

104. G. Song, A. Bowles, D.H. St. John "Corrosion resistance of aged die cast magnesium alloy AZ91D" *Mat. Sci. Eng. A* A366 (2004) 74-86

105. R. Ambat, N.N. Aung, W. Zhou "Evaluation of microstructural effects on corrosion behaviour of AZ91D magnesium alloy" *Corros. Sci.* 42 (2000) 1433-1455

106. M.C. Zhao, M. Liu, G. Song, A. Atrens "Influence of the β-phase morphology on the corrosion of the Mg alloy AZ91" *Corros. Sci.* 50 (2008) 1939-1953

107. H.Y. Hsiao, W.T. Tsai "Effect of heat treatment on anodization and electrochemical behaviour of AZ91D magnesium alloy" *J. Mater. Res.* 20 (2005) 2763-2771

108. M. Laleh, F. Kargar "Effect of surface nanocrystallization on the microstructural and corrosion characteristics of AZ91D magnesium alloy" *J. Alloys and Compounds* 509 (2011) 9150-9156

109. T. Zhang, Y. Shao, G. Meng, Z. Cui, F. Wang "Corrosion of hot extrusion AZ91 magnesium alloy: I – relationship between the microstructure and corrosion behaviour"*Corros. Sci.* 53 (2011) 1960-1968

110. 105. (46) D. Song, A.B. Ma, J.H. Jiang, P.H. Lin, D.H. Yang, J.F. Fan "Corrosion behaviour of bulk ultra-fine grained AZ91D magnesium alloy fabricated by equal channel angular processing" *Corros. Sci*. 53 (2011) 362-373

111. G. Galicia, N. Pebere, B, Tribollet, V. Viver "Local and global electrochemical impedances applied to the corrosion behaviour of an AZ91 magnesium alloy" *Corros. Sci.* 51 (2008) 1789-1794

112. H. Krawiec, S. Stanek, V. Vignal, J. Lelito, J. Suchy "The use of microcapillary techniques to study the corrosion resistance of AZ91 magnesium alloy at the microscale" *Corros. Sci.* 53 (2011) 3108-3113

113. R. Ambat, N.N. Aung, W. Zhou "Studies on the influence of chloride ion and pH on the corrosion and electrochemical behaviour of AZ91D magnesium alloy" *J. Appl. Electrochem.* 30 (2000) 865-874

Chapter Two:

Experimental

2.1 Microscopy

2.1.1 Scanning Electron Microscopy (SEM)

2.1.1.1 Instrumentation

Scanning electron microscopy (SEM) was developed in 1938 and is one of the most commonly used techniques in materials science due to the excellent image resolution achieved. SEM images are produced through the interaction of an electron beam with a sample. A schematic showing a standard SEM set up is shown in Figure 2.1 [1]. An electron gun with a W filament produces a beam of electrons (200 eV – 50 keV) and the electrons are accelerated through two electromagnetic lenses (a condenser and an objective) that reduce the diameter of the beam. Commonly found inside the objective lens are deflection coils that deflect the beam in a regular pattern onto the sample surface, a procedure called rastering. The magnification of an SEM image arises not from the strength of the objective lens as in light microscopy, but from the size of the rasterred area on the sample surface [2].

The electron beam penetrates the surface of the sample to produce secondary electrons (SE), backscattered electrons (BSE), X-rays and Auger electrons [2]. SEs are generated from inelastic collisions between the incident electrons and electrons in the k-orbital of an atom. These electrons are low energy and can only escape from a thin layer of the surface. Many of the generated SEs are reabsorbed by the sample and do not reach the detector. The SE mode of imaging is thus utilized mainly for topographic imaging as more electrons from higher positions on the surface will be deflected and appear bright,

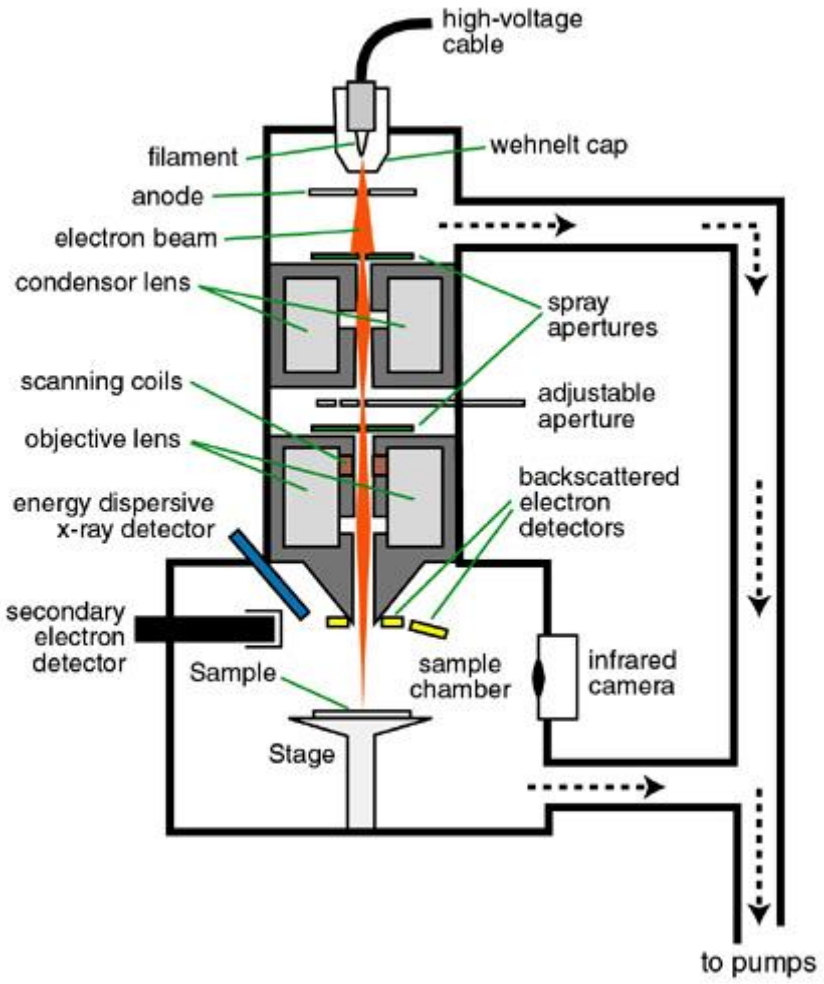

Figure 2. 1 - Schematic of a scanning electron microscope [1].

while electrons from lower points on the surface will reach the detector less regularly and appear dark. BSE are generated as a result of elastic scattering of electrons and the degree of scattering is dependent on the atomic number of the elements in the surface. The larger the atomic number, the higher the number of backscattered electrons produced, and the brighter the location will appear in the image. BSEs can be produced from deeper locations within the sample compared to SEs and this decreases the resolution when in the BSE imaging mode. However, BSEs are excellent for imaging the surface microstructure as they provide contrast based on the elemental differences in areas on the sample [2].

Quantitative elemental analysis can be achieved using X-ray energy dispersive spectroscopy (XEDS, EDX or EDS). When an electron is ejected from a core level of an atom, an electron from an outer shell can drop down in energy to fill the gap and generate an X-ray with an energy characteristic for that transition. Based on the energies of the emitted x-rays, the source elements can be identified and correlated to their position in the SEM image. Repeated scanning of a selected area can generate an XEDS map of element locations and, based on signal intensity, quantitative measurements of elemental compositions are possible. The XEDS signals arise from an excitation volume that reaches much greater depths than that from which BSEs are produced and a schematic showing the regions from which the different signals are collected is shown in Figure 2.2.

2.1.1.2 SEM Experimental Details

Unmounted samples were adhered to the SEM stage with a carbon-stickie pad. Samples which were mounted but had no exposed backing were electrically connected to the SEM stage by one of two procedures: 1) carbon paint was applied to the epoxy

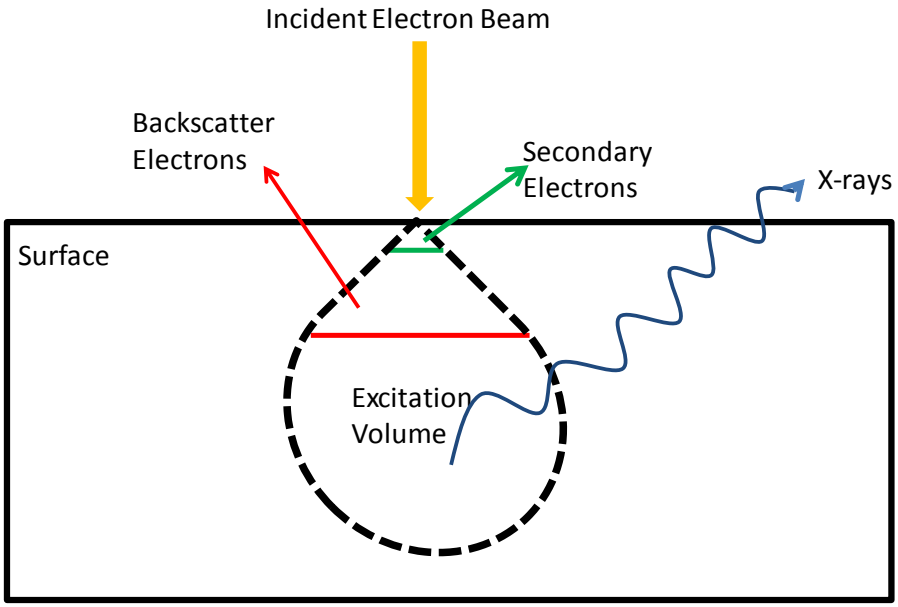

Figure 2. 2 - Schematic showing the excitation volume caused by an incident electron beam and regions from which different signals are generated.

surface and the sample edge to allow electrical connection. The paint was removed using ethanol before the sample was exposed to any corrosive environment to avoid galvanic coupling between the paint and the sample. 2) Cu tape was used to cover the epoxy resin and reduce charging, and to make electrical contact between the sample and the SEM stage. Areas of interest (AOI) on polished alloy surfaces were imaged using accelerating beam voltages of 3 keV – 20 keV in BSE mode prior to immersion. Corroded samples were imaged in both the SE and BSE modes depending on surface conditions.

2.1.2 Focused Ion Beam (FIB)

A powerful complimentary technique to SEM is the use of a Focused Ion Beam (FIB) which was first developed in the 1970's at the University of Chicago [3]. FIB serves as an electron "cutting tool" by bombarding a sample surface with heavy atoms to produce a cross section, thus enabling fine milling of a substrate [4]. Ga-ions are commonly used for the beam due to the low melting point and low vapour pressure of Ga. Solid Ga is melted and the liquid Ga moves to the tip of a W needle. A strong electric field is present at the W tip and which causes the liquid Ga to form a point source causing Ga^+ ions to be ejected from the tip. The generated ions are accelerated towards the sample by an electrical field. On contacting the sample surface the Ga^+ ions can induce an elastic collision with a surface atom, leading to ejection of the surface atom if the kinetic energy it receives is larger than its binding energy in the surface. This sputtering of the surface atoms can penetrate into the sample, producing a deep cut which can subsequently be viewed in cross section. The Ga^+ can also be implanted into the material, backscattered out of the material to reside on the surface, or undergo inelastic scattering to produce secondary electrons and X-rays. These SEs can be utilized, just as

in SEM, for imaging of the surface [5]. In this research, FIB was employed to produce cross sections allowing imaging of the corrosion product/alloy interface and to produce thin samples lifted out for transmission electron microscopy (TEM) samples.

2.1.3 Confocal Laser Scanning Microscopy (CLSM)

2.1.3.1 Instrumentation

Confocal laser scanning microscopy (CLSM), invented in 1986 at Cambridge University, is a common biological technique [6] that has also made strides as a powerful technique in corrosion research due to its high resolution imaging capabilities when compared to light microscopy [7-10]. In this research, both 2- and 3-dimensional (2D, 3D) profiles of corroded Mg alloy surfaces were collected with CLSM.

The CLSM set-up is seen in Figure 2.3 [11]. A laser beam, from a HeNe (λ = 633 nm) source, is directed through a pinhole aperture, to a dichroic mirror and into an objective lens to focus it to the sample. The light interacts with the sample and can be reflected, fluoresced or scattered back through the same objective lens. The dichroic mirror reflects the reflected light to a detector pinhole where a photomultiplier tube detector converts the incoming light to a digital image. The laser is scanned across the sample to produce a high resolution image, while limiting beam damage to the sample [6].

3-D depth profiles are produced by changing the focal plane in the Z-direction at set micrometer intervals. The images collected at each focal length are stacked to produce a 3-D profile of the corroded surface.

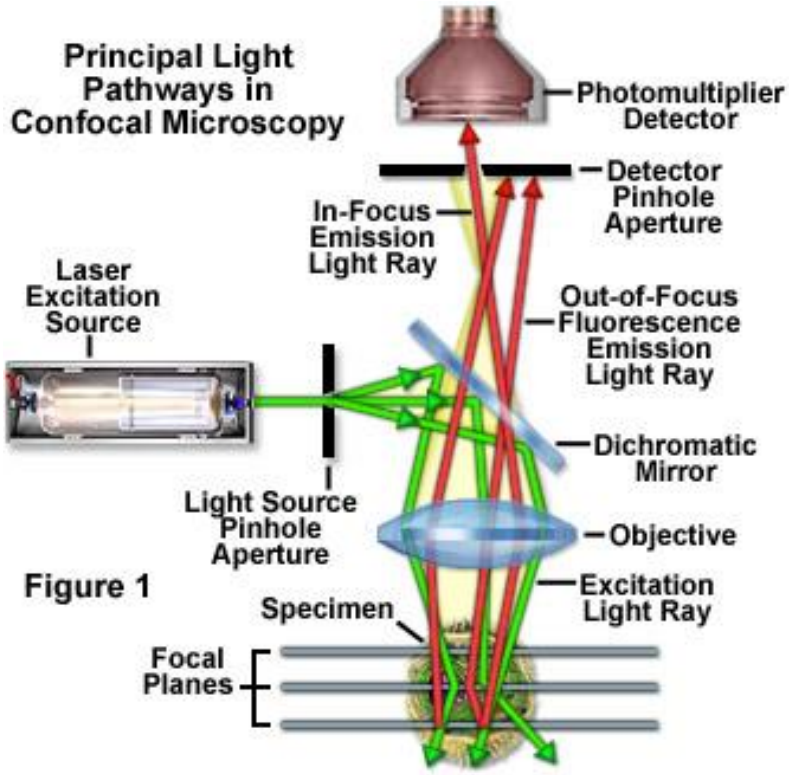

Figure 1

Figure 2. 3 - Standard configuration of a confocal laser scanning microscope [11].

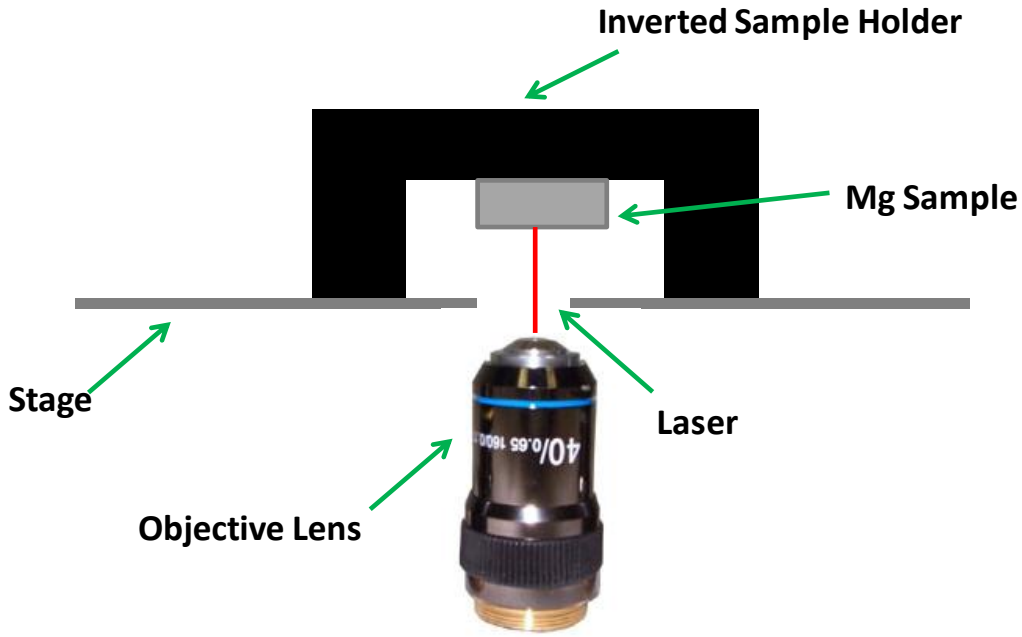

Figure 2. 4 - Customized setup for CLSM analyses of corroded samples.

2.1.3.2 CLSM Experimental Details

CLSM images were recorded on a Zeiss LSM 510 Microscope at the Integrated Microscopy Facility at the Biotron at Western. An inverted stage was used to locate the sample above the objective lens to allow reflected light image collection. The customized set up is shown in Figure 2.4. 3-D images were produced by collecting images in 1 µm – 0.1 µm z-increments. Light intensities were normalized into a depth profile by considering how many steps of known distance (slices) through the focal plane, in the z-direction, are required to reach the deepest region on the sample surface. The differences in light intensities are then converted to a distance. At depths > 30µm, the limit of clear image resolution is reached [12].

2.1.4 Transmission Electron Microscopy (TEM)

2.1.4.1 Instrumentation

Following corrosion immersion experiments on samples, TEM was utilized to study the corrosion product/alloy interface.

The principal behind TEM is similar to light microscopy. A light source is directed through a sample to a detector, employing electrons rather than visible photons to generate an image. TEM samples must be transparent to the incoming electrons and are commonly thin slices (20-300 nm) to limit loss of electrons. As for SEM, the TEM microscope contains an electron source, two condenser lenses to control focus and magnification of the beam and magnetic coils for beam alignment.

TEM images can be collected in bright field and dark field mode. In the bright field mode, the flux of the incident electrons to a detector, after passing through the

sample, dictates the brightness of the image. The size, shape and thickness of areas of the sample are determined by the rate of electron absorption/scattering which induces differential brightness in the image. In the dark field mode images are generated using the diffracted light from the sample projected onto the detector. This is done on several diffraction planes to generate an image [13].

2.1.4.2 TEM Experimental Details

The main application of the TEM was to analyze corrosion product layers produced on the Mg alloy surfaces. This required their integrity to be retained during imaging. To achieve this prior to FIB preparation of samples, a ~ 1 μm thick W protective film was deposited. Thinning of the extracted TEM sample was performed by polishing with an ion beam with a reduced voltage, decreasing from 30 kV to 1 kV. The samples were stored in a desiccator following preparation. Characterization was performed on a FEI Titan 80-300 scanning TEM (STEM) equipped with an XEDS spectrometer (XEDS-Oxford Inca, Si(Li) detector). Accelerating voltages of 200 kV or 300 kV were used to generate the images.

2.2 Sample Preparation

The focus of the research in this thesis was on the effect of microstructure on the corrosion of Mg alloys. In order to assess these effects, the microstructure of the alloys was studied prior to corrosion experiments. Etching the substrate can successfully reveal microstructural features [14], but also damages the alloy surface (grain boundary removal, height differences, removal of α-Mg). These alterations can serve as additional variables affecting the corrosion process and are not desired. The microstructure must be studied prior to immersion with limited changes to the surface during sample preparation.

Samples in this work were prepared using a custom mechanical polishing procedure. The as-received Mg alloys were machined into square or circular samples of the desired surface area. The samples were first ground successively with 800, 1000, 1200, 2400 grit SiC paper with water as a lubricant, with each step carried out until the polishing lines from the previous step were removed. In the subsequent fine polishing steps, water exposure was limited due to the immediate susceptibility of Mg alloys to corrosion when exposed to an aqueous environment. A 4000 grit SiC paper was employed with a 1:1 ethanol:isopropanol mixture as a lubricant when needed. Finer polishing steps caused a smearing on the surface resulting from the use of the 4000 grit pad. The ground alloy surface was then polished on a Struers DP-Dur cloth saturated in 3 μm Struers DP-Suspension A for 5 to 10 min with the ethanol/propanol mixture once again used as a lubricant. The final stage consisted of polishing for 2-3 min, applying pressure to the sample, on a Struers OP-Chem cloth using an equal volume mixture of Struers OP-S Suspension and ethylene glycol as an abrasive. The polished sample was rinsed and ultra-sonicated in anhydrous ethanol for 2 min, air dried and stored in a desiccator.

The visibility of the secondary microstructural features of the Mg alloy is significantly improved with each polishing step. Figure 2.5 shows the progress of polishing in revealing the microstructure of a sand cast AM50 alloy at; (a) 1200 grit SiC when the β-phase and intermetallics were masked by the polishing lines; (b) 2400 grit SiC which revealed the β-phase, although the edges were not as sharp due to polishing lines; (c) 4000 grit SiC at which the β-phase regions were clearly resolved with scratches still observable in the α-Mg matrix; (d) 3 μm diamond suspension improved the

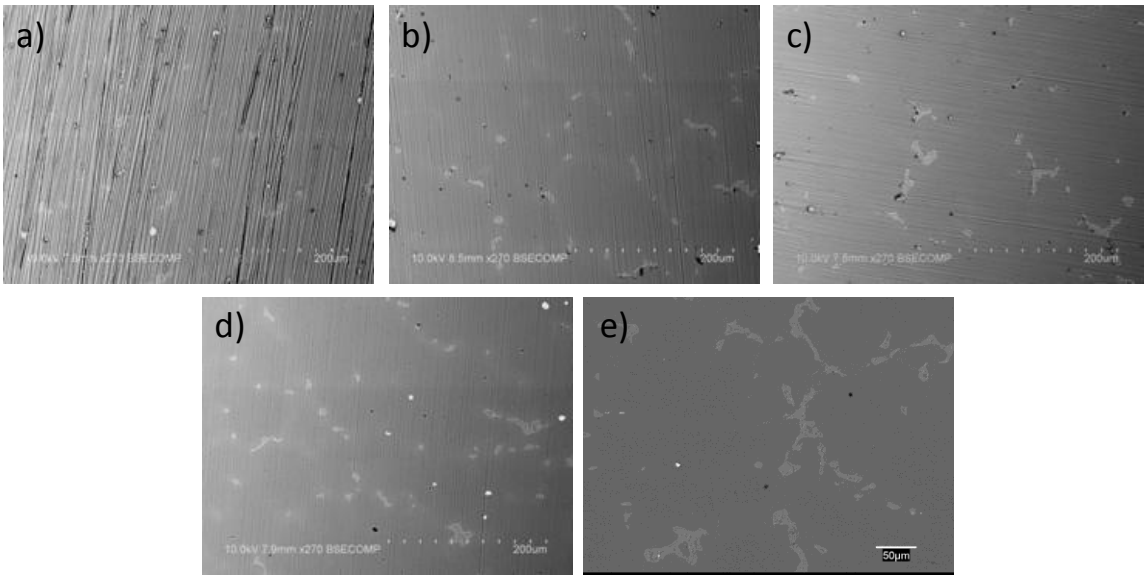

Figure 2. 5 - SEM BSE micrographs showing an AM50 Mg alloy surface in different stages of sample preparation and the gradual revealing of the alloy microstructure at a) 1200 grit SiC, b) 2400 grit SiC c) 4000 grit SiC, d) 3-µm diamond paste and e) colloidal silica polishing steps.

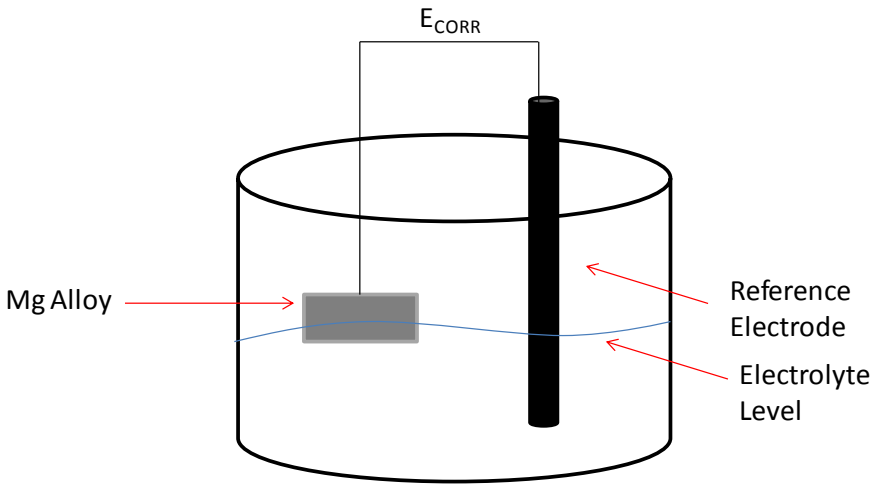

Figure 2. 6 - Experimental set up for intermittent immersion experiments.

resolution; (e) colloidal silica yielded a scratch free surface showing all the surface features to be flat.

2.3 Intermittent Immersion Experiments

The influence of secondary microstructure on the corrosion process was investigated using intermittent immersions of the Mg alloys to a corrosive environment. The Mg samples were immersed face down in the electrolyte along with a reference electrode to allow monitoring of the E_{CORR}. This set up can be seen in Figure 2.6. After a specified exposure period the sample was removed from the solution, rinsed with Nanopure® water (18 MΩ-cm), and analyzed microscopically using the techniques described in Section 2.1. The sample was then re-immersed in a new solution of the same composition and an equal volume, and the immersion step repeated.

To assess the role played by individual microstructural features, their evolution must be monitored throughout a series of immersions. This was achieved by re-locating an AOI on the sample surface after each immersion. Prior to imaging the freshly polished surface, scratches were made on the edge(s) of the alloy, so that when placed in the SEM an AOI could be located and its coordinates marked relative to the scratch. Figure 2.7 shows this process on a ZEK100 alloy which was corroded for 24 h in 0.16 wt% NaCl. Figure 2.7 (a) shows the scratch on the freshly polished surface with coordinates drawn to the AOI, shown in Figure 2.7 (b). Following a 24 h immersion in 0.16 wt% NaCl, the scratch is easily relocated, Figure 2.7 (c), and the AOI again located and imaged, Figure 2.7 (d).

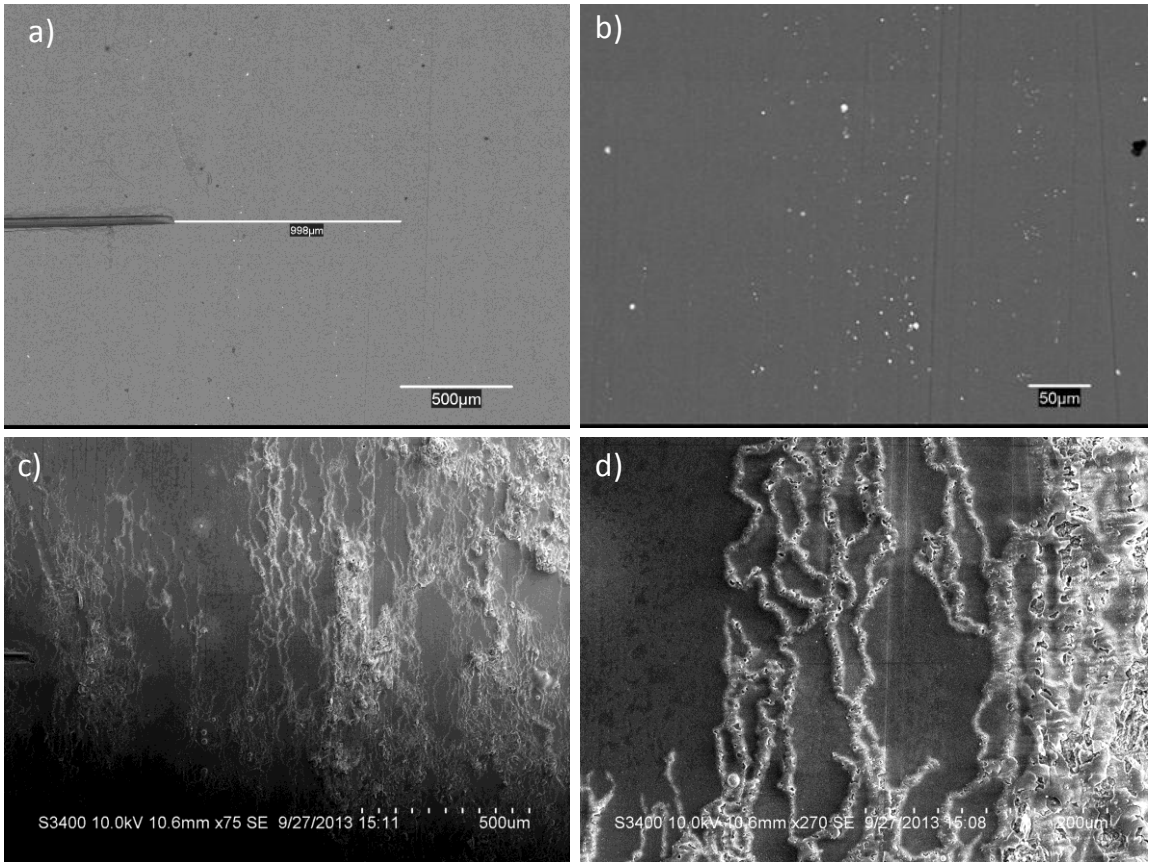

Figure 2. 7- SEM images showing relocating of a selected AOI on a ZEK100 Mg alloy: a) location of AOI relative to scratch, b) the selected AOI, c) the surface with the scratch following a 24 h immersion in 0.16 wt% NaCl, d) the corroded AOI.

The presence of the scratches did not influence the corrosion process of the alloy. Figure 2.8 (a) shows an SEM BSE micrograph of a corroded AM60 Mg alloy following 48 h immersion in 1.6 wt% NaCl near the middle of the sample. The damage observed is similar to the damage located near the artificial scratch, Figure 2.8 (b), showing the presence of the scratch does not influence the corrosion process occurring in close proximity to the scratch. Residual polishing scratches also do not influence the progress of corrosion on Mg alloys, as seen in Figure 2.9. A colloidal silica polished AM50 Mg alloy is shown in the CLSM micrograph Figure 2.9 (a) with two residual polishing scratches present, marked with green arrows. Following 96 h of immersion in 1.6 wt% NaCl the two scratches are still observed and the alloy surface has corroded independently of these residual scratches, Figure 2.9 (b).

2.4 Chromium Treatment of Mg Alloys

During the corrosion of Mg alloys several µm of $Mg(OH)_2$ corrosion product are deposited onto the alloy surface and can interfere with analytical measurements. This effect is clear in Figure 2.10 (a) which displays a CLSM micrograph of an AZ31 Mg alloy following 48 h of immersion in a 0.16 wt% NaCl solution. Resolution of the surface damage is limited due to the presence of corrosion product. To reveal the damage morphology of the bulk alloy, the corrosion product was removed using treatment with hexavalent chromium, following the ASTM standard G1-90, Designation C5.2 [15] which involves 60 s of gentle agitation in a 100 mL solution of 20 g CrO_3, 1 g $AgNO_3$, 2 g $Ba(NO_3)_2$ and NanoPure® water. A solution of 20 g CrO_3 in 100 mL NanoPure® water was also found to be equally effective when applied with 60 s of gentle agitation. The chrome treatment only removes the corrosion product and does not corrode the Mg

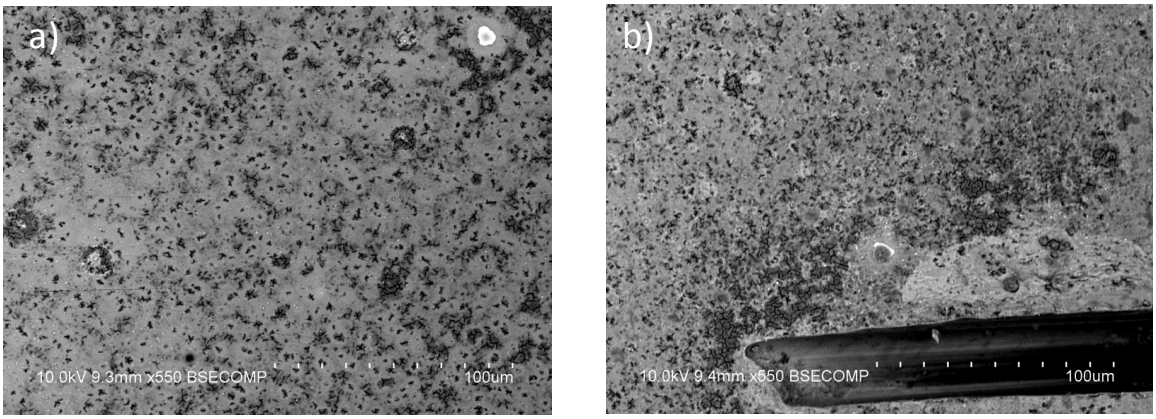

Figure 2. 8 - SEM BSE micrographs of a AM60 Mg alloy following 48 h of immersion in 1.6 wt% NaCl showing; a) the corrosion damage observed in the middle region of the sample and b) identical corrosion damage located near the artificial scratch.

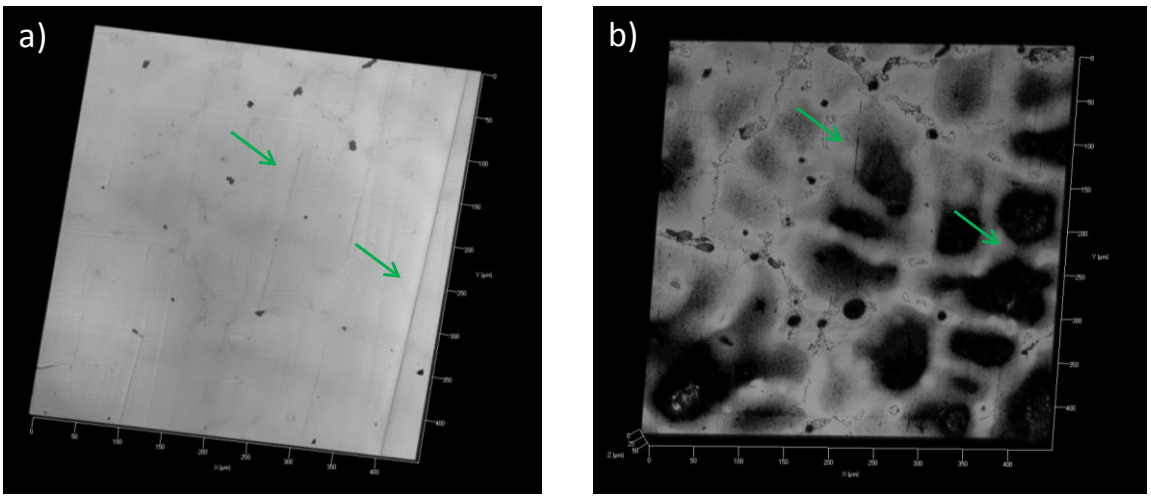

Figure 2. 9 – CLSM micrographs of a) a colloidal silica polished AM50 Mg alloy displaying residual scratches marked with green arrows, b) following 96 h of immersion in 1.6 wt% NaCl; the green arrows show the same residual scratches are still visible.

alloy itself [16]. After the treatment, the samples were sonicated in methanol for 10s to remove any residual chromium solution from the surface. Following chromium treatment a much more detailed image of the damage morphology on the corroded AZ31 sample can be detected, Figure 2.10 (b).

The chromium treatment was originally used in between each intermittent immersion to remove the corrosion product before microscopic analyses. This procedure was ceased when it was discovered that removal of the corrosion product increased the susceptibility of the sample to corrosion. An example is shown in Figure 2.11. The surface of a sand cast AM50 sample after 12 h of immersion in 1.6 wt% NaCl and removal of the corrosion product is shown in Figure 2.12 (a). Following an additional 12 h immersion, major corrosion damage is seen in this area, Figure 2.11 (b) and the damage was not limited to this area. The damage induced is a result of the removal of the corrosion product, and not an example of the major damage which eventually occurs and will be discussed in Chapter 3. Subsequently a chromium treatment was used only after the final immersion step in a sequence of immersions.

2.5 Electrochemistry

2.5.1 Electrochemical Measurements

A standard three electrode glass cell was utilized for all electrochemical measurements and was placed in a Faraday cage to eliminate interference from external electrical noise. A Pt-mesh, or Pt-plate was used as a counter electrode and the reference electrode was a saturated calomel electrode (SCE) (0.244 V vs. SHE). All electrolytes were prepared with reagent grade NaCl (Caledon), $MgCl_2$ (Caledon) and NanoPure® (18 MΩ-cm) water.

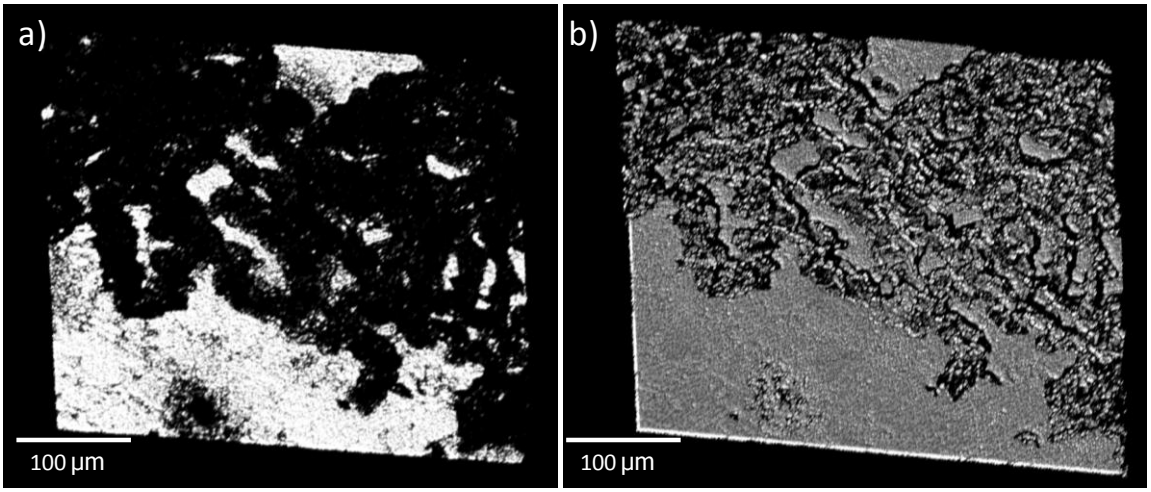

Figure 2. 10 - 3D CLSM micrograph of an AZ31 Mg alloy surface exposed for 48 h in 0.16 wt% NaCl: a) with the accumulated corrosion product on the surface and b) following removal of the corrosion product with chromium treatment.

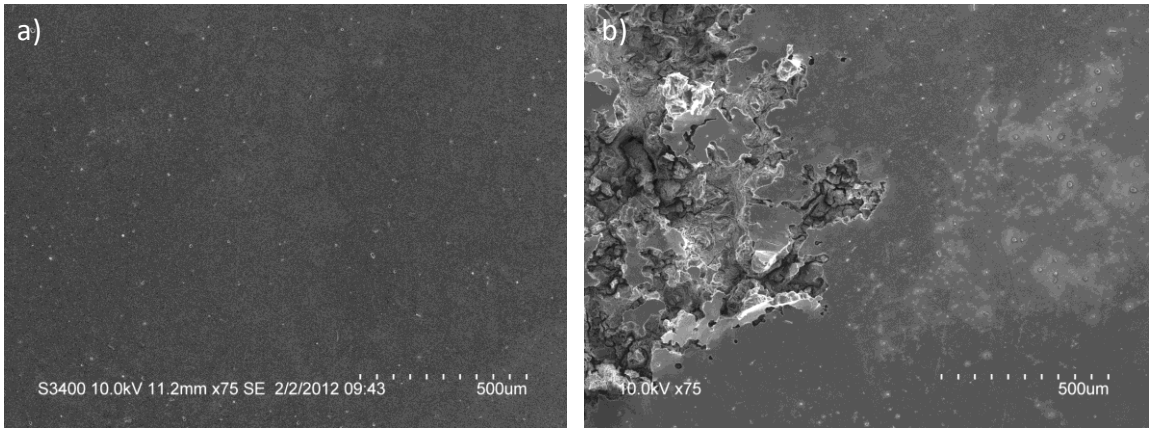

Figure 2. 11 - SEM micrographs of an AM50 sand cast sample a) after 12 h of immersion in 1.6 wt % NaCl and removal of the corrosion product and b) after a 12 h subsequent exposure of a location where major damage has occurred as a consequence of removing the corrosion product.

Prior to each experiment Mg alloy samples were prepared using the method outlined in Section 2.2 up to either 4000 grit SiC or a colloidal Si finish. E_{CORR} measurements were made with the sample placed face down in the solution suspended by a steel rod. Potentiodynamic polarization (PDP) scans were performed by allowing the Mg alloy to establish a stable E_{CORR} over a period of 1 h to 24 h prior to scanning the potential to 0.5 V, or until a current density of 1 mA/cm^2 was reached. This limited the damage to the sample. In galvanostatic measurements, the Mg alloy was placed in the solution for 5 min to reach a relatively stable E_{CORR} before application of a cathodic current.

Galvanically coupled measurements were performed in a one-pot cell with the two electrodes suspended face down by steel rods. The current flowing between the electrodes was monitored with a Keithley 6514 zero resistance ammeter controlled with an in-house software interface. The less noble material in the couple was selected as the working electrode. A SCE reference electrode was also placed in the cell to allow potential measurements, when applicable.

2.5.2 Electrochemical Impedance Spectroscopy (EIS)

Electrochemical impedance spectroscopy (EIS) is commonly applied in corrosion science to investigate film properties and surface mechanisms [17-19]. A small alternating potential perturbation, centred around E_{CORR}, (~10 mV magnitude) is applied to the working electrode. The output response is an alternating (AC) current that will be in-phase or out-of-phase with the alternating potential input depending on the characteristics of the interface. Figure 2.12 displays the frequency dependent input

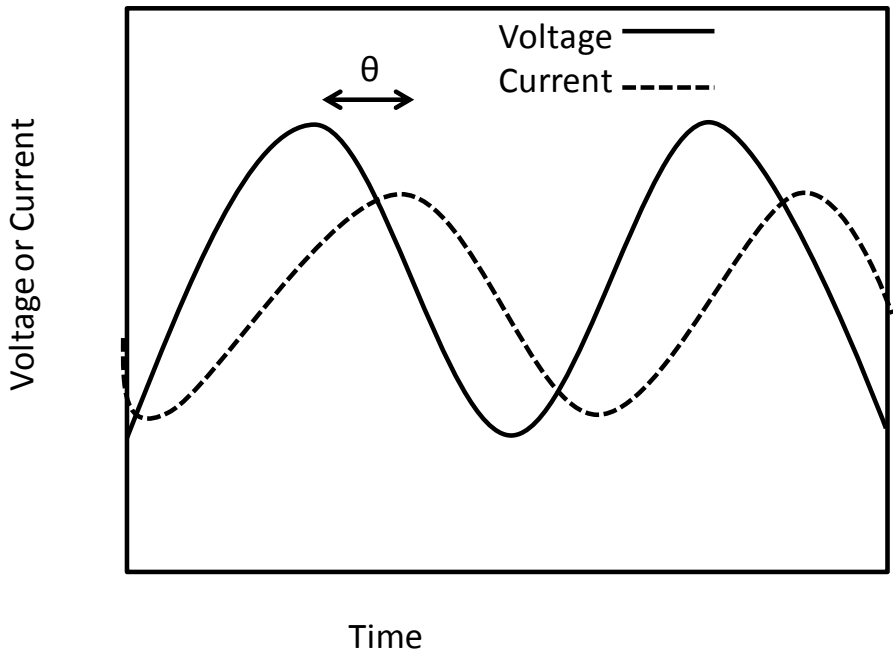

Figure 2. 12 - The current response to a sine-wave potential input expected in an EIS experiment; θ indicates the phase angle between the two signals.

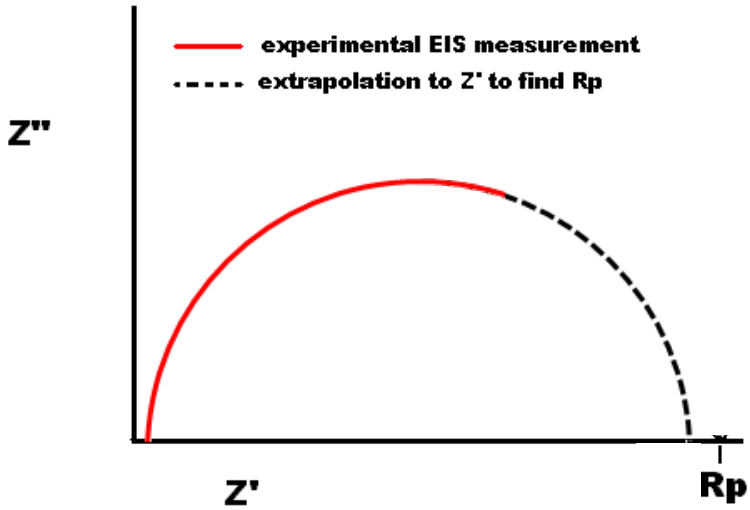

Figure 2. 13 - Example of the estimation of R_p from a Nyquist EIS plot. Using the experimental data (red) the semicircle is extrapolated to the real axis (Z') to find R_p

potential (solid line) and output current (dashed line) as a function of time. The two signals are out of phase with a phase shift of magnitude denoted by θ.

The potential and current sinusoidal signals are related by the following two expressions where V_o and I_o are the potential and current amplitudes:

$$V(t) = V_o \sin(\omega t) \tag{2.1}$$

$$I(t) = I_o \sin(\omega t + \theta) \tag{2.2}$$

and ω is the angular frequency of the sine wave (rad-s^{-1}). For a DC system, Ohm's law states that the voltage and current of a system are related by the resistance (R):

$$V = IR \text{ or } R = \frac{V}{I} \tag{2.3}$$

A capacitance (C) can be related to the current and potential by the relationship:

$$I(t) = C\frac{dV}{dt} \tag{2.4}$$

By analogy to equation 2.3, the impedance (Z) of an AC system can be calculated from the ratio of the applied potential and the resulting current by the following expression:

$$Z(\omega t) = \frac{V_o \sin(\omega t)}{I_o \sin(\omega t + \theta)} \tag{2.5}$$

The total impedance of a system can be separated into real (Z') and imaginary (Z") impedances using the imaginary unit, j:

$$Z(\omega t) = Z'(\omega t) + jZ''(\omega t) \tag{2.6}$$

The resistance of a system is contained in the real component of the total impedance and the capacitance is contained in the imaginary component:

$$Z = R - j\frac{1}{\omega C} \tag{2.7}$$

EIS measurements are commonly presented in a complex plane plot of Z" against Z', referred to as a Nyquist plot, which is the form utilized in this thesis. Since corrosion is a DC process the corrosion rate can be obtained from a zero frequency measurement. Unfortunately such a measurement cannot be made. However, extrapolation of a semicircular Nyquist plot to the real resistive axis (Z'), yields a value of the polarization resistance (R_p), shown schematically in Figure 2.13. R_p is inversely proportional to the corrosion rate, which can be calculated using the Stearn-Geary equation, where i_{CORR} is the corrosion rate, and b_a and b_c are the anodic and cathodic Tafel slopes [20]:

$$i_{CORR} = [(b_a \times b_c)/(b_a + b_c)] \times R_p^{-1} \tag{2.8}$$

Unfortunately, for corroding Mg alloys, evaluation of the Tafel slopes, especially for the anodic process, are difficult to evaluate [21].

2.5.3 EIS Experimental Details

EIS measurements were performed after 10 hr. of immersion at E_{CORR}. A sinusoidal potential perturbation of ± 10 mV was applied above and below E_{CORR}, and the current response recorded over the frequency range, 10^5 Hz to 10^{-3} Hz. Eleven data points per frequency decade were recorded. Subsequently, a one point per decade reverse scan was recorded from 10^{-2} – 10^5 Hz to ensure steady-state was maintained throughout the EIS measurement. Kramers – Kronig transforms were applied to confirm the validity of the data.

2.6 References

1. J.H. Wittke, "SEM-Microprobe: Instrumentation" Dept. Geology, Northern Arizona University, 2008 http://www4.nau.edu/microanalysis/Microprobe-SEM/Instrumentation.html

2. M.A. Hyatt "Pricniples and techniques of scanning electron microscopy" Van Nostrand Reinhold Company, New York, Vol 1. 1974

3. R. Wirth "Focused ion beam combined with SEM and TEM: Advanced analytical studies of chemical composition, microstructure and crystal structure in geomaterials on a nanometre scale" *Chem. Geol.* 261 (2009) 217-229

4. P.R. Munroe "The application of focused ion beam microscopy in the material sciences" *Mat. Character.* 60 (2009) 2-13

5. L.A. Giannuzzi, F.A. Stevie "A review of focused ion beam milling techniques for TEM sample preparation" *Micron* 30 (1999) 197-204

6. W.B. Amos, J.G. White "How the confocal laser scanning microscope entered biological research" *Biol. Cell* 95 (2003) 335-342

7. P. Jakupi, J.J. Noel, D.W. Shoesmith "The evolution of crevice corrosion damage on the Ni-Cr-Mo-W alloy 22 determined by confocal laser scanning microscopy" *Corros. Sci.* 54 (2012) 260-269

8. M. Jonsson, D. Persson, R. Gubner "The initial steps of atmospheric corrosion on magnesium alloy AZ91D" *J. Electochem. Soc.* 154 (2007) C684-C691

9. L.F. Garfias-Mesias, M Alodan, P.I. James, W.H. Smyrl "Determination of precursor sites for pitting corrosion on polycrystalline titanium by using different techniques" *J. Electrochem. Soc.* 145 (1998) 2005-2010

10. O. Schneider, G.O. Ilevbare, J.R. Scully, R.G. Kelly "Confocal laser scanning microscopy as a tool for in-situ monitoring of corrosion underneath organic coatings" *Electrochem. Solid State Let.* 4 (2001) B35-B38

11. S. W. Paddock, T. J. Fellers, M.W. Davidson "Basic Concepts: Confocal Microscopy" http://www.microscopyu.com/articles/confocal/confocalintrobasics.html

12. R.M. Asmussen, P. Jakupi, M. Danaie, G. Botton, D.W. Shoesmith "Tracking the corrosion of magnesium sand cast AM50 alloys in chloride environments" *Corros. Sci.* 75 (2013) 114-122

13. P. Hirsch, A. Howie, R. Nicholson, D.W. Pashley, M.J. Whelan "Electron microscopy of thin crystals" Butterworths/Kreiger, London 1977

14. D. Sachdeva, "Insights into microstructure based corrosion mechanism of high pressure die cast AM50 alloy" *Corros. Sci.* 60 (2012) 18-31

15. ASTM G1-90: Standard practice for preparing, cleaning and evaluating corrosion test specimens, 1999.

16. M.C. Zhao, M. Liu, G. Song, A. Atrens "Influence of the β-phase morphology on the corrosion of the Mg alloy AZ91" *Corros. Sci.* 50 (2008) 1939-1953

17. K. Juttner "Electrochemical impedance spectroscopy (EIS) of corrosion processes on inhomogeneous surfaces" *Electrochim. Acta* 35 (1990) 1501-1508

18. D. Macdonald, M.C.H. McKubre "Section 4.4 – Corrosion of materials" *Impedance Spectroscopy – Theory, Experiment and Applications* Second Edition, Wiley, 2005

19. D. Macdonald "Why electrochemical impedance spectroscopy is the ultimate tool in mechanistic analysis" *ECS Trans.* 19 (2009) 55-79

20. J.R. Scully "Polarization resistance method for determination of instantaneous corrosion rates" *Corrosion* 56 (2000)199-218

21. Z. Shi, A. Atrens "Measurement of the corrosion rate of magnesium alloys using Tafel extrapolation" *Corros. Sci.* 52 (2010) 579-588

Chapter Three

Tracking the Corrosion of Magnesium Sand Cast AM50 Alloy in Chloride Environments

3.1 Introduction

Magnesium alloys are attractive materials for industrial application due to their high strength-to-weight ratio. However, a major deficiency is their inadequate corrosion resistance when exposed to aqueous and humid environments exemplified by those encountered in automotive applications [1-3]. As the most electrochemically active structural material, magnesium, when placed in electrical contact with a dissimilar metal/alloy in an aqueous medium can establish an active galvanic couple resulting in anodic polarization and corrosion of magnesium and consequently the generation of very high current densities and corrosion rates [4].

AM50, a commercial magnesium alloy, is used for its exceptional castability [5,6]. The major microstructural constituents of AM50 are: a Mg-rich α-phase, an Al-enriched eutectic α-phase containing β-phase ($Mg_{17}Al_{12}$), and Al-Mn intermetallics [7,8]. Previous macroscale studies on AM50 and other Mg alloys suggest micro-galvanic coupling can occur between the β-phase and/or intermetallics and the α-phase, thus, accelerating the corrosion of Mg rich α-phases [9-11]. The aim of this study is to track the location of corrosion initiation and to quantify the extent of propagation (as a penetration depth) based on microstructural characteristics; specifically, the varying Al-content of α-grains and the proximity of β-phase networks on sand cast AM50 alloys. Due to the variable Al-content of α-grains [11] it is possible to have individual grains with different corrosion rates.

Alloying magnesium with aluminum has been shown to alter the microstructure [12], and significantly influence corrosion resistance [3, 13]. While corrosion resistance is usually assessed in terms of the bulk aluminum content of the alloy this study assesses corrosion damage as a function of the aluminum content at individual α-grains and its distribution throughout the sample. In this study, corrosion damage is quantified using confocal laser scanning microscopy (CLSM), a technique previously shown to quantify damage on Mg alloys and coatings [14, 15] and on other materials [16,17]. The chemical content and morphology of sub-surface corroded and un-corroded regions were also investigated by forming cross-sections using a focused-ion beam (FIB), followed by chemical analysis using x-ray energy dispersive spectroscopy (XEDS) and transmission electron microscopy (TEM). The surface and sub-surface chemistry of microstructural features was compared to their corrosion rate and damage morphology to determine which microstructural features enhance or repress corrosion resistance.

3.2 Experimental

3.2.1 Sample Preparation

As-received AM50 sand cast rods were machined into 1 × 1 × 0.7 cm electrodes. One side (1 cm^2), was tapped to accommodate a threaded rod to allow electrical connection to external circuitry. The 1 cm^2side to be examined was pre- treated using the following procedure: the sample was ground successively up to 4000 SiC grit. A thin layer of paraffin wax was applied to each SiC pad to maintain the integrity of the pad and to provide an additional lubricant. An equal volume mixture of ethanol and propanol was used as a lubricant on the SiC pad. The ground alloy surface was

then polished on a Struers DP-Dur cloth saturated in 3 μm Struers DP-Suspension A for 5 to 10 minutes with the ethanol/propanol mixture once again used as a lubricant. The final stage consisted of polishing, for 2-3 min, on a Struers OP-Chem cloth using an equal volume mixture of Struers OP-S Suspension and ethylene glycol, as an abrasive. The polished sample was rinsed and sonicated in anhydrous ethanol for 2 min and air dried and stored in a desiccator.

3.2.2 Instrumentation

AM50 electron micrographs were collected in back-scattered and secondary electron modes using a LEO 440 SEM, Hitachi 3400-N Variable Pressure SEM and a Hitachi 4500-N equipped with a Quartz One XEDS System to determine elemental concentrations of α-grains and other microstructural components.

Depth profiles on AM50 un-corroded and corroded surfaces were measured by detecting the reflected light intensity from a Zeiss 510 confocal, HeNe 633 nm laser. The polished sample surface was placed downward, suspended by a stage, facing an inverted objective. Light intensities were normalized into a depth profile by considering how many steps of known distance (slices) through the focal plane, in the z-direction, are required to reach the deepest region on the sample surface and convert the differences in light intensities to a distance. At depths of > 30μm, the limit of clear image resolution is reached.

3.2.3 Tracking Corrosion on the Microscale

Prior to corrosion experiments, the polished surface was analyzed by SEM/XEDS and confocal laser scanning microscopy (CLSM). The co-ordinates of an area of interest (AOI) were recorded (relative to a surface edge) so that the same area (275 µm × 450 µm) could be subsequently located after intermittent immersions. All experiments were performed in a naturally aerated 1.6 wt % NaCl (reagent grade, 99 % assay) solution with MilliQ® water (18 MΩ-cm^2) at ambient temperature (~ 22.5 °C). The polished side of the AM50 electrode was immersed in the electrolyte and suspended from a stainless steel rod with the electrolyte level located approximately 1 to 2 mm above the polished surface.

After immersion in the chloride solution, the corroded surface was rinsed and sonicated in anhydrous ethanol, and dried. The corroded AOI was then analyzed using SEM/XEDS and CLSM, and compared to the same location prior to corrosion. This procedure was repeated after each of a series of immersions, which simulate wet-dry cycling, to determine the evolution of damage morphology and penetration depth with time. On completion of immersion experiments (total of 96 h immersion), the sample was further analyzed with FIB (Zeiss NVision 40) for imaging and site-specific sample preparation for TEM using a FEI Titan 80-300 electron microscope equipped with an Electron Energy Loss Spectrometer (EELS).

3.2.4 Surface Montage Imaging

A 4 mm × 4 mm × 2 mm sand cast sample was mounted in Struers EpoFix™ epoxy so that only a 4 × 4 mm surface was exposed. The surface was polished as described in section 1.1. A total of 60 images, at 150 ×

magnification, were recorded across the entire 4 × 4 mm polished surface using a Hitachi SU6600 Field Emission SEM.. The images were then stitched using Image-Pro Plus 7.0® into a 10 × 6 grid to yield a final image map of the entire 4 mm × 4 mm surface. The sample was then immersed in chloride solution and corrosion analyses followed through a series of immersions as described in section 2.3. Between each immersion the surface was analyzed by SEM as described.

3.3 Results

3.3.1 Corrosion Behaviour of Sand Cast AM50 Alloys in 1.6 wt% NaCl

Figure 3.1 displays an SEM micrograph of a selected AOI (Figure 3.1 (a)) and the corresponding XEDS maps for Mg (Figure 3.1(b)), Al (Figure 3.1(c)) and Mn (Figure 3.1(d)). This area exhibits an Al-rich network of eutectic α- phase interlaced with β-phase mainly in the centre of the AOI. The presence of nine Al-Mn intermetallics is observed in the AOI. Following initial imaging with SEM and CLSM, the sample was immersed in the 1.6 wt% NaCl solution for a series of 24 h exposure periods. Between each immersion, the AOI is re-located and imaged with SEM and CLSM to monitor corrosion evolution on the surface. The SEM and CLSM light intensity images recorded after each 24 h. immersion period are

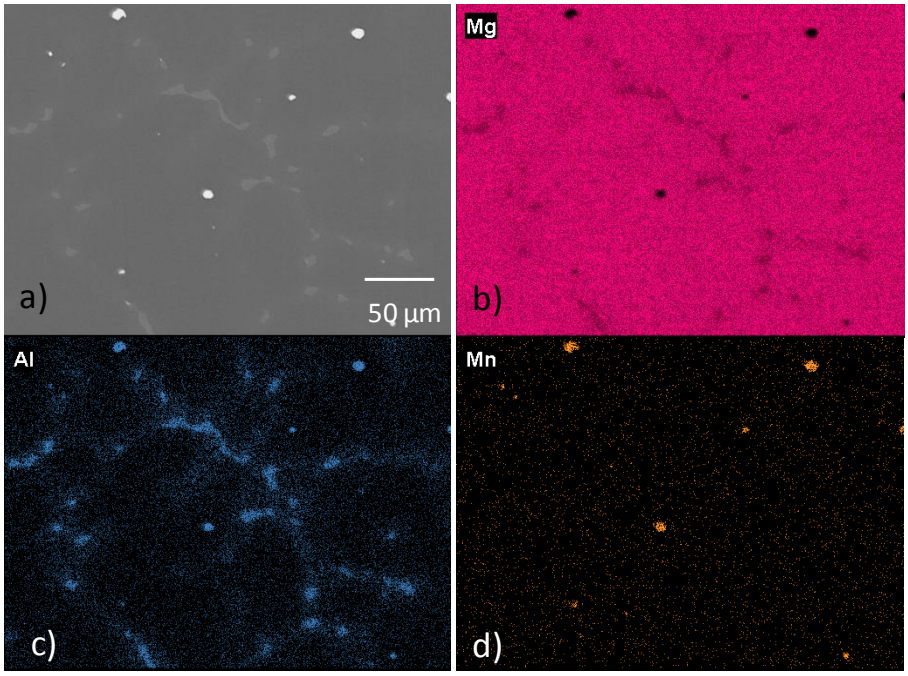

Figure 3. 1 - a) SEM backscatter image of a selected area of interest (AOI) on a sand cast AM50 alloy and the corresponding EDX maps for b) Mg, c) Al, d) Mn.

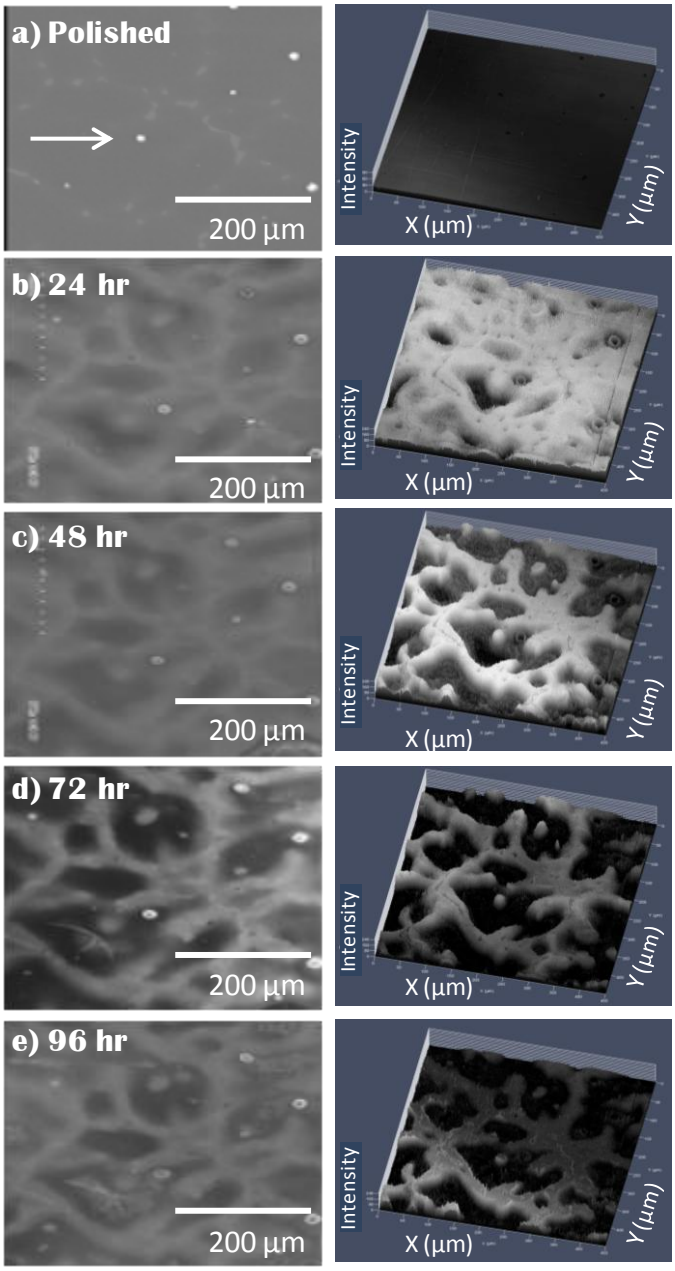

Figure 3. 2 - SEM and CLSM images of the AOI on an AM50 sample corroded through successive wet-dry cycles following a) 0 h, b) 24 h, c) 48 h, d) 72 h and e) 96 h exposure. The intermetallic marked with the arrow in a) is displayed in Figure 3.5.

presented in Figure 3.2. The initial polished surface undergoes dramatic changes after only 24 h of immersion mainly near the bottom of the AOI, where several α-grains have corroded. The Al rich regions in the centre appear to be more resistant to corrosion. After 48 h, a significantly corroded area is observed on the left-centre α-grain of the AOI. After 72 h, several other α-grains experienced extensive damage, a process which continues up to 96 h of exposure. Corrosion at the α-grains is directed inward into the alloy and leaves behind a skeletal uncorroded network. The cracking observed on some α-grains may be a result of the accumulated corrosion product drying when the sample is removed from solution and cannot be resolved at the selected magnification by the CLSM due to light scattering at the cracks. This cracking was not a result of the intermittent wet-dry cycling undergone by the sample, as it still occurs with a continuous exposure of 96 h, shown in Figure 3.3.

It is clear from Figure 3.2 that α-grains undergo preferential attack as expected from previous studies [18], whereas other microstructural constituents of the alloy display a much different behaviour. Figure 3.4 tracks an "ear-shaped" β-phase centered between two α-grains throughout a full 96 h immersion cycle. After 24 h, Figure 3.4(a), corrosion product is loosely dispersed over the area, with some change in corrosion depth on the neighbouring α-grains evidenced by the darkening in the corners of the image. The corrosion product layer becomes more pronounced in patches following 48 h of immersion, Figure 3.4(b), with the β-phase being masked by the corrosion product layer. The β-phase can still be distinguished due to a change in the morphology of the corrosion product above the β-phase compared to the surrounding coverage. As the corrosion product continues to accumulate, Figure 3.4(c) (72 h) and Figure 3.4(d) (96

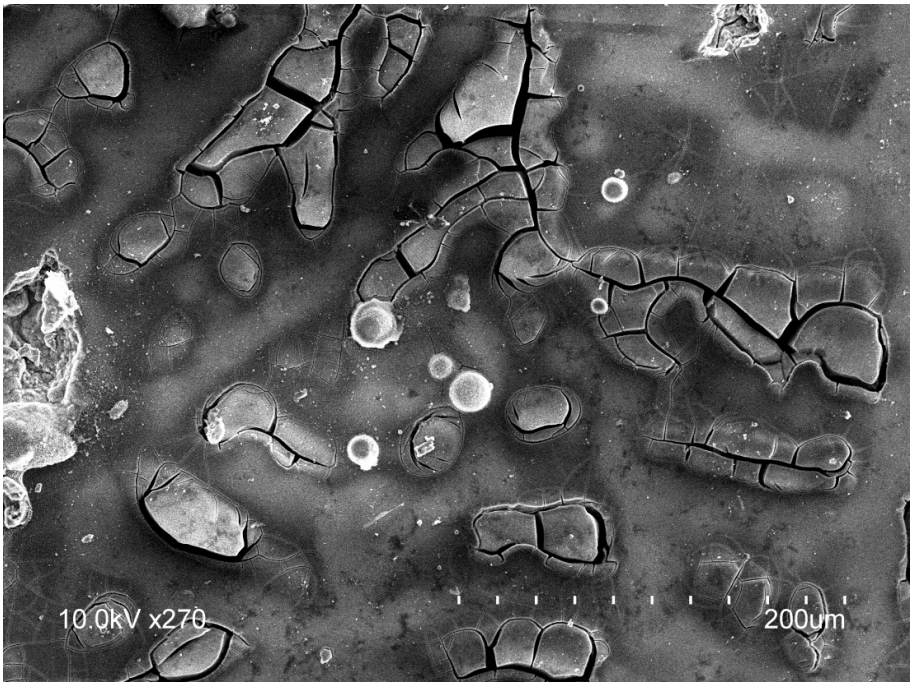

Figure 3. 3- SEM micrograph of a sand cast corroded surface after 96 h continuous exposure in 1.6 wt% NaCl.

h), the location of the β-phase is more easily resolved in the image. The corrosion product accumulated over the β-phase is more porous than the adjacent areas, but has the same composition [19]. This increased porosity can be induced by cathodic behaviour of the β-phase relative to surrounding areas.

The surface morphology of the Al-Mn intermetallics is altered throughout the corrosion process. Figure 3.5(a) shows an Al-Mn intermetallic (contained within an α-grain in the left centre of the image along with its β-phase neighbour) following 24 h immersion. A dome of corrosion product has accumulated over the intermetallic with the surrounding α-grain showing some corrosion damage, while little corrosion product is present over the β-phase region. This dome structure remains intact throughout 72 h of immersion, Figure 3.5(b) and 3.5(c), while corrosion proceeds on the α-grain. Within the next immersion cycle and 96 h of immersion, Figure 3.5(d), the dome has collapsed and the formation of a new dome of accumulated corrosion product has commenced over the exposed intermetallic. Hydrogen evolution or delamination of the intermetallic surface could have lead to this collapse. Making up the dome of corrosion product is an outer layer of $Mg(OH)_2$ and an inner structure of MgO, which was later determined from electron energy loss spectroscopy and electron diffraction, discussed in [19]. From this work, it has been reported that below this accumulated corrosion product layer there is a delamination of the intermetallic, producing a Mn_3O_4 layer and an absence of Al. These two observations suggest that a localized pH change is occurring at the intermetallics. If the intermetallics are acting as localized cathodes, hydrogen evolution can lead to an increase in pH at such sites. The presence of OH^-

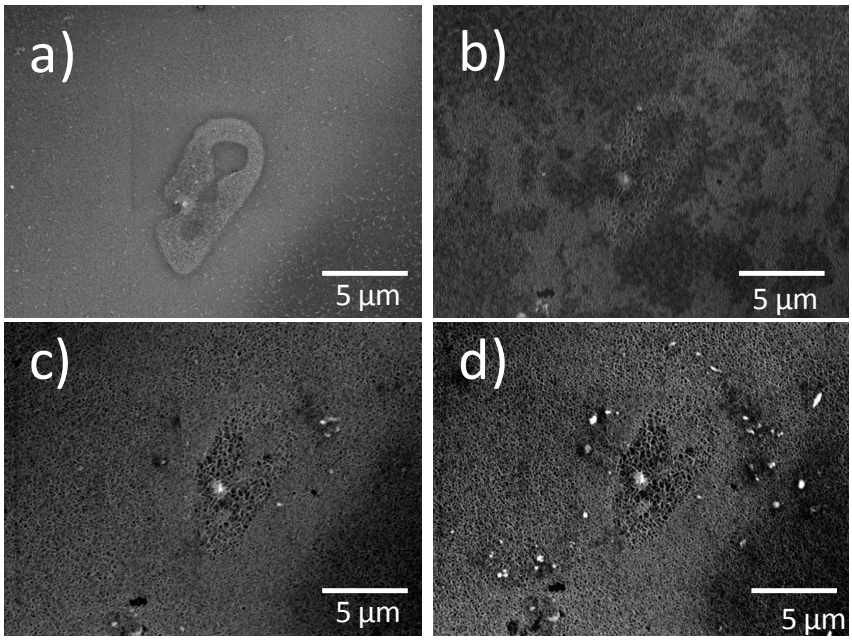

Figure 3. 4 - Progress of corrosion near a β-phase region following a) 24 h, b) 48 h, c) 72 h, and d) 96 h of immersion in 1.6 wt% NaCl.

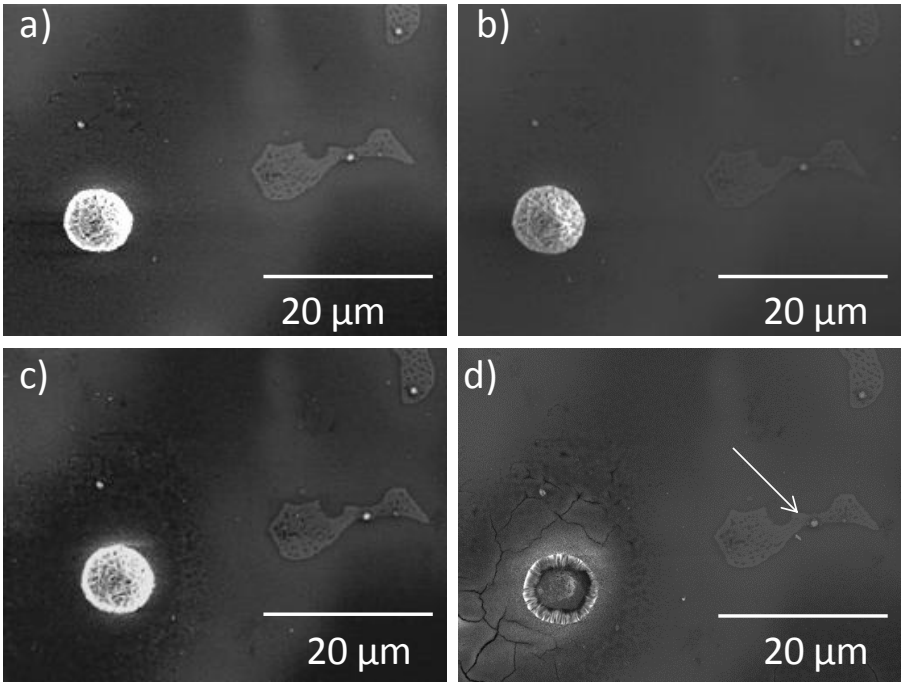

Figure 3. 5 - Progress of corrosion near an Al-Mn intermetallic from Figure 2a) following a) 24 h, b) 48 h, c) 72 h, d) 96 h of immersion in 1.6 wt% NaCl. The white arrow in d) shows a Al-Mn intermetallic with no corrosion product dome.

can produce the outer layer of $Mg(OH)_2$ while assisting the dissolution of Al from the intermetallic surface [19]. The dome structures over the intermetallics are evidence of their localized cathodic behaviour, while intermetallics free of these domes are also observed (arrow in Figure 3.5(d)). The absence of a corrosion product dome at the Al-Mn intermetallic suggests no local pH change, and thus inactivity as a cathode at that point in the corrosion process. This trait is not yet fully understood.

3.3.2 Role of Al in the Corrosion of Sand Cast AM50 Alloys

Individual α-grains contain differences in their Al-content, which can be measured from XEDS data extracted from the maps. α-grain boundaries on the sand cast alloys are not readily defined without etching, which was avoided in order to maintain the natural state of the alloy. In this case, the α-grain boundaries are delineated as regions enclosed by the Al-rich network, as shown in Figure 3.6. From the CLSM images and the measured light intensities, corrosion penetration depth profiles of the surface are recorded by linescan analysis. Figure 3.7(a) shows the CLSM linescan region of the AOI from Figure 3.2 with the green line identifying the location of the selected linescan used for depth measurement. The depths were calculated from the distance between the highest and lowest light intensities on the AOI. Figure 3.7(b) shows the absolute depth profiles recorded along this linescan after successive periods of immersion up to 72 h. The grey-shaded areas are representative of the β-phase locations encountered in the linescan. As time progressed, corrosion on the α-grains was observed accompanied by an increase in depth.

From a series of linescans, the evolution of the corrosion penetration depths (measured at the centre of the grain) on α-grains as a function of their Al-content,

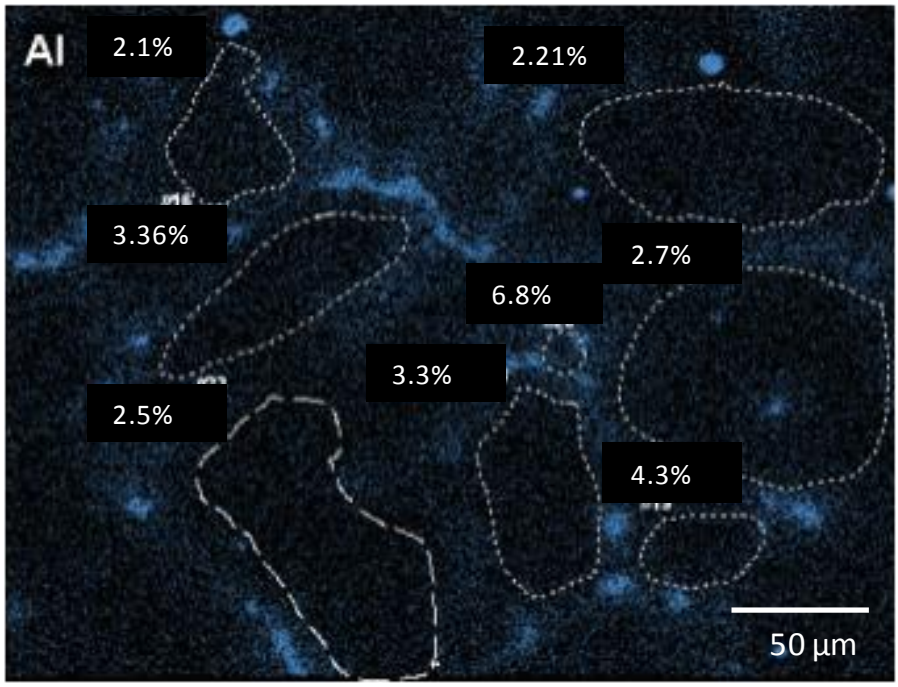

Figure 3. 6 - Identification of the location of α-grains on sand cast AM50 alloys using EDX mapping. Grains were numbered for further analysis shown in Figure 3.8.

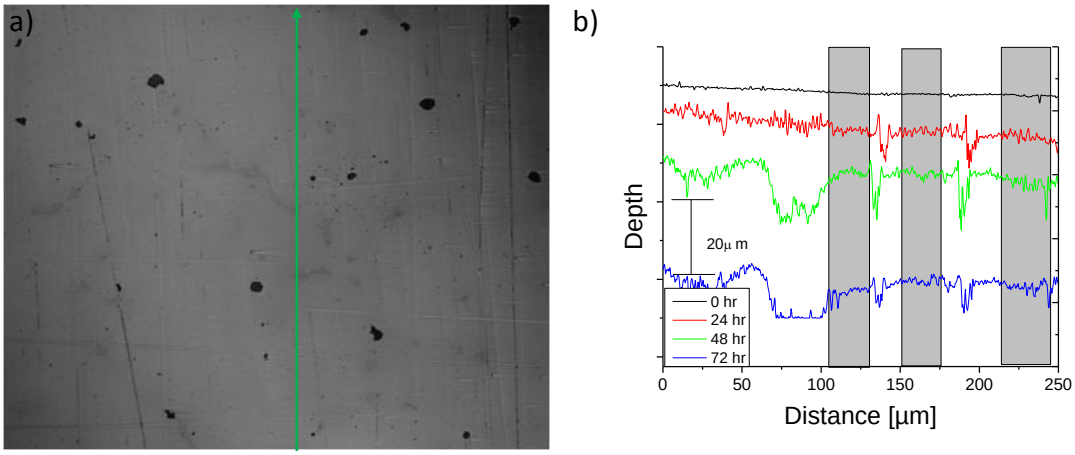

Figure 3. 7- a) CLSM image showing the location of a depth profile line scan in green (bottom to top) and b) the corresponding changes in depth throughout the successive immersions. The β-phases are highlighted in grey.

determined by XEDS, for different exposure times are obtained (Figure 3.8). The analyses of a statistically relevant number of grains recorded from 4 different sand cast samples are summarized in a plot of the corrosion penetration depth versus the Al content of α-grains (wt. %) over the sequence of immersion periods. This figure shows that grains containing lower amounts of measured Al, generally < 3 wt. %, experienced higher corrosion penetration to depths up to 25 µm. However, a linear trend does not exist, since grains with nearly identical Al content corroded at different rates, suggesting that neighbouring microstructures also influence corrosion rates. The most rapidly corroding grains (eight of which were observed), irrespective of Al content, contained Al-Mn inclusions such as the one identified in Figure 3.5, which are known to act as local cathodes [20].

Both intermetallic and β-phases can serve as cathodes coupled to anodic Mg-rich α-grains. Regions in the direct vicinity of the β-phase (the eutectic α-phase) would, therefore, be expected to be susceptible to corrosion. However, as seen in the CLSM images in Figure 3.2, areas near the β- phase are still more resistant to corrosion. These corrosion resistant regions correspond to the Al-rich network observed on the XEDS maps of Al shown in Figure 1. Following 96 h of immersion, a FIB cross-section, Figure 3.9(a), was cut from the site of a corrosion resistant β-phase region to investigate what feature(s) could be suppressing the corrosion rate at these locations. A TEM lamella was removed from this cross section and the areas marked in red and green in Figure 3.9 (b) were analyzed. The area labeled with a green frame, containing a β-phase section, was analyzed with XEDS to produce the maps shown in Figure 3.9(c). An accumulation of Al at the oxide/alloy interface can be seen in the

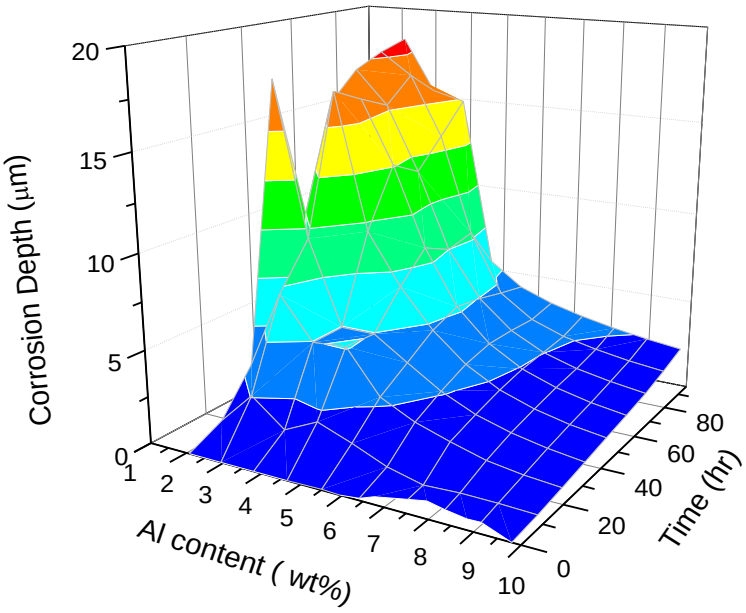

Figure 3. 8 - The relationship between corrosion depth on α-grains and their Al content as a function of corrosion exposure time.

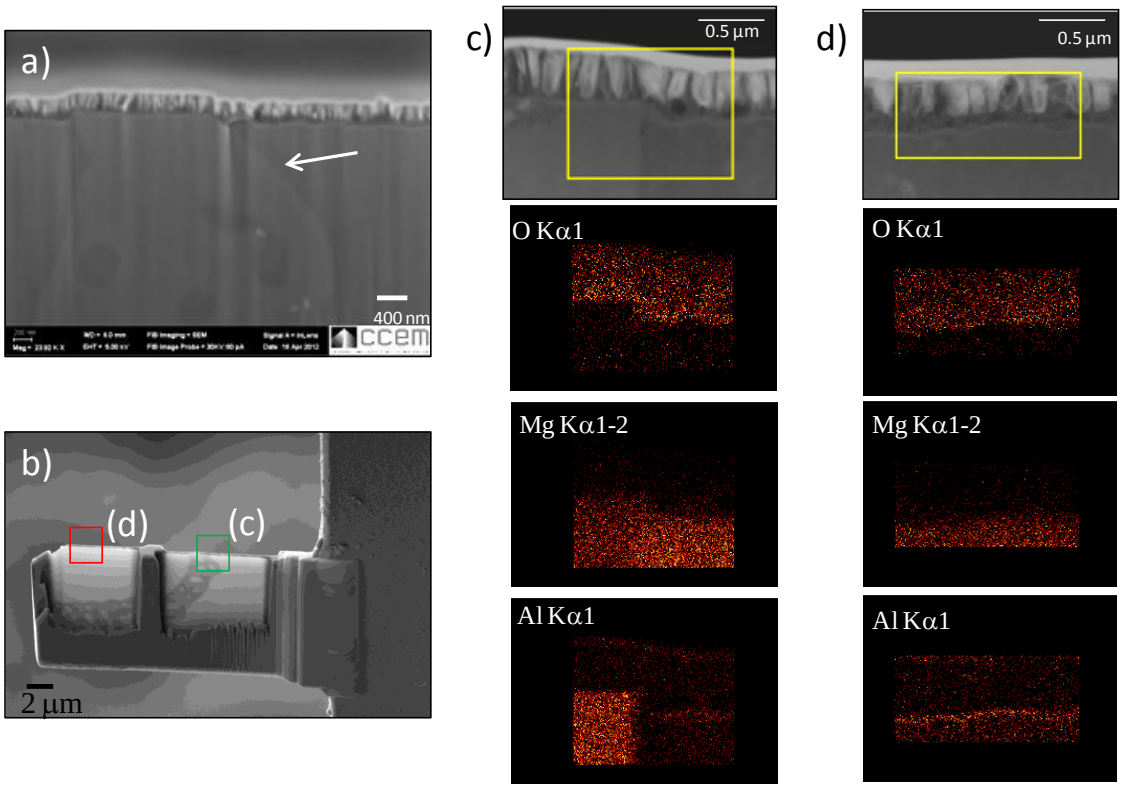

Figure 3. 9 - a) A FIB cross section of a β-phase region including the adjacent only slightly corroded region after 96 h of corrosion: b) a TEM slide of the selected region; c) O, Mg and Al EDX maps of the area marked in green; d) similar EDX maps of the red area shown in b).

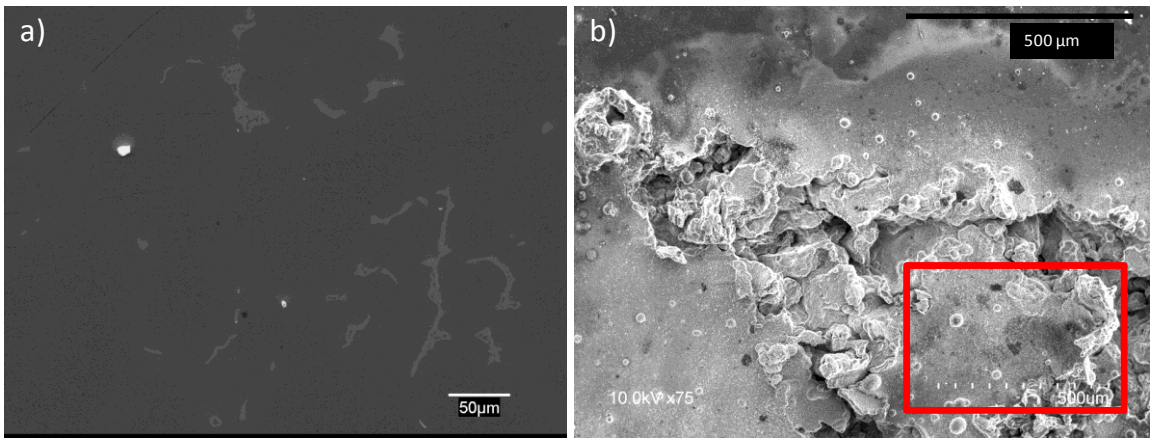

Figure 3. 10 - a) an AOI on a sand cast AM50 alloy prior to corrosion, which was subsequently immersed for 24 h in 1.6 wt% NaCl: b) the AOI (red box) following the immersion surrounded by a major corrosion event.

XEDS Al map, lying just beneath the columnar-like corrosion product layer containing oxygen and above the Mg-rich alloy. One possibility is that this Al could be present due to the proximity to the β-phase. However, analysis of an area away from the β-phase (marked in red in Figure 3.9(b)), also shows a surface Al layer, Figure 3.9(d). Based on the depth profiles shown in Figure 3.2, which demonstrate that regions enriched in Al in close proximity to β-phase (i.e., at similar locations to that analyzed in Figure 3.9(d) are more corrosion resistant compared to α-grains, it is suggested that this Al-layer is largely responsible for the improved corrosion resistance.

3.3.3 Major Corrosion Events on Sand Cast AM50 Alloys

Throughout the immersion tests, major corrosion events, characterized by damaged areas over 25 μm in diameter and penetrating upwards of hundreds of microns into the alloy, were commonly observed. These sites are not limited to edge effects on the un-mounted samples, and once initiated, corrosion propagation is not limited by any nearby microstructural features, such as Al-enriched regions. A clear example is demonstrated by the annihilation of an AOI, Figure 3.10(a), following 24 h of immersion, Figure 3.10(b).

To investigate the origin of these major corrosion events, the exposed 4 mm × 4 mm surface of an epoxy mounted sand cast alloy was entirely imaged prior to corrosion, with SEM in backscatter mode. The images were stitched together to produce

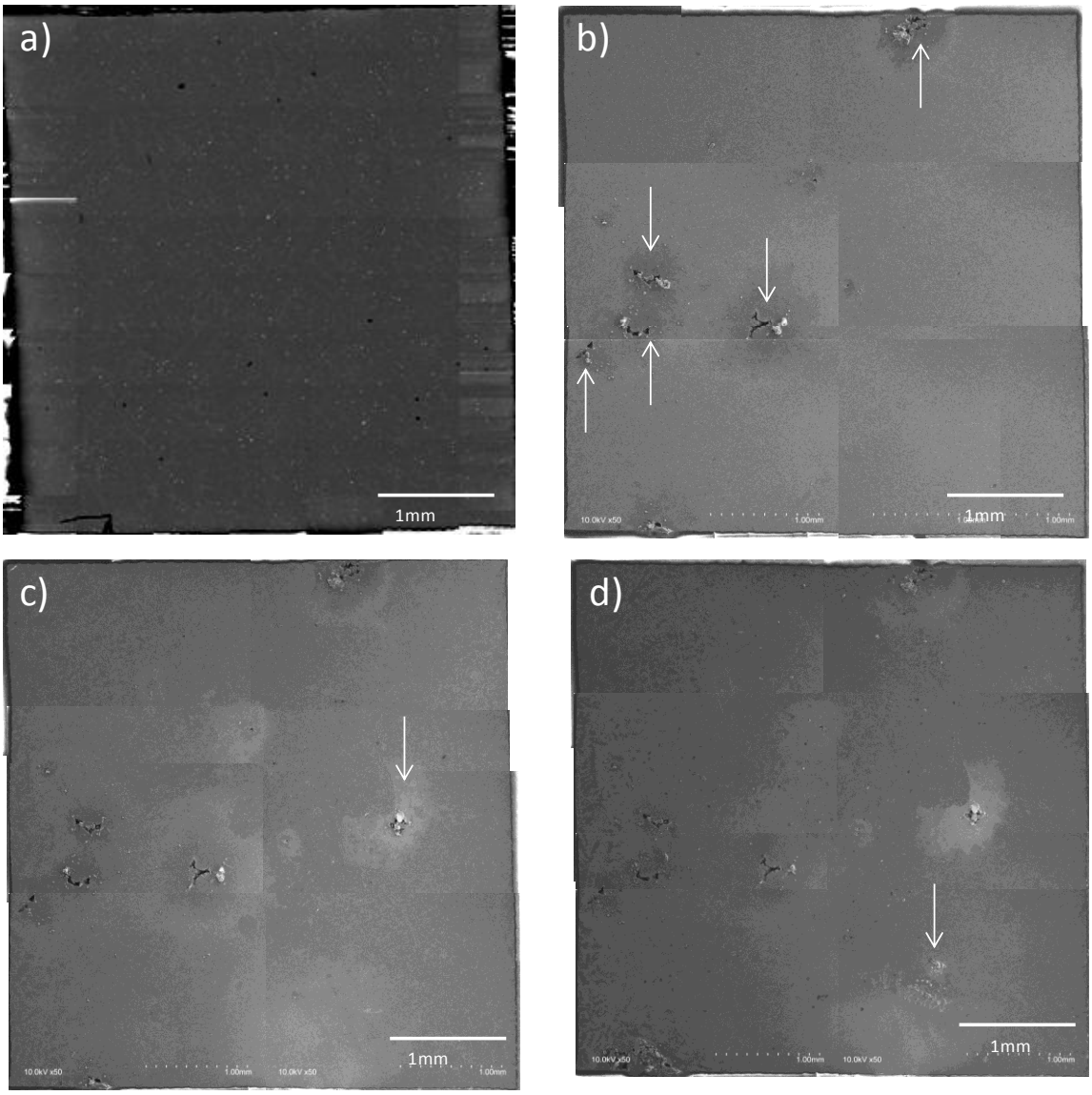

Figure 3. 11 - a) Montage image of a polished sand cast AM50 surface and images of the same area following b) 2 h, c) 3h and d) 4h of immersion in 1.6 wt% NaCl. New damage sites are marked with arrows.

the montage image shown in Figure 3.11(a). Following the first 2 h immersion, the surface was again fully mapped, and five major damage sites were observed (marked with arrows), only one of which occurs at the epoxy/sample interface and hence could be attributed to crevice corrosion, Figure 3.11 (b). After 3 h of immersion a 6th major event initiated on the right- to-middle of the sample, Figure 3.11(c). A further 1 h of immersion leads to the appearance of a 7th major site initiating on the bottom right of the sample.

As discussed above, Al-Mn inclusions can increase the corrosion rate of individual α-grains, thus, it might be expected that a region with a clustering of inclusions could lead to the initiation of these major corrosion events, as observed in Figures 3.10 and 3.11. Figure 3.12(a) and 3.12(e) show initial areas of the surface which eventually suffered major corrosion events. The positions of the major events are numbered in Figure 3.12(a), and with a red circle in Figure 3.12(e). While it was previously observed that Al-Mn intermetallics can accelerate corrosion of α-grains, no significant clustering of Al-Mn inclusions is observed at these sites. The dominant feature of these areas is the minimal presence of β-phase and the accompanying Al-rich network. These features suggest that it is areas with minimal Al content which are most susceptible to extensive corrosion propagation events, and a high population of local cathodes such as Al-Mn intermetallics does not play a substantial role. From Figure 3.12(d) and 12h it can also be seen that corrosion does not expand outward following initiation but likely is propagating deeper into the alloy. This could be lead to a major loss of structural integrity and eventual fallout of surface material, as observed in Figure 3.10(b).

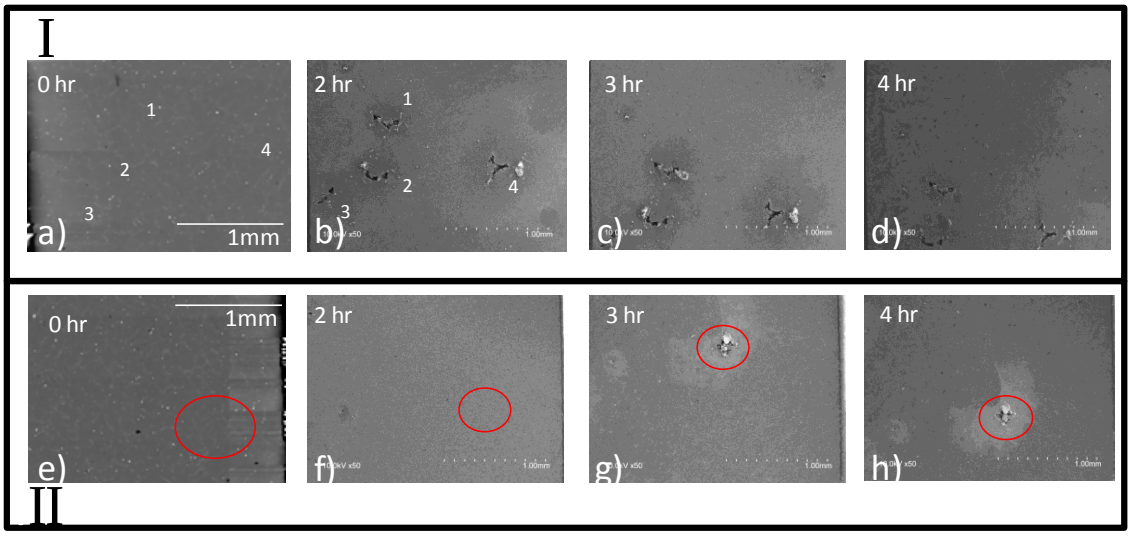

Figure 3. 12 - Progression of areas which sustained major corrosion events: the corrosion damage is observed to penetrate into the alloy but not to spread across the surface.

3.4 Discussion

By monitoring the same surface location through a series of aqueous immersion-dry cycles, the evolution of corrosion on sand cast AM50 alloys can be tracked on a microstructural scale. α-grains were continuously attacked throughout each aqueous exposure with corrosion rates dependent on Al content. Two cathodic microstructural features are present on the AM50 surface, the β-phase and Al-Mn intermetallics. Their function as cathodes is indicated by the accumulation of corrosion product at their location. Above the β-phase and in proximate regions, corrosion product still accumulated on the surface with a less dense corrosion product layer appearing over the β-phase. Based on additional studies, our analyses suggest this layer is $Mg(OH)_2$ and the difference in density above the β-phase is a purely morphological change [19]. With the expected cathodic behaviour of β-phases with respect to the α-grains in AM50 alloys, this density change in the corrosion product at the β-phases may arise from deposition of corrosion product above these sites occurring due to a localized pH change induced by reduction of water to $H_{2(g)}$ [9]. The Al-Mn intermetallics, also suspected cathodic sites on the alloy, also accumulate corrosion product with immersion time forming a domed structure on the surface. This dome is composed of an inner region of MgO and an outer region of $Mg(OH)_2$ [19] formed, presumably, in the alkaline environment prevailing at cathodic sites. The presence of an intermetallic within an α-grain, acting as a local cathode, accelerates the corrosion rate of the individual grain irrespective of the Al content of that grain. This corrosion of the α-grains leaves behind a skeletal network of corrosion resistant regions that are rich in Al, which correspond to the Al-rich areas observed in XEDS maps. Analyses of cross-sections of these corrosion resistant regions

revealed an accumulated Al-layer between the corrosion product layer and bulk alloy. Although the chemical nature of this layer is understood [19], the formation mechanism is yet to be determined.

These results show the importance of Al on the corrosion resistance of sand cast AM50 alloys, by lowering the rate of α-grain attack and generating a corrosion resistant region through surface accumulation. Its importance is emphasized by the accumulation of extensive corrosion damage over short exposure times at regions with minimal Al content. Localized cathodes (intermetallics) accelerate the corrosion of individual grains, but ultimately, it is a sparse distribution of Al that leads to the initiation of large corrosion events, further emphasizing the role played by Al in corrosion on protection on the microscale.

3.5 Summary and Conclusions

Our approach, combining microscopy and corrosion analyses on the same area after intermittent immersions has provided insight into the galvanic effects of microstructural constituents on the corrosion of sand cast AM50 alloy. The Al content is shown to be the key feature controlling the corrosion of these alloys. The distribution of Al directly effects the corrosion of the sand cast alloy, and increasing the distribution of Al can increase the areas of corrosion resistance and limit the number of sites experiencing severe corrosion damage. A more even distribution of Al throughout the alloy, possibly achievable through alterations in alloy fabrication, could lead to improved corrosion resistance. This approach can be applied to a wide range of Mg alloys to investigate in more detail the effects of microstructure on corrosion resistance.

3.6 References

1. P.J Blanchard, D.J. Hil, G.T. Bretz, R.C. McCune, "Evaluation of Corrosion Protection Methods for Magnesium Alloys in Automotive Applications" *Mag. Tech.* (2005**)**, 463
2. M. K. Kulecki, "Magnesium and its alloys application in automotive industry" *Int. J Adv Manuf Tech*, 39 (2008) 851-865
3. Song, G. "Recent progress in corrosion and protection of magnesium alloys" *Adv. Eng. Mat.* 7 (2005) 563-586
4. K.B. Desphande, "Effect of aluminum spacer on galvanic corrosion between magnesium and mild steel using numerical model and SVET experiments" Corros. Sci. 62 (2012) 184-191
5. V.Y. Gertsman, L. Jian, S. Xu, J.P. Thomson, M. Sahoo,"Microstructure and second-phase particles in low- and high-pressure die-cast magnesium alloy AM50" *Metallurg. and Mat. Trans. A*, 36A, (2005) 1989-1997.
6. C. Blawert, D. Fechner, D. Hoche, V. Heitmann, W. Dietzel, K.U. Kainer, P. Zivanovic ,C. Scharf , A. Ditze, J. Grobner, R. Schmid-Fetzer, "Magnesium secondary alloys: Alloy design for magnesium alloys with improved tolerance limits against impurities" *Corros. Sci*., 52 (2010) 2452-2468
7. Sachdeva, D. "Insights into microstructure based corrosion mechanism of high pressure die cast AM50 alloy" *Corros. Sci.* 60 (2012) 18-31
8. R.M. Wang, A. Eliezer, E.M. Gutman "An investigation on the microstructure of an AM50 magnesium alloy" *Mat. Sci. Eng. A* A355 (2003) 201-207

9. Y. Ma, J. Zhang, M. Yang "Research on microstructure and alloy phases of AM50 magnesium alloy" *J Alloys Compounds* 470 (2009) 515-521
10. G. Song, A. Atrens "Corrosion Mechanisms of Magnesium Alloys" *Adv. Eng. Mat.* 1 (1999) 11-33
11. R. Ambat, N. N. Aung, W. Zhou "Evaluation of microstructural effects on corrosion behaviour of AZ91D magnesium alloy" *Corros. Sci* 42 (2000) 1433-1455
12. J.H. Nordlien, K. Nisancioglu, S. Ono, N. Masuko "Morphology and structure of water-formed oxides on ternary MgAl Alloys" *J. Electrochem. Soc.* 144 (1997) 461-466
13. M. Jonsson, D. Persson "The influence of the microstructure on the atmospheric corrosion behaviour of magnesium alloys AZ91D and AM50" *Corros. Sci.* 52 (2010) 1077-1085
14. M. Jonsson, D. Persson, R. Gubner "The initial steps of atmospheric corrosion on magnesium alloy AZ91D" *J. Electochem. Soc.* 154 (2007) C684-C691
15. Y. Yang, H. Wu "Effect of current density on corrosion resistance of micro-arc coatings on magnesium alloy" *Trans. Nonferrous Met. Soc. China* 20 (2010) s688-s692
16. L.F. Garfias-Mesias, M Alodan, P.I. James, W.H. Smyrl "Determination of precursor sites for pitting corrosion on polycrystalline titanium by using different techniques" *J. Electrochem. Soc.* 145 (1998) 2005-2010

17. O. Schneider, G.O. Ilevbare, J.R. Scully, R.G. Kelly "Confocal laser scanning microscopy as a tool for in-situ monitoring of corrosion underneath organic coatings" *Electrochem. Solid State Let.* 4 (2001) B35-B38

18. G. Song, A. Atrens, M. Dargusch, "Influence of microstructure on the corrosion of diecast AZ91D" *Corros. Sci.* 41 (1999) 249-273

19. M. Danaie, R. M. Asmussen, P. Jakupi, D.W. Shoesmith, G.A. Botton "Site-specific Microstructure Characterization of the Surface Layer in a Sand-Cast Magnesium-Aluminum Alloy (AM50) Corroded in an Aqueous NaCl Solution " *Corros. Sci.* 77 (2013) 151-163

20. S. Mathieu, C. Rapin, J. Steinmetz "A corrosion study on the main constituent phases of AZ91 magnesium alloys" *Corros. Sci.* 45 (2003) 2741-2755

Chapter Four

The Microstructural Effects on Corrosion of AM50 Magnesium Alloy

4.1 Introduction

Mg alloys are attractive materials for automotive applications due to their high strength-to-weight ratio. However, a major deficiency is their inadequate corrosion resistance when exposed to aqueous and humid environments such as those experienced in automotive applications [1-5]. As the most electrochemically active structural material, Mg and its alloys are susceptible to galvanic coupling when in electrical contact with a second metal/alloy [6-8]. As well as microgalvanic coupling between the secondary microstructures and the α-Mg phases, both of which can rapidly accelerate corrosion [9].

Al is commonly employed to improve the corrosion resistance of Mg alloys either as a direct coating [10] or through alloying [11-13], and the corrosion resistance of Mg-Al alloys is commonly expressed in terms of the general Al content of an alloy [14,15]. However, the alloying elements in Mg are generally segregated in distinct regions making their distribution throughout the microstructure a critical feature in determining corrosion resistance. Consequently, the effects on corrosion of many microstructural features have been studied. These features include grain size [16], β-phase distribution [17, 18] , β-phase morphology [17] and the interactions between the secondary microstructures [19]. In this study the influence of the surface and sub-surface chemistry associated with the microstructural features on different casts of the AM50 alloy have been studied.

The commercial AM50 alloy, used for its exceptional castability [20-21] contains a Mg-based α-phase, a β-phase ($Mg_{17}Al_{12}$) surrounded by Al-enriched eutectic α-phase, and Al-Mn inclusions. Micro-galvanic couples between the β-phase and/or inclusions and the α-phase matrix can accelerate the corrosion of the latter in aqueous and atmospheric environments [22]. Our previous work investigated the microscale corrosion processes on a sand cast AM50 surface through repeated microscopic analyses of areas of interest in chloride solution. From this work it was reported that: (1) increasing Al content of a grain reduced the corrosion rate of that grain; (2) an Al-enrichment developed at the alloy surface in the eutectic regions of the material during the corrosion process providing protection; and (3) the distribution of Al is important in controlling the corrosion process as regions deficient in Al are susceptible to major corrosion damage. The aim of this study is to utilize the microscale approach we have developed [23] to quantify the extent and distribution of corrosion damage as an effect of microstructure size and distribution using sand, graphite and die cast AM50 alloys. By comparing three casts of the same alloy any differences in elemental composition are eliminated, the main variable becoming the size and distribution of the secondary phases and the Al content.

4.2 Experimental

4.2.1 Sample Preparation

AM50 alloys were supplied by General Motors (Canada). The as-received AM50 sand and graphite cast rods were machined into 1 ×1 × 0.7 cm electrodes. For the die cast alloy square electrodes (1 × 1 × 0.2 cm) were machined from a 0.2 cm thick plate. One side of the sample (1 cm^2) was tapped to connect to a threaded rod to allow electrical connection to external circuitry. The 1 cm^2 side of the sample to be examined was pre-

treated as previously reported [23]. The samples were ground successively up to 4000 grit SiC. The ground alloy surface was then polished on a Struers DP-Dur cloth saturated in 3 µm Struers DP-Suspension A for 5 to 10 min with the ethanol/propanol mixture used in place of water as a lubricant. The final stage consisted of polishing, for 2-3 min, on a Struers OP-Chem cloth using an equal volume mixture of Struers OP-S Suspension and ethylene glycol, as an abrasive. The polished sample was rinsed and sonicated in anhydrous ethanol for 2 min and air dried and stored in a desiccator. The grinding and polishing procedure removed the outer casting skin from the die cast alloy. For all electrochemical measurements, Struers EpoFix™ epoxy was used to mount the electrodes, leaving only the polished 1 cm^2 alloy surface exposed to electrolyte. For immersion experiments to assess surface damage only, the samples were not mounted in epoxy to facilitate subsequent analytical procedures.

4.2.2 Instrumentation

Electron micrographs were obtained in back-scattered and secondary electron modes using either a LEO 440, Hitachi 3400-N Variable Pressure Scanning Electron Microscope or LEO 1540 XB SEM/FIB. X-ray energy dispersive spectroscopy (XEDS) maps were obtained using Quartz One software®.

Depth profiles on un-corroded and corroded surfaces were measured with confocal laser scanning microscopy (CLSM) by detecting the reflected light intensity from a Zeiss 510 confocal, HeNe 633 nm laser. The polished sample surface was placed downward, suspended by a stage, facing the inverted objective. Light intensities were normalized into a depth profile by considering the number of steps (slices) through the focal plane, in the z-direction, required to reach the deepest region on the sample surface.

The differences in light intensities were then converted to a distance. Optical micrographs were collected using a Zeiss Lunar V12 microscope equipped with an Axio 1.1 camera.

4.2.3 Intermittent Immersion Experiments

Prior to a corrosion experiment, the polished surface was analyzed by SEM/EDX and CLSM. The co-ordinates of an area of interest (AOI) were recorded (relative to a surface edge) so that the same area (275 μm × 450 μm) could subsequently be located after each of a series of immersions. Immersions were performed in a naturally aerated 1.6 wt % NaCl (reagent grade, 99 % assay) solution at 22 ± 2 °C. The polished face of the electrode was immersed suspended from a stainless steel rod with the electrolyte level located ~ 1 to 2 mm above the polished surface.

After immersion, the corroded surface was rinsed with Nanopure water (18 MΩ-cm) and dried in an Ar stream. Sonication in anhydrous ethanol following each immersion was not performed as previously described [23] since this process was inconsequential in improving the analysis and any residual chloride on the surface could be removed solely with a water rinse. The corroded AOI was then analyzed using SEM/XEDS and CLSM, and compared to the same location prior to corrosion. This procedure was repeated after each of a series of immersions to determine the evolution of the corrosion damage morphology and the penetration depth with time.

To investigate the distribution of corrosion on a wider area of the surface, experiments were performed on a 4 mm × 4 mm alloy sample mounted in Struers EpoFix™ epoxy so that only a single surface was exposed. The surface was polished as described previously [23]. The epoxy of the mounted sample and a corner of the

sample were coated in carbon paint when necessary to improve conductivity of the sample surface for imaging. The paint was removed with ethanol prior to the initial immersion. The entire 4 × 4 mm polished surface was imaged at 150 x for the sand and graphite cast samples and 500 x for the die cast using a Hitachi SU6600 Field Emission SEM. The images were then stitched using Image-Pro Plus 7.0® into a final surface montage image of the entire 4 mm × 4 mm surface. The sample was then immersed in chloride solution and corrosion analyses followed through a series of immersions. Between each immersion the surface was reanalyzed by SEM and a series of montage images constructed.

4.2.4 Electrochemical Analysis

All electrochemical measurements were performed in a standard three-electrode cell with a saturated calomel reference electrode (SCE) and a 4 cm^2 Pt foil counter electrode. Solutions were prepared using NaCl (reagent grade 99 % assay) and NanoPure™ water (18.2 MΩ·cm). All experiments were performed at 22 °C ± 2 °C. After each measurement the electrolyte was discarded and the cell rinsed with NanoPure™ water.

Electrochemical responses were measured with a 1287 Solartron® potentiostat coupled to a 1260 Solartron® frequency response analyzer for electrochemical impedance spectroscopy (EIS) measurements. Prior to each potentiodynamic polarization (PDP) scan, the corrosion potential (E_{CORR}) was allowed to stabilize for 20 min. Then, a PDP scan was started 200 mV below E_{CORR} and the potential scanned in the positive direction until either the potential reached 200 mV above E_{CORR}, or, to avoid severe damage to the alloy surface, the measured current density reached 1 mA/cm^2.

EIS measurements were performed after 10 h of immersion at E_{CORR}. A sinusoidal potential perturbation of ± 10 mV was applied above and below E_{CORR}, and the current response recorded over the frequency range, 10^5 Hz to 10^{-3} Hz. Eleven data points per frequency decade were recorded. Subsequently, a one point per decade reverse scan was recorded from 10^{-2} – 10^5 Hz to ensure steady-state was maintained throughout the EIS measurement. Kramers – Kronig transforms were applied to confirm the validity of the data, and non-valid data points removed from the presented spectra [24].

4.3 Results

4.3.1 Alloy characterization

Figures 4.1 to 4.3 show SEM micrographs of selected areas of interest (AOI) on the sand cast (Figure 4.1), graphite cast (Figure 4.2) and die cast (Figure 4.3) alloys. The backscatter SEM images are shown in (a) and the corresponding XEDS maps in (b) Al , (c) Mg and (d) Mn. The differences in microstructure can best be appreciated by comparing the sizes of the β-phase structures. Measured along the longest axis of the β-phase, the sand cast ranges from > 100 µm to 10 µm, the graphite cast from 50 µm to 5 µm and the die cast is <10 µm. Smaller β-phase sizes produce a more tightly linked network of Al-rich eutectic α-phase connecting the β-phase, achieving a more even distribution of Al throughout the alloy. This network and its coverage can be seen in the Al maps of Figures 4.1 (c), 4.2 (c), and 4.3 (c). The distinct signal from Al-Mn intermetallics can also be observed in the Mn maps of Figure 4.1 (d), 4.2(d). On the die cast alloy, the Al-Mn intermetallics are much smaller (<1µm) and are not resolved at the magnification of the XEDS map in Figure 4.3(d).

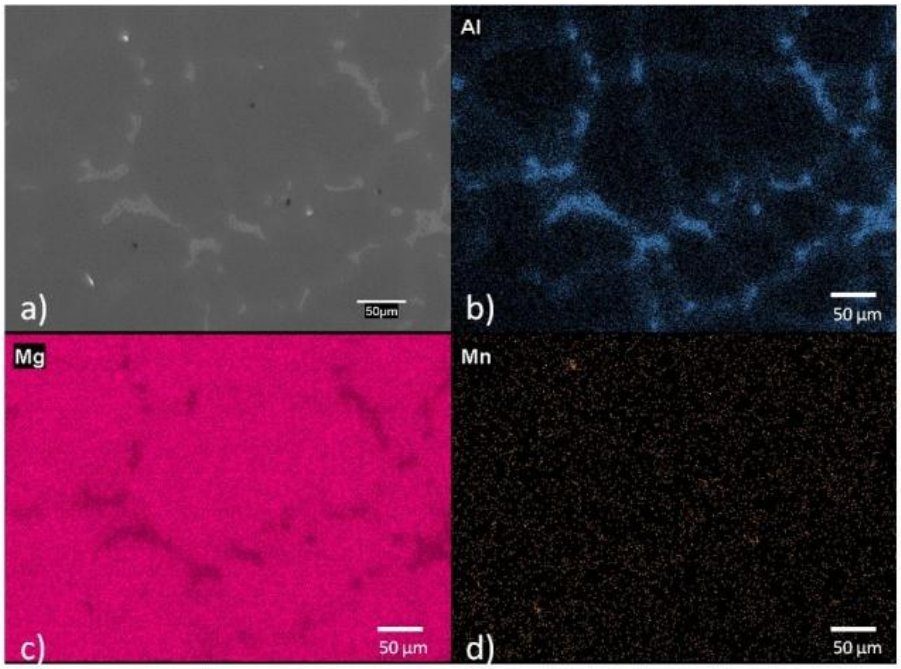

Figure 4. 1 - a) SEM image of a polished sand cast AM50 sample and the corresponding EDX maps showing the distribution of b) Al, c) Mg and d) Mn throughout the area of interest.

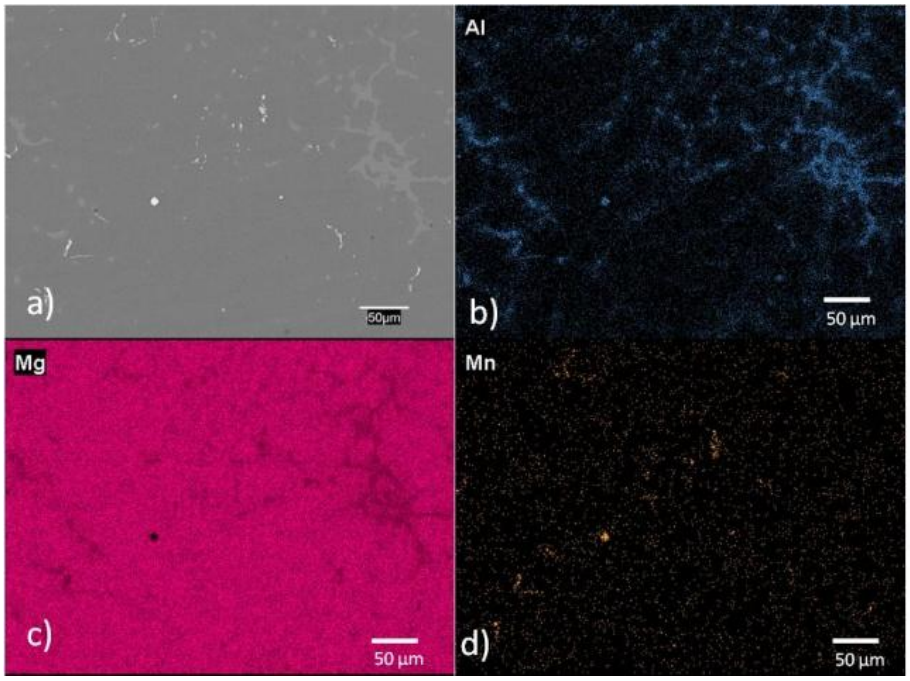

Figure 4. 2 - a) SEM image of a polished graphite cast AM50 alloy and the corresponding EDX maps showing the elemental distribution of b) Al, c) Mg and d) Mn..

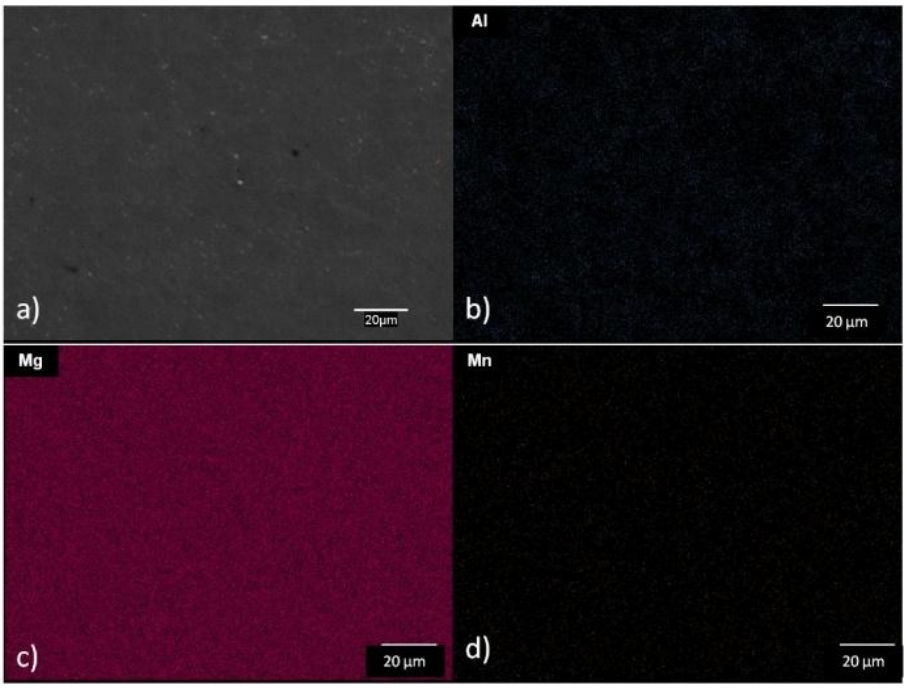

Figure 4. 3 - a) SEM image of a polished die cast AM50 sample and the corresponding EDX maps showing the distribution of b) Al, c) Mg and d) Mn throughout the AOI.

4.3.2 Electrochemical behaviour

E_{CORR} measurements over a 24 h immersion period, Figure 4.4, showed the average E_{CORR} values to be -1.59 V, -1.56 V, and -1.54 V for the sand, graphite and die cast alloys, respectively. The noise associated with these measurements was likely an electrochemical response due to the activity of individual areas of the surface as well as the generation and detachment of H_2 bubbles on/from the corroding surface. The frequency of these rapid fluctuations in E_{CORR} was increased on the graphite cast alloy compared to the sand cast and, highest on the die cast alloy which had the tightest microstructural network.

PDP measurements are presented in Figure 4.5. The casts displayed nearly identical behaviour in the cathodic region, -1.80 V to -1.55 V suggesting the kinetics of water reduction were similar on all three alloys. At potentials positive to E_{CORR}, the die and graphite cast alloys appeared to be forming a protective (at least partially) oxide layer as the current became increasingly less potential-dependent as the potential was increased. However, the sudden current increase (for E > - 1.475V) indicated the breakdown of any film formed and the onset of rapid dissolution. The die cast alloy exhibited a slightly higher breakdown potential than the graphite cast alloy. For the sand cast alloy no early attempt to form a corrosion-resistant oxide was observed with the current immediately rising to high values as the applied potential became positive to E_{CORR}.

Differences between the casts were also apparent in the EIS spectra, Figure 4.6. The Nyquist plots for the sand cast (green) and graphite cast (blue) alloys display a single capacitive and one inductive feature, with the impedance at the low frequency limit

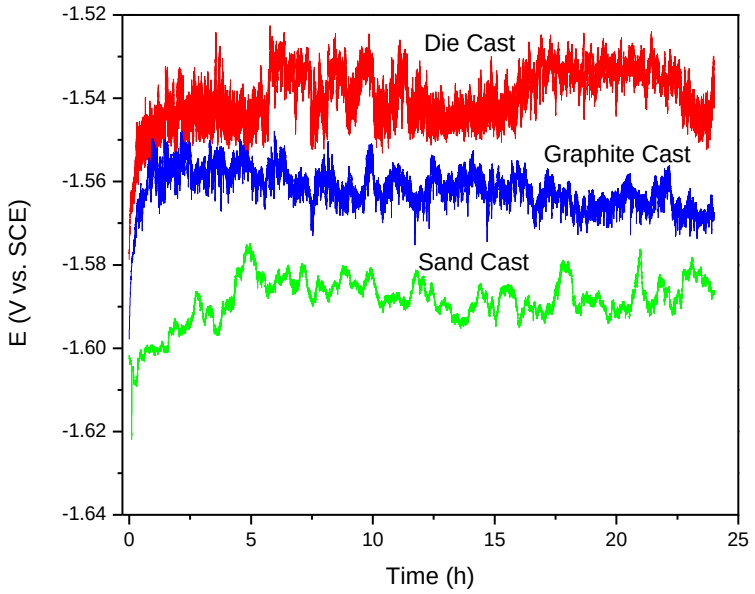

Figure 4. 5 - Progression of E_{CORR} of the polished sand cast (green), graphite cast (blue) and die cast (red) AM50 alloys recorded in 1.6 wt% NaCl.

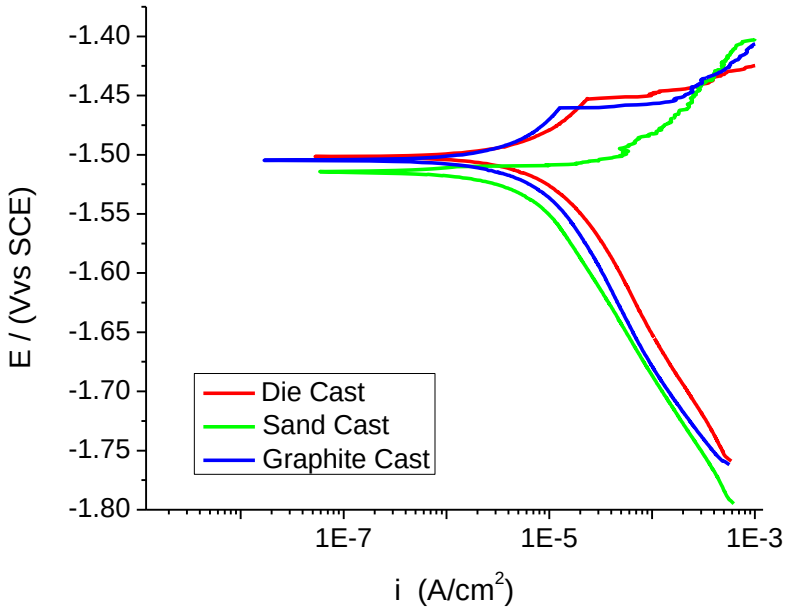

Figure 4. 4 – polarization (PDP) curves for the sand cast (green), graphite cast (blue) and die cast (red) AM50 alloys in 1.6 wt% NaCl at a scan rate of 0.5 mV/s after 20 min at E_{CORR}..

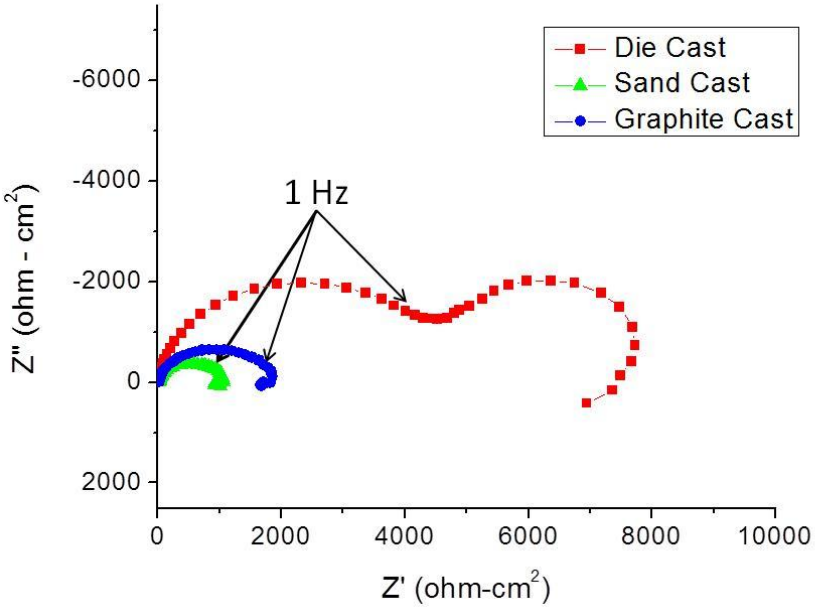

Figure 4. 6 - Nyquist plots for the sand cast (green), graphite cast (blue) and die cast (red) alloys recorded in 1.6 wt% NaCl after 10 h exposure.

higher for the graphite cast than the sand cast alloy, indicating a lower corrosion rate. The Nyquist plot for the die cast alloy (red), exhibits similar features, but also contains a second capacitive loop and the low frequency impedance is considerably larger than for the other two alloys.

4.3.3 Corrosion Behaviour in 1.6 wt. % NaCl

Information on the nature and distribution of corrosion damage was obtained using a combination of SEM and CLSM on corroded samples. Following SEM and CLSM imaging of a selected AOI on a fresh polished sample, the samples were immersed in 1.6 wt% NaCl for a sequence of 24 h exposure periods. After each immersion, the AOI was re-located and imaged again by SEM and CLSM to monitor alterations to the corroded surface. The images recorded after each 24 h immersion are presented in Figure 4.7 for the sand (a), graphite (b), and die (c) cast alloys. The larger α-Mg phases in the sand cast alloy were preferentially corroded, Figure 4.7(a). As corrosion progressed, a skeletal network rich in Al [25] was left behind and some domes of corrosion product appeared, marked with a red arrow in Figure 7 (a). A detailed description of the corrosion behaviour of this alloy has been published [23].

The graphite cast AM50 alloy, Figure 4.7 (b), developed similar corrosion morphology through an identical series of immersions, but corroded α-phase regions were considerably smaller in dimension. On the die cast alloy, Figure 4.7 (c), the corroded α-Mg regions were very small compared to those on the other two casts and the remaining uncorroded β-phases formed a much more extensive network leading to a substantial reduction in the overall extent of corrosion damage to the surface. In the SEM images recorded after 24 and 48 h of immersion, Figure 4.7(c), the dark rectangles were

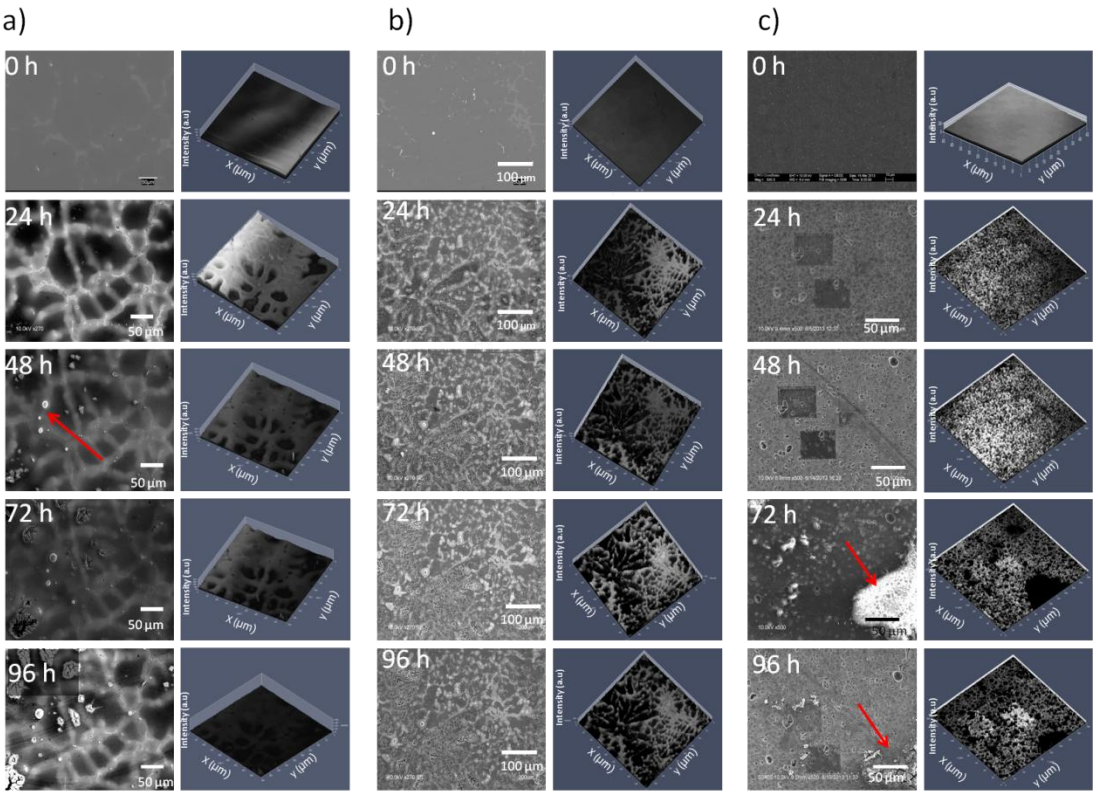

Figure 4. 7 - a): SEM micrographs and CLSM images of the sand cast AM50 alloy after a sequence of 24 h intermittent immersions in 1.6 wt% NaCl The red arrow identifies domes of corrosion product appearing over sites of higher cathodic activity, b) SEM micrographs and CLSM images of the graphite cast AM50 alloy after a sequence of 24 h immersions in 1.6 wt% NaCl c) SEM micrographs and CLSM images of the die cast AM50 alloy after a sequence of 24 h immersions in 1.6 wt% NaCl. The red arrows indicate the location of a major corrosion event.

an artifact of carbon stitching during XEDS mapping of the polished surface [26]. No influence of this procedure on the corrosion behaviour was observed. After 72 h of immersion, the dark region in the bottom of the CLSM image indicates the accumulation of white corrosion product detected in the corresponding SEM image. This mass of corrosion product did not coherently reflect the laser beam and no return signal was detected in the CLSM image. After 96 h of immersion, this corrosion product fell off, Figure 4.7(d), confirming its general lack of adherence to the alloy surface.

The occurrence of large areas of corrosion, observed here on the die cast alloy after 72 h, were also observed previously during the corrosion of the AM50 sand cast alloy [23]. While the general distribution of corrosion damage involving microgalvanic coupling could be successfully followed as illustrated in Figure 4.7, the capture of a major corrosion event in the small area imaged by CLSM was not guaranteed. Examinations of larger surface areas and the successful identification of major corrosion events were achieved by montage imaging of 4 mm x 4 mm samples of the three alloys. Using this approach we showed previously that the sand cast alloy was susceptible to such major corrosion events after < 2 h of exposure in 1.6 wt% NaCl [23]. These events were shown to initiate in regions of α-Mg grains depleted in Al content.

Surface montage images of the graphite cast AM50 alloy before, and following, short periods of corrosion are displayed in Figure 4.8. Figure 4.8 (a) shows the electron backscatter SEM montage map of the polished alloy prior to a sequence of 1 h intermittent immersions in 1.6 wt% NaCl. Following 2 h of immersion, Figure 4.8 (b), no major corrosion damage sites had initiated. The damage observed in the top left region of the montage occurred in an occluded location at the interface formed between

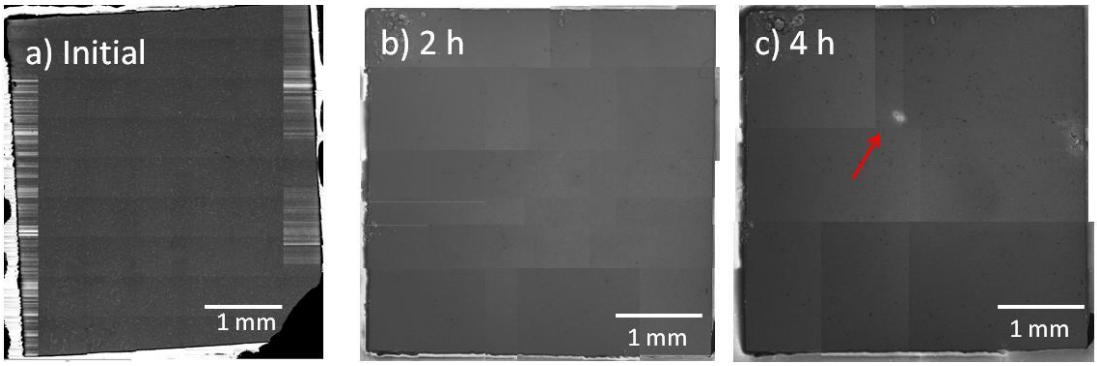

Figure 4. 8 - SEM montage micrographs of the graphite cast AM50 after a) polishing, b) 2 h and c) 4 h intermittent immersions in 1.6 wt% NaCl. The red arrow in c) shows the first major event to initiate.

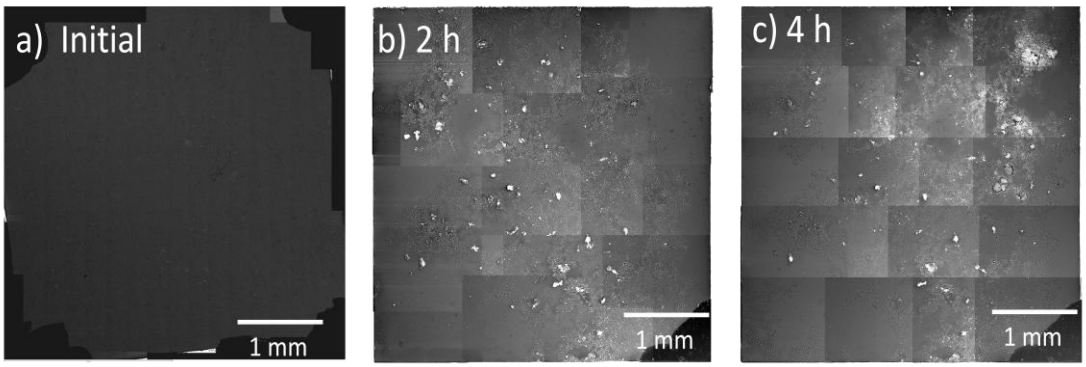

Figure 4. 9 - SEM montage micrographs of die cast AM50 after a) polishing, b) 2 h and c) 4 h intermittent immersions in 1.6 wt% NaCl.

the epoxy and the alloy edge [27], and was not representative of the planar surface behaviour. After 4 h of immersion a single major event had initiated, and is indicated in the image with a red arrow, Figure 4.8 (c).

The montage image for the freshly polished die cast alloy is shown in Figure 4.9 (a). Following two 2 h periods of corrosion in 1.6 wt% NaCl, Figure 4.9 (b), the damage morphology observed was very different to that on the graphite cast alloy. Conductive carbon paint had to be reapplied to a corner of the sample following the initial immersion to overcome charging of the corrosion product while montage imaging the damaged surface. While no major individual events were observed, corrosion damage spread apparently laterally across the surface of the alloy. After 4 h of immersion, a major event initiated and is seen in the top right of Figure 4.9 (c).

The differences in corrosion damage morphologies observed on the three cast alloys are summarized in the stereomicrographs recorded following 24 h immersion, Figure 4.10. Here the sand cast, Figure 4.10 (a), and graphite cast, Figure 4.10 (b), show the white areas characteristic of accumulated corrosion product localized on α-Mg grains at more deeply corroded locations. The occurrence of these locations has been shown to be related to the Al content of the α-phase [23]. By contrast, corrosion damage propagated laterally along the surface of the die cast alloy, Figure 4.10 (c).

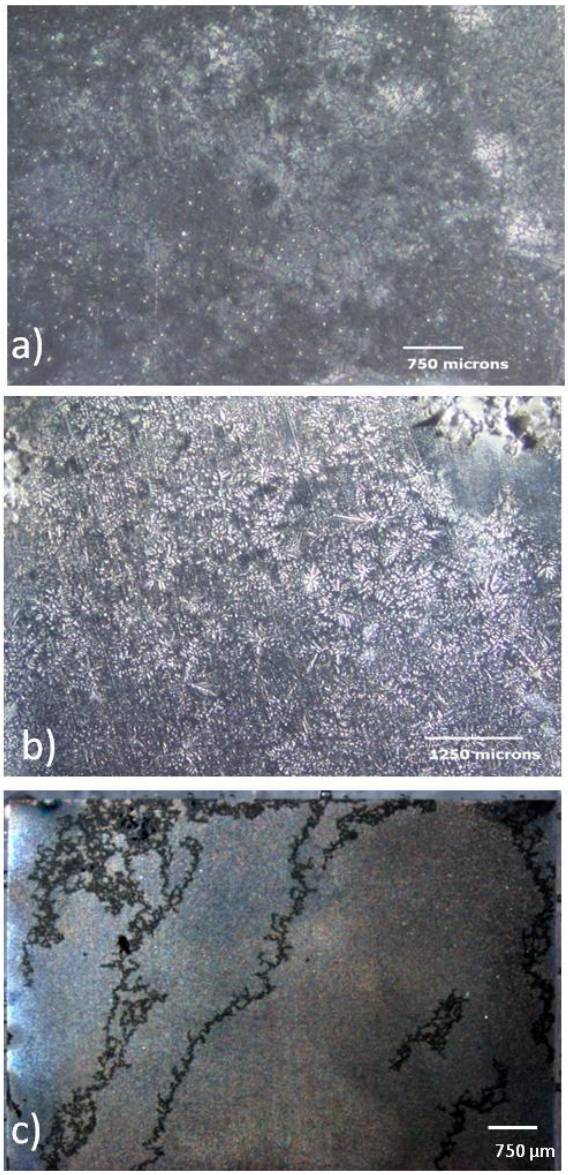

Figure 4. 10 - Stereo micrographs of the a) sand, b) graphite and c) die cast AM50 alloys following a 24 h immersion in 1.6 wt% NaCl. The white blotches on the sand and graphite cast is the accumulation of corrosion product in the α-Mg regions while damage propagates laterally on the die cast.

4.4 Discussion

The selection of three casts of the same Mg alloy removes any direct influence of composition and allows the influence of microstructure and the distribution of alloying elements to be investigated. The difference in corrosion mechanism between the three casts is evident in the E_{CORR} and EIS measurements. The PDP scans demonstrate that the kinetics of the H_2O reduction reaction do not change significantly with alloy cast. This indicates that, in general, the differences in corrosion response between the three casts were predominantly due to the differences in anodic behaviour. No attempt was made to extract corrosion rates since the Tafel extrapolation approach is unreliable for Mg materials [27].

A difference in corrosion mechanisms between the three casts is evident in the EIS measurements, which show the die cast had a significantly higher low frequency impedance than the other two casts indicating a lower general corrosion rate [28]. By contrast, the impedance at the low frequency limit is only slightly larger for the graphite than the sand cast alloy. The presence of two capacitive responses in the Nyquist plot of Mg alloys was reported for the corrosion of the Mg alloy AZ91 in Na_2SO_4 and attributed to the thickening of the corrosion product layer [38]. The sand and graphite casts exhibit only one capacitative response and an inductive response, whereas the die cast alloy yields two capacitative responses in addition to the inductive feature. The high frequency loop response has been attributed to the charge transfer process of $Mg \rightarrow Mg^{2+}$ at the alloy surface film, and the medium frequency response to the diffusion of Mg^{2+} through the thickening porous $Mg(OH)_2$ corrosion product film. On Mg materials a response involving two capacitative responses coupled to an inductive response has been attributed

to localized or microgalvanic corrosion [39]. The inductive feature observed in the Nyquist plots is common to corroding Mg and Mg alloy systems and linked either to the relaxation of surface adsorbed intermediates in the anodic reaction [31] or to the dissolution of a partially protective film [32].

The presence of the inductive feature in the spectra in Figure 4.6 indicates that the input E signal can still detect the surface processes on the substrate alloy irrespective of whether a surface corrosion product is present or not. The spectra clearly demonstrate an alteration in corrosion mechanism on the die cast when compared to the sand and graphite cast alloys, the presence of the mid-frequency response indicating corrosion inhibition by a $Mg(OH)_2$ corrosion product film. This change in EIS behaviour suggests the alloy microstructure and subsequent distribution of the alloying elements, especially Al, plays a primary role in the corrosion behaviour. A more extensive EIS study is underway.

The shift in E_{CORR} to more negative values accompanied by the general decrease in interfacial impedance is consistent with the CLSM analysis which shows the corrosion susceptible area of the surface increases in the order die cast << graphite cast < sand cast. During intermittent immersion experiments, the sand and graphite cast alloys exhibit corrosion of the α-Mg regions leaving behind an interlinked skeletal network of eutectic-α phase characterized by its high Al content. The CLSM micrographs in Figure 4.7 (a and b) show the secondary β-phases and lightly corroded eutectic network are more tightly compact on the graphite cast compared to the sand cast alloy, which would allow a more extensive area of the alloy surface to generate a protective Al-enrichment on the surface during corrosion [11, 23, 25]. This increased area of protected surface would

account for the slightly improved corrosion resistance. As demonstrated by the montage imaging, this decrease in regions of the surface depleted in Al also extends the time required to initiate extensive corrosion propagation sites. This improvement notwithstanding, both casts exhibit significant corrosion penetration into the surface via the α-Mg regions.

On the die cast alloy this skeletal network is considerably tighter than on the other two casts, leading to a higher surface density of Al-containing eutectic which appears to limit the depth of corrosion penetration on α-Mg regions leading to extensive lateral propagation of corrosion across the surface as opposed to penetration into the surface, as suggested previously [30, 33]. Since this tight network of Al enriched eutectic is three-dimensional, additional subsurface areas are exposed as corrosion progresses further hindering damage propagation into the alloy. Despite this, the possibility of initiation of a major damage site is not eliminated if there are areas where Al is more extensively depleted.

The reduction in the size of microstructural features (α-Mg grains, β-phase) leading to an increased distribution of Al on the AM50 alloy induces not only an alteration in corrosion performance, but also a change in corrosion damage morphology . Previous studies have shown that die casting improved the corrosion performance over the ingot material for AZ91 [34], and a finer grain size improves the corrosion of Mg alloys [35-37]. Our studies on the sand cast alloy showed that the Al content of individual α-phase regions directly affected the extent of corrosion damage, an influence that would be independent of grain size [23]. Along with a reduction in the α-Mg surface area, the average size of the secondary microstructural constituents also decreases,

resulting in a more widespread distribution of Al present in the eutectic α-Mg regions around the β-phase network. This increases the potential area of the surface and even the subsurface capable of acting as a corrosion resistant barrier as corrosion progresses.

4.5 Summary and Conclusions

The corrosion rates, determined qualitatively by EIS, increased in the order sand cast > graphite cast >> die cast. CLSM showed this improvement could be attributed to the increasingly compact nature of the secondary microstructure (β-phase + Al-containing eutectic) through this sequence. As corrosion progressed, the higher Al content in the eutectic surrounding the β-phase protected these regions from extensive corrosion and reduced the likelihood that major corrosion sites would initiate in the core of α-Mg grains with low Al content. Since this tight network of Al-enriched eutectic is three dimensional in the die cast alloy, the exposure of additional subsurface areas of Al-enriched eutectic forced corrosion to propagate laterally rather than penetrate deeply into this cast. Despite this improvement in corrosion resistance the initiation of major corrosion damage sites is not eliminated in the die cast alloy.

4.6 References

1. P.J Blanchard, D.J. Hil, G.T. Bretz, R.C. McCune, "Evaluation of Corrosion Protection Methods for Magnesium Alloys in Automotive Applications" *Mag. Tech.* (2005**)**, 463
2. M. K. Kulecki, Magnesium and its alloys application in automotive industry *Int. J Adv Manuf Tech*, 39 (2008) 851-865
3. G. Song "Recent progress in corrosion and protection of magnesium alloys" *Adv. Eng. Mat.* 7 (2005) 563-586

4. G. Song, D. St. John, C. Bettles, G. Dunlop "The corrosion performance of magnesium alloy AM-SC1 in automotive engine block applications" *JOM* (2005) 54-56
5. R. McCun, V. Upadhyay, Y.M. Wang, D. Battocchi "The use of AC-DC-AC methods in assessing corrosion resistance performance of coating systems for magnesium alloys" *Mag. Tech.* (2013) TMS 165-168
6. K.B. Desphande, "Effect of aluminum spacer on galvanic corrosion between magnesium and mild steel using numerical model and SVET experiments" Corros. Sci. 62 (2012) 184-191
7. L. Lacroix, C. Blanc, N. Pebere, B. Tribollet, V. Vivier "Localized approach to galvanic coupling in an aluminum-magnesium system" *J. Electrochem. Soc.* 156 (2009) C259-C265
8. K.B. Deshpande "Experimental investigation of galvanic corrosion: Comparison between SVET and immersion techniques" *Corr. Sci.*52 (2010) 2819-2826
9. G. Song, A. Atrens "Understanding magnesium corrosion – A framework for improved alloy performance" *Adv. Eng. Mat.* 5 (2003) 837-858
10. J.K. Chang, S.Y. Chen, W.T. Tsai, M.J. Deng, I.W. Sun "Improved corrosion resistance of magnesium alloy with a surface aluminum coating electrodeposited in ionic liquid" *J. Electrochem. Soc.* 155 (2008) C112-C116
11. J.H. Nordlien, K. Nisancioglu, S. Ono, N. Masuko "Morphology and structure of water-formed oxides on ternary MgAl Alloys" *J. Electrochem. Soc.* 144 (1997) 461-466

12. Lindstrom R, Svensson JE, Johansson LG. "The influence of carbon dioxide on the atmospheric corrosion of some magnesium alloys in the presence of NaCl" *J. Elec. Soc.* 149 (2002) B103-B107

13. P. Volovitch, M. Serdechnova, K. Ogle "Aqueous corrosion of Mg-Al binary alloys: roles of Al and Mg" *Corrosion* 68 (2012) 557-570

14. M. Liu, P. Uggowitzer, A. Nagasekhar, P. Schmutz, M. Easton, G. Song, A. Atrens "Calculated phase diagrams and the corrosion of die-cast Mg-Al alloys" *Corr. Sci.* 51 (2009) 602-619

15. Y.L. Cheng, T.W. Qin, H.M. Wang, Z. Zhang "Comparison of corrosion behaviours of AZ31, AZ91, AM60 and ZK60 magnesium alloys" *Trans. Nonferrous Met. Soc. China* 19 (2009) 517-524

16. K.D. Ralston, N. Birbilis, "Effect of grain size on corrosion: A review" *Corrosion* 66 (2010) 1-13

17. M. Zhao, M. Liu, G. Song, A. Atrens "Influence of the β-phase morphology on the corrosion of the Mg alloy AZ91" *Corros. Sci.* 50 (2008) 1939-1953

18. T. Zhang, Y. Shao, G. Meng, Z. Cui, F. Wang *Corros. Sci.* **53**, 1960 (2011)

19. F. Andreatta, I. Apachitei, A.A. Kondentsov, J. Dzwonczyk, J. Duszczyk "Volta potential of second phase particles in extruded AZ80 magnesium alloy" *Electrochim. Acta* 51(2006) 3551-3557

20. V.Y. Gertsman, L. Jian, S. Xu, J.P. Thomson, M. Sahoo "Microstructure and second phase particles in low and high pressure die cast magnesium alloy AM50" *Metallurg. and Mat. Trans. A*, 36A, (2005) 1989.

21. C. Blawert, D. Fechner, D. Hoche, V. Heitmann, W. Dietzel, K.U. Kainer, P. Zivanovic ,C. Scharf , A. Ditze, J. Grobner, R. Schmid-Fetzer, "Magnesium secondary alloys: Alloy design for magnesium alloys with improved tolerance limits against impurities" *Corros. Sci*., 52 (2010) 2452

22. M. Jonsson, D. Persson, R. Cubner "The initial steps of atmospheric corrosion on magnesium alloy AZ91D" *J. Electrochem. Soc.* 154 (2007) C684-C691

23. R.M. Asmussen, P. Jakupi, M. Danaie, G. Botton, D.W. Shoesmith "Tracking the corrosion of magnesium sand cast AM50 alloy in chloride environments" *Corros. Sci.* 75 (2013) 114-122

24. B. Boukamp,"A linear Kronig-Kramers transform test for immittance data validation" *J. Electrochem. Soc*., 142 (1995) 1885.

25. M. Danaie, R.M. Asmussen, P. jakupi, D. Shoesmith, G. Botton "The role of aluminum distribution on local corrosion resistance of the microstructure in a sand-cast AM50 alloy" *Corros. Sci.* 77 (2013) 151-163

26. D. Lau, A. E. Hughes, T. M. Muster, T. J. Davis, A. M. Glenn "Electron beam induced carbon contamination on silicon: characterization using raman spectroscopy and atomic force microscopy" *Microscopy and Microanal.* 16 (2010) 13-20

27. A. Atrens "Overview of the Mg corrosion mechanism" *ECS Trans.* 50 (2013) 335-344

28. G. Galicia, N. Pebere, B. Tribollet, V. Vivier "Local and global impedances applied to the corrosion behaviour of an AZ919 magnesium alloy" *Corros. Sci.* 51 (2009) 1769-1794

29. J.B. Jorcin, M.E. Orazem, N. Pebere, B. Tribollet "CPE analysis by local electrochemical impedance spectroscopy" *Electrochim. Acta* 51 (2006) 1473-1479

30. D. Sachdeva "Insights into microstructure based corrosion mechanism of high pressure die cast AM50 alloy" *Corros. Sci.* 60 (2012) 18-31

31. G. Baril, C. Blanc, N. Pebere "AC impedance spectroscopy characterizing time-dependent corrosion of AZ91 and AM50 magnesium alloys" *J. Electrochem. Soc.* 148 (2001) B489-496

32. W. Liu, F. Cao, A. Chen, L/ Chang, J. Zhang, C. Cao "Effect of chloride ion concentration on electrochemical behaviour and corrosion product of AM60 magnesium alloy in aqueous solution" *Corrosion* 68 (2012) 045001-1 – 045001-14

33. G. Song, A. Atrens "Corrosion Mechanisms of Magnesium Alloys" *Adv. Eng. Mat.* 1 (1999) 11-33

34. R. Ambat, N. N. Aung, W. Zhou "Evaluation of microstructural effects on corrosion behaviour of AZ91D magnesium alloy" *Corros. Sci* 42 (2000) 1433-1455

35. M. Alvarez-Lopez, M.D. Pereda, J.A. del Valle, M. Fernandez-Lorenzo, M.C. Garcia-Alonso, O.A. Ruano, M.L. Escudero "Corrosion behaviour of AZ31 magnesium alloy with different grain sizes in simulated biological fluids" *Acta Biomater.* 6 (2010) 1763-1771

36. G.R. Argade, S.K. Panigrahi, R.S. Mishra "Effects of grain size on the corrosion resistance of wrought magnesium alloys containing neodymium" *Corros. Sci.* 58 (2012) 146-151

37. N. N. Aung, W. Zhou "Effect of grain size and twins on corrosion behaviour of AZ31B magnesium alloy" *Corros. Sci.* 52 (2010) 589-594

38. G. Galicia, N. Pebere, B. Tribollet, V. Vivier "Local and global electrochemical impedances applied to the corrosion behaviour of an AZ91 magnesium alloy" *Corros.Sci.* 51 (2009) 1789-1794

39. F. Cao, Z. Shi, J. Hofstetter, P. Uggowitzer, G. Song, M. Liu, A. Atrens "Corrosion of ultra high purity Mg in 3.5% NaCl solution saturated with $Mg(OH)_2$" *Corros. Sci.* 75 (2013) 78-99

Chapter Five

Simulating the Corrosion Behaviour of a Cathodic Site in Mg Alloy Corrosion : The Electrochemical Behaviour of Al-Mn Intermetallics in NaCl and $MgCl_2$

5.1 Introduction

Lightweight Mg alloys have promising applications in the automotive and aerospace fields due to their high strength to weight ratio [1,2], but are generally unstable when coupled to a more noble material [3]. Contaminants found in Mg alloys such as Fe and Cu [4,5] are inevitably detrimental to the corrosion properties of the alloy, but their distribution can be limited through addition of Mn which can scavenge these species into secondary phases [6]. Consequently in Al-containing Mg alloys, Al-Mn precipitates are commonly found in the alloy microstructure.

The α-Mg phase is susceptible to microgalvanic corrosion by coupling to secondary microstructural constituents. Al-Mn intermetallics have been identified as strong cathodes driving the corrosion of the α-Mg phase [7] and an increase in their Fe content increases their cathodic activity [8]. Following corrosion, Al-Mn intermetallics have been observed to either accumulate a corrosion product deposit [9, 10] or to remain exposed [9]. Recently we have claimed that the domes of corrosion product are a result of the cathodic behaviour of the Al-Mn intermetallic in a microgalvanic couple [11]. In such a scenario, the cathodic reaction on the intermetallic is the reduction of water to H_2 [6]

$$2H_2O + 2\,e^- \rightarrow H_{2(g)} + 2\,OH^-{}_{(aq)}$$

As $H_{2(g)}$ evolution proceeds, the local pH increases creating two observable features: (1) deposition $Mg(OH)_2$ above the cathodic site, and (2) delamination of the intermetallic surface [11] due to dissolution of Al from the intermetallic.

Studies of Al-Mn alloys and materials have sporadically appeared in the literature, with a patent for Al-Mn alloys first published in 1933 [12]. Al-Mn materials have been studied previously, in the form of layered oxides as battery materials [13], with lithium as a battery cathode [14], as corrosion resistant layers protecting Mg alloys [15] and steel [16], as electrodeposited materials with exceptional hardness [17], and as anodically oxidized coatings [18]. These studies focus mainly on the Al-Mn alloy physical properties, and anodic electrochemical and natural corrosion behaviour.

Despite their known function as cathodes in Mg alloy corrosion, little is known about the cathodic behaviour of Al-Mn materials in chloride environments similar to those experienced in automotive applications. More recently, research on cathodic processes on Mg and its alloys has focused on the influence of Fe enrichment on the cathodic regions on a corroding Mg surface [19] and on the decreased cathodic behaviour of a secondary Mg-As phase [20].

When forming a microgalvanic couple to the less noble α-Mg grains the Al-Mn intermetallic phase is cathodically polarized to the corrosion potential (E_{CORR}) of the alloy (~ -1.60 V) and becomes a location supporting water reduction. An understanding of the activity of the Al-Mn phase as a cathode is a key requirement in understanding the overall behaviour of the microstructural constituents on a corroding Mg alloy surface. In this study we have electrochemically simulated the cathodic behaviour on macroscale Al-Mn alloys in an attempt to determine the microscopic evolution of the surface of the Al-Mn intermetallics under cathodic conditions. This was done to confirm that the accumulation of corrosion product domes on

corroding Mg alloys is an indication of the cathodic activity of the feature located below the dome.

5.2 Experimental

5.2.1 Materials

Mg alloy AZ31 was provided in a rolled sheet of 1 mm thickness by General Motors-Canada. The AZ31 samples were machined into 1 cm × 1 cm × 1 mm pieces. The Mg alloy materials were ground successively with 800, 1000, 1200, 2400 grit SiC, followed by 3 µm diamond suspension with ethanol-isopropanol as a lubricant and a final finish in 0.5 µm colloidal silica with ethylene glycol as a lubricant. Following polishing, the sample was rinsed in ethanol and dried in an ultra high purity Ar stream.

Two Al-Mn intermetallic materials were used in this study, Al-11 wt% Mn (Al-11Mn) and Al- 25 wt% Mn (Al-25Mn) which were received from CANMET Materials in Hamilton, ON, Canada. The samples were machined into 1 cm × 1cm × 0.7 cm pieces and one face threaded to allow electrical connection to external circuitry. All samples were mounted in Struers EpoFix® epoxy resin to limit exposure to solution to a single face of the intermetallic. Prior to each experiment the samples were ground successively with 800, 1000, 1200, 2400 and 4000 grit SiC paper using water as a lubricant. Reagent grade NaCl and $MgCl_2$-$6H_2O$ from Caledon were used for solution preparation in NanoPure® water (18 MΩ-cm).

5.2.2 Electrochemical Measurements

All electrochemical experiments were carried out in a standard three-electrode electrochemical cell with a Pt-foil counter electrode and a saturated calomel reference electrode (SCE). Immersion experiments placed the samples face down in solution, suspended by a steel rod for a set duration. Electrochemical control was provided by a Solartron® 1480 MultiStat. In cathodic potentiodynamic polarization (PDP) measurements the sample was placed in solution for 1 h to 3 h to establish a stable E_{CORR}, then polarized at 1 mV/s from E_{CORR} to -1.55 V vs. SCE, and held for 20 h.

5.2.3 Surface Analysis

Stereo-micrographs were collected on a Zeiss SteReo Lumar V12 Microscope equipped with an Axio 1.0 camera. Scanning electron microscopy (SEM) and energy dispersive x-ray spectroscopy (XEDS) were performed on either a Hitachi 3400-N Variable Pressure scanning electron microscope, a LEO 440 scanning electron microscope equipped with a Quartz XOne EDX detector, or a LEO (Zeiss) 1540 XB/SEM equipped with an Oxford instruments EDX detector. Focused ion beam (FIB) cross-sections were produced with the LEO 1540 XB/SEM using a Ga ion beam. X-ray diffraction (XRD) was carried out using a Bruker D8 fully automated diffractometer employing Co Kα radiation (λ=1.78897 Å) and peak identification was confirmed with X-Pert High Score Plus software.

5.3 Results

5.3.1 Al-Mn Intermetallics

This study was performed to replicate the behaviour of Al-Mn intermetallic materials present in a corroding Mg alloy system. An example of the size and distribution of such intermetallic precipitates in a polished AZ31 Mg alloy is shown in Figure 5.1 (a). The large intermetallic marked with the white arrow is magnified in Figure 5.1 (b). The contrast observed within the intermetallic structure is due to the presence of segregated regions with different Al:Mn ratios, as confirmed by XEDS analyses, Figure 5.1 (c), of the two sites marked in Figure 5.1 (b). The quantitative XEDS data (in wt%) is presented in Table 1. Converting to atomic %, Site 1 has an Al:Mn ratio of 8:3, and Site 2 of 3:2. The different regions of this intermetallic contained differing amounts of Al and Mn and such variations in composition can be expected based on the Al-Mn phase diagram [21] and studies showing multiple compositions of Al-Mn intermetallics in Mg alloys ranging from $Al_{19}Mn_4$ to Al_8Mn_5 [22]. Following exposure of this alloy to 0.275 M NaCl, domes of corrosion product were observed above the Al-Mn intermetallics, Figure 5.1 (d). The location of these intermetallics is marked with the red arrow in Figure 5.1 (a). In our previous study [11] the accumulation of such a corrosion product dome was interpreted that the intermetallic functions as a cathode galvanically-coupled to the corroding α-Mg matrix.

Figure 5.2 (a-I) shows a BSE SEM micrograph of the surface of the Al-11Mn alloy. The darker areas on the surface were higher in Al content, confirmed by the XEDS map in Figure 5.2 (a-II), whereas the brighter bands were rich in Mn, Figure 5.2(a- IV).

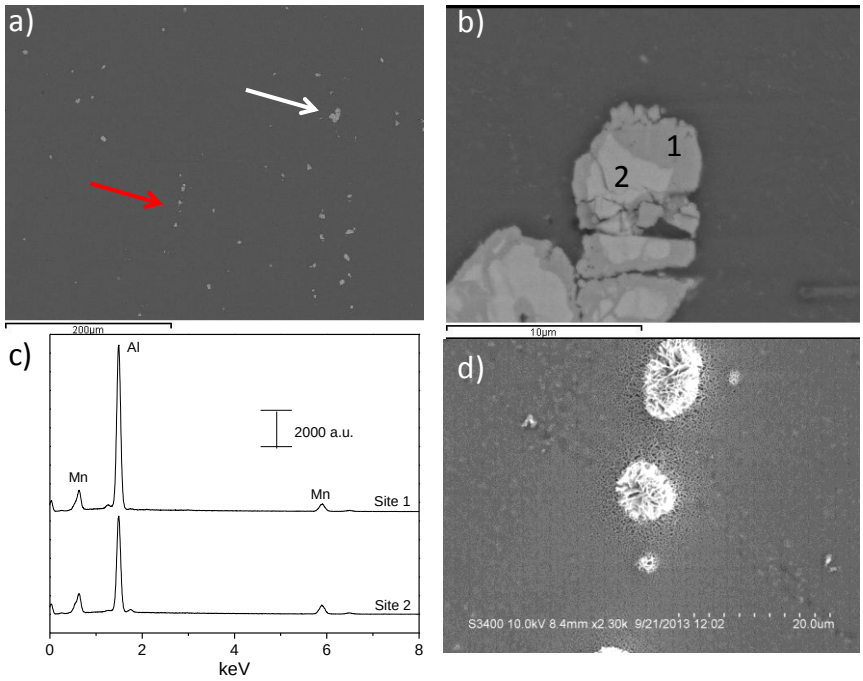

Figure 5. 1 - a) SEM micrograph of a polished AZ31 Mg alloy surface, b) SEM micrograph of the Al-Mn intermetallic marked with the white arrow in (a), c) XEDS spectra of the locations marked in (b), d) SEM micrograph of the domes of corrosion product that appeared above the Al-Mn intermetallic particles marked with the red arrow in (a) following 24 h immersion in 0.275 M NaCl.

Table 5. 1 - Quantitative XEDS data of the major elements from the corresponding spectra in Figure 1 (c).

Element (wt%)	Site 1	Site 2
Mg	1.03	0.38
Al	53.76	41.97
Mn	42.78	54.31
Zn	0	0

The Mn-containing regions had a Mn content ranging from 9 wt% to 25 wt% while little Mn was present outside these locations, similar to previously reports on Al-Mn alloys [23]. Small locations containing Si were also present, Figure 5.2 (a-III). A similar set of images and analyses shows the Al-25Mn has a more dendritic appearance with compositions of 13 wt% to 25 wt% Mn, Figure 5.2 (b), with a more uniform distribution of Mn and a smaller number of Si-containing locations. The composition of these Mn-containing areas in the Al-11Mn and Al-25Mn materials, expressed as an atomic %, ranges from 4.6 at% to 15 at% which is within the measured ranges for Al-Mn precipitates present in Mg alloys.

5.3.2 Electrochemical Behaviour

Electrochemical measurements were performed on both materials in solutions with similar chloride concentrations of either 0.275 M NaCl or 0.138 M $MgCl_2$. The Mg^{2+} solution was chosen to simulate the supply of Mg^{2+}anticipated from adjacent

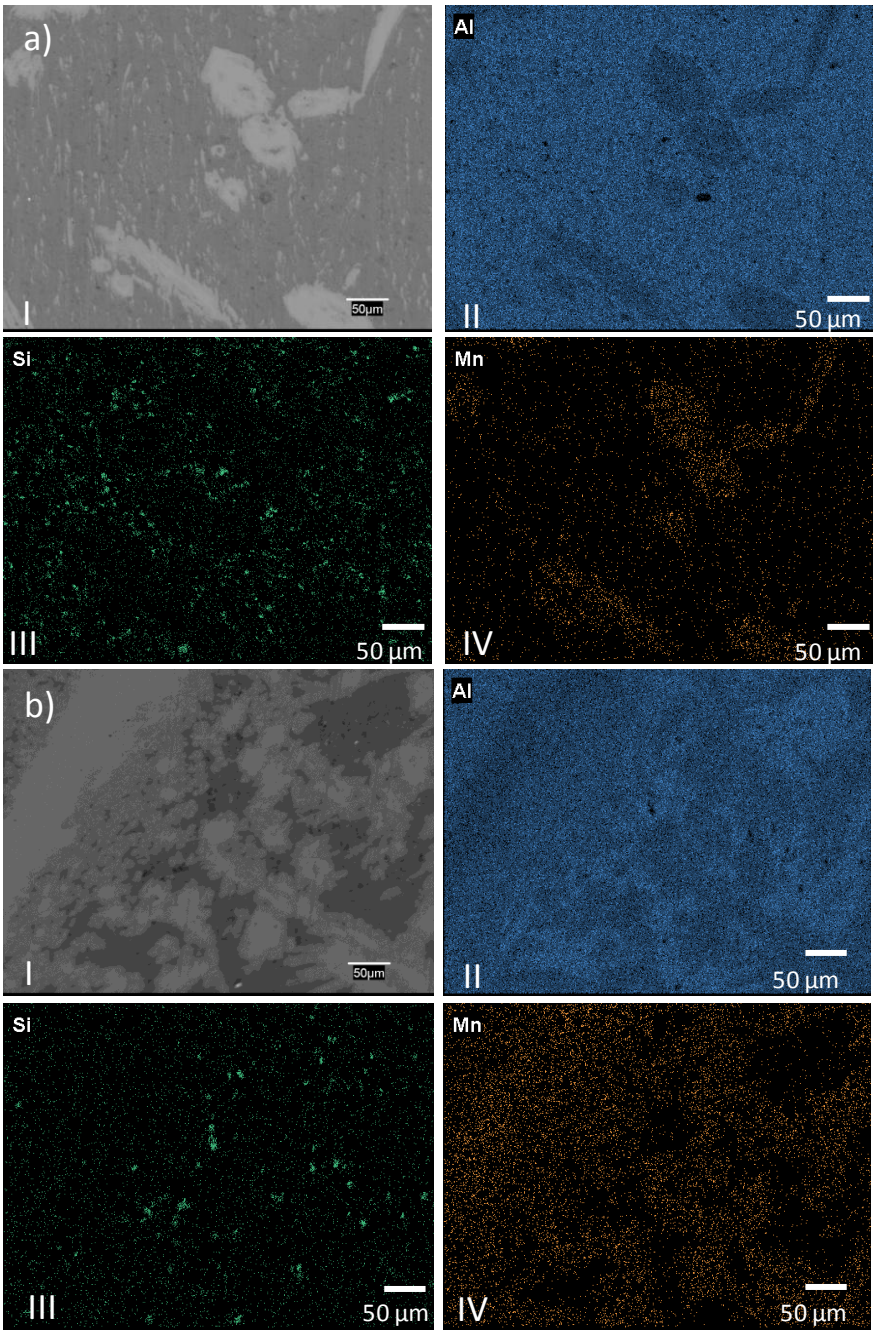

Figure 5. 2 - a) I) SEM backscatter micrograph of the a) Al-11Mn and b) Al-25Mn surface following polishing and the corresponding XEDS maps for II) Al, III) Si and IV) Mn.

corroding α-Mg locations when Al-Mn particles are galvanically-coupled within a Mg alloy. A concentration of 0.138 M was chosen since it is within the range of the measured [Mg^{2+}] above a galvanically coupled corroding Mg sample measured using potentiometric scanning electrochemical microscopy [24].

Figure 5.3 shows the E_{CORR} values measured on the Al-11Mn and Al-25Mn electrodes over an ~12 h period of immersion in these solutions, with the Al-11 Mn electrode exhibiting a more positive E_{CORR} than the Al-25Mn electrode in both solutions. The cathodic PDP curves are plotted in Figure 5.4. Consistent with the results in Figure 5.3, the Al-11Mn electrode again exhibited more positive E_{CORR} values than the Al-25Mn electrode. In PDP scans from E_{CORR} to -1.55 V both materials displayed similar currents in the 0.138M $MgCl_2$ solution for potentials more negative than -1.0 V. In 0.275 M NaCl, slightly larger currents were observed especially for the Al-11Mn which exhibited a sharp increase in current at potentials < -1.1 V. At -1.55 V, the electrodes all showed currents in the region of -100 μA/cm^2.

To study alterations in the surface of the electrodes as a consequence of cathodic activity, the samples were polarized at -1.55 V for 20 h: i.e., in the potential range where an Al-Mn intermetallic would be polarized if acting as a galvanically-coupled cathode in a corroding Mg alloy. The resulting current-time profiles are presented in Figure 5.5. In 0.138 M $MgCl_2$ both the Al-11Mn and Al-25Mn electrodes exhibited an initial rapid decrease in cathodic current density to eventual steady state values of -100 μA/cm^2 and -40 μA/cm^2, respectively. In NaCl, the Al-25 Mn electrode showed similar behaviour,

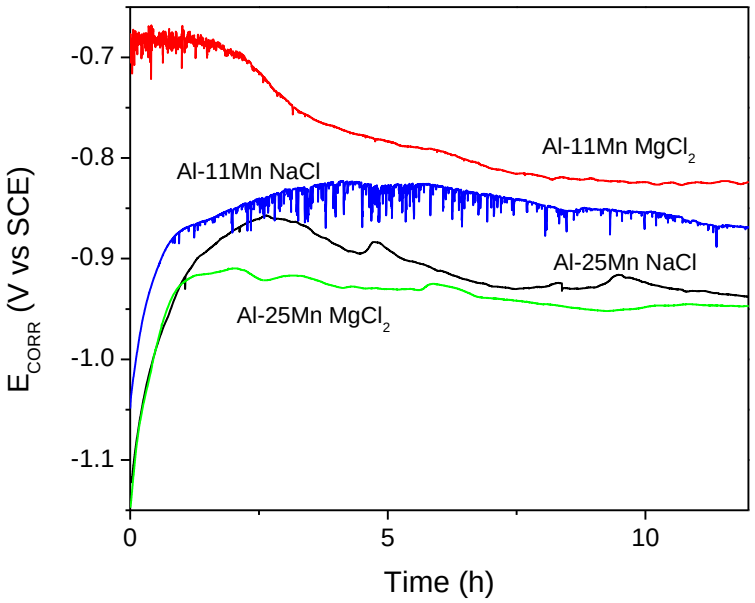

Figure 5. 3 - Evolution of E_{CORR} over a 12 h period of immersion in 0.275 M NaCl and 0.138 M $MgCl_2$ for the Al-11Mn and Al-25Mn electrodes.

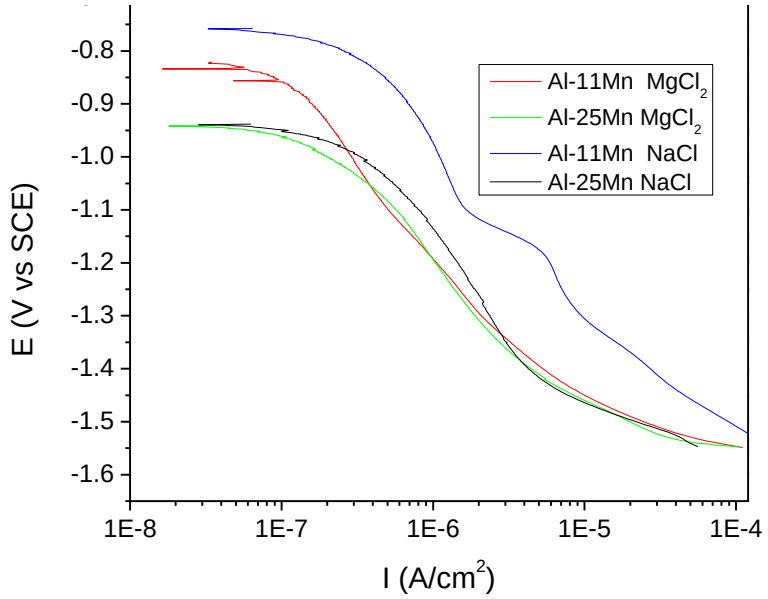

Figure 5. 4 - PDP scans recorded on the Al-11Mn and Al-25Mn intermetallics in 0.275 M NaCl and 0.138 M $MgCl_2$ from E_{CORR} to -1.55 V at a scan rate of 1 mV/s.

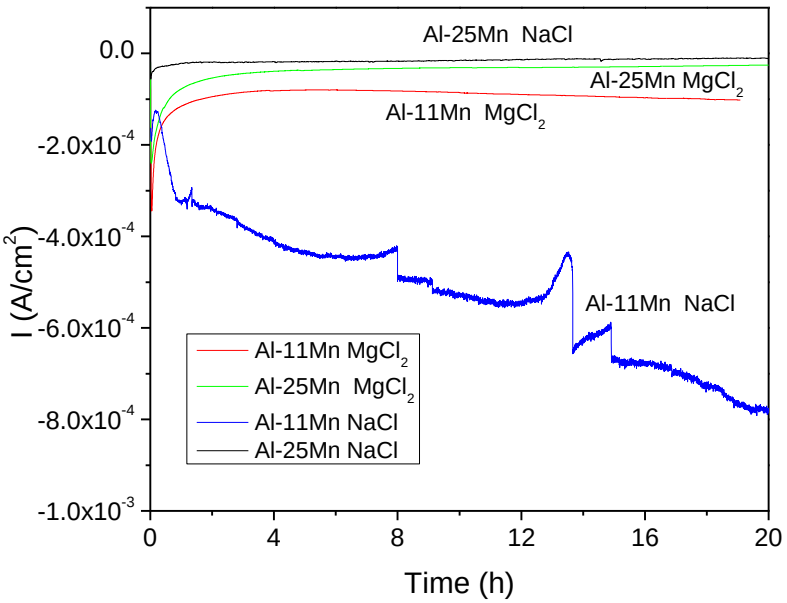

Figure 5. 5 - Potentiostatic current density vs. time profiles recorded on the Al-11Mn and Al-25Mn electrodes at -1.55 V in 0.138 M $MgCl_2$ and 0.275 M NaCl.

and established a steady current of -20 µA/cm^2 after ~1 h of polarization. By contrast, on the Al-11Mn electrode the current steadily increased to a final cathodic current density of -800 µA/cm^2. Over this 20 h period, the cathodic current peaked and began to decrease on a number of occasions before suddenly increasing again. A particularly large transient such event can be observed between 11 and 13 h.

5.3.3 Surface Behaviour

Following the exposure and electrochemical experiments, the surfaces of the Al-Mn samples were investigated optically and by SEM. Here, only examinations of the surface of the Al-11Mn electrode are shown since this alloy exhibited the strongest cathodic behaviour in the two solutions. Optical micrographs of this electrode following

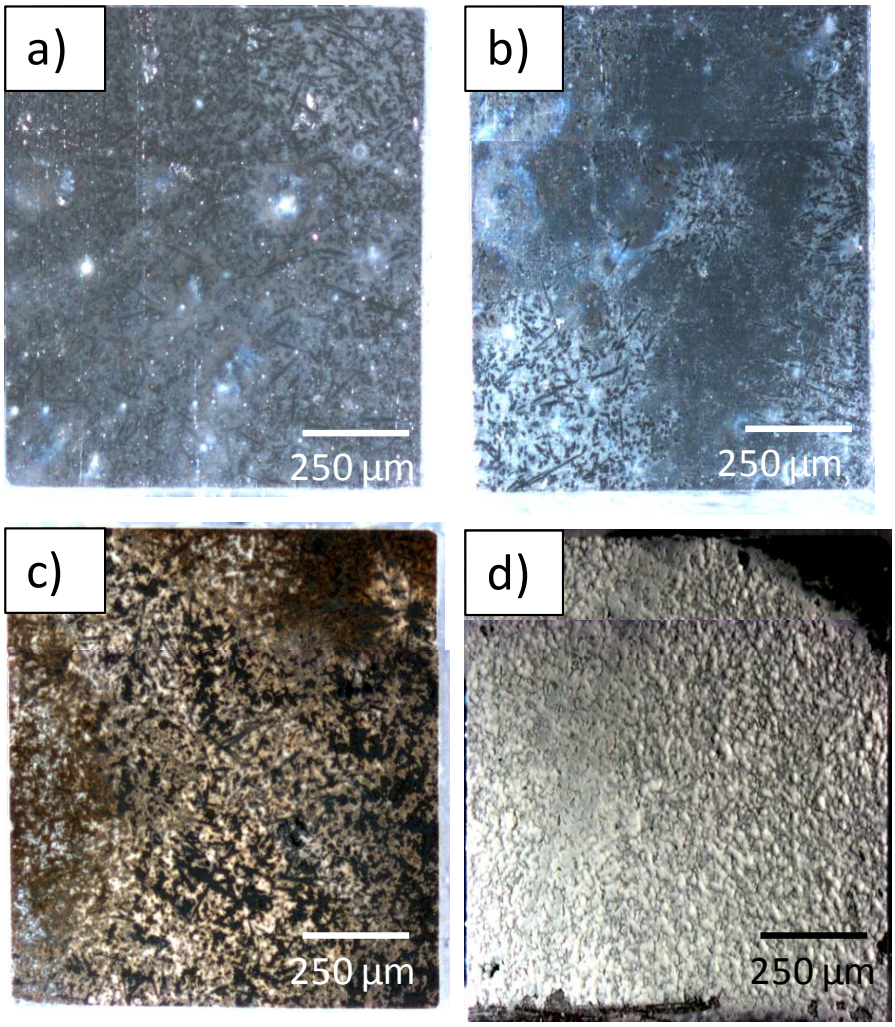

Figure 5. 6 - optical micrographs of the Al-11Mn surface following a 20 h exposure to a) 0.275 M NaCl at E_{CORR}, b) 0.138 M $MgCl_2$ at E_{CORR} , b) 0.275 M NaCl at -1.55 V, and c) 0.138 M $MgCl_2$ at -1.55 V.

the 20 h electrochemical treatments (Figure 5.5) are displayed in Figure 5.6. Figure 5.6 (a) shows the Al-11Mn surface after 20 h at E_{CORR} in 0.275 M NaCl, and Figure 5.6 (b) the surface after a similar 20 h exposure in 0.138 M $MgCl_2$. No distinct surface deposits were observed and the electrodes retained their metallic character. Figure 5.6 (c) shows that, after potentiostatic treatment at -1.55 V for 20 h, a distinct discolouration of the Al-11Mn surface was observed. This is in stark contrast to the surface of this electrode potentiostatically treated in 0.138 M $MgCl_2$ for 20 h on which a dense, white deposit accumulated, Figure 5.6 (d).

The changes on the Al-11Mn electrode surface after the potentiostatic treatment in NaCl were clearly visible by SEM, Figure 5.7 (a). Two distinct areas were apparent on the surface. Some areas were covered with columnar crystals as seen on the left and right of the image, while other areas are free of such crystals and covered with a finer deposit. The XEDS analyses of these regions, Figure 5.7(b), showed the crystal-covered Site 1 was comprised of an Al oxide whereas the crystal-free Site 2 had a lower Al signal and an observable Mn signal.

A FIB cross section of the interface between these two areas revealed the underlying surface and the morphology of the surface layer, Figure 5.8 (a). The base material can be seen in the cross section at location 1, the XEDS signal in Figure 5.8 (b) confirming the presence of Al and Mn and the absence of O. The transition between oxide/hydroxide and the Al-Mn substrate is designated with a red dashed line in Figure 5.8 (a). Locations 2 and 3 in Figure 5.8 (a) contain primarily Al-oxide, Figure 5.8 (c),

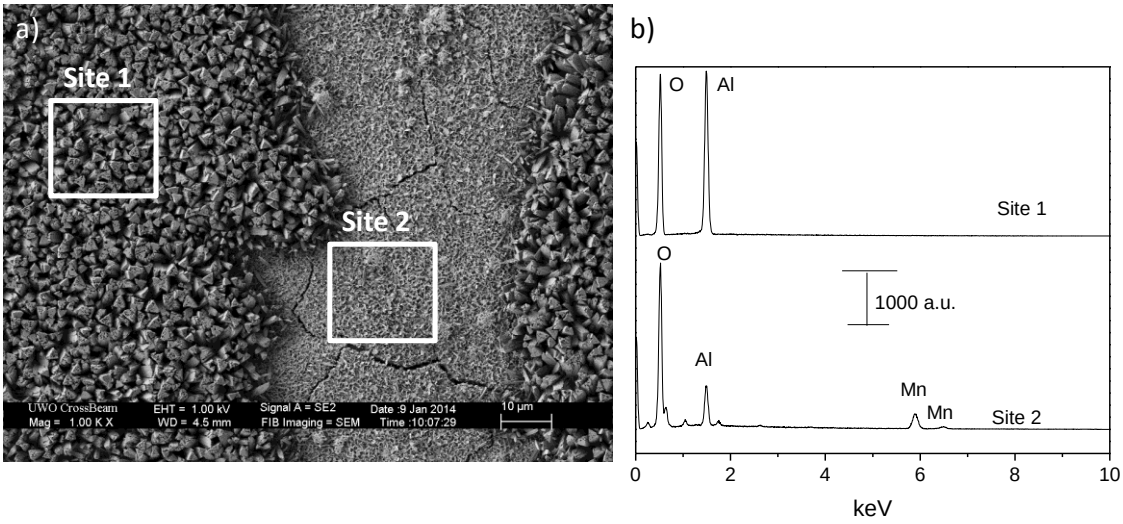

Figure 5. 7 - a) SEM micrograph of the surface of the Al-11Mn electrode and b) the corresponding XEDS spectra recorded after 20 h cathodic polarization at -1.55 V in 0.275 M NaCl.

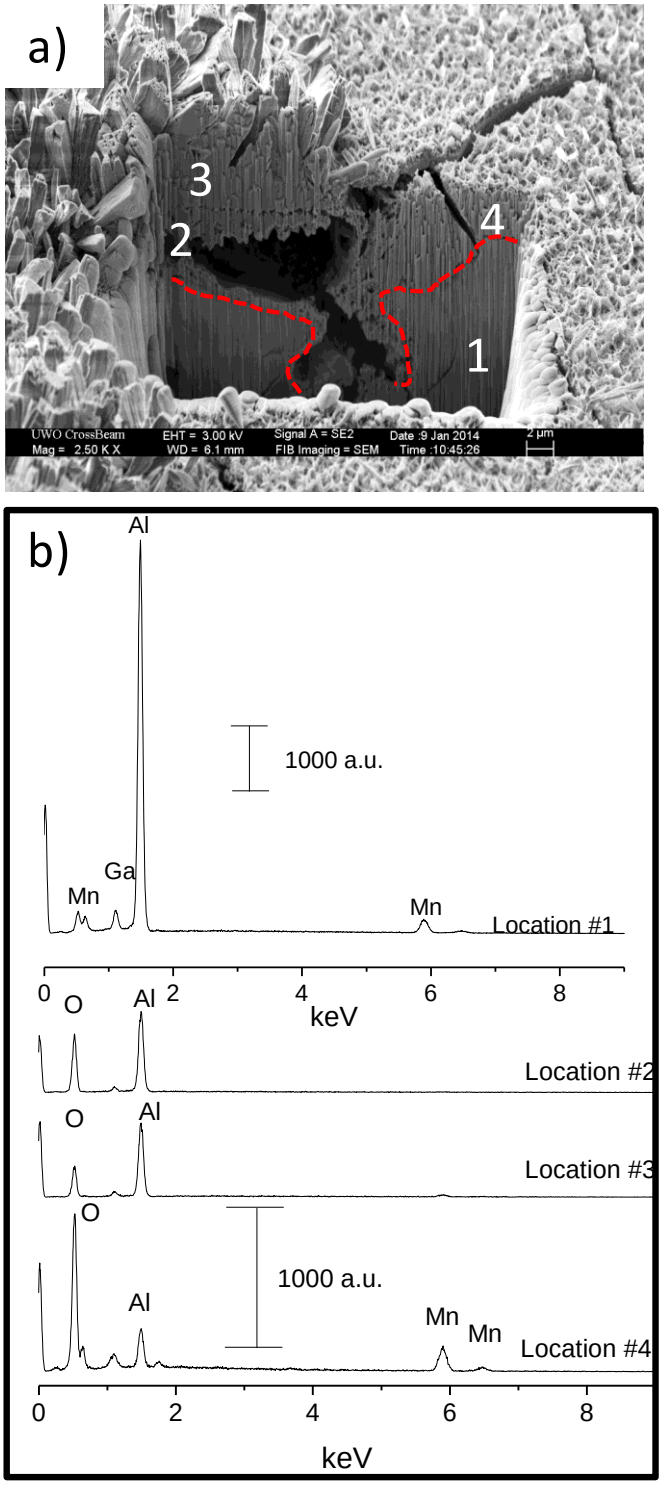

Figure 5. 8 - a) SEM image of a FIB on the Al-11Mn electrode after cathodic polarization at -1.55 V in 0.275 M NaCl. The oxide/base metal interface is marked with the dashed line b) corresponding XEDS spectra for the locations indicated in (a).

with extensive damage observed immediately below this region. The thickness of the accumulated layer at this crystal covered location is, on average, ~8 to 10 µm. By contrast, the finer deposit at location 4, Figure 5.8 (a), was only ~ 3 to 4 µm thick and exhibited strong Mn and O signals, Figure 5.8 (c). In addition very little damage to the Al-Mn substrate is observed beneath this location.

The surface of the Al-11Mn electrode after potentiostatic polarization at -1.55 V in 0.138 M $MgCl_2$ showed a much different morphology. The surface was covered with mounds of deposit, Figure 5.9 (a). The cracking observed most likely occurred on drying the surface after removal from the cell. A FIB cross section of the surface, Figure 5.9 (b), revealed a much thicker deposited layer of ~20 µm compared to that formed in the NaCl solution. XEDS analyses, Figure 5.9 (c), showed the layer at Site 1 to be a mainly Mg-containing oxide with a small, but significant, Al content. Analysis of Site 2 yielded much stronger Mg and O signals compared to Al. The overall increase in signal strength compared to Site 1 is likely a result of the lower porosity of the layer at Site 2, Figure 5.9 (b). Very little surface damage is observed at locations below the accumulated layer, Figure 5.9 (b).

XRD spectra were recorded on the Al-11Mn electrodes after cathodic polarization in both solutions, and are shown in Figure 5.10. On the electrode polarized in NaCl the Al, detected by XEDS in (Figure 5.7 (b)), is shown by XRD to be $Al(OH)_3$, Figure 5.10 (a). A strong signal for crystalline Al was also observed, as expected, from the base material. No signal from the various possible Al-Mn phases in the bulk material are

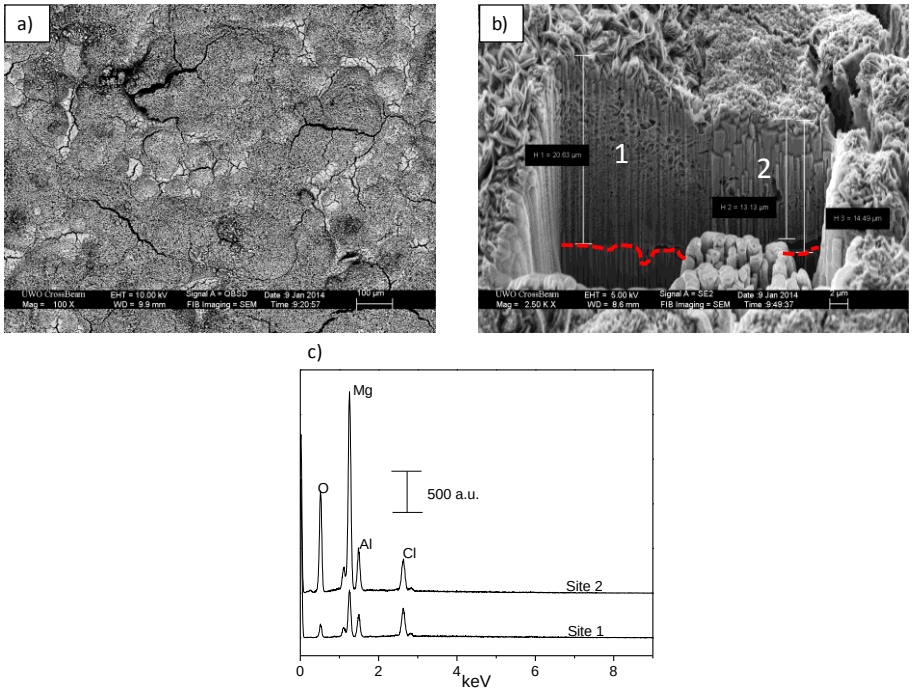

Figure 5. 9 - a) SEM micrograph of the Al-11 Mn surface following cathodic polarization for 20 h at -1.55 V in 0.138 M $MgCl_2$, b) FIB cross section through the surface layer with the red dotted line denoting the substrate/layer interface and c) XEDS spectra recorded at the locations labelled in (b).

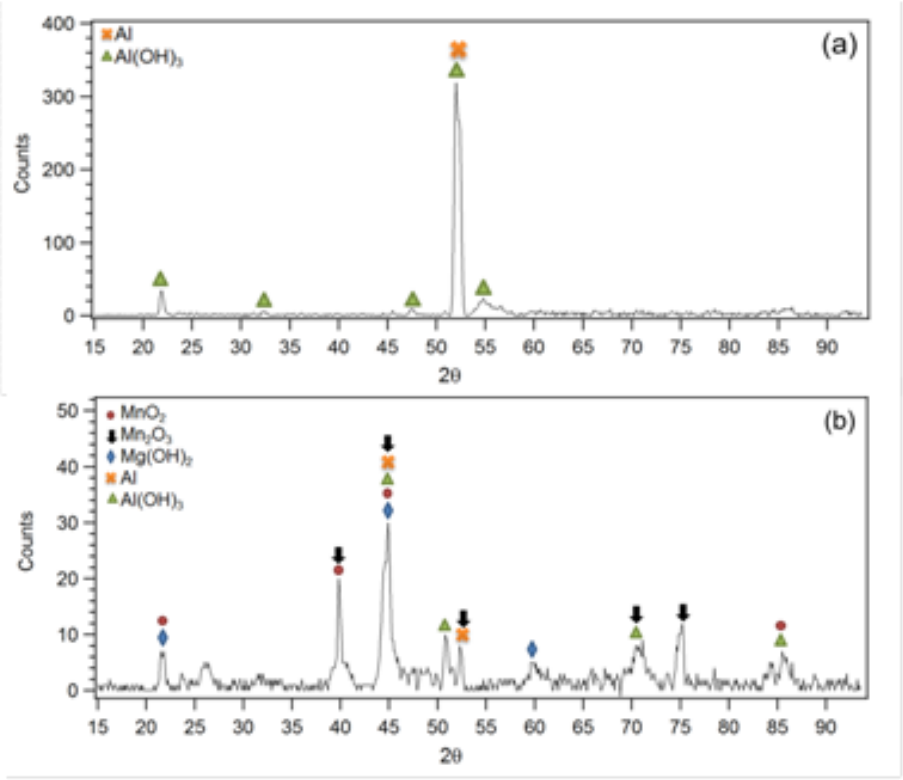

Figure 5. 10 - spectra identifying the phases present on the Al-11Mn electrodes after cathodic polarization in (a) 0.275 M NaCl and (b) 0.138 M $MgCl_2$ solution.

observed in the spectrum. Figure 5.10 (b) shows the XRD spectra recorded on the Al-11Mn electrode after potentiostatic treatment in $MgCl_2$ solution. The peaks for $Mg(OH)_2$ confirm the dominance of Mg identified in the XEDS spectrum in Figure 5.9 (c). In addition, MnO_2, Mn_2O_3, $Al(OH)_3$ and crystalline Al were also detected.

5.4 Discussion

The Al-Mn materials used in this study are representative of the Al-Mn intermetallic particles found in Mg alloys. The Mn-containing regions in the Al-Mn alloys used in this study have a Mn content in the range 9 to 25 wt%, while multiple Al-Mn intermetallic phases are feasible and known to be widely dispersed with varying Mn content as previously reported [21,22]. In this study, the E_{CORR} of the alloys, in both NaCl and $MgCl_2$ solutions, shifted to more negative values as the fraction of the surface covered by Mn-containing areas increased, Figure 5.3. This trend is consistent with previous observations on the influence of Mn content in Al-Mn alloys [18], and has been attributed to the decreased potential difference between the basically Al matrix and the Mn-containing intermetallic [8].

The Al-11Mn electrode displayed an unstable E_{CORR} over the first 3 h of exposure to 0.138 M $MgCl_2$ and throughout the 12 h exposure to 0.275 M NaCl. The potential transients observed indicated local metastable film breakdown events possibly associated with the boundaries between the Al matrix and Mn-containing areas [25]. Similar events were not observed in E_{CORR} measurements on the Al-25Mn electrode. This increased stability in chloride solution of an Al-Mn alloy with increased Mn content has previously been reported and attributed to the ability of Mn to improve the resistance to film breakdown due to the slight cathodic polarization of the surface yielding a more negative E_{CORR} [8,26]. Interestingly, the noise is only transitory in $MgCl_2$ compared to NaCl perhaps as a consequence of the accumulation of small amounts of $Mg(OH)_2$. This would be supported by the lower cathodic currents observed in the

PDP scans (Figure 5.4) in the $MgCl_2$ solution compared to the NaCl solution at potentials only slightly cathodic to E_{CORR}.

Despite these transitory events the electrodes maintain their metallic appearance (Figure 5.6 (a) and (b)) after exposure at E_{CORR}. However, following cathodic polarization to -1.55V (i,e., the potential expected if the Al-Mn were acting as a galvanically coupled cathode in a corroding Mg alloy) major changes to the surface are observed, Figure 5.6 (c) and (d), suggesting the Al-Mn alloys were unstable under these conditions.

The low cathodic current densities established on the Al-25Mn electrode in both NaCl and $MgCl_2$ suggest this alloy is a stable, but inefficient cathode. By contrast, the considerably higher cathodic current densities measured on the Al-11Mn electrode suggest a more efficient but unstable cathode, especially in NaCl solution. These generally higher cathodic current densities on the Al-11Mn alloy can be attributed, at least partially, to the higher exchange current density for H_2 evolution on Al (~ 10^{-8}A·cm^{-2}) [27] compared to Mn (~ 10^{-11} A·cm^{-2}) [28]. It is possible this difference could be larger since the value for Al was measured on the oxide-covered metal and the metal may not be passive at the pH conditions in the present experiment. This claim is consistent with previous studies which showed the cathodic reaction rate on an Al-Mn-Fe phase in a Mg alloy decreased as the Mn content increased [29]. This was attributed to the presence of a higher ratio of Mn:Fe in the phase making it less cathodic. In a separate study, bulk additions of Mn (up to 2 wt%) were found to improve the corrosion resistance of a Mg-Zr system with a measured decrease in cathodic kinetics corresponding to the small additions of Mn [30]. In the present case the Al-Mn phase appears free of contaminants, especially Fe, and the cathodic reactivity is decreased by an increase in Mn content. This is contrary to a previous report that Al-rich intermetallic particles will exhibit lower cathodic reactivity [31].

The marked differences in cathodic current behavior for the Al-11Mn electrode in NaCl and $MgCl_2$ reflects the suppression of H_2O reduction by the deposition of $Mg(OH)_2$ from the $MgCl_2$ solution. The rise in cathodic current density on the Al-11Mn electrode and the erratic behavior show this electrode is unstable under cathodic polarization, and the lower steady cathodic current observed in $MgCl_2$ shows the presence of the $Mg(OH)_2$ deposit stabilizes this electrode. That this stabilization may not be complete is suggested by the slow increase in cathodic current in $MgCl_2$ over the 20 h duration of polarization.

The distinctly different surface features observed on the Al-11Mn electrode after cathodic polarization show some heavily corroded and some partially protected areas on the surface, Figures 5.7 and 5.8. The area with the thicker surface deposit (site 1, Figure 5.7) is the most heavily corroded area (Figure 5.8 (a)), XRD showing that the deposit is dominantly $Al(OH)_3$. The more extensive corrosion of the electrode at this location can be attributed to the generation of OH^- by H_2O reduction. After 20 h of polarization the bulk solution pH was 10.3 and at the surface of a cathode galvanically coupled to corroding Mg, local pH values as high as 14 have been measured [24]. Over this pH range Al is unstable in H_2O, unprotected by a passive oxide, and will corrode to yield AlO_2^-[32]. This would account for the formation of the columnar, non-protective layer of $Al(OH)_3$ over deeply corroded surface locations, as seen in the SEM image of the FIB cross section (Figure 5.8 (a)).

The corrosion process destabilizes the alloy surface leading to the fracture and delamination of the $Al(OH)_3$ layer as observed in the FIB cross section (Figure 5.8 (a)). This sequence of processes would account for the current instabilities observed potentiostatically (Figure 5.5). Etching experiments on Al-Mn alloys in alkaline solutions [33] indicate that corrosion proceeds via a preferential dealloying process involving the loss by corrosion of Al to yield an Mn_3O_4 substrate surface layer. While these previous etching experiments were conducted at E_{CORR} (i.e., at a potential in the range -0.7V to -1.0V (Figure 5.3)) de-alloying of Al

remains thermodynamically possible at -1.55V. The tendency of the current density to plateau and decrease (Figure 5.10) can be attributed to two features: the decrease in H_2O reduction current as the Al content of the surface is reduced, and partial blockage of the surface by the accumulation of $Al(OH)_3$. However, fracturing and delamination of this deposit, and possibly also the residual Al-depleted Mn oxide layer, would lead to re-exposure of the Al-containing subsurface and, under cathodic polarization, a rapid revival of the H_2O reduction current (Figure 5.5). The on-going sequence of such events would lead to an increase in the cathodically active surface area.

This process is more advanced on some locations (site 1, Figure 5.7(a)) than others (site 2, Figure 5.7(a)) where the leached surface layer, an Al-containing MnO_2 (Figure 5.8, location 4), appears only partially leached and still attached to the substrate alloy. Inspection of the potential-pH diagram for Mn suggests Mn(II) (as $Mn(OH)_2$) should be the stable oxidation state at -1.55V (vs SCE) as opposed to open circuit etching [33, 34] when $Mn_3O_4/Mn_2O_3/MnO_2$ are thermodynamically possible. Whether or not the MnO_2 observed by XRD reflects air oxidation on extraction of the electrode from the cell is not known.

When Mg^{2+} was present in the solution cathodic polarization lead to the deposition of a thick surface layer of $Mg(OH)_2$ as indicated by XEDS (Figure 5.10 (b)) and XRD (Figure 5.11) measurements. This is not surprising given the solubility product for $Mg(OH)_2$ ($K_{sp} = 1.8 \times 10^{-11}$) since its precipitation would be feasible for pH $\geq$ 9 [35]. At the electrode surface the local pH would be expected to be considerably higher (up to 14 [24]). The accumulation of this deposit would account for the very rapid decrease in cathodic current density on first applying cathodic polarization, Figure 5.5. The maintenance of a cathodic current density of ~ 100 $\mu A \cdot cm^{-2}$ indicates that H_2O reduction continues probably at the base of the pores shown to be present in the FIB cross section (Figure 5.9 (b)). This porosity would also explain the Al and Cl signals observed in the XEDS spectrum (Figure 5.10). The presence of Al (as $Al(OH)_3$) and

Mn_2O_3/MnO_2indicates some dealloying of the substrate occurs under the alkaline conditions prevailing at that location. The relatively undamaged electrode/deposit interface (Figure 5.9 (a)) compared to that after polarization in the absence of Mg^{2+} (Figure 5.8 (a)) confirms the partial protectiveness of the $Mg(OH)_2$ deposit. The strong Cl signal can be attributed to the deposition of $MgCl_2$ within the pores when the electrode was removed from the cell and dried.

In a previous electron microscopy study of Al-Mn intermetallics on a corroded AM50 Mg alloy [11], three key observations were made: (1) domes of corrosion product comprised of $MgO/Mg(OH)_2$ deposited on the surfaces of Al-Mn intermetallic particles in the alloy; (2) fracture and delamination of the surfaces beneath the domes was accompanied by a depletion of Al in the surface, and (3) the collapse and apparent reconstruction of domes occurred on some Al-Mn intermetallics. The first two of these features have been reproduced on the Al-Mn intermetallic phase (Al-11Mn) used in this study when the alloy is polarized to the potential it would experience within an actively corroding Mg alloy.

These studies show that while Al-Mn intermetallics will function as the key cathodic locations on a corroding Mn-containing Mg alloy their reactivity will become limited by the deposition of Mg^{2+}, transported from reactive anodic sites. The accumulation of this deposit is driven by the high pH due to H_2O reduction on the Al-Mn surface. According to the results in this paper this deposit is porous and the on-going destruction of the surface of the Al-Mn, which is relatively slow when a $Mg(OH)_2$ dome is present, confirms that alkaline conditions, sufficient to destabilize Al in the presence of H_2O, prevail at the surface of the intermetallic. This indicates that H_2O reduction occurs on the surface of the Al-Mn, the $Mg(OH)_2$ dome acting as a partially protective permeable barrier.

This offers a possible explanation why, during corrosion on Mg alloys, these domes of deposits sometimes collapse and then regrow. It is possible this could be caused by a

combination of two processes. The demand for cathodic current on a rapidly corroding alloy would require a large current density on the small intermetallic particles and the consequent build up of H_2 pressure within the pores in the dome could lead to its fracture and/or detachment. This process of fracturing/detachment could be assisted by the accompanying dealloying of the intermetallic as Al is dissolved in the alkaline environment. Both this study and our previous one [11] have shown that fracture/delamination of the surface occur. This would lead to a sudden surge in H_2 evolution on the freshly exposed Al-containing (and hence cathodically active) surface of the intermetallic. This sudden surge of current could assist the detachment of the dome and regenerate the cycle leading to its reformation.

Some intermetallics have been shown not to accumulate corrosion product domes following corrosion under aqueous [9] and atmospheric conditions [36]. In these situations, the intermetallics are present within the eutectic α-phase, which has a higher Al-content than the α-Mg grains. Since these locations tend to passivate by the enrichment of Al near the oxide/alloy interface [9] they are isolated from the α-Mg grains and unable to microgalvanically couple. Clearly, the presence of a dome of accumulated corrosion product can be taken as an indicator of the cathodic activity of that particular intermetallic during corrosion of the Mg alloy.

5.5 Summary and Conclusions

The cathodic behavior of Al-Mn materials, which commonly act as galvanically-coupled cathodes in corroding Mg alloys, has been studied in both NaCl and $MgCl_2$ solutions. The latter solution was used to simulate the conditions expected at the surface of a corroding Mg alloy when a significant concentration of Mg^{2+} would be present. Two Al-Mn alloys were investigated, Al-11Mn and Al-25Mn. Under corrosion conditions both alloys appear stable with the higher Mn-containing alloy exhibiting more negative E_{CORR} values and suppression of the metastable breakdown events observed on the Al-11Mn alloy. When polarized to a potential representative of that occurring on a corroding Mg alloy, the Al-25Mn alloy behaves as a stable, but inefficient,

cathode. By contrast, the Al-11Mn is unstable in NaCl solution as it undergoes dealloying. This leads to the formation of an $Al(OH)_3$ deposit and a Mn oxide surface which fractures and delaminates. In $MgCl_2$ this dealloying is significantly suppressed by the deposition of a porous $Mg(OH)_2$ layer due to the alkaline conditions generated at the Al-Mn surface by H_2O reduction. This situation simulates the behavior previously shown to occur when Al-Mn intermetallic particles act as microgalvanically-coupled cathodes in corroding Mg alloys.

5.6 References

1. Song, G. "Recent progress in corrosion and protection of magnesium alloys" *Adv. Eng. Mat.* 7 (2005) 563-586
2. Mordike B.L., Ebert T., "Magnesium: Properties, Applications, Potential" *Mater. Sci. Eng. A* 302 (2001): p. 37-45
3. Deshpande, K. B. "Experimental investigation of galvanic corrosion: Comparison between SVET and immersion techniques" *Corros. Sci.,52* (2010) 2819-2826.
4. Matsubara, H., Ichige, Y., Fujita, K., Nishiyama, H., & Hodouchi, K. (2012). "Effect of impurity Fe on corrosion behavior of AM50 and AM60 magnesium alloys". *Corros. Sci*. 66 (2013) 203-210
5. Song, G., & Atrens, A. "Understanding magnesium corrosion—a framework for improved alloy performance: *Adv. Eng. Mat. 5* (2003) 837-858.
6. Ballerini, G., Bardi, U., Bignucolo, R., & Ceraolo, G. "About some corrosion mechanisms of AZ91D magnesium alloy" *Corros. Sci. 47*,(2005) 2173-2184.
7. Mathieu S., Rapin C., Steinmetz J. "A corrosion study on the main constituent phases of AZ91 magnesium alloys" *Corros. Sci.* 45 (2003) 2741-2755
8. Zamin, M. "The role of Mn in the corrosion behaviour of Al-Mn alloys" *Corrosion* 37 (1981) 627-632

9. R.M. Asmussen, P. Jakupi, M. Danaie, G. Botton, D.W. Shoesmith "Tracking the corrosion of magnesium sand cast AM50 alloys in chloride environments" *Corrosion Science,* 75 (2013) 114-122
10. A. Pardo, M.C. Merino, A.E. Coy, R. Arrabal, F. Viejo, E. Matykina "Corrosion behaviour of magnesium/aluminum alloys in 3.5 wt% NaCl" *Corros. Sci.* 50 (2008) 823-834
11. M. Danaie, R.M. Asmussen, P. Jakupi, D.W. Shoesmith, G. Botton "The Cathodic behaviour of Al-Mn precipitates during atmospheric and saline aqueous corrosion of a sand-cast AM50 alloy" *Corros. Sci.* 83 (2014) 299-309
12. Bossert, T.W. "Aluminum Manganese Alloy" US Patent 1,928,641 1933
13. Wang, L., Sakai, N., Ebina, Y., Takada, K., Sasaki, T. "Inorganic multilayer films of manganese oxide nanosheets and aluminum olyoxocations: fabrication, structure and electrochemical behaviour" *Chem. Mater*. 17 (2005) 1352-1357
14. Chaing, Y.T., Sadoway, D.R., Jang, Y.I., Huang, B., Wang, H. "High capacity temperature stable lithium aluminum manganese oxide cathodes for rechargeable batters" *Electrochem. Solid State Lett.* 2 (1999) 107-110
15. Zhang, J., Zhang, W., Yan, C., Du, K., Wang, F. "Corrosion behaviours of Zn/Al-Mn alloy composite coatings deposited on magnesium alloy AZ31B (Mg-Al-Zn)" *Electrochim. Acta* 55 (2009) 560-571
16. Reffass, M., Berziou, C., Rebere, C., Billard, A., Creus, J. "Corrosion behaviour of magnetron sputtered Al_{1-x}-Mn_x coatings in neutral saline solution" *Corros. Sci.* 52 (2010) 3615-3623

17. Ruan, S., Schuh, C. "Electrodeposited Al-Mn alloys with microcrystalline, nanocrystalline, amorphous and nano-quasicrystalline structures" *Acta Materialia* 57 (2009) 3810-3822

18. Crossland, A.C., Thompson, G.E., Smith, C.J.E., Habazaki, H., Shimizu, K., Skeldon, P. "Formation of manganese-rich layers during anodizing of Al-Mn alloys" *Corros. Sci.* 41 (1999) 2053-2069

19. Taheri, M., Kish, J. R., Birbilis, N., Danaie, M., McNally, E. A., McDermid, J. R. "Towards a Physical Description for the Origin of Enhanced Catalytic Activity of Corroding Magnesium Surfaces" *Electrochimica Acta*, 116 (2014) 396-403.

20. Birbilis, N., Williams, G., Gusieva, K., Samaniego, A., Gibson, M. A., & McMurray, H. N. "Poisoning the corrosion of magnesium".*Electrochem. Commun.*, *34*,(2013) 295-298

21. X.J. Liu, I. Ohnuma, R. Kainuma, K. Ishida "Thermodynamic assessment of the aluminum-manganese (Al-Mn) binary phase diagram" *J. Phase Equil.* 20 (1999) 45-56

22. M.C. Merino, A. Pardo, R. Arrabal, S. Merino, P. Casajus, M. Mohedano "Influence of chloride ion concentration and temperature on the corrosion of Mg-Al alloys in salt fog" *Corros. Sci.* 52 (2010) 1696-1704

23. M. Pokova, M. Cieslar, J. Lacaze "TEM investigation of precipitation in Al-Mn alloys with addition of Zr" *Manuf. Tech.* 12 (2012) 212-217

24. Izquierdo, J., Nagy, L., Bitter, I., Souto, R.M., Nagy, G. "Potentiometric scanning electrochemical microscopy for the local characterization of the electrochemical behaviour of magnesium-based materials" *Electrochim. Acta* 87 (2013) 283-293

25. Moffat T.P., Stafford G.R., Hall D.E., "Pitting corrosion of electrodeposited aluminum-manganese alloys" *J. Electrochem. Soc.* 140 (1993) 2779-2786

26. Szklarska-Smialowska Z. "Pitting corrosion of aluminum" *Corros. Sci.* 41 (1999) 1743-1767

27. Vijh, A.K. "Electrolytic hydrogen evolution reaction on aluminum, oxide covered electrodes" *J. Phys. Chem.* 78 (1969) 506-513

28. Belanger, A., Vijh, A.K. "Hydrogen evolution reaction on vanadium, chromium, manganese and cobalt" *J. Electrochem. Soc.* 121 (1974) 225-230

29. Lunder, O., Aune, T.K., Nisancioglu, K. "Effect of Mn additions on the corrosion behaviour of mould-cast magnesium ASTM AZ91" *Corrosion* 43 (1987) 291-295

30. D.S. Gandel, M.A. Easton, M.A. Gibson, N. Birbilis 'Influence of Mn and Zr on the corrosion of Mg alloys: Part 1 – Impact of Mn and Zr on Mg alloy electrochemistry and corrosion" *Corrosion* 69 (2013) 744-751

31. R.C. Zeng, J. Zhang, W.J. Huang, W. Dietzel, K.U. Kainer, C. Blawert, W. Ke "Review of studies on corrosion of magnesium alloys" *Trans. Nonferrous. Met. Soc. China* 16 (2006) s763-s771

32. Pourbaix, M. (1974). "Atlas of electrochemical equilibria in aqueous solutions." National Association of Corrosion Engineers, 1974.

33. C.Yu, R.Wang, Y.Zhang and Y.Ding. "A general corrosion route to nanostructured metal oxides" Nanoscale 2 (2010) 906-909

34. D.S. Gandel, M.A. Easton, M.A. Gibson, N. Birbilis 'Influence of Mn and Zr on the corrosion of Mg alloys: Part 1 – Electrochemical behaviour of Mn and Zr" *Corrosion* 69 (2013) 666-671

35. Lide, D. R. (Ed.). (2004). *CRC Handbook of Chemistry and Physics 2004-2005: A Ready-Reference Book of Chemical and Physical Data*. CRC press.

36. M. Jönsson, D. Persson, R. Gubner, The Initial Steps of Atmospheric Corrosion on Magnesium Alloy AZ91D, *J. Electrochem. Soc.* 154 (2007) C684–C691

Chapter Six

The Influence of Microstructure on the Corrosion of Magnesium Alloy ZEK100

6.1 Introduction

Mg alloys are excellent candidates for inclusion in automobiles since they would reduce vehicle weight, leading to improved fuel efficiency and/or more viable electric vehicles. However, their use has been limited by their poor corrosion resistance [1-2]. With this application in mind, the corrosion behaviour of many common Mg alloys have been investigated [3], with considerable attention being paid to the AZ [4-6] and AM-series [7-11]. However, the use of these alloys in practical applications has been restricted due to their poor formability and ductility at room temperature [12]. The addition of rare earths (RE) to these alloys improves their castability, formability and resistance to creep [13] through refinement of the microstructure [14]. Included in this category of alloys with improved room temperature ductility is the Mg alloy ZEK100, which can be used in automobile applications for doors, decklids, liftgate inner panels and seat backs [15].

These improved mechanical properties have stimulated many studies on the various effects of RE's on the corrosion behaviour of Mg materials. La and Ce additions to the AM60 alloy improved its corrosion resistance by limiting the β-phase fraction and increasing the compactness of the corrosion product layer [16]. Their addition also improved the corrosion resistance of the AZ91 alloy [17]. While an increase in Gd content in a Mg-Y-Zr system induced a reduction in corrosion resistance [18], an improved resistance to stress corrosion cracking was achieved when Gd was combined with Nd and other rare earths. This improvement was attributed to the development of a

robust oxide/hydroxide layer [19]. Nd additions of < 0.8 wt% to AM50 and AZ91D alloys improved corrosion resistance through the suppression of microgalvanic coupling between secondary phases and the α-Mg matrix [20]. By contrast increasing the RE content (Ce, La, Nd) of the binary Mg-RE system caused a direct increase in corrosion rate [21].

Study of the corrosion behaviour of the ZEK100 alloy has so far been limited to biomedical applications [22-24]. In this study the role of alloying elements on the corrosion of ZEK100 has been investigated. In particular, the factors controlling the corrosion rate and distribution of corrosion damage have been investigated by comparing alloy behaviour in solutions with different chloride concentrations.

6.2 Experimental

6.2.1 Sample Preparation

Rolled ZEK100 alloy sheets were supplied by General Motors, Warren, MI. The sheets were cut into 1cm x 1cm x 2mm samples and threaded on one side to allow electrical connection to external circuitry via a steel rod. All samples were mounted in Struers EpoFix^{TM} so that only a single face of the sample was exposed to solution. The samples were ground with successive SiC papers of 800, 1200, 2400, 4000 grit and polished with a 3 µm diamond paste using ethanol/isopropanol as a lubricant. Samples were sonicated in methanol following each step. A final polish was applied using colloidal silica with ethylene glycol as a lubricant. Following this treatment the sample was sonicated in methanol and dried in an Ar gas stream.

6.2.2 Instrumentation

Scanning electron microscopy (SEM) was performed in either secondary electron (SE) or back scattered electron (BSE) mode using either a LEO 440, Hitachi 3400-N Variable Pressure Scanning Electron Microscope or a LEO 1540 XB SEM/FIB. X-ray energy dispersive spectroscopy (XEDS) maps were obtained using Quartz One software®. Confocal laser scanning microscopy (CLSM) was performed on a Zeiss 510 confocal microscope equipped with a HeNe 633 nm laser. The sample surface was suspended downward facing the inverted objective. Optical stereo micrographs were collected using a Zeiss Lunar V12 microscope equipped with an Axio 1.1 camera.

6.2.3 Electrochemical Measurements

Electrochemical measurements were performed in a standard three-electrode glass cell with a saturated calomel reference electrode (SCE) and a Pt-plate counter electrode. Solutions were prepared using reagent grade NaCl (99% Assay, Caledon) and NanoPure™ water (18.2 MΩ-cm).

Electrochemical control was provided by a Solartron 1480 MultiStat®. Potentiodynamic polarization (PDP) scans were performed after first allowing the sample to acquire a stable corrosion potential (E_{CORR}) for 1 h and then scanning the potential at 0.167 mV/s from 150 mV below the E_{CORR} to either -1.2 V or until a current density of 1 mA/cm^2 was reached. This current maximum was set to limit damage to the sample surface.

6.2.4 Intermittent Immersion Experiments

Polished ZEK100 samples were first imaged with SEM/XEDS to locate an area of interest (AOI) whose position was then recorded relative to a scratch at the edge of the sample surface. Immersions were performed in naturally aerated 1.6 wt% NaCl, 0.16 wt% NaCl, and NanoPure^{TM} water by suspending the polished surface in the solution using a stainless steel rod. Following 24 h of exposure, the sample was removed, rinsed with NanoPure^{TM} water and dried in an Ar stream. The AOI was located and imaged by SEM and CLSM, and then re-immersed in the solution for a further exposure period. A series of such immersions followed by imaging was performed. On completion of this series the accumulated corrosion product was removed through a 20 s immersion in gently agitated 1 M CrO_3. Focused-ion beam (FIB) analyses of the samples were performed using a Ga ion beam on a LEO 1540 XB SEM/FIB.

6.3 Results

6.3.1 Surface Imaging

An AOI on the polished ZEK100 surface is shown in the SEM micrograph in Figure 6.1 (a), along with the corresponding XEDS maps for Mg (Figure 6.1(b)), Zn (Figure 6.1 (c)) and Zr (Figure 6.1 (d)). Mg is seen to be uniformly distributed. The many small secondary features could not be resolved at this magnification in the Zn and Zr maps, except for a single Zr intermetallic (marked with a blue arrow) in the top left of the AOI. A second intermetallic particle is marked in Figure 6.1 (a) by a red arrow.

Further analyses of these particles revealed differences in their composition. Figure 6.2 (a) shows the SEM micrograph of the particle marked with a blue arrow in Figure 6.1(a). Two sites were analyzed by XEDS: Site 1 outside the particle and Site 2

within it. The XEDS spectra in Figure 6.2 (c), show the matrix (Site 1) was dominantly Mg, while the particle at Site 2 was comprised of Zr. The SEM micrograph of the particle marked with the red arrow in Figure 6.1 (a) is shown in Figure 6.2 (b), and the XEDS spectrum reveals that it contains Zn and Nd. This composition is confirmed in the XEDS maps shown in Figure 6.3, which show the apparent absence of Mg (Figure 6.3 (b)), and the coexistence of Nd (Figure 6.3 (c)) and Zn (Figure 6.3 (d)). This particle is likely the T-phase (Mg_7Zn_3RE) which has been identified as present in RE-containing Mg-Zn alloys [25]. Despite the apparent absence of a Mg signal in the XEDS maps,

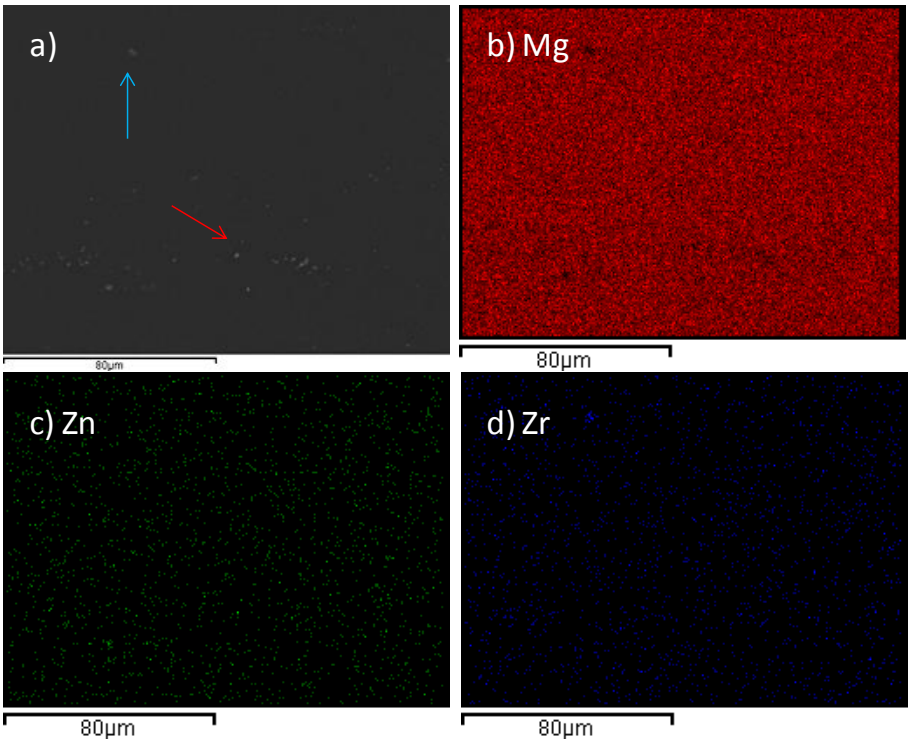

Figure 6. 1 - a) BSE SEM micrographs of the ZEK 100 surface. An intermetallic particle is marked with the red arrow. The corresponding XEDS maps for b) Mg, c) Zn, d) Zr.

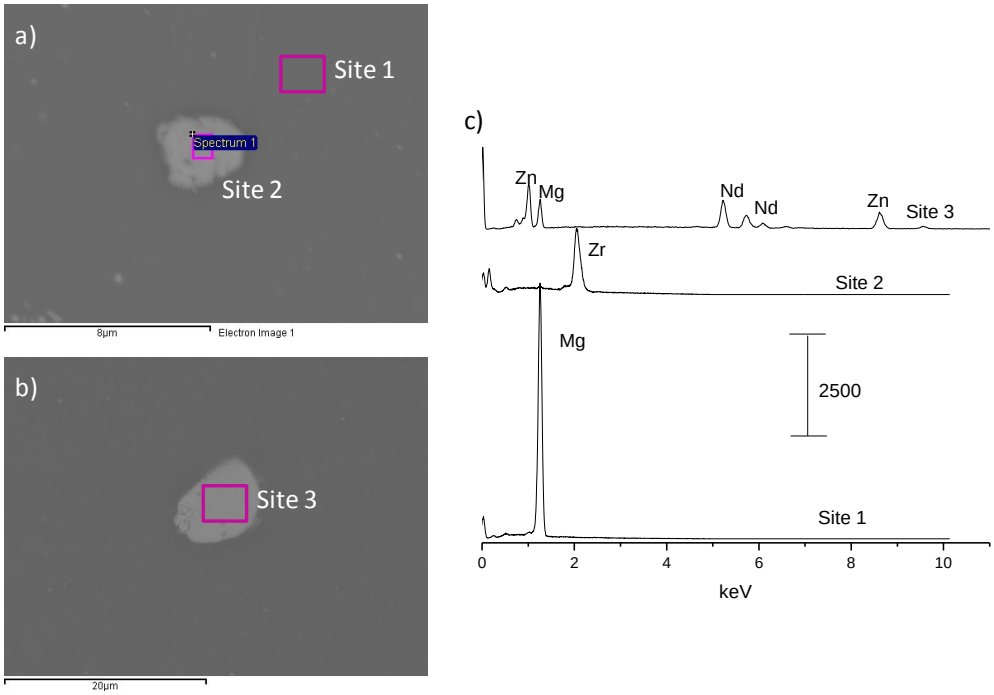

Figure 6. 2 - a) SEM micrographs of the particle marked by the blue arrow in Figure 1a), b) SEM micrograph of the particle marked with the red arrow in Figure 1a); and c) the XEDS spot analysis of the corresponding areas marked in the SEM images.

Figure 6.3 (b), the presence of Mg is clearly indicated in the XEDS spectrum for this site shown in Figure 6.2 (c).

6.*3.2 Electrochemical Effect of Chloride Ion Concentration*

The effect of varying the chloride ion concentration of the solution on the electrochemical behaviour of ZEK100 was studied using PDP measurements, Figure 6.4. While the cathodic behaviour was only marginally influenced by the chloride concentration, significant differences in anodic behaviour are observed. In 1.6 wt% NaCl, an increase in current density occurred at -1.55V almost immediately after the net current becomes anodic at -1.57 V, indicating rapid oxide/hydroxide breakdown and the establishment of an extremely active surface. On reducing the chloride content to 0.16 wt% NaCl, similar behaviour, but with a slightly decreased reactivity is observed, film breakdown leading to an extremely reactive surface not being established until the potential exceeded -1.48 V. When the chloride concentration is further reduced to 0.016 wt% NaCl, a significant potential range within which the alloy is partially protected is observed, and the establishment of a reactive surface is delayed until the potential is > -1.38 V. In addition the magnitude of the active current (i.e., the current observed at potentials positive to the breakdown potential) is significantly reduced as the chloride concentration is decreased.

6.*3.3 Intermittent Immersions in Chloride Solutions*

Figure 6.5 shows SEM micrographs of the heavily damaged ZEK100 surface following two consecutive 24 h immersions in 1.6 wt% NaCl. Due to the extensive corrosion, 1.6 wt% NaCl is too aggressive a solution to allow study of the behaviour of

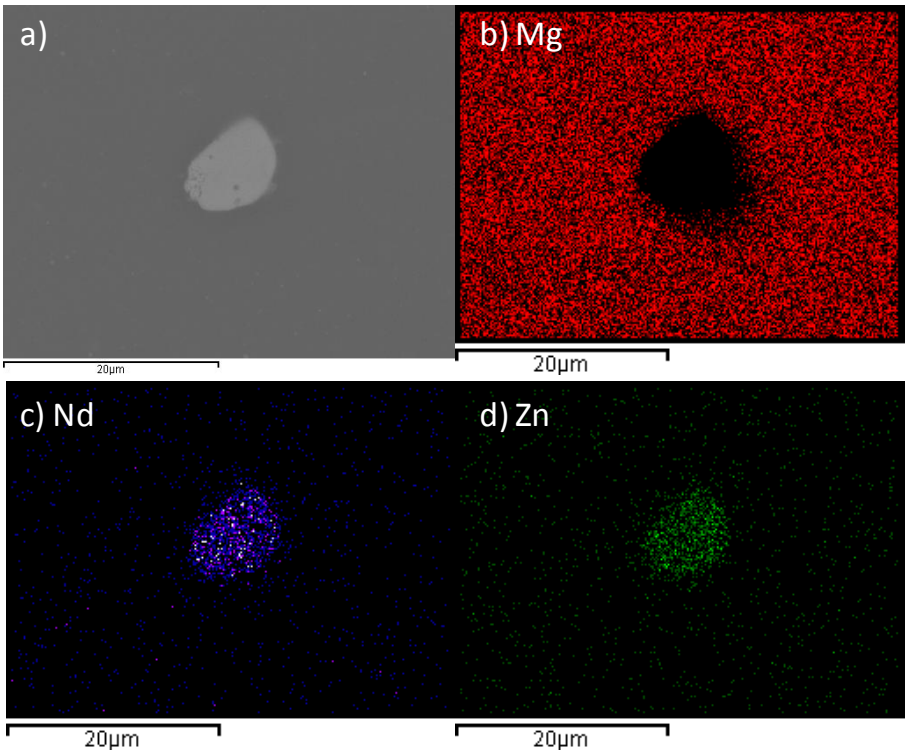

Figure 6. 3 - a) BSE SEM micrograph of the particle in Figure 2 (b) and the corresponding XEDS maps for b) Mg, c) Nd and d) Zn.

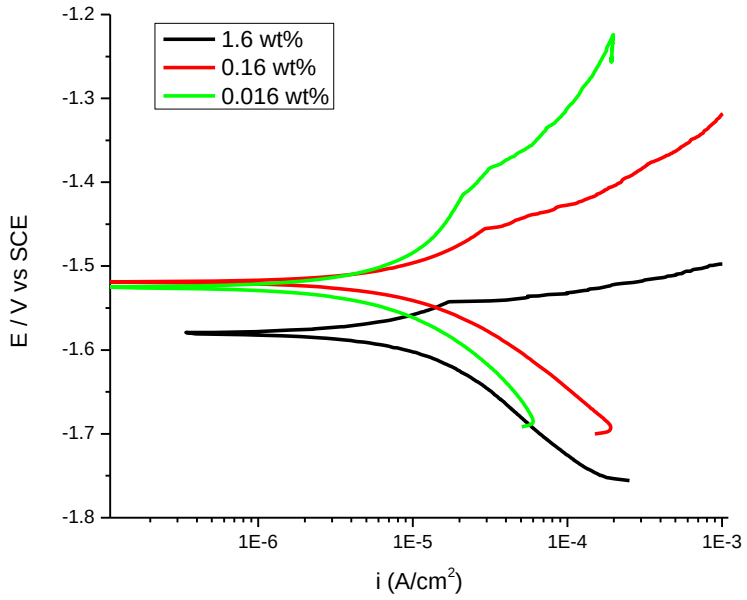

Figure 6. 4 – Potentiodynamic polarization scans recorded on a freshly polished ZEK100 sample at a scan rate of 0.167 mV/s following 1 h at E_{CORR} in 1.6 wt% NaCl (black), 0.16 wt% NaCl (red) and 0.016 wt% NaCl.

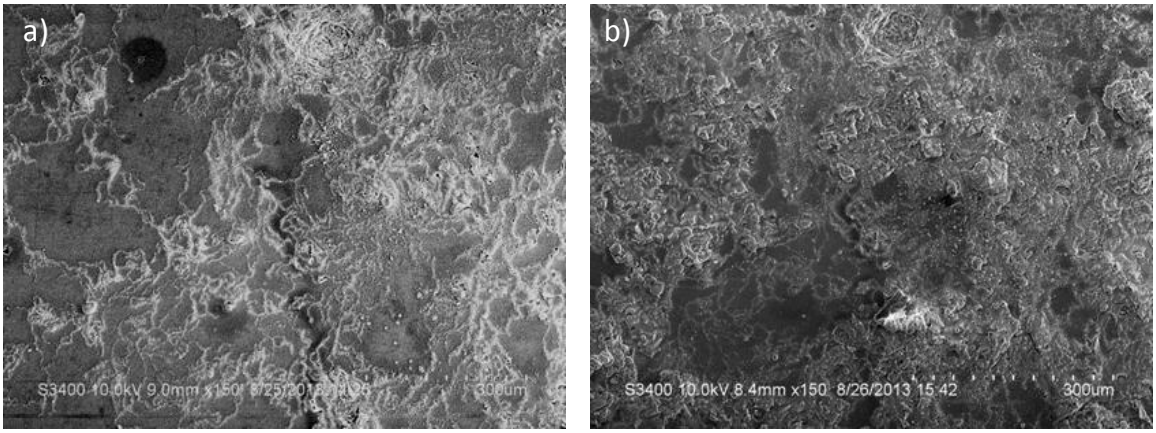

Figure 6. 5 - SE SEM micrographs of a ZEK100 sample following a) 24 h, and b) 48 h immersions in a 1.6 wt% NaCl solution.

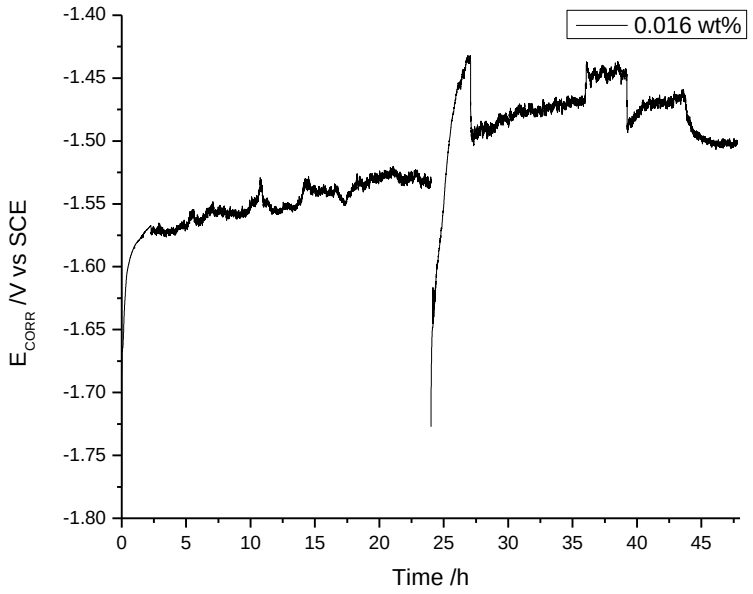

Figure 6. 6 - Evolution of E_{CORR} recorded on a ZEK100 sample in a 0.16 wt% NaCl solution. At 24 h the sample was removed for analysis, and then re-immersed again in a new solution for an additional 24 h.

the microstructural constituents. A 0.16 wt% NaCl solution was, therefore, used in subsequent experiments.

The evolution of the E_{CORR} measured on ZEK100 over two 24 h immersions in 0.16 wt% NaCl is shown in Figure 6.6. During the first immersion, E_{CORR} rose rapidly over the first 2 h to -1.57 V, and then steadily increased to -1.55 V after 24 h. The noise associated with the measurement is likely due to the localized activity of the ZEK100 sample. After 24 h, the sample was removed for further analysis of the AOI. On re-immersion, E_{CORR} again rose rapidly to -1.45 V at 27h. The subsequent sharp drop in E_{CORR} indicates the re-establishment of active conditions, possibly due to the breakdown of a thin oxide formed on air exposure between the two immersion periods.

Figure 6.7 shows the corroded surface after the two 24 h immersion periods (Figure 6.6). SEM micrographs of the polished ZEK100 surface are shown in Figure 6.7 (a) and Figure 6.7 (d). The red arrow in Figure 6.7 (a) indicates the location of two particles which act as reference points when re-viewing the area after corrosion. Following 24 h of immersion in the 0.16 wt% NaCl solution, the AOI was again located and SEM micrographs are shown in Figure 6.7 (b) and Figure 6.7 (e). Corrosion damage was observed to track along the grain boundaries of the sample, running laterally along the rolling direction of the alloy. Following the second 24 h immersion period, the corrosion damage was still predominantly associated with the grain boundaries, but had spread only slightly into the α-matrix, Figures 6.7 (e) and 6.7 (f).

The 3-dimensional propagation of corrosion damage is best appreciated in CLSM micrographs, Figure 6.8. The grain boundary attack was evident after the 24 h

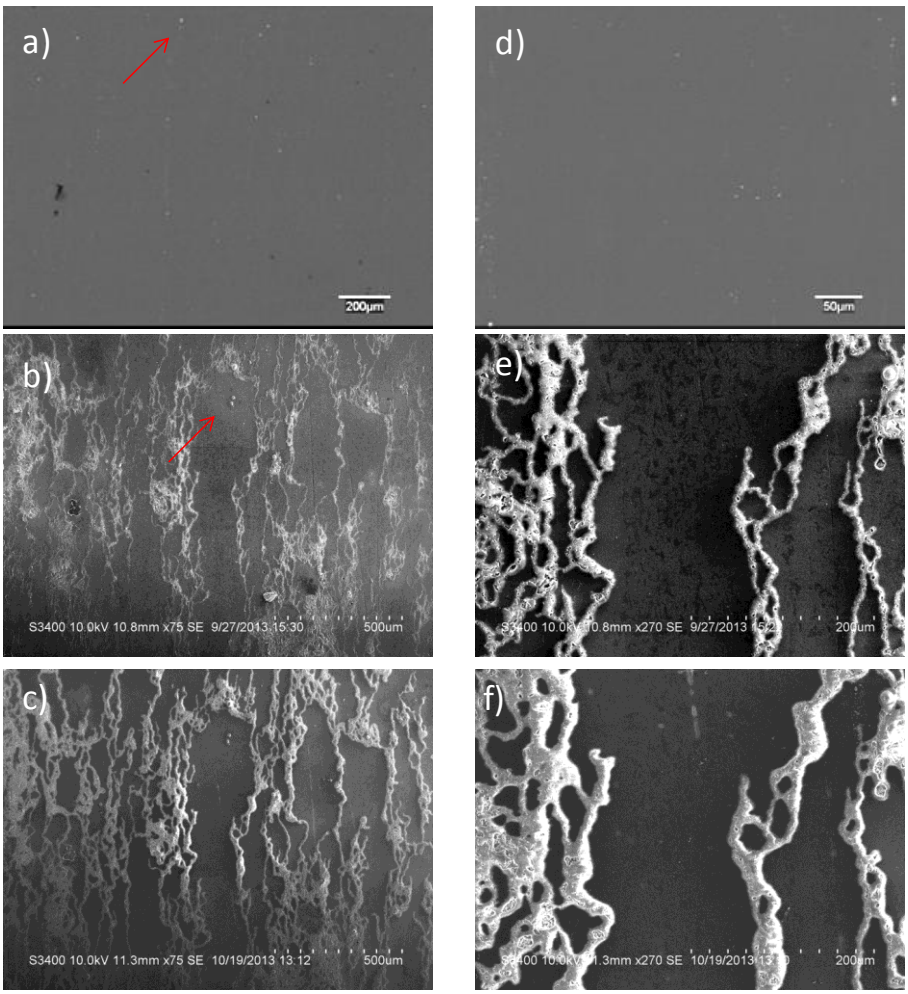

Figure 6. 7 - SEM micrographs of a selected area of interest on a ZEK100 sample: a) and d) original polished surface after 24 h of immersion (b) and e)) and 48 h of immersion (c) and f)) in a 0.16 wt% NaCl solution. The red arrows are reference points for two particles present in the AOI.

immersion, Figure 6.8 (a), and its limited spread into the α-Mg grains after 48 h of immersion can be seen in Figure 6.8 (b). In these micrographs, the dark regions correspond to the locations of corrosion product which, due to its random, porous structure, scatters rather than reflects the laser beam. An improved perception of corrosion depth is apparent in the 3D CLSM reconstruction of the surface shown in Figure 6.8 (c), although scattering is still blocking analysis of the true extent of the damage. Removal of the corrosion product by treatment with chromic acid reveals more clearly the extent of corrosion damage, Figure 6.8 (d). This micrograph shows propagation into the sample occurs, most deeply in the grain boundaries initially observed to corrode, Figure 6.8 (a).

The resulting damage morphology in the grain boundary regions is seen in the SEM micrographs in Figure 6.9. Figure 6.9 (a) shows a corroded grain boundary region covered with protruding corrosion product following 48 h of immersion in 0.16 wt% NaCl. When the corrosion product was removed, Figure 6.9 (b), the damage was seen to have propagated by tunneling along the boundaries, possibly by the coalescence of pits as previously claimed for the ZE41 alloy [26]. Some general, but shallow, damage occurred on the top surfaces which remained generally intact. Figure 6.9 (c) shows that corrosion penetration into the alloy was limited to a depth between 2 and 5 μm and occurred primarily in the centre of the boundary.

The corrosion of Mg alloys is strongly supported by microgalvanic coupling to secondary phases and it has been suggested that active cathodes can be identified by their tendency to accumulate corrosion product domes of $Mg(OH)_2$ [27]. Figure 6.10 (a) shows such a corrosion product dome located within a corroded grain boundary following

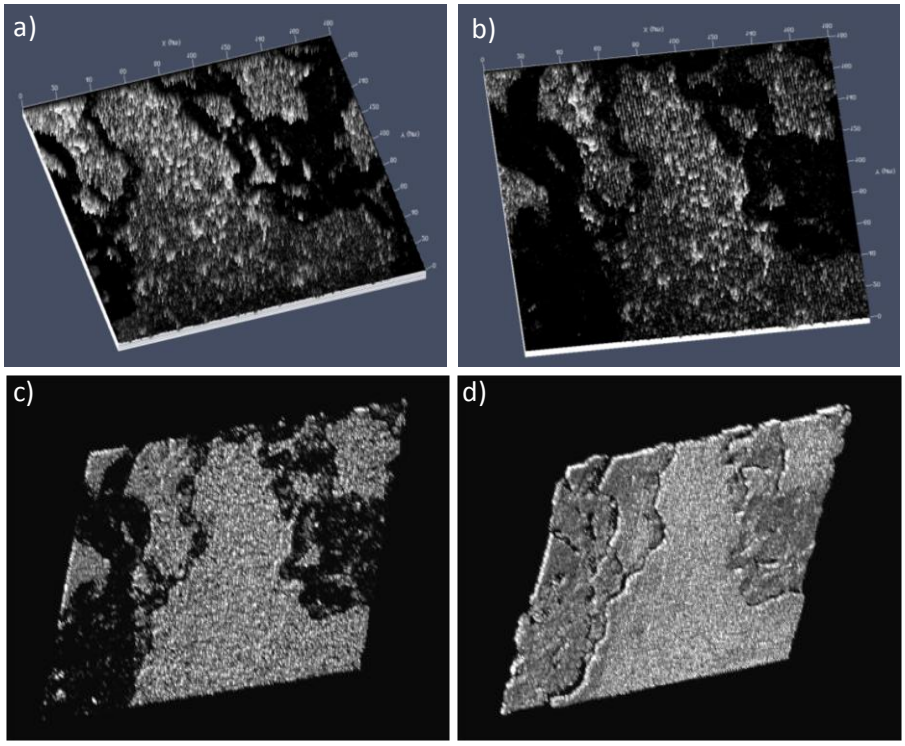

Figure 6. 8 - 2.5D CLSM micrographs of an AOI on the ZEK100 following a) 24 h and b) 48 h immersion in a 0.16 wt% NaCl solution. A3D CLSM reconstruction of the AOI following c) 48 h immersion in a 0.16 wt% NaCl solution and d) following a chrome treatment to remove corrosion product.

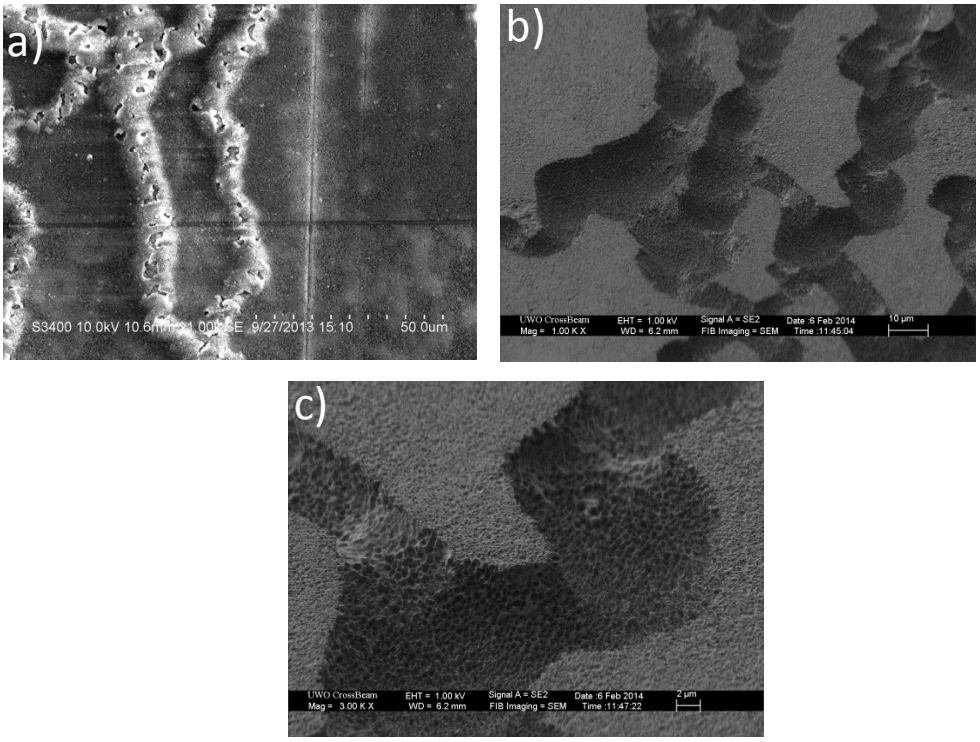

Figure 6. 9 – SE SEM micrographs of the ZEK100 sample surface after 48 h of immersion in a 0.16 wt% NaCl solution showing a) the grain boundary regions filled with corrosion product, b) following removal of the corrosion product, c) magnified image of the corroded grain boundary.

48 h of corrosion in 0.16 wt% NaCl. When the corrosion product was removed, the particles on which it had accumulated could be seen, Figure 6.10 (b). XEDS mapping shows the presence of two Zn-Nd particles (labelled 1 and 2), Figure 6.10 (c) and Figure 6.10 (d), and a Zr particle contaminated with Fe (labelled 3) , Figure 6.10 (e) and Figure 6.10 (f).

Short term immersions in the 0.16 wt% NaCl solution yielded further insight into the function of active cathodes in the early stages of corrosion. Figure 6.11(a) shows two particles located on the ZEK100 surface prior to immersion. The small particle on the left is pure Zr as identified in the XEDS map of Zr, Figure 6.11 (c), and no Fe can be detected in this particle, Figure 6.11 (d). The larger particle on the right contains Nd, Figure 6.11 (e), and Zn, Figure 6.11 (f), and minor amounts of Fe, Figure 6.11(d). Re-examination after 6 h of immersion in 0.16 wt% NaCl showed that neither of these particles accumulated a dome of corrosion product indicating cathodic activity, Figure 6.12 (a). On a different region of the surface, Figure 6.12 (b), corrosion product domes indicating cathodic activity are observed. XEDS mapping of the domed structure (marked with the red box in (b)) Figure 6.12 (c) revealed Zr, Figure 6.12 (e), and Fe, Figure 6.12 (f), located below the accumulated corrosion product. The weak Mg signal from the dome structure, Figure 6.12 (d), which is comprised of $MgO/Mg(OH)_2$, can be attributed to the low density of the corrosion product , and the comparative strength of the Mg signal from the adjacent alloy surface.

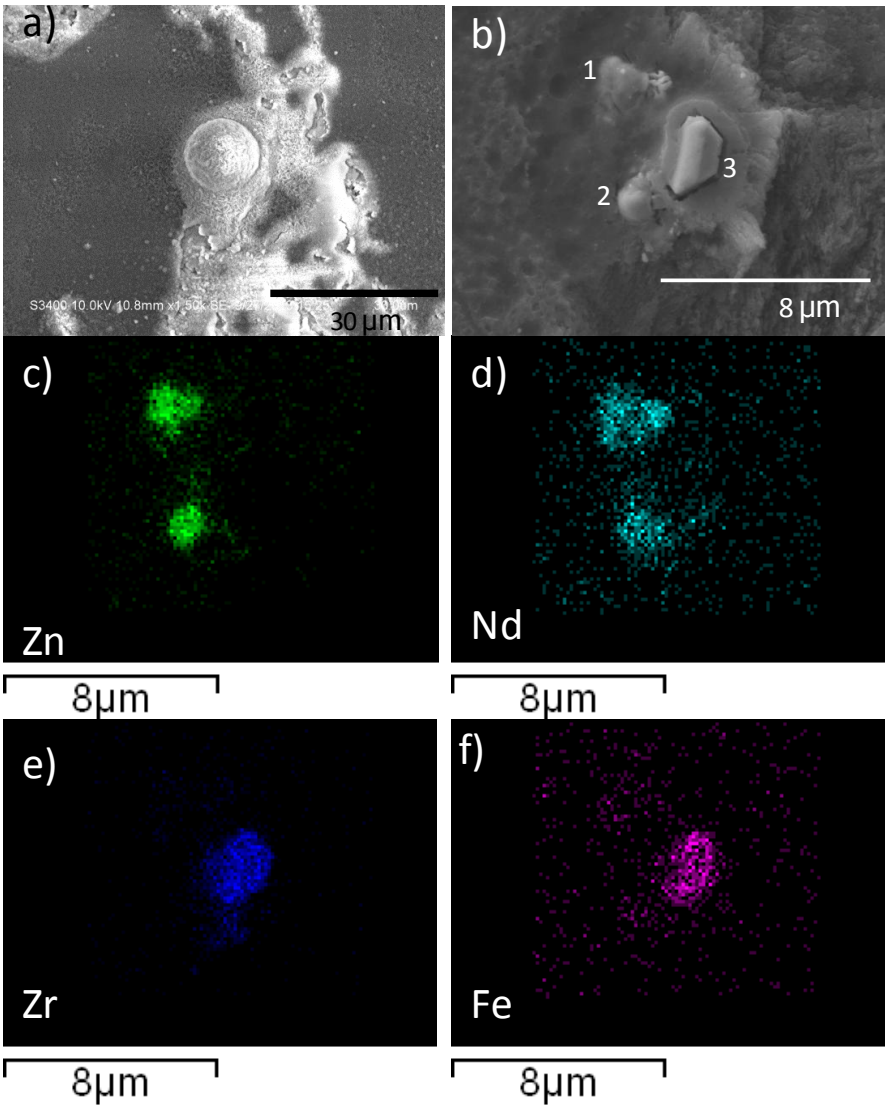

Figure 6. 10 - SE SEM micrograph of a) a corrosion product dome present on the ZEK100 after 48 h corrosion in a 0.16wt% NaCl solution, and b) following removal of the corrosion product showing the particles beneath the deposit: XEDS maps for c) Zn, d) Nd, e) Zr, f) Fe

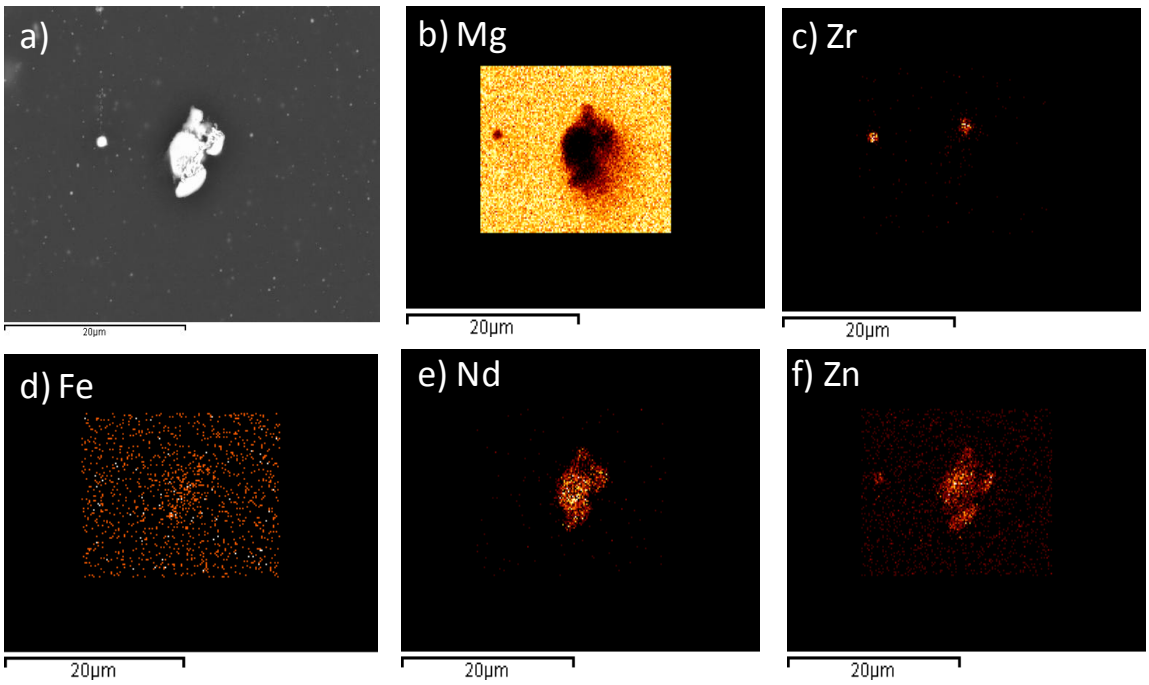

Figure 6. 11 - a) SEM image of two particles on the ZEK100 surface prior to corrosion and the corresponding XEDS maps for b) Mg, c) Zr, d) Fe, e) Nd, f) Zn.

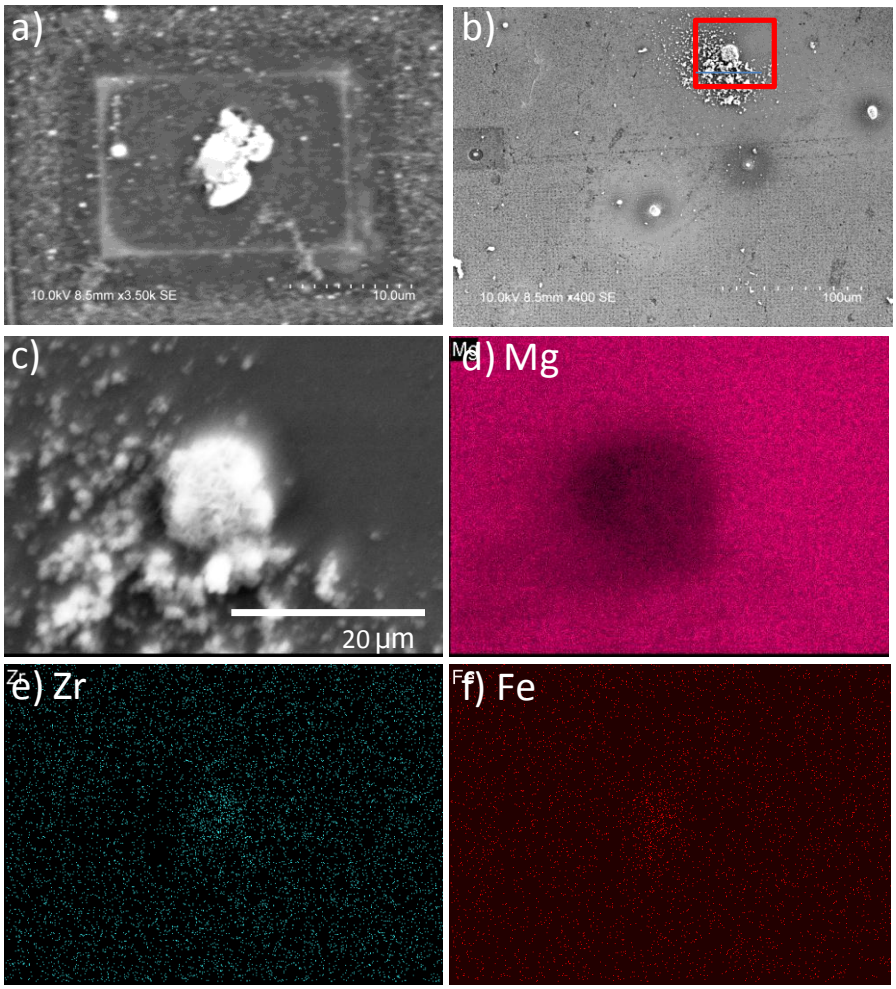

Figure 6. 12 – a) SE SEM micrograph of the particles shown in Figure 11 following 6 h of immersion in a 0.16 wt% NaCl solution, b)SE SEM micrograph of the cathodic sites on the same sample after 6 h of immersion, c) dome of corrosion product indicating cathodic behaviour of the particle shown in the red box in (b): and the corresponding XEDS maps of the site for d) Mg, e) Zr, f) Fe.

6.*3.4 Intermittent Immersions in Pure Water*

To avoid the extensive propagation of corrosion damage a series of consecutive exposures to NanoPure™ water were conducted over a total exposure period of 192 h, Figure 6.13. Within the selected AOI, Figure 6.13 (a), three distinct intermetallic particles were recognizable as bright spots. These particles were covered with corrosion product indicating cathodic activity, as shown for the bottom particle in Figure 6.13 (e). As expected, very little damage to the bulk surface was observed, and no grain boundary damage was sustained. After 48 h of immersion, the bulk surface displays minor accumulation of corrosion product, Figure 6.13 (f), while after 96 h of immersion, more significant morphological changes were observed, Figure 6.13 (c) and Figure 6.13 (g). Rings of corrosion damage, located around the particles, and slight cracking of the corrosion product at the outer edges of these regions had occurred. The bulk surface developed some topographical texture as corrosion product accumulated over the whole surface. After 192 h of immersion, sufficient corrosion product had accumulated on the surface for cracks to appear when the sample was removed from the cell and dried. The corrosion product domes remained intact over the particles. In addition, there was no clear evolution in either the size or morphology of the particle shown in Figure 6.13 ((e) to (h)) suggesting the corrosion product dome formed rapidly and did not grow as corrosion progressed.

Figure 6.14 (a) shows a BSE SEM micrograph of the ZEK100 surface following 192 h of immersion in water. The white areas in the image are the secondary phases (particles) on the alloy surface. The two particles located in the top right corner of the images had accumulated corrosion product zones indicating cathodic activity while the

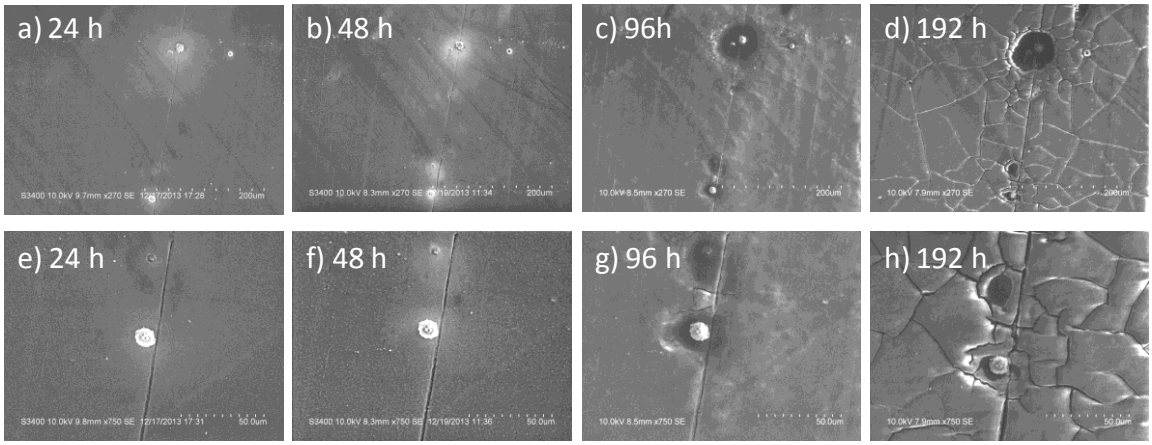

Figure 6. 13 – The progress of corrosion of on a ZEK100 sample in NanoPure^{TM} water monitored by SEM showing an AOI after a) 24 h, b) 48 h, c) 96 h, d) 192 h: the progress of corrosion around the particle at the bottom of the AOI after e) 24 h, f) 48 h, g) 96 h, h) 192 h of immersion.

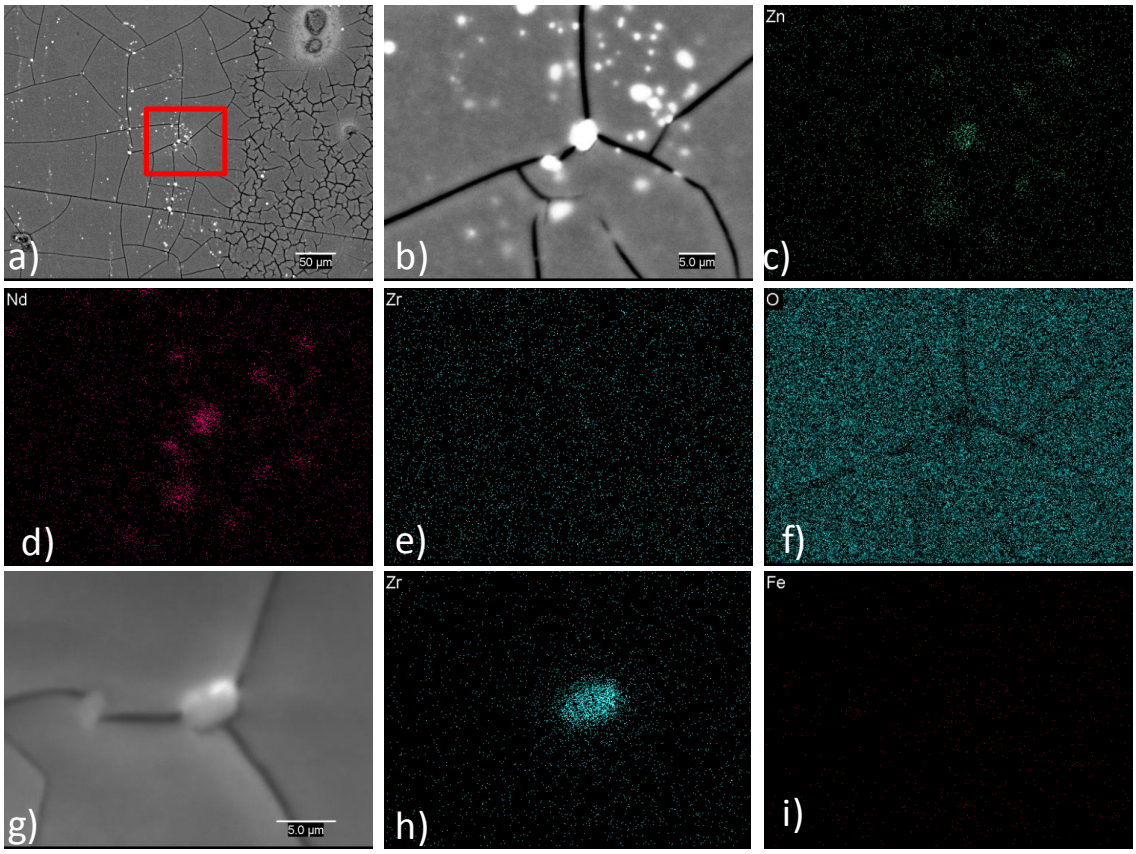

Figure 6. 14 – a) BSE SEM micrograph of the ZEK 100 surface after 192 h of immersion in water, b) BSE SEM micrograph of the area marked with the red box in (a) and the corresponding XEDS maps for c) Zn, d) Nd, e) Zr and f) O, g) SE SEM micrograph of a separate particle on the ZEK100 surface and its corresponding XEDS maps for h) Zr and i) Fe.

majority of particles on the surface had not. A magnified view of the particles located within the red box in Figure 6.14 (a) is shown in the SEM micrograph in Figure 6.14 (b), and XEDS analyses shows the presence of Zn and Nd, Figure 6.14 ((c) and (d)) suggesting they are the T-phase. Additionally, this area is free of Zr, Figure 6.14 (e). The absence of any enhanced XEDS signal for O on these particles compared to the surrounding surface is consistent with the absence of any corrosion product deposits. Analysis of a separate particle on the surface, also free of corrosion product, Figure 6.14 (g), showed it to be Zr, Figure 6.14 (h), with no detectable Fe content, Figure 6.14 (i).

A particle which did accumulate a corrosion product dome following 192 h of exposure in water was FIB cross-sectioned, Figure 6.15 (a). A cracked ring of corrosion damage was visible surrounding the particle. At a location 0.25d in from the edge of the dome (d is the diameter of the dome) damage had penetrated up to 4-5 μm into the alloy and the corroded location was filled with dense corrosion product, Figure 6.15(b). At 0.45d a second damaged location was detected, Figure 6.15 (c). The maximum height of the dome is ~ 8-10μm compared with a general depth of corrosion product of 1-2 μm on the adjacent surface just beyond the edge of the dome, Figure 6.15 (c). A particle is also observed, marked with a red arrow in Figure 6.15 (d), at the bridge between two corroded regions, which XEDS, Figure 6.15 (e), shows was composed of Zr with some Fe.

These results show that, in the absence of chloride, corrosion damage on ZEK100 was confined to locations near active cathodic sites, while in the presence of chloride propagation occurs along grain boundaries. The stereomicrographs in Figure 6.16 illustrate the differences in these general patterns. Figure 6.16 (a) shows the ZEK100 surface following 24 h of exposure in 0.16 wt% NaCl when corrosion can be seen to have

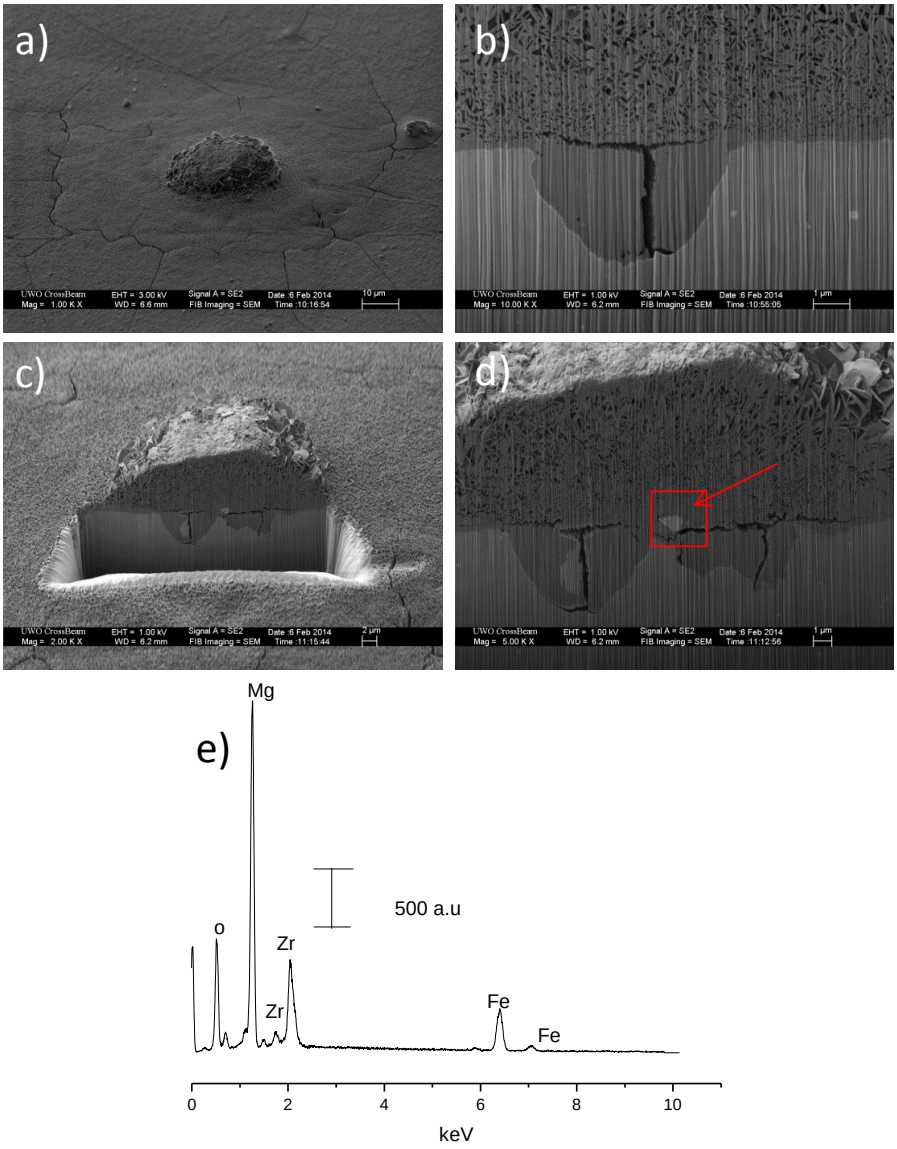

Figure 6. 15 – a) SE SEM micrograph of a corrosion product dome on the surface of the ZEK100 sample after 192 h of immersion in NanoPure water: b) SE SEM micrograph of a FIB cross at ¼ depth into the dome, c) FIB cross section at a location deeper into the dome; d) SEM image revealing particle below corrosion product dome (marked with red arrow), e) XEDS spectrum of the region marked with the red box in d).

tracked along the alloy surface. By contrast, in the absence of chloride, Figure 6.16 (b), damage remains isolated near secondary phases on the ZEK100 surface. Additionally, the bright spots in Figure 6.16 (b) clearly show the general distribution of a large number of intermetallic particles (secondary phases) with overlapping zones of corrosion linking closely located particles. Additionally, of the particles available on the alloy surface only a relatively small fraction have stimulated microgalvanic corrosion.

6.4 Discussion

The ZEK100 alloy was found to be a dominantly α-Mg matrix containing a wide dispersion of Zr intermetallic particles and a Mg-Zn-Nd secondary phase, most likely the T-phase (Mg_7Zn_3RE) which has been shown to be present in the ZE41 alloy [25,26]. In contrast to ZEK100, the latter alloy contains considerably more RE, and especially Zn, leading to the separation of extended T-phase ligaments along grain boundaries.

As observed previously for the ZE41 alloy the rate and extent of corrosion decreased as the chloride concentration decreases. The PDP curves in Figure 6.4 show this was predominantly an anodic effect, the cathodic kinetics of water reduction being only marginally influenced. In 1.6 wt% NaCl, any protection from corrosion by a surface film was marginal, rapid breakdown being observed at potentials only a few mV anodic of E_{CORR}, Figure 6.4. This inability to provide protection was confirmed by the SEM micrographs in Figure 6.5 which show generally distributed corrosion damage after 24h and 48h of exposure to this solution.

Reducing the chloride concentration to 0.16wt% extended the partially protective properties of the film to ~ -1.48V and a further reduction to 0.016 wt% to ~ -1.40V. The

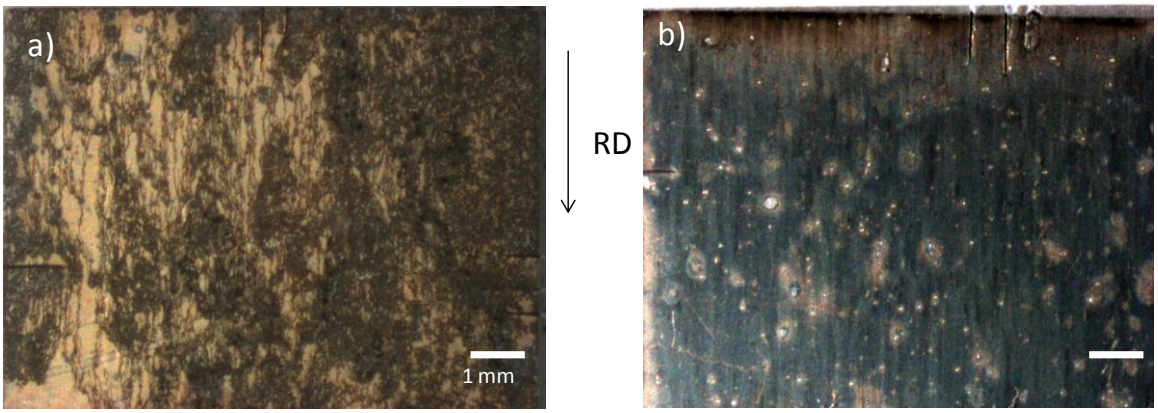

Figure 6. 16 – Stereo micrographs comparing the bulk corrosion damage on the ZEK100 following a) 24 h of exposure in 0.16wt% NaCl and b) 192 h of exposure in NanoPure™ water. The rolling direction (RD) of the samples is indicated with the arrow.

E_{CORR} measured during exposure to 0.16 wt% NaCl was generally below the breakdown potential measured in the PDP scan although it steadily increased towards this value over the two 24 h exposure periods. Commonly, an E_{CORR} less than the film breakdown potential would indicate metastable localized corrosion. Consistent with this expectation, general corrosion of the surface was not observed, corrosion damage being restricted to the grain boundaries with only slight propagation into the grains. The increase in E_{CORR} with time then reflected the increased area of the surface exposed.

Corrosion preferentially within grain boundaries has been reported previously for Mg-Zn-RE alloys and attributed to the presence in the boundaries of the T-phase and the depletion of alloying elements at grain boundaries housing this phase [25]. In the ZK60 alloy, containing Zn and Zr without REs, grain boundary attack was linked to the presence of Mg-Zn precipitates and the depletion of Zn in the grain boundary regions. A similar grain boundary depletion could account for the distribution of damage observed here on the ZEK100 alloy, with the tracks of corrosion damage interlinking the secondary phase particles dispersed throughout the alloy.

The presence and distribution of Zr in Mg alloys has been shown to significantly influence the corrosion kinetics of Mg alloys, the overall effect appearing to be significantly influenced by the size and distribution of Zr particles. When finely distributed these particles appear to produce a more robust and protective oxide [28,29]. However, it has been claimed that, due to their cathodic nature [30] they can accelerate cathode kinetics [31] leading to deep corrosion in regions with higher Zr content [26]. Zr and Nd together are added as grain refiners with the general claim that Zr has a negative

effect on corrosion while Nd reduces the cathodic activity of the phase which hosts it [32].

In the presence of chloride both T-phase and Zr particles were located in the corroded grain boundaries with Zr particles containing Fe appearing to be the dominant microgalvanically-coupled cathodes. By initiating corrosion in pure water it was possible to limit the extent of corrosion damage due to this coupling to the vicinity of the coupled cathodes. Over the 192 h total exposure period employed in these experiments minimal general corrosion damage occurred, only 1 to 2 μm of corrosion product accumulating on the alloy surface, leading to the cracks observed on removing the electrode from the cell and drying it. In addition small zones of corrosion around intermetallic particles enabled actively functioning cathodes to be separated from inert particles.

While Zn-Nd particles were clearly identified on the alloy surface they did not accumulate corrosion product deposits or small encircling corrosion zones indicating they were generally inactive. In addition many Zr particles were identified but only those containing Fe were observed to accumulate the corrosion product confirming their cathodic activity. These observations were consistent with those made in the chloride solution, and demonstrate that the dominant cathodes are the Fe-contaminated Zr particles. Based on these observations and the available published literature, limiting the size and controlling the distribution and purity of Zr particles would be an effective way to mitigate micro-galvanically coupled cathodic behaviour.

While chloride is well known to enhance localized corrosion on passive alloys as described in the point defect model [33], this is unlikely to be the key effect on the

ZEK100 alloy since Mg alloys can never be considered passive in aqueous environments. Grain boundaries in Mg-Zn-RE-Zr systems have been noted to be depleted in Zn [34] and would be expected to be the locations most anodically susceptible in a similar manner to Al-depleted areas on the surface of AM50 alloys which experienced the highest degree of corrosion [35]. Given the wide dispersion and close proximity of particles in ZEK100 alloys even the limited reactivity of Mg in pure water might have been expected to lead to interlinked grain boundary corrosion. However, if active cathodes are limited to a smaller number of widely separated Zr/Fe particles then this would prove difficult as indicated in Figure 16 which shows only minor interlinking of corroded locations is achieved, at least on the limited time scale of this experiment.

6.5 Summary and Conclusions

The ZEK100 alloy has been shown to be a basically α-Mg alloy containing a wide dispersion of secondary phases predominantly the T-phase and Zr particles. In contrast to the ZE41 alloy, which has a considerably higher Zn and RE content, these particles are fine and extensive grain boundary ligaments of the T-phase are not observed. The distribution of corrosion damage was shown to depend on the chloride concentration. In concentrated solutions corrosion damage was general and universally distributed across the alloy surface. At lower concentrations damage was confined to the grain boundaries and appeared to track in the rolling direction interlnking the network of secondary phases many of which supported corrosion by acting as microgalvanically-coupled cathodes. Three distinct types of secondary phase particles were identified and characterized; the T-phase, Zr and Fe-containing Zr. Of these the Fe-containing Zr was the most active cathode sustaining water reduction. This was most clearly shown in corrosion

experiments in pure water, when the lack of solution conductivity confined corrosion to a small region in the vicinity of the active cathodes. This work investigated the corrosion of ZEK100 in varying chloride contents and NanoPure^{TM} water. Zr-rich particles contaminated with Fe were identified as strong cathodes in microgalvanic coupling driving the corrosion process. In water, corrosion damage is most present localized near the cathodic sites, while in chloride damage is most heavily seen on the grain boundaries. Increasing chloride content increased the corrosion rate of the ZEK100, likely through improving the conductivity of solution and improving the range of cathodes to microgalvanically couple.

6.6 References

1. M. K. Kulecki, Magnesium and its alloys application in automotive industry *Int. J Adv Manuf Tech*, 39 (2008) 851-865
2. G. Song "Recent progress in corrosion and protection of magnesium alloys" *Adv. Eng. Mat.* 7 (2005) 563-586
3. E. Ghali, W. Dietzel, K. Kainer "General and localized corrosion of magnesium alloys: A critical review" *J. Mat. Eng. Perform.* 22 (2013) 2875-2891
4. G. Song, A. Atrens, X. Wu, B. Zhang "Corrosion behaviour of AZ21, AZ501 and AZ91 in sodium chloride"
5. G. Song, Z. Xu "The surface, microstructure and corrosion of magnesium alloy AZ31 sheet" *Corros. Sci.* 55 (2010) 4148-4161
6. T. Kawamura, S. Sunada, H. Notoya, K. Kondo, K. Majima "Influence of Al content on corrosion characteristics of AZ series Mg alloys" *J. Japan. Inst. Metals* 72 (2008) 216-223

7. H. Matsubara, Y. Ichige, K. Fujita, H. Nishiyama, K. Hodouchi "Effect of Fe impurity on corrosion behaviour of AM50 and AM60 magnesium alloys" *Corros. Sci.* 66 (2013) 203-210
8. D. Sachdeva "Insights into microstructure based corrosion mechanism of high pressure die cast AM50 alloy" *Corros. Sci.* 60 (2012) 18-31
9. W. Liu, F. Cao, A. Chen, L. Chang, J. Zhang, C. Cao "Effect of chloride ion concentration on electrochemical behaviour and corrosion product of AM60 magnesium alloy in aqueous solutions" *Corrosion* 68 (2012)
10. H. Martin, R. Alvarez, J. Danzy, M. Horstemeyer, P. Wang "Quantification of corrosion pitting under immersion and salt spray environments of an as-cast AM60 magnesium alloy" *Corrosion* 68 (2012) 571-585
11. W. Song, H. martin, A. Hicks, D. Seely, C. Walton, W. Lawrimore II, P. Wang, M. Horstemeyer "Corrosion behaviour of extruded AM30 magnesium alloy under salt-spray and immersion environments" *Corros. Sci.* 78 (2014) 353-368
12. S. Kurukuri, A. Bardelcik, M. Worswick, R. Mishra, J. Carter "High strain rate characterization of ZEK100 magnesium rolled alloy sheet" *EPJ-Proc. Of DYMAT 2012* 2012
13. M.B. Kannan, W. Dietzel, C. Blawert, A. Atrens, P. Lyon "Stress corrosion cracking of rare-earth containing magnesium alloys Z41, QE22 and Elektron 21 (EV31A) compared with AZ80" *Mat. Sci. Eng. A* 480 (2008) 529-539
14. Y. Wang, G. Wu, W. Liu, S. Pang, Y. Zhang, W. Ding "Effects of chemical composition on the microstructure properties of gravity cast Mg-xZn-yRE-Zr alloy" *Mat. Sci. Eng. A* 594 (2014) 52-61

15. J. Min, L. Hector Jr., J. Lin, J. Carter "Analytical method for forming limit diagram prediction with application to a magnesium ZEK100-0 alloy' *J. Mat. Eng. Perform.* 22 (2013) 3324-3336

16. W. Liu, F. Cao, L. Chang, Z. Zhang, J. Zhang "Effect of rare earth element Ce and La on corrosion behaviour of AM60 magnesium alloy" *Corros. Sci.* 51 (2009) 1334-1343

17. G. Wu, Y. Fan, H. Gao, C. Zhai, Y. Zhu "The effect of Ca and rare earth elements on the microstructure, mechanical properties and corrosion behaviour of AZ91D" *Mat. Sci. Eng. A* 408 (2005) 255-263

18. J. Chang, X. Guo, S. He, P. Fu, L. Peng, W. Ding "Investigation of the corrosion for Mg-xGd-3Y-0.4Zr alloys in a peak aged condition" *Corros. Sci* 50 (2008) 166-177

19. B. Padekar, R. Singh Raman, V. Raja, L. Paul "Stress corrosion cracking of a recent rare-earth containing magnesium alloy, EV31A, and a common Al-containing alloy, AZ91E" *Corros. Sci.* 71 (2013) 1-9

20. R. Arrabal, A. Pardo, M. Merino, M. Mohedano, P. Casajus, K. Paucar, G. Garces "Effect of Nd on the corrosion behaviour of AM50 and AZ91D magnesium alloys in 3.5 wt% NaCl solution" *Corros. Sci.* 55 (2012) 301-312

21. N. Birbilis, M. Easton, A. Sudholz, S. Zhu, M. Gibson "On the corrosion of binary magnesium-rare earth alloys" *Corros. Sci.* 51 (2009) 683-689

22. T. Huehnerschulte, N. Angrisani, D. Rittershaus, D. Bormann, H. Windhagen, A. Meyer-Lindenberg "In vivo corrosion of two novel magnesium alloys ZEK100

and AX30 and their mechanical suitability as biodegradable implants" *Materials* 4 (2011) 1144-1167

23. H. Waizy, A. Weizbauer, C. Modrejewski, F. Witte, H. Windhagen, A. Lucas, M. Kieke, B. Denkena, P. Behrens, A. Meyer-Lindberg, F.W. Bach, F. Thorey "In vitro corrosion of ZEK100 plates in Hank's balanced salt solution" *Biomed. Eng. Online* 11 (2012) 1-14
24. D. Dziuba, A. Meyer-Lindberger, J. Seitz, H. Waizy, N. Angrisani, J. Reifenrath "Long-term in vivo degradation behaviour and biocompatibility of the magnesium alloy ZEK100 for use as a biodegradable bone implant" *Acta Biomaterialia* 9 (2013) 8548-8560
25. A. Coy, F. Viejo, P. Skeldon, G. Thompson "Susceptibility of rare-earth-magnesium alloys to micro-galvanic corrosion" *Corros. Sci.* 52 (2010) 3896-3906
26. W. Neil, M. Forsyth, P. Howlett, C. Hutchinson, B. Hinton "Corrosion of magnesium alloy ZE41- The role of microstructural features" *Corros. Sci.* 51 (2009) 387-394
27. M. Danaie, R.M. Asmussen, P. Jakupi, D.Shoesmith, G. Botton "The Cathodic behaviour of Al-Mn precipitates during atmospheric and saline aqueous corrosion of a sand-cast AM50 alloy" *Corros. Sci. Accepted* 83 (2014) 299-309
28. G. Ben-Hamu, D. Eliezer, K.S. Shin, S. Cohen, *J. Alloys and Compounds* 431 (2007) 269–276.
29. J.W. Chang, X.W. Guo, P.H. Fu, L.M. Peng, W, J. Ding, *Trans. Nonferrous Metals Soc. China* 17 (2007) 1152–1157.

30. M. Sun, G. Wu, W. Wang, W. Ding "Effect of Zr on the microstructure, mechanical properties and corrosion resistance of Mg-10Gd-Y magnesium alloy" *Mat. Sci. Eng. A* 523 (2009) 145-151

31. D. Gandel, M. Easton, M. Gibson, T. Abbott, N. Birbilis "The influence of zirconium additions on the corrosion of magnesium" *Corros. Sci.* 81 (2014) 27-35

32. J. Chang, J. Duo, Y. Xiang, H. Yang, W. Ding, Y. Peng "Influence of Nd and Y additions on the corrosion behaviour of extruded Mg-Zn-Zr alloys" *Int. J. Miner. Metallurgy and Mat.* 18 (2011) 203-209

33. L.F. Lin, C.Y. Chao, D.D. Macdonald "A point defect model for anodic passive films – II Chemical breakdown and pit initiation" *J. Electrochem. Soc.*128 (1981) 1194-1198

34. R. Zeng, K.U. Kainer, C. Blawert, W. Dietzel "Corrosion of an extruded magnesium alloy ZK60 component – The role of microstructural features" *J. Alloys and Compounds* 509 (2011) 4462-4469

35. R.M. Asmussen, P. Jakupi, M. Danaie, G. Botton, D.W. Shoesmith "Tracking the corrosion of magnesium sand cast AM50 alloys in chloride environments" *Corrosion Science*, 75 (2013) 114-122

Chapter Seven

Sacrificial Anode and Cathodic Protection of Mg Alloys

7.1 Introduction

Mg alloys have long been sought after for automotive applications due to their high strength to weight ratio and good castability [1]. AM50 magnesium alloys have attracted interest for such applications, and, thus, its corrosion behaviour has been previously investigated [2-7] However, the high corrosion rates experienced by Mg alloys have limited their application [8]. Many approaches to protecting Mg alloys have been sought including conversion coatings [9], organic coatings [10], electroplating [11], cold spray coating [12], anodizing [13], sol-gel fabricated coatings [14], ionic liquids [15] and many other coatings [16]. In addition, a number of alloying elements have also shown to improve corrosion resistance including Al [7, 17], Zr [18], and Zn [19].

With their low nobility compared to other metals Al, Zn and Mg are good candidates for use as sacrificial anode materials. Al and Zn anodes have been used most prominently due to their high current efficiency, while Mg is preferred in high resistivity environments [20]. Examples exist outside of these environments with Mg-based materials having been shown to be effective coatings to protect carbon steel [21] and as anodes in simulated backfill [22]. Contrarily, Mg was found to be ineffective in the protection of muffler materials in simulated automotive environments due to its high consumption rate [23].

An interesting scenario is plausible in the cathodic protection of Mg alloys using Mg. Yu and Uan demonstrated a thin film of Mg was able to protect an AZ91 substrate [24]. Mg rich primers have also been successful in the cathodic protection of their Mg

substrates [25-27]. Due to their alloying additions, the Mg alloys will be nobler than pure Mg and the potential for cathodic protection exists.

This chapter focuses on the application of this cathodic protection effect on AM50 Mg alloys using high purity Mg. The magnitude of the current passed between the materials was used to electrochemically simulate the protective effect Mg would have on the die cast AM50 alloys in chloride environments.

7.2 Experimental

7.2.1 Sample Preparation

AM50 sand cast, graphite cast and die cast alloys were supplied by GM (Canada). The sand and graphite cast rods were machined into 1 × 1 × 0.7 cm electrodes. Die cast AM50 alloy 1 × 1 × 0.2 cm electrodes were machined from a 0.2 cm thick plate. High purity Mg (99.9%) (Sigma Aldrich Canada) was machined into 1 × 1 × 1 cm electrodes and 1.4 cm diameter circular electrodes. One side of the sample was tapped to accommodate a threaded steel rod to allow for electrical contact to external circuitry. All samples were mounted in Struers EpoFix epoxy to limit exposure to solution to one face of the sample.

The samples were ground successively up to 4000 SiC grit. An equal volume mixture of ethanol and propanol was also used as a lubricant on the 4000 SiC pad, and water used as lubricant on the other pads . The ground surface was then polished on a Struers DP-Dur cloth saturated in 3 µm Struers DP-Suspension A for 5 to 10 min. The ethanol/propanol mixture was used as a lubricant. The final polishing step was performed, for 2-3 min, on a Struers OP-Chem cloth using an equal volume mixture of

Struers OP-S Suspension and ethylene glycol. If necessary, ethylene glycol was used as a lubricant. The polished sample was rinsed and sonicated in anhydrous ethanol for 2 min and air dried in a desiccator.

7.2.2 *Microscopy*

Electron micrographs were recorded in back-scattered (BSE) and secondary electron (SE) modes using a LEO 440 and a Hitachi 3400-N Variable Pressure Scanning Electron Microscope. Optical micrographs were collected using a Zeiss Lunar V12 microscope equipped with an Axio 1.1 camera.

7.2.3 Galvanic Coupling Experiments

Prior to solution exposure, all samples were polished according to the procedure described in section 2.1. All experiments were preformed in aerated 1.6 wt% NaCl (reagent grade, 99% assay) solutions at 23 °C ± 2 °C. The polished surface was suspended in the solution using a steel rod. The samples to be coupled were suspended in a glass cell with their centres 10 cm apart. The galvanic current was measured using a Keithley 6514 Zero Resistance Ammeter with a software interface (written in-house) used for data collection. The samples were exposed for a known time, and then removed from the solution, rinsed with NanoPure water (18 MΩ - cm) and dried in a stream of Ar.

7.2.4 *Galvanostatic Control*

Galvanostatically controlled experiments were preformed in a standard three electrode cell filled with 1.6 wt% NaCl employing a Pt mesh counter electrode and a saturated calomel reference electrode (SCE). All samples were polished (as described in section 2.1) prior to immersion. Upon exposure to solution, the samples were left at open

circuit for 5 min followed by application of a cathodic current to the alloy sample. Currents ranging from -0.1 μA to -100 μA were applied to the 1 cm^2 electrodes for times ranging from 48 h to 400 h. On completion of an experiment samples were rinsed with NanoPure water (18 MΩ-cm) and dried in a stream of Ar.

7.3 Results

7.3.1 AM50 Alloy Coupled to Pure Mg

Figure 7.1 displays the current-time plots for the sand, graphite and die cast AM50 alloys galvanically coupled to Mg in 1.6 wt% NaCl with the current recorded at the Mg working electrode. For all three galvanic couples, the current increased over the first hour, and then steadily decreased for a short period before eventually exhibiting a longer transient peak. Eventually steady currents were established with values in the order: graphite cast (~30 μA) > die cast (~25 μA) > sand cast (~15 μA). The damage accumulated on the Mg anode is shown in the inset of Figure 7.1. The heavier damage is observed on the left side of the sample, which was, as expected, the edge nearest to the AM50 coupled electrode.

The net anodic currents measured at the Mg electrode surface are equal, and opposite in sign to the net cathodic current passed on the AM50 surface. The influence of galvanic coupling to the AM50 alloy can be seen in the stereomicrographs in Figure 7.2. Figures 7.2 (a) – (c) display the AM50 alloy surfaces following 48 h of uncoupled immersion in 1.6 wt % NaCl. On the sand cast AM50, Figure 7.2 (a), and graphite cast AM50, Figure 7.2 (b), extensive corrosion accumulated on the upper half of the sample. On the die cast AM50, Figure 7.3 (c), corrosion propagated laterally along the alloy surface leaving behind damage tracks. These damage profiles were consistent with those

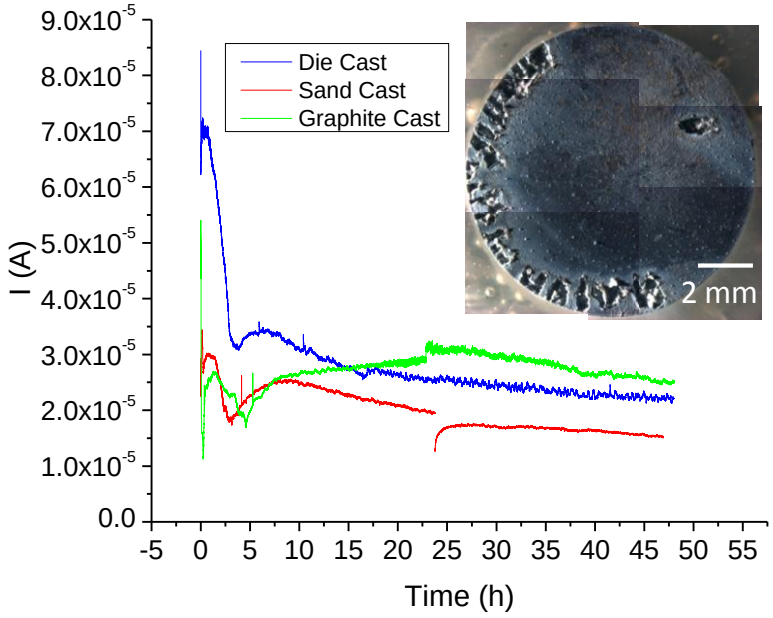

Figure 7. 1 - Coupling current-time profiles measured on a galvanic couple between pure Mg and sand cast (red), graphite cast (green) and die cast (blue) AM50 alloys. The Mg surface served as the working electrode and the corrosion damage accumulated is shown in the inset.

reported previously for the different AM50 alloy casts in chloride environments [28]. When coupled to Mg in 1.6 wt% NaCl solution, stark differences in the extent of surface damage were evident, Figure 2 (d) – (f). On the sand cast, Figure 7.2 (d), graphite cast, Figure 7.2 (e), and die cast, Figure 7.2 (f), no evidence of heavily damaged areas was seen after 48 h of galvanic coupling to Mg. While the AM50 alloys do not retain their pristine polished surfaces, propagation of extensive corrosion was mitigated through coupling to Mg.

7.3.2 Chronopotentiometric Control of Die Cast AM50 Corrosion

In the coupled experiments, currents between 15 µA and 30 µA were measured between the 1 cm^2 electrodes, with these currents being sufficient to inhibit extensive damage to the AM50 surface. To further investigate the behaviour observed in the galvanic coupling experiments, the die cast AM50 was studied under chonopotentiometric control. Selected current densities were applied to the AM50 die cast electrode in 1.6 wt% NaCl for 96 h durations and the resulting potential-time plots are displayed in Figure 7.3. When -100 µA/cm^2 was applied to the die cast AM50, an initial sharp increase in potential from -1.69 V to -1.62 V was observed followed by a consistent slow decrease to -1.66 V after 85 h. A subsequent increase in potential and rapid decrease was then observed before a final potential of -1.71 V was established after 96 h. Lowering the applied current density to -1 µA/cm^2 yielded a less negative applied potential to the die cast AM50. In the initial 5 h the potential decreased only slightly from -1.52 V to -1.53 V. Subsequently, the potential rose again, but only slowly to a value of -1.52 V after 96 h. A similar potential profile was produced when a current of -0.1 µA/cm^2 was applied. The initial potential rose from -1.57 V to -1.53 V.

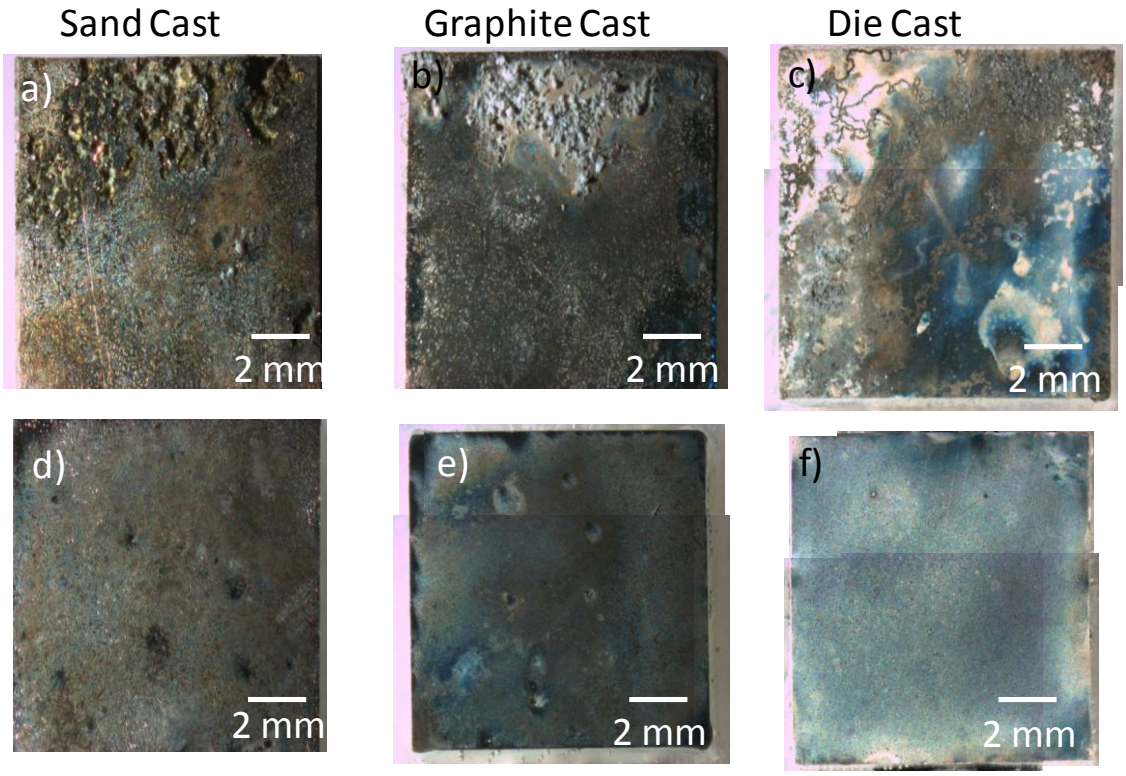

Figure 7. 2 - Stereomicrographs showing the distribution of corrosion damage following a 48 h immersion uncoupled in a1.6 wt% NaCl solution of a) sand cast , b) graphite cast , c) die cast AM50 alloys and following 48 h of galvanic coupling of the d) sand cast, e) graphite cast and f) die cast AM50 alloys to pure Mg

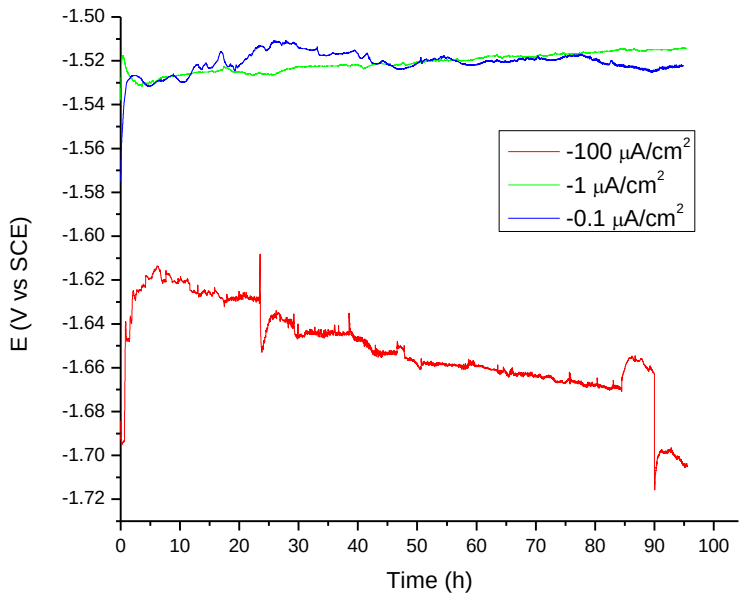

Figure 7. 3 - Chronopotentiometric profiles recorded on the die cast AM5O in a 1.6 wt% NaCI solution with applied cathodic current densities of -100 μA/cm^2 (red), -1 μA/cm^2 (green) and -0.1 μA/cm^2 (blue).

Subsequently, several fluctuations were observed between -1.53 V and -1.52 V up to 40 h, beyond which the potential remained effectively constant. A final value of -1.53 V was achieved after 96 h.

Stereomicrographs of the die cast AM50 surface following the 96 h chronopotentiometric experiments are shown in Figure 7.4. Figure 7.4 (a) shows the alloy surface following the 96 h immersion in 1.6 wt% NaCl solution without applied current or potential. Several tracks of corrosion damage can be seen having propagated laterally across the AM50 surface. Following application of -100 $\mu A/cm^2$ very little damage is observed and no corrosion tracks are seen, Figure 7.4 (b). The feature extending from the bottom left is a reflection from a surface stain. In Figure 7.4 (c) the surface of the alloy following the -1$\mu A/cm^2$ chronopotentiometric experiment had a less reflective surface than that after the -100 $\mu A/cm^2$ experiment, Figure 7.4 (b). The left and bottom edge of the sample were slightly scratched to improve conductivity of the surface and improve SEM imaging. No corrosion tracks are observed on the alloy after the chronopotentiometric experiment at -0.1 $\mu A/cm^2$, Figure 7.4 (d).

The alloy surfaces in Figure 7.4 (c) and Figure 7.4 (d) show some discolouration consistent with the accumulation of corrosion product which can be seen in the SEM micrographs in Figure 7.5. Figure 7.5 (a) shows the nature of corrosion damage sustained by the alloy under natural corrosion conditions in a 1.6 wt% NaCl solution. After the chronopotentiometric experiment at -1 $\mu A/cm^2$, some corresponding minor corrosion damage is observed, Figure 7.5 (b). Similar small amounts of surface damage with a similar damage morphology was observed on the alloy when a current of - 0.1 $\mu A/cm^2$ was applied, Figure 7.5 (c). The application of a cathodic current does not

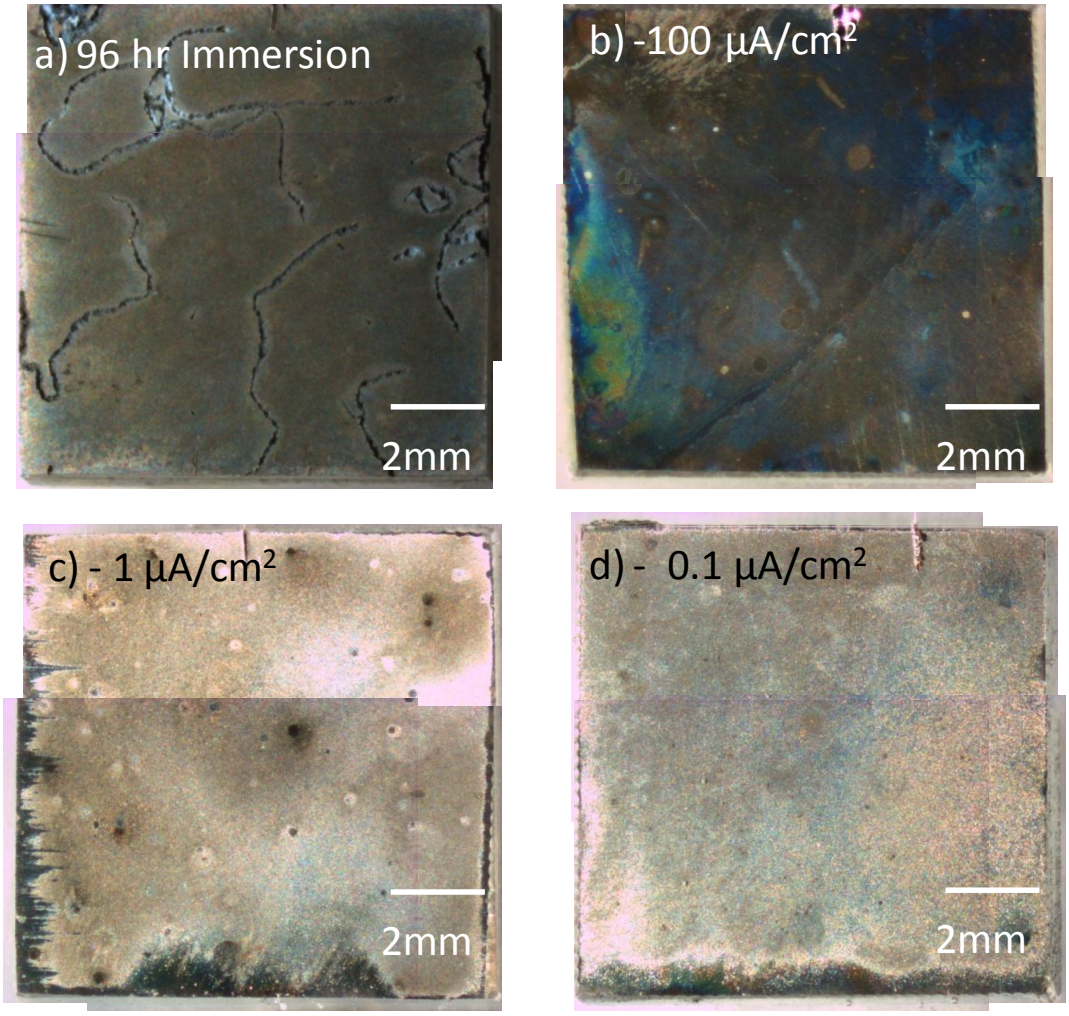

Figure 7. 4 - Stereomicrographs of the die cast AM50 alloy following 96 h of immersion in a1.6 wt % NaCl solution: a) immersion with no electrochemical control, b) -100 $\mu A/cm^2$, c) -1 $\mu A/cm^2$ and d) -0.1 $\mu A/cm^2$ applied cathodic currents.

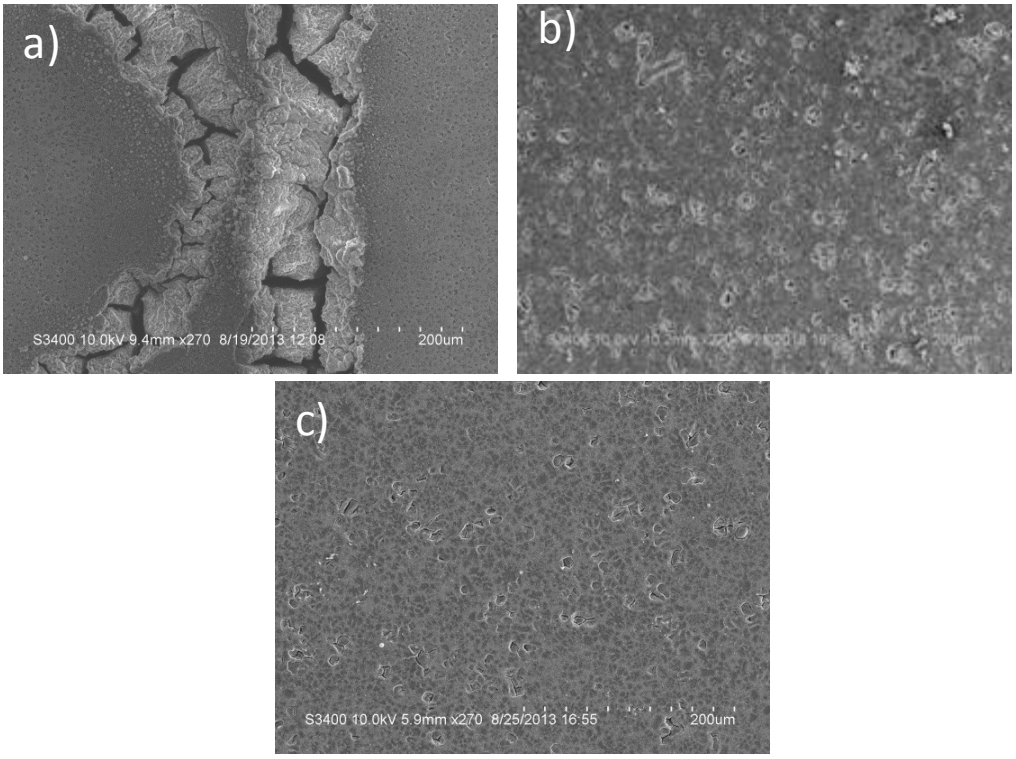

Figure 7. 5 - SEM micrographs of die cast AM 50 following 96 hr of immersion in a 1.6wt% NaCl solution: a) natural corrosion conditions; b) -1 $\mu A/cm^2$ cathodic current applied; c) -0.1 $\mu A/cm^2$ cathodic current applied.

completely arrest corrosion of the alloy, but the onset of major damage, such as that seen in Figure 7.5 (a) under natural corrosion conditions, is delayed.

With an applied current the possibility of the initiation of a significant corrosion event is decreased. However, as corrosion damage accumulates, the applied current may eventually be insufficient to oppose such an event. Longer immersion times with applied cathodic currents were investigated to determine the duration how long protection could be sustained at various currents. Figure 7.6 (a) first displays the E_{CORR} of the freely corroding alloy in 1.6 wt% NaCl (blue line). The E_{CORR} was between -1.53 V and -1.56 V and noisy over the full 200 h exposure period as new damage sites were initiated and corrosion spread over the surface rapidly. This continuous damage development is evident from the surface of the alloy shown in the stereomicrograph in Figure 7.6 (b). Several deep corrosion tracks were observed, and extensive corrosion damage had occurred in the top right quadrant of the sample. The potential measured when a current of -10 $\mu A/cm^2$ was applied to the alloy is shown also in Figure 7.6 (a) (red). Again the measured potential was in the range between -1.55 V and -1.54 V but considerable less noisy than observed for natural corrosion. At 162 h, a sharp decrease in potential occurred, after which the potential recovered slowly back to -1.54 V. This sharp drop in potential was likely the result of the onset of a significant corrosion initiation event on the alloy surface. The most likely location indicated with a red arrow in Figure 7.6 (c). The alloy surface appears similar to those shown in Figures 7.4 (c) and 7.4 (d), when no significant damage was observed. However, in this case a single track initiated in the top left quadrant, marked with a red arrow in Figure 7.6 (c) and shown in the magnified image in Figure 7.6 (d).

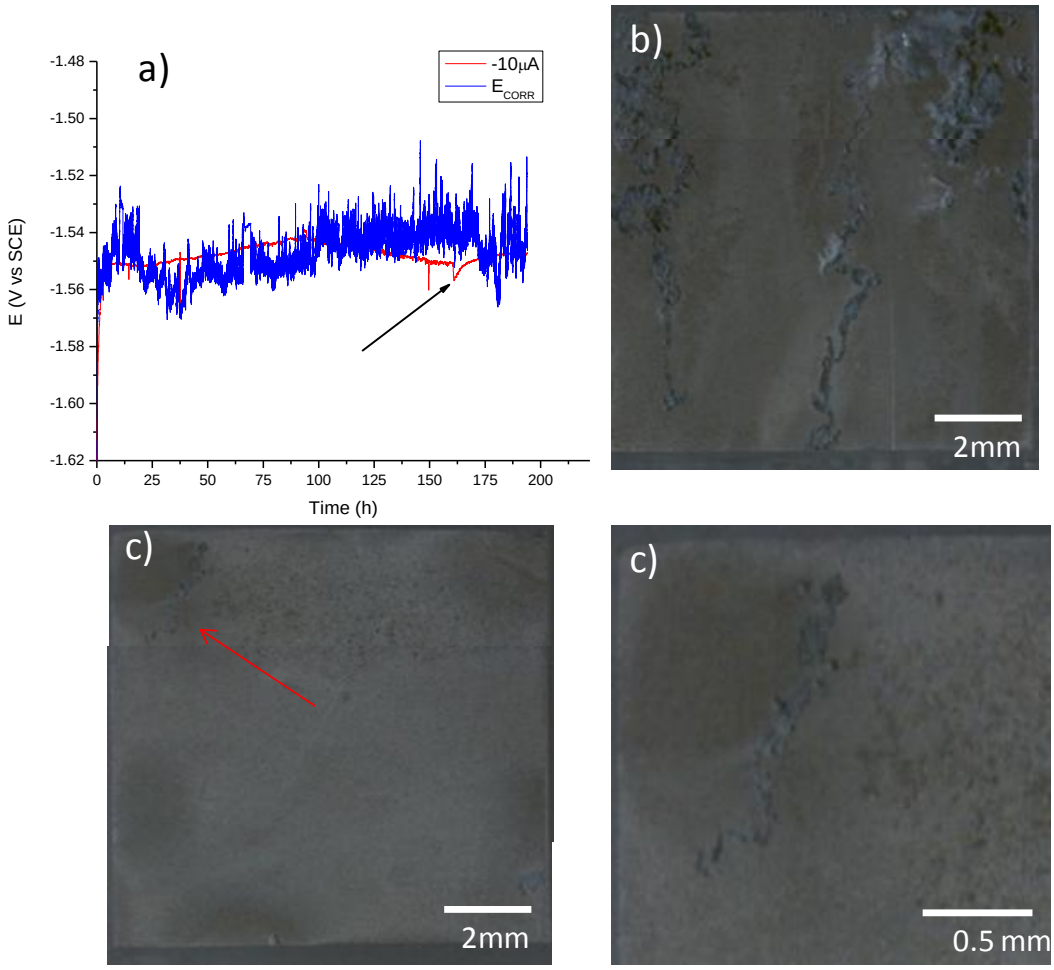

Figure 7. 6 - a) The progression of E_{CORR} on a die cast AM50 alloy (blue) and potential recorded with an applied current hold of -10 μA (red) in a 1.6 wt% NaCl solution. The black arrow marks the location of a significant corrosion event. Stereomicrographs showing the surface of die cast AM50 alloy after exposure at b) E_{CORR} and c) -10μA galvanostatic hold and d) magnified view of the corrosion track initiated.

The duration of the protective cathodic effect was also investigated at lower current densities. Figure 7.7 (a) shows the potential-time profile observed in a chronopotentiometric experiment at -1 $\mu A/cm^2$. The potential was observed to steadily increase from -1.55 V to -1.54 V after 110 h, after which the potential becomes noisy suggesting rapid corrosion is occurring as observed under rapid natural corrosion conditions (Figure 7.6 (a)). When a current of -0.1 $\mu A/cm^2$ is applied to the alloy, several rapid transients are observed, the base potential being ~ -1.55 V. These transients were to more negative potentials suggesting that major corrosion events are initiated but were stifled by the applied current. However, after 33 h the applied current was no longer sufficient to reverse these initiations and the measured potential became unstable, resembling that observed under freely corroding conditions.

7.4 Discussion

Due to the rapid nature of Mg alloy corrosion, exposure to a corrosive environment can lead to the immediate onset of extensive corrosion damage to the alloy leading to loss of structural integrity of the material. The suppression of extensive damage propagation on AM50 Mg alloys was investigated using two approaches: galvanic coupling of the alloy to pure Mg, and application of a net cathodic current to the alloy. The coupling of pure Mg to three casts of AM50 lead to net anodic currents at the Mg electrode in the order of: graphite cast > die cast > sand cast. Following a 48 h of galvanic coupling to pure Mg, no sign of extensive corrosion damage was observed on the alloy surfaces, suggesting Mg could be used as a sacrificial anode to protect a Mg alloy. Previous evidence shows deposition of thin layers of Mg materials on the surface of Mg alloys can protect the substrate surface [20-22]. This possibility is not surprising

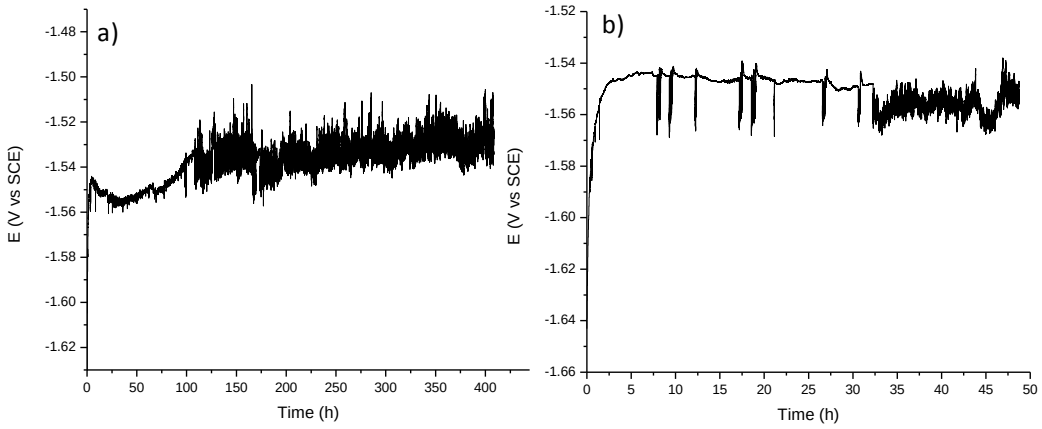

Figure 7. 7 - Chronopotentiometric plots recorded the die cast AM50 alloy in a 1.6 wt % NaCl solution with application of a) -1 µA/cm^2 and b) -0.1 µA/cm^2.

based on the nobility of the alloys compared to pure Mg. Increasing the Al-content of binary Mg-systems has been to enhance their nobility towards pure Mg in a galvanic couple [29]. AM50 Mg alloys with their ~5% Al content would thus be more noble than pure Mg, and act as a potential cathode in a galvanic couple while the pure Mg electrode experiences accelerated corrosion.

However, in the galvanic coupling to Mg, currents of 15 µA – 30 µA were measured at the pure Mg surface meaning identical cathodic currents were experienced by the AM50 alloys. This net cathodic current was sufficient to prevent the initiation of rapid corrosion leading to extensive damage on the alloy surface. To investigate the influence of current in suppressing corrosion an external current source was used to determine the response of the alloy to the applied current level.

Application of -100 µA/cm^2 to the die cast AM50 alloy successfully prevented extensive damage over a 96 h exposure to a 1.6 wt% NaCl solution. The E_{CORR} was ~-1.55 V, and the application of -100 µA/cm^2 polarized the potential to between -1.62 V and -1.72 V, a significant polarization from the natural corrosion condition. While cathodic polarization will have a protective effect on the anodic half reaction [30] it will also alter the condition of the surface due to excessive cathodic hydrogen evolution [1]. However, conditions near the E_{CORR} were maintained when currents of -1 µA/cm^2 and -0.1 µA/cm^2 were applied. In these cases, only a minor polarization was required to prevent extensive corrosion, which involves a much lower energy input.

The application of cathodic current does not generate a “stainless” Mg alloy condition, but does slow the initiation of extensive corrosion damage. Minor corrosion

attack was observed on the AM50 samples prior to the eventual onset of extensive corrosion and the induction period prior to the onset varies: a current of -10 $\mu A/cm^2$ was found to supply, at the least, 162 h of protection before the onset of a single major corrosion event. Minimum induction periods of 116 h were achieved with the application of -1 $\mu A/cm^2$ and 33 h with -0.1 $\mu A/cm^2$. A possible explanation for this reduction in corrosion rate under cathodic chronopotentiometric control is illustrated in Figure 7.8. The well accepted mechanism of the microgalvanic coupling experienced on Mg alloys surfaces is displayed in Figure 7.8 (a), in which Al-Mn intermetallics and β-phase particles can serve as cathodes, reducing water and driving the loss of Mg^{2+} from the Mg α-phase. In this schematic only the Al-Mn intermetallic is shown cathodically active since our previous results show this to be the dominant cathode, Chapter 4. Under these coupled conditions the two electrons liberated into the bulk material as Mg oxidizes to Mg^{2+} are consumed at the cathodic sites to evolve H_2. Figure 7.8 (b) shows the suggested mechanism occurring under chronopotentiometric control of the Mg alloy. The cathodic current applied to the alloy results in external electrons being constantly injected into the material. These external electrons would be utilized for the reduction of water at the sites best suited to sustain this reaction. In doing so, the cathodic sites would become saturated with incoming electrons and as Mg attempts to convert to Mg^{2+}, the two electrons generated are not required in the microgalvanic couple, similar to an observation using ICP-MS [36]. Eventually, these electrons will be utilized in the cathodic reaction. The electrons from the corrosion process can be envisioned as of having to "wait in line" due to the externally applied electrons, slowing the corrosion

process while still enabling some corrosion attack to occur. The major corrosion events generally observed on Mg alloys [7] required

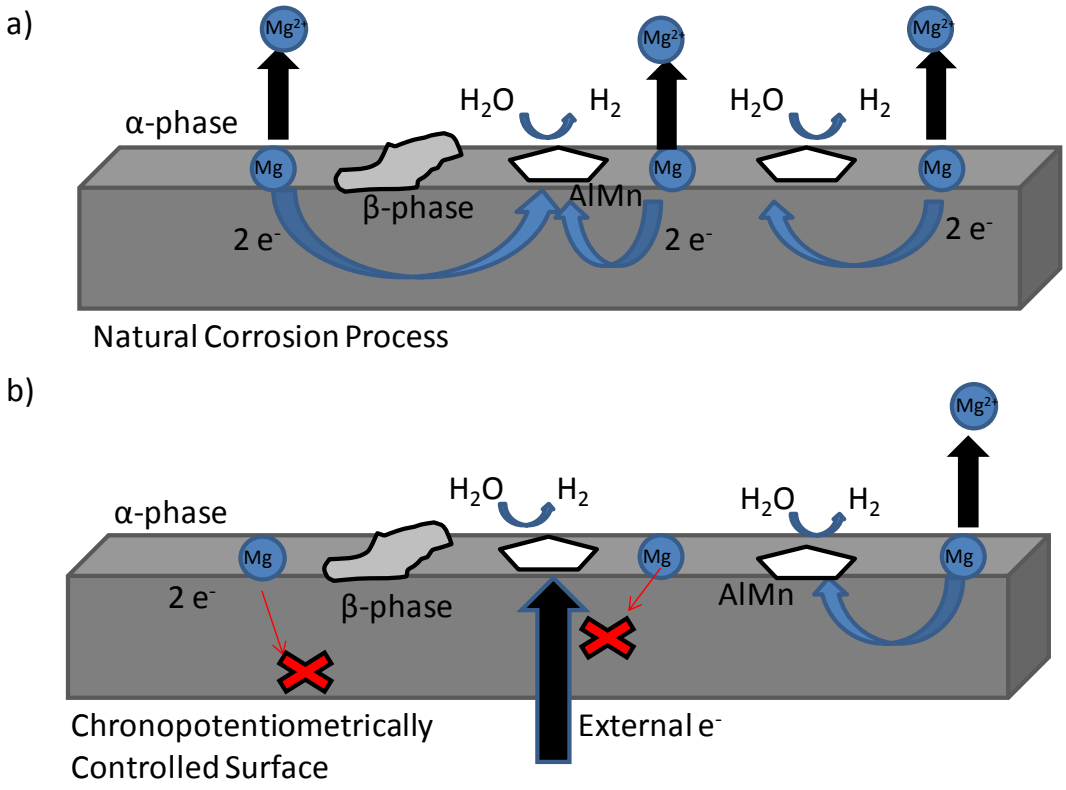

Figure 7. 8 - Schematic illustration showing the microgalvanic coupling process on a Mg alloy : a) naturally corroding AM50 surface and b) a chronopotentiometrically controlled surface.

extensive cathodic behaviour to sustain the high levels of damage occurring at the sites. When an external current is applied a sufficient number of cathodes are not available to initiate and sustain a major corrosion event. However, slowed corrosion of the α-phase is still occurring and as it proceeds will reveal more cathodic surfaces originally unexposed on the alloy surface. When this occurs the applied current is more widely distributed and the current density at any individual cathodic site is reduced. As a consequence the demand for current via galvanic coupling to the anodic dissolution of Mg increases. It was also observes that the application of a lower current decreased the induction time. At the lower current the exposure of few additional cathodes would be required before the applied current is overwhelmed by the internal microgalvanic current.

The key finding in this study is that the application of a minute current (between 100 $\mu A/cm^2$ and 0.1 $\mu A/cm^2$) can significantly delay the onset of major corrosion events. While protection of an fully exposed Mg alloy may require large cathodic currents, only small currents would be required to protect a minor exposure of a Mg alloy, such as one through a breached coating. Application of self-healing coatings on Mg alloys in automobiles is an option for successful protection of the alloys. Self healing coatings for Mg alloys have been studied [31-34] and the healing time scales and damage coverages vary. Recently a microcapsule self healing coating was shown to function on a carbon steel substrate in 7 h [35]. On such a time scale, the application of a small cathodic current directed at a coating fracture site could prevent major corrosion damage from initiating under the exposed coating, allowing ample time for the coating to repair itself. As research into self healing coatings moves forward, specifically on Mg alloys, consideration of an electrochemical back up protection mechanism should be considered.

7.5 Summary and Conclusions

The extensive corrosion which normally occurs on the surfaces of AM50 Mg alloys in chloride solutions can be "prevented by" coupling to pure Mg. The less noble pure Mg served as a sacrificial anode providing a net cathodic current to the coupled alloys. This effect can be simulated through the chronopotentiometric application of small cathodic currents. Applied current densities between -10 $\mu A/cm^2$ and -0.1 $\mu A/cm^2$ were found to delay the initiation of major corrosion events for between 33 h – 162 h. The initial period of protection is attributed to the supple of external current which partially decouples the internal microgalvanic coupling process. However, as slow corrosion continues the exposure of additional internal cathodes increases the demand for current. When this increased demand becomes too large for the external current to satisfy, the corrosion process overwhelms the cathodic protection and extensive corrosion initiates.

7.6 References

1. G. Song "Recent progress in corrosion and protection of magnesium alloys" *Adv. Eng. Mat.* 7 (2005) 563-586
2. G. Baril, C. Blanc, N. Pebere "AC impedance spectroscopy characterizing time-dependent corrosion of AZ91 and AM50 magnesium alloys" *J. Electrochem. Soc.* 148 (2001) B489-496
3. H. Matsubara, Y. Ichige, K. Fujita, H. Nishiyama, K. Hodouchi "Effect of Fe impurity on corrosion behaviour of AM50 and AM60 magnesium alloys" *Corros. Sci.* 66 (2013) 203-210

4. S.U. Mariani, A. Da Forno, M. Bestetti "Corrosion behaviour of high pressure die-cast and semi solid cast AZ91, AM60 and AM50 alloys" *Solid State Phenomena* 192-193 (2013) 231-237
5. M. Jonsson, D. Persson "The influence of the microstructure on the atmospheric corrosion behaviour of magnesium alloys AZ91D and AM50" *Corros. Sci.* 52 (2010) 1077-1085
6. M. Danaie, R.M. Asmussen, P. jakupi, D. Shoesmith, G. Botton "The role of aluminum distribution on local corrosion resistance of the microstructure in a sand-cast AM50 alloy" *Corros. Sci.* 77 (2013) 151-163
7. R.M. Asmussen, P. Jakupi, M. Danaie, G. Botton, D.W. Shoesmith "Tracking the corrosion of magnesium sand cast AM50 alloys in chloride environments" *Corrosion Science*, 75 (2013) 114-122
8. G. Song, Z. Xu "The surface microstructure and corrosion of magnesium alloy AZ31 sheet" *Electrochimica Acta* 55 (2010) 4148-4161
9. X.B. Chen, N. Birbilis, T.B. Abbott "Review of corrosion resistant conversion coatings for magnesium and its alloys" *Corrosion* 67 (2011) 035005-1 -16
10. R.G. Hu, S. Zhang, J.F. Bu, C.J. Lin, G. Song "Recent progress in corrosion protection of magnesium alloys by organic coatings" *Prog. Org. Coat.* 73 (2012) 129-141
11. X.B. Chen, H.Y. Yang, T.B. Abbott, M.A. Easton, N. Birbilis "Corrosion resistant electrochemical platings on magnesium alloys: A state of the art review" *Corrosion* 68 (2012) 518-535

12. B.S. DeForce, T.J. Eden, J. K. Potter "Cold pray Al-5% Mg coatings for the corrosion protection of magnesium alloys" *J. Therm. Spray Tech* 20 (2011) 1352-1358

13. C. Blawert, W. Dietzel, E. Ghali, G. Song "Anodizing treatments for magnesium alloys and the effect on corrosion resistance in various environments" *Adv. Eng. Mater.* 8 (2006) 511-533

14. F. Brusciotti, D. V. Snihirova, H. Xue, M.F. Montemor, S.V. Lamaka, M.G.S. Ferreira "Hybrid epoxy-silane coatings for improved corrosion protection of Mg alloy" *Corros. Sci.* 67 (2013) 82-90

15. P. Huang, J.A. Latham, D.R. MacFarlane, P.C. Howlett, M. Forsyth "A review of ionic liquid surface film formation on Mg and its alloys for improved corrosion performance" *Electrochimica Acta* 110 (2013) 501-510

16. J.E. Gray, B. Luan "Protective coatings on magnesium and its alloys – a critical review" *J. Alloys Compounds* 336 (2002) 88-113

17. P. Volovitch, M. Serdechnova, K. Ogle "Aqueous corrosion of Mg-Al binary alloys: roles of Al and Mg" *Corrosion* 68 (2012) 557-570

18. J.W. Chang, X.W. Guo, P.H. Fu, L.M. Peng, W, J. Ding, *Trans. Nonferrous Metals Soc. China* 17 (2007) 1152–1157.

19. E. Zhang, D. Yin, L. Xu, L. Yang, K. Yang "Microstructure, mechanical and corrosion properties and biocompatibility of Mg-Zn-Mn alloys for biomedical application" *Mat. Sci. Eng. C* 29 (2009) 987-993

20. J.A. Juarez-Islas, J. Genesca, R. Perez "Improving the efficiency of magnesium sacrificial anodes" *JOM* 1993 42-44

21. S.B. Hassen, L. Bousselmi, E.M. Rezrazi, P. Bercot, E. Triki "Corrosion behaviour of carbon steel coated with magnesium electrodeposited from methyl magnesium chloride solution" *J. Coat Technol. Res.* 10 (2012) 277-284

22. J.G. Kim, S.J. Koo "Effect of alloying elements on electrochemical properties of magnesium-based sacrificial anodes" *Corrosion* 56 (2000) 380-388

23. Y.S. Choi, D.H. Shin, J.G. Kim "Sacrificial anode cathodic protection of aluminum coated steel for automotive mufflers" *Corrosion* 63 (2007) 524-530

24. B.L. Yu, J.Y. Uan "Sacrificial Mg film anode for cathodic protection of die cast Mg-9 wt%" *Scripta Materialia* 54 (2006) 1253-1257

25. X. Lu, Y. Zuo, X. Zhao, Y. Tang, X. Feng "The study of a Mg rich epoxy primer for protection of AZ91D magnesium alloy" *Corros. Sci.* 53 (2011) 153-160

26. X. Lu, Y. Zuo, X. Zhao, Y. Tang "The improved performance of a Mg-rich epoxy coating on AZ91D magnesium alloy by silane pretreatment" *Corros. Sci.* 60 (2012) 165-172

27. Y.P. Wang, X.H. Zhao, X.Y. Lu, Y. Zuo "Corrosion protection of ceria particles in Mg-rich primer on AZ91D magnesium alloy" *Acta Phys.-Chim. Sin.* 28 (2012) 407-413

28. R.M. Asmussen, W. J. Binns, P. Jakupi, D.W. Shoesmith "The microstructural effects on corrosion of AM50 alloys" *Proc. MetSoc 2013*

29. S. Mathieu, C. Rapin, J. Steinmetz "A corrosion study on the main constituent phases of AZ91 magnesium alloys" *Corros. Sci.* 45 (2003) 2741-2755

30. G.R. Hoey, M. Cohen "Corrosion of anodically and cathodically polarized magnesium in aqueous media" *J. Electrochem. Soc.* 105 (1958) 245-250

31. A.S. Hamdy, I. Doench, H. Mohwald "Vanadia-based coatings of self-repairing functionality for advanced magnesium Elektron ZE41 Mg-Zn-rate earth alloy" *Surf. Coating Tech.* 206 (2012) 3686-3692

32. F. Luo, Q. Li, X.K. Zhong, H. Gao, Y. Dai, F.N. Chen "Corrosion electrochemical behaviours of silane coating coated magnesium alloy in NaCl solution containing cerium nitrate" *Mat. Corros.* 63 (2012) 148-154

33. A. Yabuki, M. Sakai "Self-healing coatings of inorganic particles using a pH-sensitive organic agent" *Corros. Sci*. 53 (2011) 829-833

34. M. Forstyh, P. Howlett, S.K. Tan, D.R. MacFarlane, N. Birbilis "An ionic liquid surface treatment for corrosion protection of magnesium alloy AZ31" *Electrochem. Solid State Let.* 9 (20060 B52-B55

35. W. Wang, L. Xu, X. Li, Y. Yang, E. An "Self healing properties of protective coatings containing isophorone diisocyanate microcapsules on carbon steel surfaces" *Corros. Sci.* 80 (2014) 528-535

36. L. Rossrucker, K.J.J Mayrhofer, G.S. Frankel, N. Birbilis "Investigating the real time dissolution of Mg using online analysis by ICP-MS"*J. Electrochem. Soc.* 161 (2014) C115-C119

Chapter Eight

Reducing the Corrosion Rate of Magnesium Alloys Using Ethylene Glycol For Advanced Electrochemical Imaging

8.1 Introduction

Mg alloys possess several desirable properties for use in the automotive and aerospace industries, such as their high strength to weight ratio and good castability [1]. A deterrent to their application is their high corrosion rates in aqueous media. Driving the corrosion of Mg alloys is the microgalvanic coupling between the α-Mg matrix and the secondary microstructural constituents, such as β-phase and intermetallic particles [1-2] with the cathodic reactivity of the latter increased if it contains contaminant elements such as Fe [3]. Understanding the behaviour of these microstructural features during corrosion is essential if alloys with improved corrosion properties are to be developed. Separating the responses of individual microstructural components acting as cathodes is inherently difficult using standard electrochemical measurements.

Scanning probe techniques provide valuable insights on a microscale with high spatial resolution. Such techniques have been applied to study the corrosion of Mg alloys including localized electrochemical impedance spectroscopy (LEIS) [4-5], scanning Kelvin probe force microscopy (SKPFM) [6-7], scanning vibrating electrode (SVET) [8-12], and different modes of scanning electrochemical microscopy (SECM) [13-17]. Monitoring corrosion processes above Mg alloys in aqueous environment with these techniques is challenging because of large H_2 fluxes evolving as corrosion progresses and can interfere with mediator detection at the microelectrode tip and create a convective media at the corroding surface. Recently, these fluxes of H_2 have been used to monitor the corrosion process on Mg alloy [18].

To overcome this issue we have focussed on controlling the corrosion rate, and hence, the amount of H_2 produced, using ethylene glycol as the corrosion medium since it limits the availability of water, the primary cathodic reagent during corrosion. The corrosion of Mg alloys in ethylene glycol solutions has previously been investigated with a primary focus on the behaviour of Mg alloys as potential engine block materials which use ethylene glycol based coolants [19-22]. In these studies increasing the ratio of ethylene glycol to water was found to decrease the corrosion rate of the Mg alloys, although little detail was paid to pure ethylene glycol or to this solvent containing only small percentages of water. Corrosion was also not investigated on the microscale.

Here, we present the study of the corrosion of the AM50 Mg alloy in ethylene glycol using a range of electrochemical techniques including SECM to compare the corrosion behaviour to that observed in aqueous solution. Scanning electron microscopy (SEM) and Energy Dispersive X-ray analyses (XEDS) were used to locate and elementally analyze the alloy microstructure and to locate and correlate surface microstructural features with an *in-situ* SECM map. Confocal scanning laser microscopy (CLSM) was used to observe the locations of corrosion damage.

8.2 Experimental

8.2.1 Materials

AM50 sand cast and graphite Mg alloy rods were received from General Motors Canada. The sand cast and graphite cast AM50 rods were cut into 1 cm x 1 cm x 0.7 cm samples, and the AM50 sand cast into 4 mm x 4 mm x 0.5 cm samples for SECM measurements. All samples were threaded on the backside to allow connection to external circuitry, and Struers EpoFix epoxy resin was used to seal the samples allowing

only the exposure of a single face to the aqueous solution. Solutions were prepared with ethylene glycol (ACP), reagent grade NaCl (Caledon), ferrocenemethanol (FcMeOH) (97% Sigma Aldrich Canada), and NanoPure® (18.2 MΩ-cm) water.

8.*2.2 Sample Preparation*

The mounted AM50 samples were ground successively with 800, 1200, 2400 grit SiC paper with a 50:50 ethanol/isopropanol solution as a lubricant, and subsequently polished with a Struers DP-Dur cloth saturated in 3 µm Struers DP-Suspension A for 5 to 10 min with the ethanol/propanol mixture once again used as a lubricant. A final 2-3 min polish was performed on a Struers OP-Chem cloth using an equal volume mixture of Struers OP-S Suspension and ethylene glycol, as an abrasive. The polished sample was then rinsed and sonicated in anhydrous ethanol for 2 min, Ar dried, and stored in a desiccator.

8.*2.3 Electrochemical Measurements*

Electrochemical measurements were carried out in a standard three electrode cell with a Pt-mesh counter electrode and a saturated calomel reference electrode (SCE) in aerated solutions at ~22 °C. Electrochemical responses were measured with a Solartron® 1287 potentiostat coupled to a Solartron® 1255B frequency response analyzer for electrochemical impedance spectroscopy (EIS) measurements.

For corrosion potential (E_{CORR}) measurements the samples were placed in solution, face down for selected durations. Potentiodynamic polarization (PDP) scans were performed following a 2 h exposure to solution by scanning (at 0.167 mV/s) from -200 mV below E_{CORR} to 500 mV or until a current density of 1 mA/cm^2 was measured to

limit the extent of surface damage to the sample. EIS measurements were performed by application of a sinusoidal potential perturbation of ± 10 mV vs E_{CORR}. The current response was recorded over the frequency range, 10^5 Hz to 10^{-3} Hz, and a one point per decade reverse scan was recorded from 10^{-2} – 10^5 Hz to ensure steady-state was maintained throughout the measurement.

8.*2.4 Electron Microscopy*

Scanning electron microscopy (SEM) images were collected in secondary electron (SE) and back scattered electron (BSE) modes on either a LEO 440, Hitachi 3400-N Variable Pressure SEM, LEO 1540 XB SEM, or a Hitachi SU6600 Field Emission SEM. X-ray energy dispersive spectroscopy (XEDS) maps were collected using Quartz XOne XEDS system. Confocal laser scanning microscopy (CLSM) was performed by measuring the reflected light intensity from a Zeiss 510 confocal with a HeNe 633 nm laser.

8.*2.5 Scanning Electrochemical Microscopy (SECM)*

Prior to SECM measurements, a montage image of a polished 4 mm × 4 mm area on an AM50 sand cast alloy sample was collected at 150x magnification using a Hitachi SU6600 Field Emission SEM. A complete map of the surface was produced by stitching the images using Image-Pro Plus 7.0®. SECM characterization was performed using an ElProScan 1 system (HEKA, Germany; bipotentiostat model PG340) by positioning a 25 µm Pt microelectrode over the alloy surface immersed in 1 mM FcMeOH solution (Sigma Aldrich) in ethylene glycol (Fisher Scientific). An approach curve was performed using feedback current from the FcMeOH mediator at and approach speed of 1 µm/s in order to position the microelectrode at a known distance of 10 µm from the

surface. The microelectrode tip was polarized to 500 mV and rastered at 5 µm/s over an area of interest (AOI). A 0.5 mm diameter (as drawn) Pt counter electrode (99.99%, Goodfellow Cambridge Limited, Huntingdon, England) and a Ag|AgCl quasi-reference wire electrode (fabricated as reported elsewhere [23] using a Ag wire of 1.0 mm diameter, annealed 99.99% from Goodfellow) were employed to record electrochemical data.

8.3 Results

8.3.1 AM50 Alloy Microstructure

The main microstructural constituents of the AM50 alloy are shown in the SEM micrograph in Figure 8.1 (a), in which one of the many β-phase particles ($Mg_{17}Al_{12}$) is marked with a green arrow and an Al-Mn intermetallic with a red arrow. These compositions are confirmed in the XEDS maps for Mg, Figure 8.1 (b), confirming the general distribution of Mg throughout the alloy matrix. The Al is present in both the β-phase and the intermetallic, Figure 8.1 (c), with some enrichment in the network running between the β-phases corresponding to eutectic α-Mg. The Mn, Figure 8.1 (d), is present within the ten Al-Mn intermetallics in the imaged region

8.3.2 Electrochemical Behaviour

The electrochemical behaviour of the AM50 sand cast alloy was investigated in 3 mM NaCl in both NanoPure® water and ethylene glycol. The chloride was added to enhance solution conductivity. Figure 8.2 displays the E_{CORR} measured in 3 mM NaCl + H_2O (black) and 3 mM NaCl + ethylene glycol (red). In water, E_{CORR} initially rises over the first 2 h of immersion from -1.56 V to -1.50 V, and then increases slowly over the 24 h to -1.49 V accompanied by a number of small fluctuations. This value is in the range

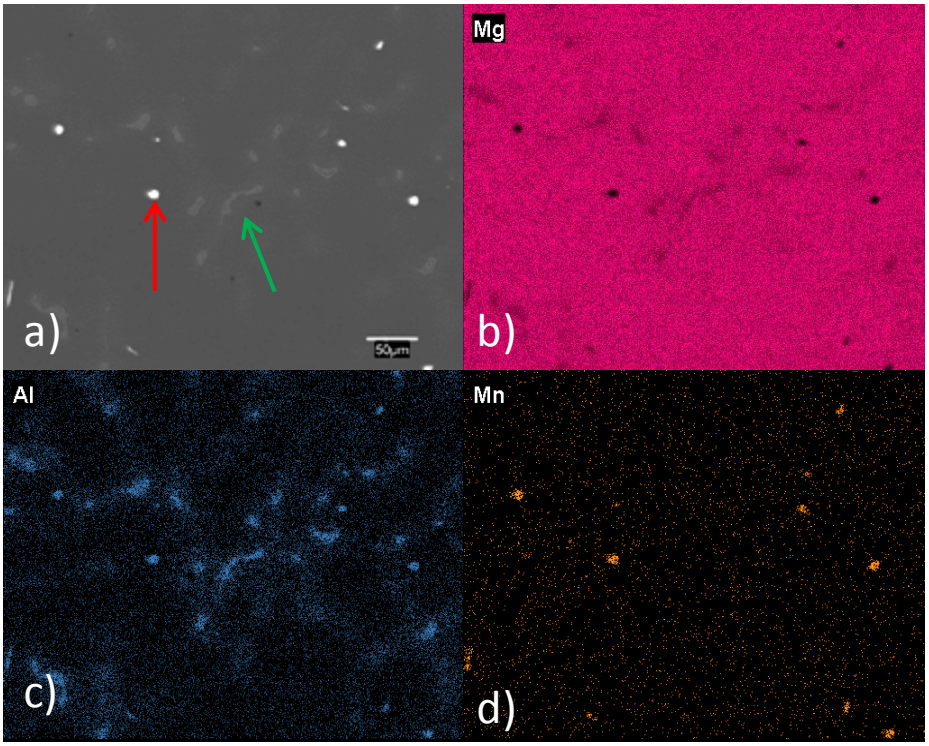

Figure 8. 1 - The microstructure of a sand cast AM50 Mg alloy displaying the common microstructural features in a) SEM BSE image, and XEDS maps of (b) Mg, (c) Al, and (d) Mn. A β-phase structure is marked in the images with a green arrow and an AlMn intermetallic particle with a red arrow.

expected for AM50 in aqueous chloride solutions [24]. In ethylene glycol E_{CORR} initially decreases from -1.05 V to -1.4 V over the first 2 h of immersion before increasing to a final steady-state value of ~ -1.26 V after 24 h.

The PDP behaviour of the alloy in both solutions is shown in Figure 8.3. As expected the cathodic current at potentials less than E_{CORR} was considerably higher in water than in ethylene glycol. In water (black), once the net current became anodic at -1.45 V it increased (region I). For higher potentials the current increases sharply (region II). These features are typical of the behaviour observed on this alloy [25] with an attempt to grow a partially protective film in region I followed by film breakdown and the onset of rapid dissolution in region II. In ethylene glycol (red), a similar initial event is observed with region I persisting to a potential of -1.10 V. The subsequent increase in reactivity is minor, currents < 1μA/cm^2 being maintained before final film breakdown for E > ~ -0.8V (region II). Only at these high potentials does the current recorded exceed that observed in region I in water when the surface is partially protected by corrosion product. For all potentials anodic to E_{CORR} the currents measured in ethylene glycol are ~ 10^3 less than those observed in water.

The suppression of corrosion rate in ethylene glycol compared to water is evident in the Nyquists plots in Figure 8.4, which were recorded after 20 h of immersion. Extrapolation of these plots at the low frequency limit to the real axis yields a measure of the polarization resistance (R_P) which is inversely proportional to the corrosion rate. The value obtained for R_P in water (~6 kΩ·cm^2) is an order of magnitude lower than that in ethylene glycol (~67 Ω·cm^2). The Nyquist plot recorded in water exhibits two capacitative responses (I and II), the one at high frequencies being shown in the inset to

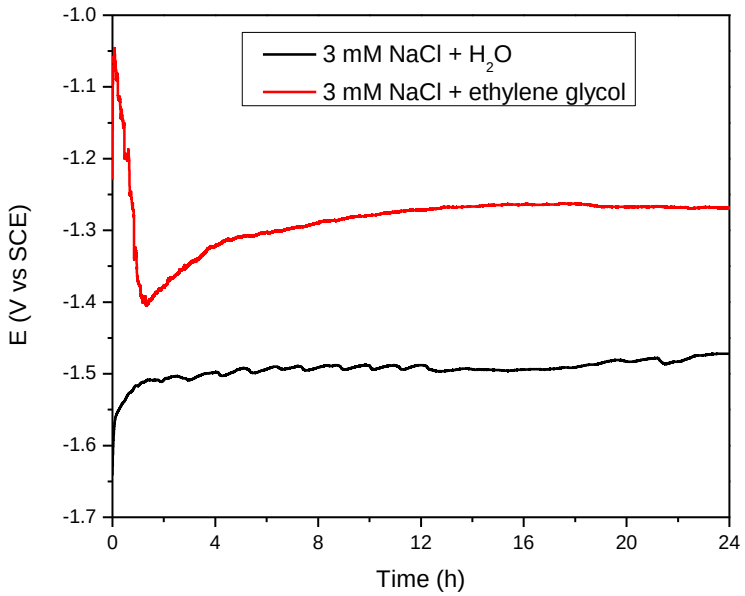

Figure 8. 2 - Evolution of E_{CORR} measured on a sand cast AM50 Mg alloy in 3 mM NaCl in water (black) and ethylene glycol (red

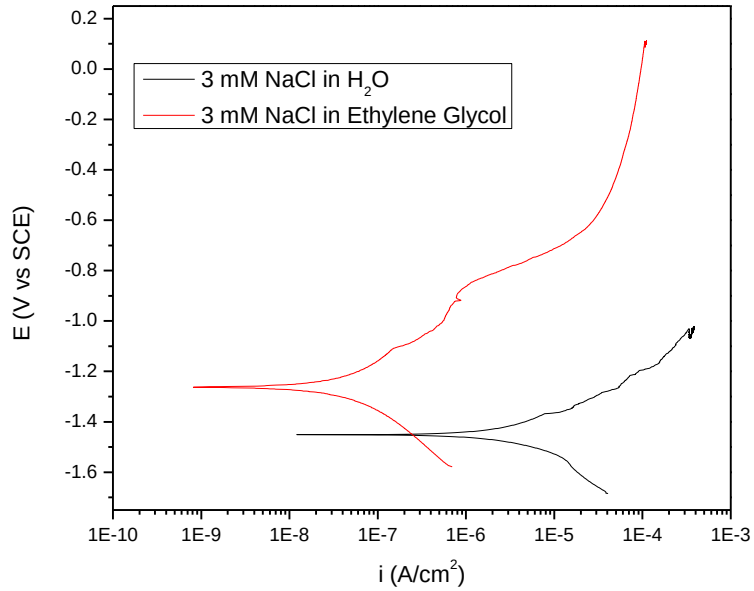

Figure 8. 3 - A PDP scan measured on a sand cast AM50 Mg alloy in 3 mM NaCl in ethylene glycol (red) and 3 mM NaCl in water

Figure 8.4. The plot recorded in ethylene glycol exhibits two, possibly three capacitative responses (I, II and III) although whether or not the response at high frequencies (I) is a true response or a result of cell geometry remains to be determined and further investigation into this behaviour is ongoing. The characteristic frequency of the low frequency response in water (0.5 Hz) is approximately the same as the characteristic frequency of the low frequency response in ethylene glycol, a possible indication of the signals arising from the same process at the electrode surface.

8.*3.3 Corrosion Process Control*

The addition of water to the ethylene glycol system has an intriguing effect, Figure 8.5. The E_{CORR} of the sand cast AM50 alloy in the ethylene glycol solution initially increases to ~ -1.32V and appears to be approaching the same steady-state value previously observed (Figure 2). On addition of 2 mL of water after 2 h, E_{CORR} immediately drops to -1.66V before recovering to a value of ~ -1.45V over the next 24 h, which is within the range expected in water (Figure 2). Subsequently, E_{CORR} increases steadily to a value of ~ -1.25V; i.e., a value close to that measured in ethylene glycol with no water addition (Figure 2). A second addition of 2 mL of water induced a similar drop in E_{CORR} although the recovery over the subsequent 24 h was similar but not as complete as observed after the first water addition.

Figure 8.6 (a) shows the E_{CORR} behaviour of the sand cast AM50 alloy in 0.016 wt% NaCl + ethylene glycol to Figure 8.5. Prior to the addition of 25 mL of water after 2 h, (a larger addition of water used to ensure that the effect is sustained for the duration of EIS measurement) E_{CORR} is significantly more negative than measured in the previous experiment (Figure 8.2). Since the E_{CORR} measured in water is significantly lower than in

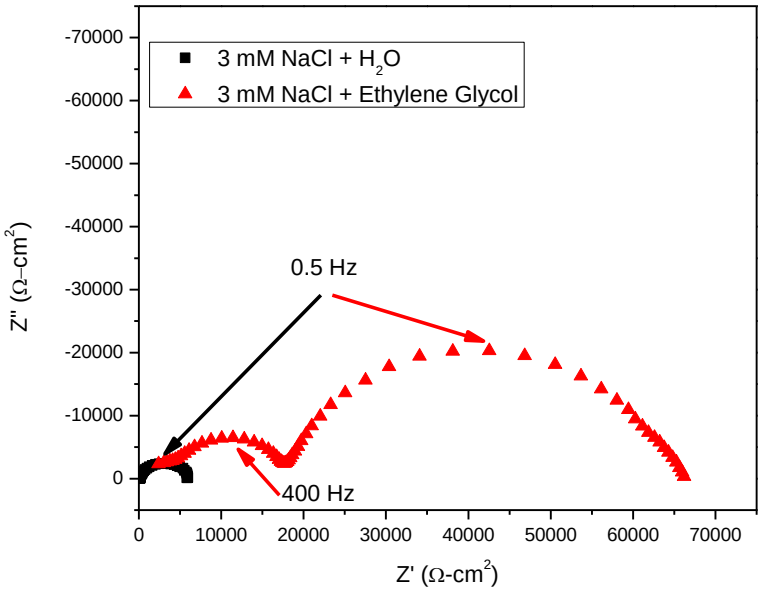

Figure 8. 4 - Nyquist plots recorded on a sand cast AM50 Mg alloy after 20 h exposure in 3 mM NaCl in water (black) and ethylene glycol (red). Inset: magnification of the high frequency response in the aqueous solution.

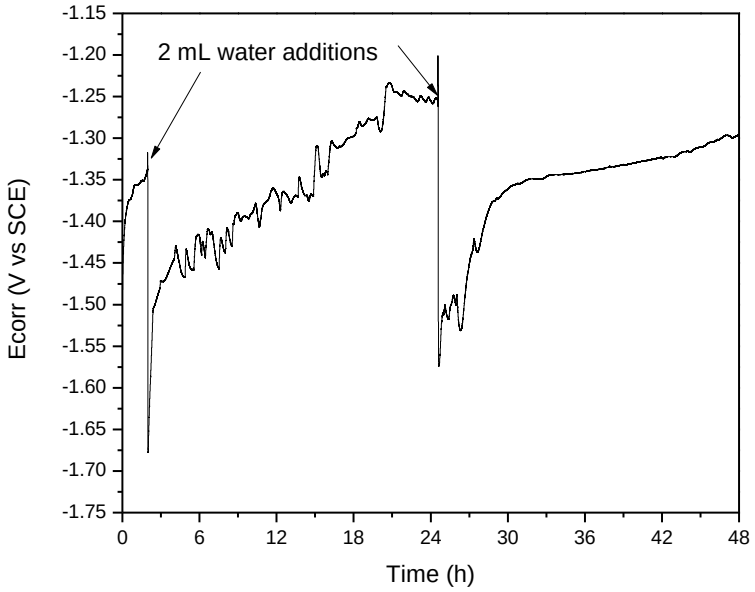

Figure 8. 5 - Progression of E_{CORR} measured on a sand cast AM50 Mg alloy over a 48 h exposure period in 3 mM NaCl + ethylene glycol with 2 mL additions of water made after 3 h and 25 h.

ethylene glycol (Figure 8.2), this suggests that in this case the ethylene glycol contains more water than in the previous experiment.

This sensitivity to water content of the ethylene glycol is further indicated by a comparison of the impedance spectra recorded in the two experiments, the overall impedance of the alloy/solution interface being considerably lower in this second experiment. This can be appreciated by a comparison of the Nyquist plots in Figures 8.4 and 8.6 (b). In the first experiment in which the water content of the ethylene glycol appears to be low, extrapolation of the low frequency response to the real axis would yield an R_P value of ~ 67 $k\Omega \cdot cm^2$compared to ~ 35 $k\Omega \cdot cm^2$ in this second experiment.

In the second experiment (Figure 8.6 (a)) EIS measurements were performed just prior to and following the addition of water, Figure 8.6 (b,c,d). Comparison of the characteristic frequencies for the two capacitative responses observed shows they are the same for both spectra and similar to the spectrum in ethylene glycol in Figure 8.4. This similarity in response is confirmed by the Bode plots in Figure 8.6 (c and d) which show only a small change in both time constants after water addition. The key difference is in the overall impedance which decreases by a factor of ~2 on the addition of water. In both cases the spectra show a low frequency response at < 10^{-1} Hz which suggests some contribution from diffusion, most likely of water in the glycol.

8.3.4 Microstructure Behaviour in Ethylene Glycol

Our previous results show that Al-Mn intermetallics can act as cathodes in the corrosion of AM50 alloys in saline aqueous environments [26-27], and that the presence of an accumulated dome of corrosion product (predominantly $Mg(OH)_2$) is evidence of

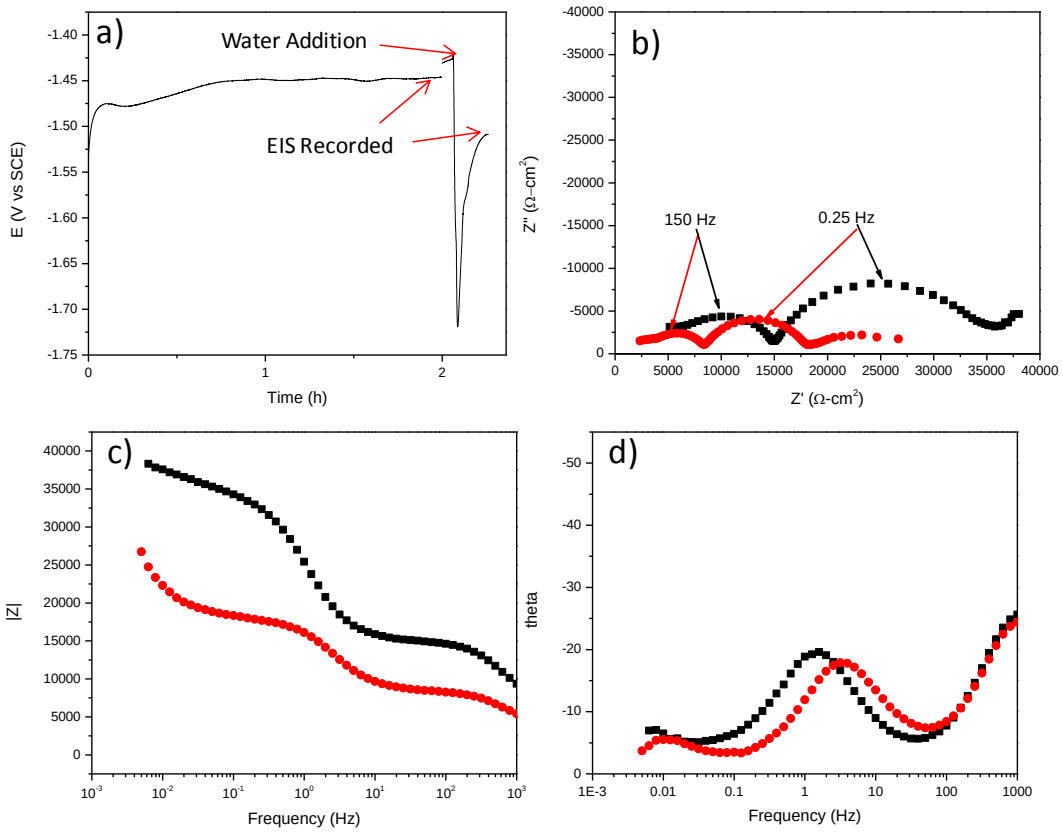

Figure 8. 2 - a) Progress of E_{CORR} measured on a sand cast AM50 Mg alloy in 3 mM NaCl + ethylene glycol. EIS measurements were made just before and after the addition of 25 mL of water at ~ 2h: (b) Nyquist plots, and (c), (d) Bode plots recorded just before (black) and after (red) water addition.

this function [28]. This corrosion product is formed as a consequence of the alkalinity generated by water reduction to H_2 gas on the intermetallics which leads to the precipitation of soluble Mg^{2+} transported to this location from adjacent anodically dissolving areas of the surface. Figure 8.7 (a) shows a backscattered SEM image of the freshly polished alloy. The β-phase network is clearly visible as irregular light strips in the image, and a large bright Al-Mn intermetallic is visible in the top right corner. A magnified image of this particle is shown in Figure 8.7 (c). Figure 8.7 (b and d) show the same particle after 72 h of exposure to the ethylene glycol solution. The low magnification image, Figure 8.7 (b) shows slight corrosion damage of the α-Mg matrix has occurred as indicated by the green arrow. No observable change in the β-phase network was visible. The Al-Mn intermetallic particle, which appears dark in Figure 8.7 (b) had accumulated a deposit of corrosion product, Figure 8.7 (d) clearly indicating its function as a cathode actively supporting the corrosion of the surrounding α-matrix.

8.3.5 *Scanning Electrochemical Microscopy in Ethylene Glycol*

Figure 8.8 shows a 4 mm x 4mm area of the surface of the AM50 alloy which was montage imaged to identify the area to be mapped by SECM. This imaging process allows us to identify an area within which we can cross-correlate the SECM measurements with the distribution of microstructural features in the surface. The selected AOI for SECM measurements is marked with the red box.

In SECM experiments, the sample was exposed to a 1 mM solution of FcMeOH in ethylene glycol. A cyclic voltammogram recorded with a 25 μm Pt microelectrode in this solution at a scan rate of 10 mV/s and is shown in Figure 8.9 (a). A steady state current (for the oxidation $FcMeOH \rightarrow FcMeOH^+ + e^-$) was observed for E > 400 mV

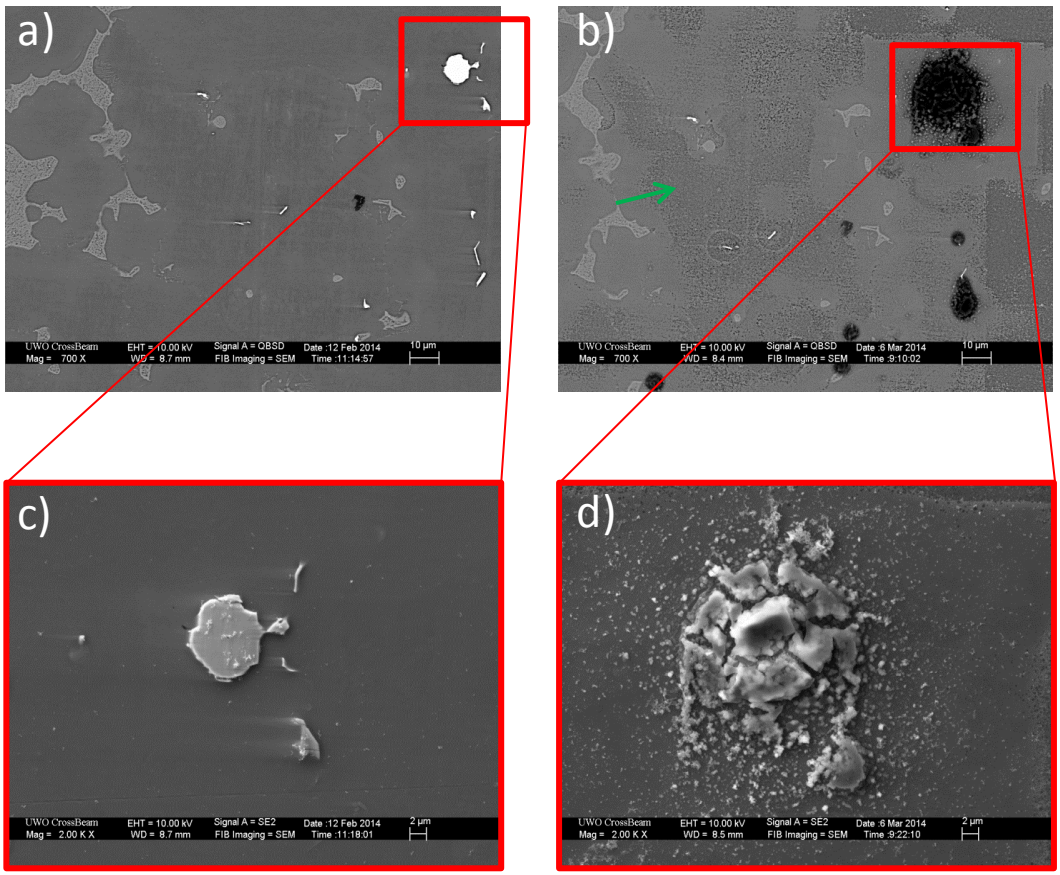

Figure 8. 3 - Back-scattered SEM micrographs of graphite cast AM50 Mg alloy a) polished surface, b) following 72 h in 0.016 wt% NaCl in ethylene glycol, c) an AlMn intermetallic marked in (a), d) the intermetallic following exposure having collected a mass of corrosion product.

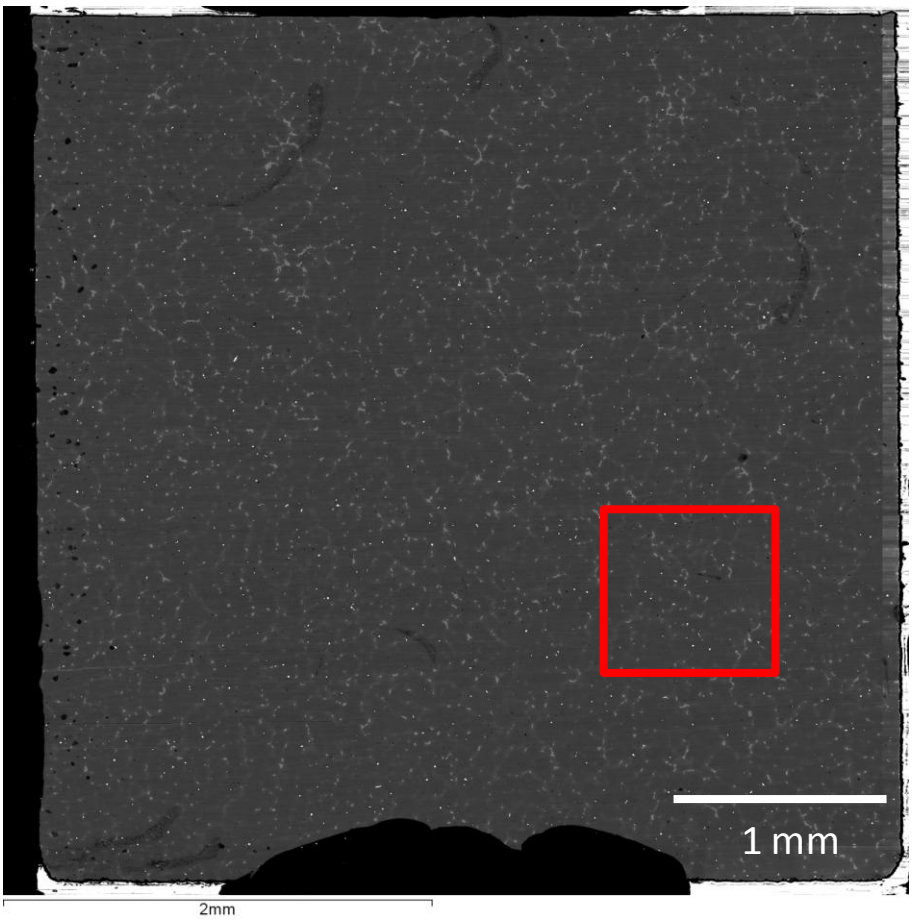

Figure 8. 4 - Montage SEM map recorded on a sand cast AM50 Mg alloy.

The red box shows the location chosen for SECM measurements.

and 500 mV was selected as the microelectrode potential during SECM measurements. To position the probe at a 10 µm tip to substrate distance, a feedback current probe approach curves with an approach speed of 1 µm/s were recorded, Figure 8.9 (b), at the locations marked 1 and 2 in Figure 8.10 (a).

Following positioning, the microelectrode was rastered over a 500 µm x 500 µm area at a scan rate of 5 µm/s with a potential of 500 mV applied to the tip. The SECM map recorded, Figure 8.10 (a), shows clearly distinguishable regions with the microelectrode tip current varying between 300 and 400 pA.

The approach curve recorded at location 2 yields negative feedback indicating low reactivity while that at location 1 yields slight positive feedback, Figure 8.9 (b). Due to a regeneration of the oxidized mediator at the microelectrode tip, $FcMeOH^+$ diffuses towards the surface being reduced back to FcMeOH. Heterogeneous rate constants (k_o) can be extracted to quantify the rate at which the mediator is regenerated at these locations. By fitting the approach curves to an analytical approximation [29], values of $k_1 = 1.02 \times 10^{-2}$ cm/s and $k_2 = 3.13 \times 10^{-3}$ cm/s are obtained, clearly demonstrating the difference in reactivity between these locations. For comparison purposes, the analytical approximation for full positive (diffusion controlled reactivity) and negative (no reactivity on an insulating surface) feedback are also shown, plots (I) and (II) in Figure 8.9 (b), respectively.

Figure 8.10 (b) shows the SECM image (Figure 8.10 (a)) superimposed on the SEM image of the polished AM50 sample with the red arrow highlighting the two Al-Mn intermetallics and a circular arrangement of β-phase. These overlaid images show that the

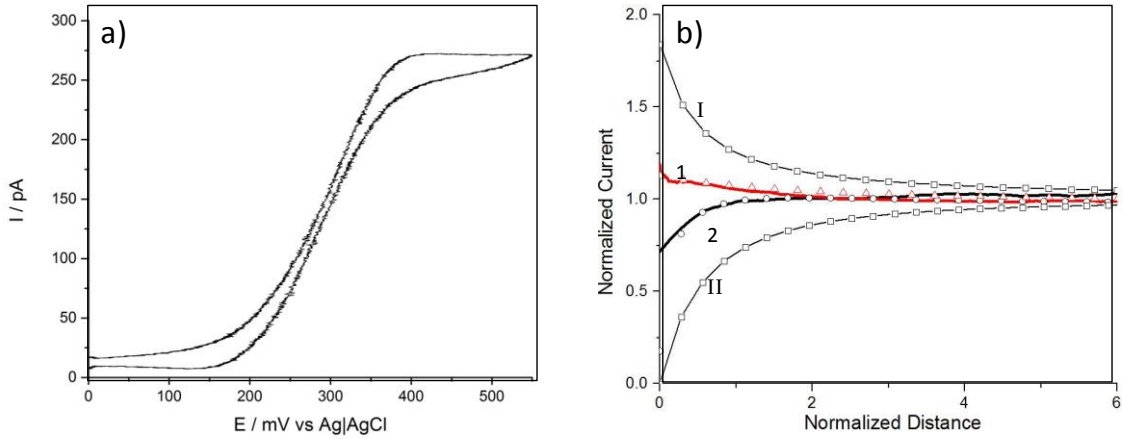

Figure 8. 9 - (a) A cyclic voltammogram recorded on the Pt microelectrode in 1 mM FcMeOH in ethylene glycol at 10 mV/s; (b) approach curves recorded at locations 1 and 2 (Figure 8.10 (a)) and the theoretically fitted approach curves (△ and ○) . I and II show the calculated approach curves for a diffusion limited reaction and an insulating unreactive surface, respectively.

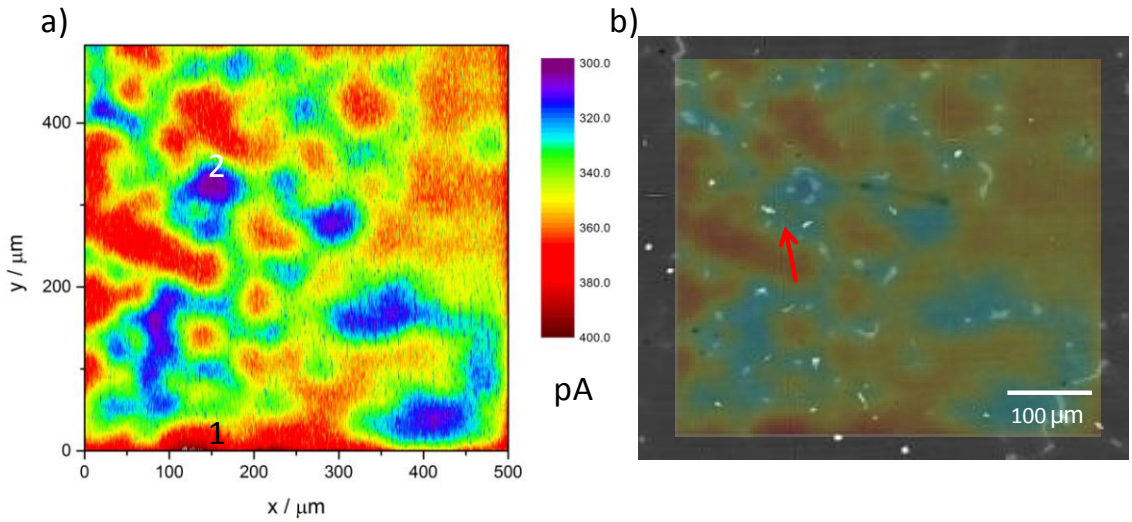

Figure 8. 10 - (a) SECM map recorded on a sand cast AM50 Mg alloy in 1 mM FcMeOH + ethylene glycol using a Pt microelectrode polarized at 500 mV located 10 µm above the surface and rastered across the surface at 10 µm/s: (b) an overlay of SEM and SECM images of the same area. The red arrow indicates two Al-Mn particles used to relocate this area in images.

reactive areas (positive feedback in the probe approach curve) are associated with the α-Mg locations on the surface and the regions of low reactivity (negative feedback) with β-phase ligaments and surrounding eutectic regions.

Following the SECM experiment the AOI was re-examined and both BSE and SE micrographs are shown in Figure 8.11 (a) and 8.11 (b), respectively. To assist in image comparison, two Al-Mn intermetallics are identified by the red arrow. The SE image in Figure 8.11 (b) shows the collection of some corrosion product (identified as the slightly lighter regions) on the α-Mg areas of the surface.

Figure 8.12 shows two 3D CLSM images of the AOI imaged by SECM. The image in Figure 8.12 (a) shows an area of an AM50 alloy surface imaged after exposure to the ethylene glycol solution for 24 h and Figure 8.12 (b) the AOI imaged by SECM after exposure to the ethylene glycol + FcMeOH solution. The red arrow again identifies the location of the two Al-Mn structures highlighted in Figures 8.10 and 8.11.

It is clear from these images that the surface is much more extensively damaged after exposure to the ethylene glycol containing FcMeOH than it is in the ethylene glycol alone. The darker areas in the CLSM image in Figure 8.12 (b) coincide with the corrosion product-covered α-Mg areas (dark since the laser beam is scattered rather than reflected) and the lighter areas with the less corroded β-phase/eutectic skeletal-like structure. Comparison of this CLSM image with the overlaid SEM/SECM map (Figure 8.10 (b)) confirms that $FcMeOH^+$ is active in corroding the alloy surface and that it is consumed primarily at α-Mg locations.

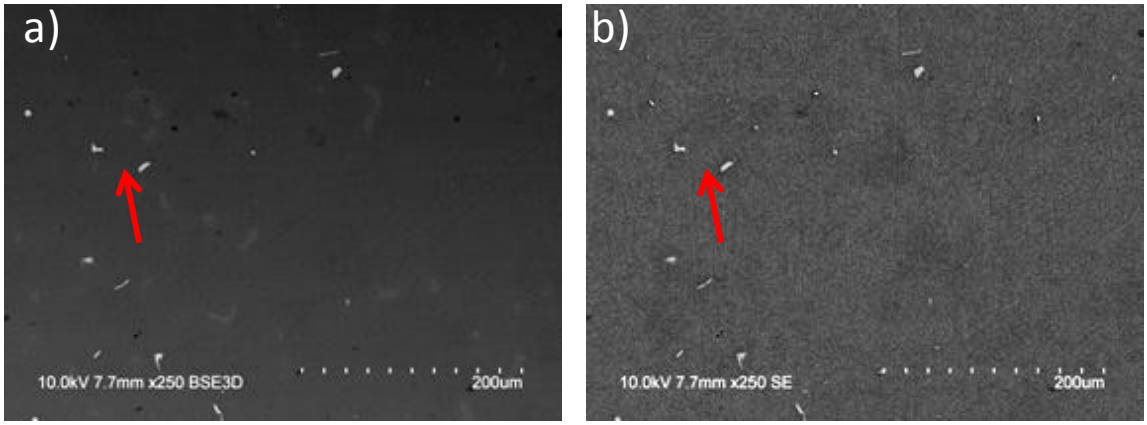

Figure 8. 11 - (a) SEM BSE micrograph of the AOI on the sand cast AM50 Mg alloy following the SECM measurement shown in Figure 8.10; and (b) SEM SE micrograph of the AOI. Red arrows identify the same AlMn intermetallics in each micrograph

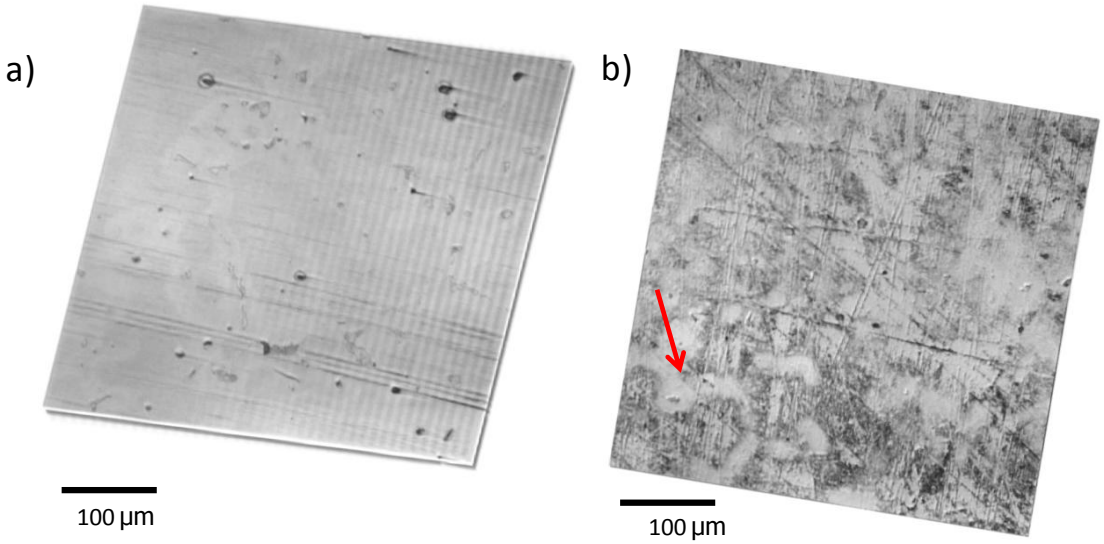

Figure 8. 12 - 3D CLSM micrographs of a) AM50 Mg alloy exposed for 24 h in ethylene glycol and b) the AOI on the AM50 Mg alloy following the SECM measurement in Figure 8.10 showing slight damage accumulation in regions which generated positive feedback current in the SECM experiment; The red arrow shows the location of the two Al-Mn intermetallic particles.

8.4 Discussion

The goal of this project was to demonstrate that the corrosion of a Mg alloy, which proceeds rapidly in aqueous solution with the production of copious amounts of H_2 [30], could be slowed down without changing the basic mechanism by using ethylene glycol to allow the reaction to be followed using high resolution electrochemical microscopic techniques. In ethylene glycol, which will contain only small amounts of water, the cathodic reactions have been reported to be oxygen reduction and the less likely reduction of the ethylene glycol [31].

However, the large positive shift in E_{CORR} (Figure 8.2) and ~ 10^2 drop in cathodic current in the PDP scans (Figure 8.3) on switching from an aqueous solution to the ethylene glycol solution suggests that H_2O, even when present in small amounts in ethylene glycol, will be the dominant cathodic reagent. This appears to be confirmed by the influence of adding small amounts of H_2O on E_{CORR} and the EIS spectra. The immediate drop in E_{CORR} (Figure 8.5) confirms the spontaneous effect of H_2O on the corrosion process. The subsequent rise in E_{CORR} over a period of ~ 22 h to the value expected prior to H_2O addition suggests the water is being consumed in the corrosion process. A second addition leads to similar behaviour.

This influence of adding H_2O on the impedance of the alloy/solution interface is clear in Figure 8.4, the polarization resistance (estimated by extrapolating the spectra to the zero frequency limit) increasing by approximately an order of magnitude. Despite this change, the Nyquist plots in aqueous solution and ethylene glycol both exhibited two capacitative responses, comparable features to previously reported systems in water and ethylene glycol [5,32]. In aqueous systems the high frequency response has been

attributed to the charge transfer process ($Mg \rightarrow Mg^{2+}$) and film capacitance at the alloy surface and the lower frequency response to the diffusion of Mg^{2+} through the thickening $MgO/Mg(OH)_2$ corrosion product film [5]. If these assignments are accepted then the Nyquist plots show the characteristic frequency (an indication of the time constant of the response) is considerably larger in water (~3000 Hz) than in ethylene glycol (~400 Hz); i.e., the kinetics of the initial charge transfer process are considerably faster in water. By contrast the characteristic frequencies for the lower frequency response are approximately the same despite the large increase in overall resistance. A speculative explanation might be that, besides a significant decrease in diffusion coefficient for Mg^{2+} within the film, the film formed is more compact and less polarizable. Such features would be consistent with the PDP behaviour which shows that a low current density, indicative of the presence of a compact, generally protective corrosion product, is sustained to potentials well positive of E_{CORR}. This is in contrast to the behaviour in water when film breakdown and rapid corrosion occur almost immediately the potential is increased beyond E_{CORR}.

The SEM micrographs in Figure 8.7 confirm that corrosion in ethylene glycol proceeds via the same microstructural processes observed for the corrosion of this alloy in aqueous chloride solutions, but with a much lower rate of damage accumulation. Damage generally accumulated on the α-Mg grains (Figure 8.7 (b)) with the Al-Mn intermetallic particles acting as the dominant microgalvanically-coupled cathodes (Figure 8.7 (d)) [26, 27]. The extent of damage to the α-Mg grains is minimal after 72 h of exposure consistent with SEM observations (Figure 8.11 (b)) that these areas, while corroded, are uniformly covered with a thin layer of corrosion product. In addition, as also observed after corrosion in aqueous systems [26], the β-phase regions and the areas

of eutectic phase surrounding the β-phase remain uncorroded. In the case of the eutectic regions this was attributed to their enrichment in Al compared to the core of the α-matrix which lead to their protection by the enrichment of Al at the alloy/oxide interface [26].

With the corrosion rate, and hence H_2 production rate, suppressed in this manner it was possible to map the corrosion process using SECM, distinct differences in feedback current being observed on the different microstructural regions on the surface. The observed spatial variations in current could arise from two scenarios; (1) migration of the $FcMeOH^+$ species from the microelectrode tip to a region based on the Volta potential of that region, or 2) $FcMeOH^+$ acts as an oxidant involved in the corrosion of the α-Mg when generated at the microelectrode tip. As discussed above the alloy surface contains a number of phases for which different average Volta potentials have been reported relative to the α-Mg matrix phase, i.e., Al-Mn + 257 mV, β-phase + 152 mV [33]. These differences could lead to the preferential migration of the $FcMeOH^+$ to the less noble regions, and would lead to an SECM map in which the relative feedback currents reflected the Volta potential differences. However, if such a contribution to the tip current exists, it is minimal since no difference in current resolution is detected between the β-phase and the Al-Mn in the system, the regions surrounding these features all showing low currents, Figure 8.10.

The CLSM evidence in Figure 8.12 confirms that the presence of FcMeOH is driving a slow but significant corrosion process, an influence requiring further investigation. However, as opposed to water, which is reduced predominantly on features such as the Al-Mn particles leading to corrosion of the α-matrix by microgalvanic coupling, the generated Fc^+ at the microelectrode tip reacts at the most

anodically reactive locations. According to the SECM and SEM maps in Figure 8.10 this order of reactivity is

α-Mg matrix > Al-containing eutectic > β-phase/Al-Mn

In this regard SECM provides a map of the anodic reactivity of the surface. While this may be intuitively surprising since $FcMeOH^+$ is a localized cathodic reagent, it most likely reflects the rapid kinetics of the $FcMeOH^+$/FcMeOH couple which dictates that reduction occurs on the most conductive location. In this somewhat surprising manner, SECM using an $FcMeOH^+$ mediator gives an excellent indication of the corrosivity of individual surface locations. A comparison of the SECM map to the CLSM image obtained for the corrosion of this alloy in an aqueous system confirms that the mechanism of corrosion in ethylene glycol is the same as in water, just considerably slower [26].

8.5 Summary and Conclusions

The corrosion of a sand cast AM50 Mg alloy was studied in ethylene glycol with and without added water. A combination of electrochemical and microscopic investigations showed that the mechanism of corrosion was the same in ethylene glycol as in water but considerably slower. Experiments in which water was added to the ethylene glycol demonstrated that water is the key cathodic reagent in this solvent not oxygen reduction or reduction of the ethylene glycol. By slowing the corrosion process and avoiding excessive H_2 production it was possible to map the corrosion response of the alloy by SECM using the redox mediator FcMeOH. The $FcMeOH^+$ produced at the microelectrode tip acted as an oxidant in the alloy surface taking part corrosion. Due to its rapid electron transfer kinetics the Fc^+ was reduced on the most conducting surface

locations to yield a map of the spatial distribution of anodic reactivity. The reactivity of the different surface phases were found to be in the order α-Mg matrix > Al-containing eutectic > β-phase/Al-Mn intermetallic confirming that the corrosion mechanism of the alloy is the same in ethylene glycol as it is in water. Reducing the corrosion rate of Mg alloys, without a large mechanistic change, through solvent selection presents a potentially valuable approach to analyzing the corrosion processes on Mg alloys with increased resolution and detail.

8.6 References

1. M.C. Zhao, M. Liu, G. Song, A. Atrens "Influence of β-phase morphology on the corrosion of the Mg alloy AZ91" *Corros. Sci.* 50 (2008) 1939-1953
2. S. Mathieu, C. Rapin, J. Steinmetz "A corrosion study on the main constituent phases of AZ91 magnesium alloys" *Corros. Sci.* 45 (2003) 2741-2755
3. H. Matsubara, Y. Ichige, K. Fujita, H. Nishiyama, & K. Hodouchi, "Effect of impurity Fe on corrosion behavior of AM50 and AM60 magnesium alloys". *Corros. Sci*. 66 (2013) 203-210
4. G. Baril, C. Blanc, M. Keddam, N. Pebere "Local electrochemical impedance spectroscopy applied to the corrosion behaviour of an AZ91 magnesium alloy" *J. Electrochem. Soc.* 150 (2003) B488-B493
5. G. Galicia, N. Pebere, B. Tribollet, V. Vivier "Local and global electrochemical impedance applied to corrosion behaviour of an AZ91 magnesium alloy" *Corros. Sci*. 51 (2009) 1789-1794

6. D. Bengtsson Blucher, J.E. Svensson, L.G. Johansson, M. Rohwerder, M. Stratmann "Scanning Kelvin probe force microscopy: A useful tool for studying atmospheric corrosion of MgAl alloys *in-situ*" *J. Electrochem. Soc.* 151 (2004) B621-B626
7. M. Jonsson, D. Thierry, N LeBozec "The influence of microstructure on the corrosion of AZ91D studied by scanning Kelvin probe force microscopy and scanning Kelvin probe" *Corros. Sci.* 48 (2006) 1193-1208
8. G. Williams, H.N. McMurray "Localized corrosion of magnesium in chloride containing electrolyte studied by a scanning vibrating electrode technique" *J. Electrochem. Soc.* 155 (2008) C340-C349
9. G. Williams, N. Birbilis, H.N. McMurray "The source of hydrogen evolved from a magnesium anode" *Electrochem. Commun.* 36 (2013) 1-5
10. K. B. Deshpande "Experimental investigation of galvanic corrosion: comparison between SVET and immersion techniques" *Corros. Sci.* 52 (2010) 2819-2826
11. Z.P. Cano, J.R. Kish, J.R. McDermid "Effect of surface condition on the localized corrosion behaviour of magnesium alloy AZ31B" *Magnesium Technology* 2014 335-339
12. D. Trihn, P. Dauphin Ducharme, U.M. Tefashe, J.R. Kish, J. Mauzeroll "Influence of edge effects on local corrosion rate of magnesium alloy/mild steel galvanic couple" *Anal. Chem.* 84 (2012) 9899-9906
13. S.V. Lamaka, O.V. Karavai, A.C. Bastos, M.L. Zheludkevich, M.G.S. Ferreira "Monitoring local spatial distribution of Mg^{2+}, pH and ionic currents" *Electrochem. Commun.* 10 (2008) 259-262

14. J. Izquierdo, L. Nagy, I. Bitter, R. Souto, G. Nagy "Potentiometric scanning electrochemical microscopy for the characterization of the electrochemical behaviour of magnesium-based materials" *Electrochim. Acta* 87 (2013) 283-293.
15. R.M. Souto, A. Kiss, J. Izquierdo, L. Nagy, I. Bitter, G. Nagy "Spatially resolved imaging of concentration distributions on corroding magnesium based materials exposed to aqueous environments by SECM" *Electrochem. Commun*. 26 (2013) 25-28
16. W. Liu, F. Cao, Y. Xia, L. Chang, J. Zhang "Localized corrosion of magnesium alloys in NaCl solutions explored by scanning electrochemical microscopy in feedback mode" *Electrochim. Acta* 132 (2014) 377-388
17. S.S. Jamali, S.E. Moulton, D.E. Tallman, M. Forsyth, J. Weber, G. G. Wallace "Applications of scanning electrochemical microscopy for local characterization of AZ31 surface during corrosion in a buffered media" *Corros. Sci.* (2014) *In-press*
18. U.M. Tefashe, M.E. Snowden, P. Dauphin Ducharme, M. Danaie, G.A. Botton, J. Mauzeroll 'Local flux of hydrogen from magnesium alloy corrosion investigated by scanning electrochemical microscopy" *J. Electroanal. Chem.* 720-721 (2014) 121-127
19. A.M. Fekry, M.Z. Fatayerji "Electrochemical corrosion behaviour of AZ91D in ethylene glycol" *Electrochim. Acta* 54 (2009) 6522-6528
20. D. Seifzadeh, H. Basharnavaz "Corrosion protection of AZ91 magnesium alloy in cooling systems" *Trans. Nonferrous Met. Soc. China* 23 (2013) 2577-2584

21. G. Song, D. St. John "Corrosion behaviour of magnesium in ethylene glycol" *Corros. Sci.* 46 (2004) 1381-1399

22. L. Wang, T. Zhou, J. Liang "Corrosion and self healing behaviour of AZ91D magnesium alloy in ethylene glycol/water solutions" *Mat. Corros.* 63 (2012) 713-719

23. T. J. Smith, K. J. Stevenson, *Handbook of Electrochemistry* (Ed.: C. G. Zoski), Elsevier, Amsterdam, **2007**, pp. 73-110

24. T. Cain, L.G. Bland, N. Birbilis, J.R. Scully "A compilation of corrosion potentials for magnesium alloys" *Corrosion* (2014) *in-press*

25. R.M. Asmussen, W. J. Binns, P. Jakupi, D.W. Shoesmith "Microstructural effects on the corrosion of AM50 Mg alloys" *J. Electrochem. Soc.* (2014) *submitted*

26. R.M. Asmussen, P. Jakupi, M. Danaie, G. Botton, D.W. Shoesmith "Tracking the corrosion of magnesium sand cast AM50 alloys in chloride environments" *Corros. Sci.*, 75 (2013) 114-122

27. M. Danaie, R.M. Asmussen, P. Jakupi, D.W. Shoesmith, G. Botton "The Cathodic behaviour of Al-Mn precipitates during atmospheric and saline aqueous corrosion of a sand-cast AM50 alloy" *Corros. Sci.* 83 (2014) 299-309

28. R.M. Asmussen, W.J. Binns, P. Jakupi, D. Shoesmith "Simulating the Corrosion Behaviour of a Cathodic Site in Mg Alloy Corrosion : The Electrochemical Behaviour of Al-Mn Intermetallics in NaCl and $MgCl_2$" *Electrochim. Acta* (2014) *submitted*

29. R. Cornut, S. Griveau, C. Lefrou "Accuracy study on fitting procedure of kinetics SECM feedback experiments" *J. Electroanal. Chem.* 650 (2010) 55-61

30. G.S. Frankel, A. Samaniego, N. Birbilis "Evolution of hydrogen at dissolving magnesium surfaces" *Corros. Sci*. 70 (2013) 104-111

31. G.A. Zhang, L.Y. Xu, Y.F. Cheng "Mechanistic aspects of electrochemical corrosion of aluminum alloy in ethylene glycol-water solution" *Electrochim. Acta* 53 (2008) 8245-8252

32. E. Slavcheva, G. Petkova, P. Andreev "Inhibition of corrosion of AZ91 magnesium alloy in ethylene glycol solution in presence of chloride anions" *Mat. Corros.* 56 (2005) 83-87

33. F. Andreatta, I. Apachitei, A.A. Kodentsov, J. Dzwonczyk, J. Dusczczyk "Volta potential of second phase particles in extruded AZ80 magnesium alloy" *Electrochim. Acta* 51 (2006) 3551-3557

Chapter Nine

Summary and Future Work

9.1 Summary

This thesis investigated the influence of microstructure on the corrosion of Mg alloys and approaches to reducing their high corrosion rates. A primary focus was placed on the importance of the cathodic behaviour in the microgalvanic coupling of the α-Mg matrix to the incorporated secondary phases.

A sand cast AM50 Mg alloy was used in initial studies to develop a methodology to analyze the importance of specific microstructural features on corrosion. From these studies the role of Al in the alloy was found to be three-fold: 1) increased Al content of individual α-Mg grains decreased the corrosion rate of the grain; 2) higher Al content in the eutectic α-Mg regions generated enrichment of Al at the alloy surface during the corrosion process, providing corrosion protection on these areas of the surface; and 3) depletion of the overall Al content in regions of the alloy led to their extensive corrosion.

Due to the important role of Al in the corrosion of the AM50 series of alloys, the effect of its distribution on the corrosion of the alloys was investigated. Three casts of the AM50 alloy (sand, graphite and die cast) were selected to limit compositional effects on corrosion and make the main variable the size and distribution of secondary microstructural features. The die cast AM50 alloy, comprised of the smallest microstructural features, was found to have the highest corrosion resistance. By reducing the size of the microstructural features, an alteration in corrosion damage morphology was also observed. The graphite cast and sand cast alloys sustained damage penetrating into the alloy, with the graphite cast showing a slightly enhanced resistance to major

corrosion events due to its more even distribution of Al. By contrast the die cast alloy showed damage propagation laterally along the alloy surface, a feature attributed to the more even distribution of Al which prevented penetration of corrosion into the alloy.

In the AM50 alloy studies, domes of corrosion product were observed to form during the corrosion process, mainly above Al-Mn intermetallics. In order to simulate the behaviour of the Al-Mn intermetallics on the Mg alloy surface, the cathodic behaviour of bulk Al-Mn alloys was studied in solutions of NaCl and $MgCl_2$. It was found that increased Mn content in the Al-Mn alloy decreased its cathodic activity towards water reduction. The implication of this observation is that Al-Mn intermetallics on Mg alloys with higher Mn content will be weaker cathodes if microgalvanically coupled to the α-Mg matrix. When cathodically polarized in NaCl, the Al-Mn alloy sustained extensive damage in Al rich regions and the growth of large $Al(OH)_3$ crystals and a much thinner Mn-oxide containing layer. These observations were a direct simulation of the delamination of Al and growth of Mn-oxides on Al-Mn intermetallic particles following corrosion of a Mg alloy. Contrarily, when cathodically polarized in $MgCl_2$, the Al-Mn alloys exhibited lowered currents and accumulated a layer of $Mg(OH)_2$ on their surface which reduced the damage sustained by the alloy to that observed in NaCl. These observations confirm that the presence of a corrosion product dome on a Mg alloy surface is an *ex-situ* indicator of cathodic behaviour on the feature beneath, and that development of such a dome reduces cathodic activity at that site.

Using the methodology developed to analyze the microscale corrosion of Mg alloys and identify localized anodes and cathodes, one of the first investigations into the corrosion behaviour of the Mg alloy ZEK100 was performed. The ZEK100

microstructure is comprised of an extensive α-Mg matrix, containing a wide dispersion of a Mg-Zn-Nd phase and Zr particles (some which have Fe contamination). Increasing the concentration of chloride in the solution was found to have a deleterious effect on the corrosion of ZEK100. The corrosion damage was observed to track laterally along the alloy surface, following the rolling direction of the alloy sheet. Domes of corrosion product were observed, an indication of cathodic activity, mainly above Zr-particles contaminated with Fe. By contrast pure Zr particles and the Mg-Zn-Nd phase were observed to remain free of corrosion product. To isolate the strongest cathodes in the microstructure the ZEK100 alloy was corroded in NanoPure® water, where corrosion damage was found to be restricted to areas around active cathodes. A large number of Mg-Zn-Nd and pure Zr particles were observed to be free of any corrosion product accumulation. FIB cross-sectioning of corrosion product domes on the alloy surface revealed Zr-Fe particles to be the primary locations sustaining cathodic activity. These findings demonstrated a solution ionic strength effect on the progress of corrosion damage on ZEK100, a preferential grain boundary attack in chloride solutions and that the strongest microgalvanically coupled cathodes to the α-Mg matrix were Zr particles contaminated with residual Fe.

When galvanically coupled to pure Mg, the AM50 Mg alloys were found to produce a net cathodic current. As a result of this galvanically coupled behaviour, the pure Mg acted as a sacrificial anode while the coupled AM50 alloys were much less corroded compared to freely immersed samples. This cathodic protection effect was simulated electrochemically by galvanostatically applying a cathodic current to the AM50 alloys. It was found that currents as low as -0.1 μA were successful in delaying

the onset of extensive corrosion without significantly polarizing the alloy away from its natural corrosion conditions. This effect was attributed to the ability of the applied current to satisfy the cathodic demand for current at the microstructural features such as the Al-Mn intermetallics, leading to a temporary decoupling of the microgalvanic linkage between these particles and the α-Mg matrix.

It is not only electrochemical control that can reduce the cathodic behaviour of features on Mg alloys. The corrosion behaviour of Mg alloys in ethylene glycol was studied and compared with the corrosion behaviour observed in aqueous environments. Ethylene glycol was selected to limit exposure of the Mg alloy to water and thus limit the kinetics of the dominant cathodic half reaction, water reduction. A large reduction in corrosion rate, was observed in ethylene glycol without any significant change in the morphology of the overall corrosion process. Upon introduction of water to a slowly corroding Mg alloy in ethylene glycol, a sharp increase in corrosion rate was observed. This reduced corrosion rate in ethylene glycol was exploited to monitor the corrosion process of the Mg alloy using SECM. The FcMeOH redox mediator provided an indicator of anodic activity on the Mg alloy surface with very high resolution. This study opens the door for future studies on the corrosion of Mg alloys using advanced analytical techniques to monitor hydrogen evolution and corrosion on Mg alloy surfaces.

An understanding of the role of cathodic sites is imperative in developing a full understanding of the Mg alloy corrosion mechanism. All Mg alloys will be susceptible to microgalvanic coupling and thus accelerated corrosion. Although a thermodynamic driving force for the dissolution of Mg will always exist in water, the corrosion processes

are governed by the kinetics of the cathodic reaction. The work done in this thesis supports the notion that the corrosion of Mg alloys is in fact under cathodic control.

9.2 Future Work

The methodology developed in this thesis, a combination of electrochemical corrosion testing with same spot analyses of areas of interest on an alloy surface with advanced electron microscopy techniques, is not limited to the AM50 and ZEK100 alloys presented here. The approach can be applied further to a wider range of Mg alloys, both novel and commercial to better understand the influence of microstructure on Mg alloy corrosion.

The enrichment of Al observed on the AM50 alloy surface during the corrosion process serves to protect the alloy. However, the mechanism by which it is achieved is not yet fully understood. To improve this understanding requires studies of different Al-containing Mg alloys, binary Mg-Al alloys, and the exposure of pure Mg to solutions containing Al^{3+} to determine whether the Al-rich layer develops via solid state process or by redeposition of the Al following its dissolution from the alloy surface.

Varying the size and distribution of microstructural features on the AM50 alloy was found to improve the corrosion resistance and induce an alteration in damage morphology on the alloy surface. A more detailed investigation of how microstructure size controls the damage morphology would help determine optimum microstructural features. This may be possible by studying a wedge cast Mg alloy, in which a single ingot has a consistently varying microstructure from the bottom to the top of the wedge. Investigating different casts of other Mg alloys is also a plausible next step.

In the ZEK100 study, the presence of chloride was found to allow longer distance coupling between the most active points on the alloy surface (grain boundaries) and the cathodic sites. Whether this is a result of solution conductivity, or a specific role played by chloride can be determined. Changing the electrolyte from chloride to other halides, or other anions such as sulphate, would present a logical approach to this investigation using a similar scope of work as employed throughout this thesis. If varying the anion is found to have a role in the overall corrosion rate and damage morphology, the exposure environment would need to be considered more widely in Mg corrosion analyses.

The corrosion rate of Mg alloys was found to be controllable through application of small cathodic currents to the alloy. The duration of this effect at different applied currents, its ability to reduce the corrosion rates on other Mg alloys and the determination of whether this is a static process or can be turned on/off, all remain unresolved. This area of research should be pursued due to the potential practical application of this phenomenon in automobile design. Addition of a current source near a Mg component susceptible to corrosion attack, such as a door panel, could be beneficial in increasing the lifetime of the component. Electrochemical detection of the onset of corrosion of the component, possibly by an impedance measurement, would initiate application of the current and potentially block the onset of extensive corrosion damage detrimental to the component's structural integrity. A combination of this technology with self-healing coatings could also be investigated, since it may be possible for a small applied current to protect the component for the time required for the coating repair process.

A reduction in the corrosion rate, and thus hydrogen production, on corroding Mg alloys to allow for advanced *in-situ* analytical techniques to function was achieved by

immersing Mg alloys in ethylene glycol. The use of electrochemical probe techniques, such as SECM and SVET can produce high resolution images and valuable information on local behaviour. By slowing down the overall corrosion the quantitative application of these techniques to Mg corrosion becomes possible. Studies in this area have the potential to allow presently intractable mechanistic details to be resolved.

The microscale analysis of Mg alloys presented in this thesis represents a further step in understanding the corrosion of Mg alloy. As with all science, the step following understanding is being able to successfully predict behaviour. This data and any collected in the future can be utilized in developing a successful and all-encompassing model to accurately predict the corrosion behaviour of Mg alloys. Initial steps in developing such a model can be utilizing knowledge of Al-distribution, growth of protective layers and cathode strength in microgalvanic couples to predict corrosion rates on single grain and small systems. In the future, accumulation rates of corrosion product on the alloy surfaces, localized pH changes and the hierarchy of cathodic sites in the alloy need to be determined experimentally and added to a successful model.

Curriculum Vitae

R. Matthew Asmussen
Department of Chemistry, University of Western Ontario

Education

Sept 2010- Jul 2014
PhD. Chemistry
University of Western Ontario
Thesis: The influence of microstructure on the corrosion of magnesium alloys
Supervisor: Dr. David Shoesmith

Sept 2007- Sept 2009
MSc. Chemistry
Lakehead University
Thesis: Electrochemical and *in-situ* infrared spectroscopic studies of Pt-based nanomaterials
Supervisor: Dr. Aicheng Chen

Sept 2003-Apr 2007
HBSc. Chemistry
Lakehead University

Research Employment

Sept 2009-Jul 2010
Research Assistant
Lakehead University
Project; Development and scale up of bifunctional electrode system for waste water treatment
Supervisor: Dr. Aicheng Chen

May – Aug 2006, 2007
Summer Research Student
Lakehead University
Supervisor: Dr. Aicheng Chen

Publications

1. **R.M. Asmussen**, W. Binns, P. Jakupi, D.W. Shoesmith "The influence of microstructure on the corrosion of magnesium alloy ZEK100" *Corrosion, Submitted June 2014*
2. **R.M. Asmussen**, W. Binns, P. Jakupi, P. Dauphin-Ducharme, U.M. Tefashe, J. Mauzeroll, D.W. Shoesmith "Reducing the corrosion rate of magnesium alloys using ethylene glycol for advanced electrochemical imaging" *Corrosion Science, Submitted June 2014*
3. **R.M. Asmussen**, W. Binns, P. Jakupi, R. Partovi-Nia, D.W. Shoesmith "Simulating the Corrosion Behaviour of a Cathodic Site in Mg Alloy Corrosion : The Electrochemical Behaviour of Al-Mn Intermetallics in NaCl and $MgCl_2$" *Electrochimica Acta, Submitted May 2014*
4. **R.M. Asmussen**, W. Binns, P. Jakupi, D.W. Shoesmith "The microstructural influences on the corrosion of magnesium alloys" *Journal of the Electrochemical Society, Submitted Apr 2014*
5. M. Danaie, **R.M. Asmussen**, P. Jakupi, D.W. Shoesmith, G. Botton "The cathodic behaviour of Al-Mn precipitates during atmospheric and saline aqueous corrosion of a sand-cast AM50 alloy" *Corrosion Science* 2014, 83, 299-309
6. M. Danaie, **R.M. Asmussen**, P. Jakupi, D.W. Shoesmith, G. Botton "The role of aluminum distribution on the local corrosion of the microstructure in a sand cast AM50 alloy" *Corrosion Science*, **2013**, 77, 151-163
7. **R.M. Asmussen**, P. Jakupi, M. Danaie, G. Botton, D.W. Shoesmith "Tracking the corrosion of magnesium sand cast AM50 alloys in chloride environments" *Corrosion Science*, **2013** , 75, 114-122
8. J. Chen, **R. M. Asmussen**, D. Zagidulin, J.J. Noel, D. W. Shoesmith "Electrochemical and Corrosion Behaviour of SS304 Based Metal Alloy in Six Solutions. *Corrosion Science*, **2012** , 66, 142-152
9. **Robert M. Asmussen**, B. Adams, A. Chen "Synthesis of Facile Pt-Pd nanodendrites for methanol oxidation" *Journal of Electroanalytical Chemistry*, **2012** 688, 151-157
10. B. Adams, **Robert Asmussen**, A. Chen, R. Mawhinney. " Interaction of carbon monoxide with small metal clusters: A DFT, electrochemical, and FTIR study" *Canadian Journal of Chemistry* **2011,** 89(12), 1445
11. **R. Matthew Asmussen**, P. Holt-Hindle, S. Nigro, A. Chen, "A comparative study of nanoporous Pt, PtRu and PtRuIr catalysts using electrochemical FTIR spectroscopy" *Journal of Electrochemistry* **2010**, V16(03), 263
12. M. Tian, J. Wen, D. MacDonald, **R.M. Asmussen**, A. Chen. "A novel approach for lignin modification and degradation" *Electrochemistry Communications* **2010**, 12, 527
13. **R. M. Asmussen**, M. Tian, A. Chen. "A novel approach to waste water remediation using bifunctional electrodes". *Environmental Science and Technology*, 2009, 43, 5100 (Featured by MIT's *Technology Review*, June 15, 2009; Highlighted by *The New York Times Syndicate*, June 2009; Profiled by the *Industrial Wastewater Newsletter* in October 2009)

14. M. Tian, B. Adams, J. Wen, **R. M. Asmussen**, A. Chen. "Photoelectrochemical oxidation of salicylic acid and salicylaldehyde on titanium dioxide nanotube arrays" *Electrochemica Acta*, 2009, 54, 3799
15. J. Wang, **R. M. Asmussen**, B. Adams, D. Thomas, A. Chen "Facile synthesis and electrochemical properties of intermetallic PtPb nanodendrites" *Chemistry of Materials*, 21, 2009, 1716
16. P. Holt-Hindle, S. Nigro, **R.M. Asmussen**, A. Chen. "Amperometric glucose sensor based on platinum-iridium nanomaterials" *Electrochemistry Communications* 10, 2008, 1438

Conference Proceedings

1. **R.M. Asmussen**, J. Binns, P. Jakupi, M. Danaie, G. Botton, D. Shoesmith "The microstructural effects on corrosion of AM50 alloys" Materials Science and Technology 2013, Montreal, QC, Oct 27-31 2013
2. **R.M. Asmussen**, D. Shoesmith, "Microelectrochemical and corrosion behaviour of metal alloy waste forms" Canadian Nuclear Society – 33rd Annual Conference of the Canadian Nuclear Society and 36th CNS/CAN Student Conference 2012: Building on Our Past..Building for the Future 2, 1346-1351
3. Aicheng Chen, **Robert M. Asmussen**, Shuai Chen, Christina Asmussen, Rachelle Laurin. "Synthesis and electrochemical study of Pd-based nanomaterials" *Physical Chemistry of Interfaces and Nanomaterials*: *Proc. Of SPIE*, **2011** Vol 8098, 80980Y-1

Patents

1. A. Chen, **R, M. Asmussen**, M. Tian: U.S. Provisional Patent Application No. 61/213,241 "Method and system for combined photocatalytic and electrochemical treatment of wastewater" Filed May 30, 2009
2. World Intellectual Property Office PCT Patent Application Serial # PCT/CA2010/000793, filed May 19, 2010
3. India Patent Application Serial Number 2751MUMP/2011, filed December 20, 2011
4. China Patent Application Serial Number 201080033251.X filed January 20, 2012
5. USA Patent Application Serial Number 13/321,425 filed November 18, 2011
6. Canadian Patent Application Serial Number 2762209 filed November 16, 2011

Conference Presentations (* denotes presenting author)

1. **R.M. Asmussen**, J. Binns, P. Jakupi, D. Shoesmith "Electrochemical impedance spectroscopy investigation of microstructural effects on the corrosion of magnesium alloys" 15th Topical Meeting of the International Society of Electrochemistry, Niagara Falls, ON, Canada. Apr 30, 2014
2. **R.M. Asmussen**, S. Wallon, D. Zagidulin, J.Noel, J. Chen, D. Shoesmith "The corrosion behaviour of metal alloy waste forms for the immobilization of Tc" NACE Corrosion 2014, San Antonio, TX, USA, Mar 10, 2014 **Winner: 1st place, Best Poster in Corrosion Engineering**
3. **R. M. Asmussen**, J. Chen, D. Zagidulin*, J. Noel, S. Wallon, U. Tefashe, J. Mauzeroll, D. Shoesmith "The corrosion behaviour of passive multi-phase metallic nuclear waste forms" 224th ECS Meeting, San Francisco, CA, USA, Oct 28, 2013
4. **R.M. Asmussen***, J. Chen, D. Zagidulin, J. Noel, D. Shoesmith "Corrosion behaviour of a metallic waste form for the immobilization of Tc" Materials Science and Technology, Montreal, QC, Oct 27-31, 2013
5. **R.M. Asmussen***, J. Binns, P. Jakupi, M. Danaie, G. Botton, D. Shoesmith "The microstructural effects on corrosion of AM50 alloys" Materials Science and Technology 2013, Montreal, QC, Oct 27-31 2013
6. M. Danaie*, **R. Asmussen**, P. Jakupi, D. Shoesmith, G. Botton "Site-specific microstructure characterization of the surface layer in a sand-cast Mg AM50 alloy corroded in aqueous NaCl solution" Materials Science and Technology 2013, Montreal QC, Oct 27-31, 2013
7. **R.M. Asmussen*,** S. Wallon, L. Wu, J. Chen, D. Zagidulin, J.J. Noel, D.W.Shoesmith "Effect of β-radiation on the corrosion of a metal alloy waste form" NACE Student Symposium, London, ON June 24, 2013
8. **R.M. Asmussen***, J. Chen, D. Zagidulin, J. Noel, D.W. Shoesmith "Development, evaluation and surface behaviour of metallic alloy waste forms" Surface Canada 2013, London, ON, May 8-10, 2013
9. **Asmussen R.M.***, Binns W.J., Jakupi P., Shoesmith D.W. "*Evaluation of the Surfaces of Corroding Magnesium Alloys"* Surface Canada 2013, London, ON, May 8-10, 2013 (Poster)
10. W.J. Binns*, **R.M. Asmussen**, P. Jakupi, D.W. Shoesmith "Electrochemical and microscopic investigations of the corrosion performance of AM50 magnesium alloys" Surface Canada 2013, London, ON May 8-10, 2013 (Poster)
11. S. Wallon*, **R.M. Asmussen**, D. Zagidulin, J. Chen. J. Noel, D.W. Shoesmith "The effect of H_2O_2 on the corrosion of metal alloy waste forms" Surface Canada 2013, London, ON May 8-10, 2013 (Poster)
12. **R.M. Asmussen***, D. Zagidulin, J.J. Noel, J Chen, D.W. Shoesmith "Electrochemical, microelectrochemical and scanning electrochemical probe investigations of the corrosion of multiphase alloy waste forms (MAWF)" Surface Canada 2013, London, ON May 8-10, 2013 (Poster)
13. **R. Matthew Asmussen***, P. Jakupi, W. Binns, P. Dauphin Ducharme, U. Telfase, J. Mauzeroll, D.W. Shoesmith "The effect of microstructure on the corrosion of Mg alloys" NACE Corrosion 2013, Orlando, FL, USA, Mar 17-21 2013 (Poster)

14. **R. Matthew Asmussen***, P. Jakupi, D.W. Shoesmith "Comparing and Tracking the Corrosion Behaviour of Die, Sand, and Graphite Cast AM50 alloys on the Microscale" NACE Northeast Area Meeting, Toronto, ON Oct 28-31 2012
15. **R. M. Asmussen***, P. Jakupi, D. W. Shoesmith "A Cumulative Approach to Tracking the Corrosion of Mg Alloys on the Microscale" PRiME 2012, Honolulu, HI, USA Oct 7 – 12, 2012
16. **R. Matthew Asmussen***, P. Jakupi, D.W. Shoesmith "A Novel Approach to Tracking the Corrosion of Mg Alloys" Gordon Research Conference, New London, NH, USA, Jul 8-13 2012 (Poster)
17. **R. Matthew Asmussen***, P. Jakupi, D.W. Shoesmith "A Novel Approach to Tracking the Corrosion of Mg Alloys" Gordon Research Seminar, New London, NH, USA, Jul 6-7 2012 (Poster)
18. **R. Matthew Asmussen*,** P. Jakupi, D.W. Shoesmith "Tracking the Corrosion of Mg Alloy AM50 on the Microscale" NACE Northeastern Student Conference, Toronto, ON, June 25 2012
19. **R. Matthew Asmussen***, D.W. Shoesmith "Microelectrochemical and Corrosion Behaviour of Metal Alloy Waste Forms" 2012 Annual Conference of the Canadian Nuclear Society, Saskatoon, SK, June 10-13 2012 (Poster)
20. **R. Matthew Asmussen***, D.W. Shoesmith "Large Scale and Microelectrochemical study of Fe" NACE Northeastern Conference, Ottawa, ON, August 2011 (Poster)
21. A. Chen*, J. Wang, **R. M. Asmussen**, B. Adams, G. Wu, P. Holt-Hindle and D. Thomas "Synthesis and electrochemical study of Pt-based nanostructured materials" Electrochemical Society Annual Meeting, Vancouver, BC, June 2010
22. A. Chen*, **R. M. Asmussen**, M. Tian, J. Wen, N. Matyasovsky, Tolba, R "Photoelectrochemical catalysis based on bifunctional electrodes" 93rd Canadian Society for Chemistry Annual Conference, Toronto, ON, May, 2010
23. **R. M. Asmussen***, A. Chen. "Bifunctional electrodes: A new approach to wastewater treatment" Surface Canada Conference, Hamilton, ON June 2009
24. **R. M. Asmussen***, A. Chen. "Electrochemical and spectroscopic study of Pt-based nanomaterials" 92nd Canadian Society for Chemistry Annual Conference, Hamilton, ON, May 2009
25. **R. Matthew Asmussen***, Aicheng Chen. "Development of an *in-situ* electrochemical ATR-FTIR system for the study of Pt Nanomaterials" Lakehead University Graduate Conference, Feb 2009, Thunder Bay, ON (Poster)
26. G. Wu*, J. Wen, D. MacDonald, **R. M. Asmussen**, A. Chen "Photoelectrochemical treatment of lignin and lignin model compounds" PAPTAC Conference, Montreal, QC, Feb 2009
27. **R. M. Asmussen***, A. Chen "A New Approach to Water Purification Using Photoelectrochemical Bifunctional Electrodes" Lakehead University Graduate Conference, Feb 29, 2008
28. JP Wang*, **R. Matthew Asmussen**, Aicheng Chen, "Synthesis and characterization of Pt-Nanomaterials" Canadian Nanoforum, Windsor, ON, Jun. 2007 (Poster)

29. JP Wang*, **R. Matthew Asmussen**, Aichen Chen "Pt, Pt-Au, Pt-Bi nanomaterials, synthesis and study" Canadian Society of Chemists Annual Conference, Winnipeg, MB, May 2007 (Poster)
30. **R. M. Asmussen***, A. Chen, "Novel Bifunctional Electrodes for Remediation of Waste Water" Canadian Society of Chemists Annual Conference, Winnipeg, MB, May 2007 (Poster)
31. **R. Matthew Asmussen***, Aicheng Chen, "The development of novel bifunctional electrodes" Lakehead University Graduate Conference, Thunder Bay, ON, Feb 2008
32. **R. M. Asmussen***, A. Chen, "Electrochemical ATR-FIT System Design and Development" Electrochemical Society Of Canada Symposium, Thunder Bay, ON, Sept 2006 National (Poster)

Awards

1. Dr. N. Stewart McIntyre Award in Surface Science, May 2014
2. 1st Place Poster, Mars Fontana Corrosion Engineering Category, NACE Corrosion 2014 Conference, March 2014
3. Ontario Graduate Scholarship, May 2013
4. NACE Foundation International Student Academic Scholarship, Mar 2013
5. Ontario Graduate Scholarship, May 2012
6. Queen Elizabeth II Graduate Scholarship in Science and Technology, May 2012 (declined)
7. CSC 2004 Student Travel Award, Apr 2012
8. Ontario Graduate Research Scholarship, May, 2011
9. Western Graduate Research Scholarship, Sept 2010
10. Lakehead University Student Innovation Award, Apr 2010
11. Northern Ontario Heritage Fund Internship, Lakehead University, Oct 2009 – Jul 2010
12. David Jones Scholarship, Lakehead University, Sept 2007
13. Silver Jubilee Scholarship, Lakehead University, Sept 2007
14. Undergraduate Research Travel Award, Canadian Society for Chemistry, Analytical Division, May 2007
15. Ross Rogers Award in Science, Lakehead University, Aug 2003
16. Lakehead University Entrance Award, Aug 2003

"Would you rather have a good meal or great sex?"

"That's really a qualitative answer, depends on who's cooking and who's …"

-Anthony Bourdain